

# Functionalization of harmonic nanoparticles for drug release and multimodal imaging applications

Présentée le 23 février 2024

Faculté des sciences de base  
Groupe SCI SB SG  
Programme doctoral en chimie et génie chimique

pour l'obtention du grade de Docteur ès Sciences

par

**Adrian Stefan GHEATA**

Acceptée sur proposition du jury

Dr R. Hovius, président du jury  
Prof. S. Gerber, directrice de thèse  
Prof. I. Herrmann, rapporteuse  
Prof. O. Mongin, rapporteur  
Prof. K. Severin, rapporteur



## Acknowledgment

During those four years of doctoral studies, I was lucky to work in an exciting environment at EPFL and work with some delightful people, whom I would like to thank for their participation and support.

First of all, I would like to warmly thank Prof. Sandrine Gerber-Lemaire for giving me the chance to work on this exciting and stimulating project in her group. Her counsel, support and dedication to her students make her an incredible supervisor, and I am very grateful for all the help she has provided me during this thesis and manuscript redaction.

I would like to cordially thank the members of the jury, Prof. Severin Kay, Prof. Inge Herrmann and Prof. Olivier Mongin, for taking their precious time to examine my manuscript and evaluating my thesis. I would also like to thank the chair of the jury, Dr. Rudolf Hovius.

I am deeply grateful to all members of the SYMME team from Annecy, especially Prof. Ronan Le Dantec, Prof. Yannick Mugnier, Florian Riporto and Ammeni Dhoub for all their help synthesizing and delivering the nanoparticle samples vital to this work.

My sincere thanks to our collaborators from the Nonlinear BioImaging group. I would like to thank Prof. Luigi Bonacina for welcoming me in Geneva, for his support all along this project and his expertise on the physical side. My deep thanks to Geoffrey Gaulier and Paulí Llussà for their invaluable help with all the imaging-related experiments, without whom this thesis would have been impossible.

I wish to warmly thank Prof. Dario Diviani, Dr. Davide Staedler, Simon Kaiser and Ivan Gautschi from UNIL for their kind assistance with the biological evaluation of our nanoparticle samples.

An enormous thanks to Dr. Anne-Sophie Chauvin for all her support with the lanthanide luminescence experiments, and for the time she took helping me with the manuscript redaction. I would also like to thank Dr. Aurélien Bornet and Dr. Laura Piveteau from the NMR service, and Dr. Katarzyna Pierzchala from the CIBM for their help evaluating the MRI properties of gadolinium-functionalized nanoparticles.

I would like to thank the members of the MS platform at EPFL, especially Dr. Daniel Ortiz for his dedication and support. My warm thanks to Dr. Rita Therisod from the CIME facility for her kindness and all her help with the TEM analysis and training. I also want to thank the personnel of the CH magasin, in particular Jacques Gremaud and Maurizio Maio for their good mood and their continuous assistance.

I would like to especially thank all present and former members of the GBF group with whom I shared this lab. Luca, for the times we spent together gossiping around a beer, Laura, for her incredible kindness and joyfulness, Perrine, for the coffee-break discussions and dedication to maintaining an impeccable lab, Mayoutz, for our spontaneous and improbable amazing trips, Franky, for his chill vibes and for being a great fumehood neighbor, Alessandra, for her patience and for working with me on this project, Ali, for his warmheartedness, and Anna, for the late nights in the lab and the climbing sessions. My special thanks to all the apprentices and master students I had the chance to supervise during this project, who were all a huge help: Elias, Amelie, Laetitia, Selena, Mael, Manon, and particularly Simswim, who had the courage to endure me for two consecutive projects. Thanks also to Jérémy, Céline, Élise, Ines, Sara, Pauline and Vanessa, who helped create a great atmosphere. I would also like to thank Lorenz and the LPDC lab, with whom I shared some fun times during this PhD.

My special thanks to Raph, from whom I inherited this project, my desk, my fumehood and apparently somehow many work habits: for our unending DnD campaigns, culinary escapades and all the great people he has introduced me to. I am also very grateful to all my friends, for all the good times spend together: Remrem, Steph, Charline, Quentin, Marie, Raph, Pam, Nancy, Manu, Fred, Thomas, Luca, Lea, and Ylann.

Finally, my deepest gratitude to my family, and particularly my mom and dad, who have always driven me to do my best, who have always been there for me, for their unwavering support and without whom I wouldn't have achieved any of this. Vă mulțumesc din suflet.



## Abstract

Cancer is among the leading causes of death worldwide, and as knowledge of the disease continues to grow there is an increasing interest towards precision medicine: more specifically towards the theranostics field, i.e the development of targeted molecular probes combining specific diagnosis and treatment modalities. The theranostic paradigm involves merging, in a single agent, specific tumor biomarker targeting, multimodal imaging techniques which allow to overcome the inherent limitations of classical methods, and the controlled delivery of anticancer compounds. This strategy thus aims at high diagnosis sensitivity for earlier tumor detection and the reduction of off-target effects, which are critical factors in patient survival rates. In this context, inorganic nanoparticles emerge as promising tools owing to their surface properties, which are amenable to post-functionalization, and their imaging properties.

The goal of this project is to usher in the development of such multimodal theranostic tools based on harmonic nanoparticle (HNP) materials. These metal oxide nanomaterials, characterized by a crystalline structure lacking inversion symmetry (e.g  $\text{LiNbO}_3$ ), exhibit a non-linear optical response by generating second- and third- harmonic signals upon laser excitation. A silica-based coating layer allows for improved biocompatibility of the inorganic HNPs and for the introduction of surface azide moieties, which are exploited for subsequent functionalization through bioorthogonal copper-free click reaction with cyclooctyne-modified ligands, or standard copper-catalyzed click chemistry with alkyne-modified ligands.

Light-sensitive drug carriers are produced by the grafting of chemotherapeutics to the surface of HNPs through photosensitive tethers based on coumarinyl moieties. Irradiation of the HNPs with near-infrared (NIR) light allows switching between imaging and treatment modalities by tuning of the excitation energy. Excitation at high wavelengths ( $> 1000$  nm) is used for multi-harmonic detection, while lower wavelengths ( $\sim 800$  nm) results in the harmonic emission of ultraviolet light, inducing cleavage of the phototrigger and release of the therapeutic cargo.

In addition, the HNPs can be covalently conjugated to a lanthanide (III) chelate, potentially acting as an MRI/X-ray contrast agent or a luminescent probe depending on the lanthanide atom chosen while maintaining the intrinsic optical properties of HNPs, thereby paving the way for multimodal imaging.

In summary, this project aims at developing a theranostic nanoplatform for controlled therapeutic cargo delivery upon NIR irradiation and multimodal detection by combining optical and magnetic resonance imaging, based on nanoparticle platforms functionalized by bioorthogonal reactions. Those nanoprobles have the potential to provide a high level of sensitivity for the early detection of cancer, and high potency for *in vivo* cancer treatment.

**Keywords:** harmonic nanoparticles, silanization, drug delivery, photo-release, multimodal imaging, theranostic

## Résumé

Le cancer est l'une des principales causes de décès dans le monde et, à mesure que les connaissances sur la maladie continuent de croître, la médecine de précision gagne de plus en plus d'intérêt : plus particulièrement le domaine de la théranostique, soit le développement de sondes moléculaires ciblées combinant des modalités de diagnostic et de traitement spécifiques. Le paradigme théranostique implique la fusion, en un seul agent, du ciblage de biomarqueurs tumoraux spécifiques, de techniques d'imagerie multimodales qui permettent de surmonter les limites inhérentes aux méthodes classiques et de l'administration contrôlée de composés anticancéreux. Cette stratégie a ainsi pour objectif une sensibilité de diagnostic élevée pour une détection précoce des tumeurs et la réduction des effets secondaires, qui sont des facteurs critiques pour le taux de survie des patients. Dans ce contexte, les nanoparticules inorganiques apparaissent comme des outils prometteurs en raison de leurs propriétés de surface, susceptibles d'être fonctionnalisées, et de leurs propriétés d'imagerie.

L'objectif de ce projet est à terme le développement de tels outils théranostiques multimodaux basés sur des matériaux à nanoparticules harmoniques (HNP). Ces nanomatériaux d'oxyde métallique, caractérisés par une structure cristalline dépourvue de symétrie d'inversion (par exemple  $\text{LiNbO}_3$ ), présentent une réponse optique non linéaire en générant des signaux de deuxièmes et troisièmes harmoniques lors de l'excitation avec un laser. Une couche de revêtement à base de silice permet d'améliorer la biocompatibilité des HNPs inorganiques et d'introduire des groupements azide de surface, qui sont exploités pour une fonctionnalisation ultérieure par une réaction clic bio-orthogonale sans cuivre avec des ligands modifiés par cyclooctyne, ou une chimie clic standard catalysée au cuivre avec des ligands comportant un alcyne.

Les supports de médicaments photosensibles sont produits par greffage de produits chimiothérapeutiques à la surface des HNPs via des ligands photosensibles basés sur des dérivés de coumarine. L'irradiation des HNPs avec une lumière proche infrarouge (NIR) permet de basculer entre les modalités d'imagerie et de traitement en modifiant l'énergie d'excitation. L'excitation aux longueurs d'onde élevées ( $> 1000$  nm) est utilisée pour la détection multi-harmonique, tandis que les longueurs d'onde inférieures ( $\sim 800$  nm) entraînent l'émission harmonique de lumière ultraviolette, induisant le clivage du ligand photosensible et la libération de la cargaison thérapeutique.

De plus, les HNPs peuvent être conjugués de manière covalente à un chélate de lanthanide (III), agissant potentiellement comme un agent de contraste IRM/rayons X ou une sonde luminescente en fonction de l'atome de lanthanide choisi tout en conservant les propriétés optiques intrinsèques des HNPs, ouvrant ainsi la voie vers l'imagerie multimodale.

En résumé, ce projet vise à développer une nano-plateforme théranostique pour l'administration contrôlée de marchandises thérapeutiques par irradiation NIR et détection multimodale en combinant l'imagerie par résonance optique et magnétique, basée sur des plateformes de nanoparticules fonctionnalisées par des réactions bio-orthogonales. Ces nano-sondes ont le potentiel de fournir un niveau élevé de sensibilité pour la détection précoce du cancer et une grande capacité de traitement du cancer *in vivo*.

**Mots clés :** nanoparticules harmoniques, silanisation, administration de médicaments, ligand photosensible, imagerie multimodale, théranostique.





## Abbreviations

<b>ACN</b>	Acetonitrile
<b>AcOH</b>	Acetic acid
<b>APTES</b>	(3-Aminopropyl)triethoxysilane
<b>aq.</b>	Aqueous
<b>AuNPs</b>	Gold nanoparticles
<b>BFO</b>	Bismuth ferrite, BiFeO <sub>3</sub>
<b>Boc</b>	Tert-butoxycarbonyl
<b>calcd.</b>	Calculated
<b>CM</b>	Coumarin
<b>CT</b>	Computed tomography
<b>CTC</b>	2-chlorotriethyl chloride
<b>DAPI</b>	4',6-diamidino-2-phenylindole
<b>DCC</b>	<i>N,N'</i> -Dicyclohexylcarbodiimide
<b>DCE</b>	Dichloroethane
<b>DCM</b>	Dichloromethane
<b>DIBO</b>	4-Dibenzo-cyclooctyne
<b>DIPEA</b>	<i>N,N</i> -Diisopropylethylamine
<b>DLS</b>	Dynamic light scattering
<b>DMA</b>	Dimethyl acetamide
<b>DMAP</b>	4-Dimethylaminopyridine
<b>DMEM</b>	Dubelcco's modified Eagle medium
<b>DMF</b>	Dimethylformamide
<b>DMSO</b>	Dimethyl sulfoxide
<b>DNA</b>	Deoxyribonucleic acid
<b>DOX</b>	Doxorubicin
<b>EDC</b>	1-Ethyl-3-(3-dimethylaminopropyl)carbodiimide
<b>EGFR</b>	Epidermal growth factor receptor
<b>EPR</b>	Enhanced permeability and retention

<b>eq.</b>	Equivalent
<b>ELA</b>	Erlotinib-amine
<b>ESI-MS</b>	Electrospray ionization-mass spectrometry
<b>Et<sub>3</sub>N</b>	Triethylamine
<b>EtOAc</b>	Ethyl acetate
<b>EtOH</b>	Ethanol
<b>EDX</b>	Energy-dispersive X-ray spectroscopy
<b>FBS</b>	Fetal bovine serum
<b>FC</b>	Flash chromatography
<b>FCS</b>	Fetal calf serum
<b>FDA</b>	Food and drug administration
<b>Fmoc</b>	Fluorenylmethyloxycarbonyl
<b>Gly</b>	Glycine
<b>h</b>	Hour
<b>HATU</b>	Hexafluorophosphate azabenzotriazole tetramethyl uronium
<b>HNPs</b>	Harmonic nanoparticles
<b>HOBt</b>	Hydroxybenzotriazole
<b>HRMS</b>	High Resolution Mass Spectrometry
<b>IONPs</b>	Iron oxide nanoparticles
<b>IR</b>	Infrared
<b>LNO</b>	Lithium niobate, LiNbO <sub>3</sub>
<b>Lys</b>	Lysine
<b>MDR</b>	Multi-drugs resistance
<b>MeOH</b>	Methanol
<b>MONB</b>	<i>meta</i> -methoxy- <i>ortho</i> -nitrobenzyl
<b>MRI</b>	Magnetic resonance imaging
<b>MSNs</b>	Mesoporous silica nanoparticles
<b>NaAsc</b>	Sodium Ascorbate
<b>NHS</b>	<i>N</i> -Hydroxysuccinimide
<b>NIR</b>	Near-infrared
<b>NMR</b>	Nuclear magnetic resonance

<b>NPs</b>	Nanoparticles
<b>ONB</b>	<i>ortho</i> -Nitrobenzyl
<b>PAT</b>	Photoacoustic tomography
<b>PBS</b>	Phosphate-buffered saline
<b>PDT</b>	Photodynamic therapy
<b>PE</b>	Petroleum ether
<b>PEG</b>	Polyethylene glycol
<b>PEI</b>	Polyethylene-imine
<b>PET</b>	Positron-emission tomography
<b>PFP-OH</b>	Pentafluorophenol
<b>ppm</b>	Parts-per-million
<b>PTT</b>	Photothermal therapy
<b>Py</b>	Pyridine
<b>QDs</b>	Quantum dots
<b>r.t.</b>	Room temperature
<b>redox</b>	Reduction-oxidation
<b>RES</b>	Reticuloendothelial system
<b>RNA</b>	Ribonucleic acid
<b>ROS</b>	Reactive-oxygen species
<b>RP</b>	Reverse phase
<b>rpm</b>	Rotation per minute
<b>sat.</b>	Saturated
<b>SHG</b>	Second-harmonic generation
<b>siRNA</b>	Small interfering ribonucleic acid
<b>SPECT</b>	Single-photon-emission computerized tomography
<b>SPION</b>	Superparamagnetic iron oxide nanoparticles
<b>SPR</b>	Surface plasmon resonance
<b>STEM</b>	Scanning transmission electron microscopy
<b>TEG</b>	Tetraethylene glycol
<b>TEOS</b>	Tetraethyl orthosilica
<b>TFA</b>	Trifluoroacetic acid

<b>THF</b>	Tetrahydrofuran
<b>THG</b>	Triple-harmonic generation
<b>THTPA</b>	Tris(3-hydroxypropyltriazolylmethyl)amine
<b>TLC</b>	Thin layer chromatography
<b>Trp</b>	Tryptophan
<b>UCNPs</b>	Upconversion nanoparticles
<b>UHPLC</b>	Ultra High Performance Liquid Chromatography
<b>US</b>	Ultrasound
<b>UV</b>	Ultra-violet
<b>XIC</b>	Extracted ion chromatograms



# Table of Contents

Acknowledgment.....	iii
Abstract.....	vi
Résumé.....	vii
Abbreviations.....	x
<b>1. Introduction.....</b>	<b>1</b>
1.1. Context.....	1
1.2. Cancer Diagnosis and treatment.....	2
1.3. Nanoparticles in oncology.....	4
1.3.1. <i>Inorganic nanoparticles</i> .....	6
1.3.2. <i>Harmonic nanoparticles</i> .....	8
1.3.3. <i>Nanoparticle surface functionalization</i> .....	10
1.4. Light-triggered drug release.....	13
1.4.1. <i>Photosensitive systems</i> .....	13
1.4.2. <i>NIR light responsive nanomaterials</i> .....	15
1.5. Multimodal imaging.....	18
<b>2. Presentation of the project.....</b>	<b>23</b>
<b>3. Results and Discussion.....</b>	<b>27</b>
3.1. Silica coatings of nanoparticles and introduction of reactive moieties.....	27
3.1.1. <i>Silanization by standard Stöber process</i> .....	29
3.1.2. <i>Coating by water-in-oil microemulsion</i> .....	32
3.1.3. <i>Surface peptide functionalization</i> .....	36
3.2. Stimuli responsive nanocarriers.....	42
3.2.1. <i>Synthesis of the drug delivery system</i> .....	43
3.2.2. <i>Nanoparticle functionalization with the drug delivery system</i> .....	46
3.2.3. <i>In vitro tests</i> .....	50
3.3. Lanthanide functionalization towards multimodal HNPs.....	53
3.3.1. <i>Synthesis of alkyne-lanthanide complexes and HNP functionalization</i> .....	54
3.3.2. <i>Synthesis of cyclooctyne-lanthanide complexes and HNP functionalization</i> .....	57
3.3.3. <i>Assessment of dual imaging capabilities</i> .....	61
<b>4. Conclusion and outlooks.....</b>	<b>70</b>
<b>5. Experimental.....</b>	<b>74</b>
5.1. General Information.....	74
5.2. Synthesis of cyclooctyne derivatives.....	76
5.3. Synthesis of coumarinyl linker.....	83
5.4. Synthesis of erlotinib delivery system.....	91
5.5. Synthesis of DIBO-ELA control.....	97
5.6. Synthesis of L-homoserine derivative.....	99
5.7. Synthesis of bi-substituted triazacyclononane TACNB.....	103
5.8. Synthesis of the alkyne lanthanide (III) ligand and Ln complexes.....	108
5.9. Synthesis of the cyclooctyne lanthanide (III) ligand and Ln complexes.....	113
5.10. Synthesis of azide modified APTES.....	128
5.11. Synthesis of carboxyl modified APTES: APTES-COOH.....	133
5.12. Synthesis of azidolysine (Alys) amino acid.....	135
5.13. Synthesis of triazidoalysine (Talys) peptide.....	139

5.14. Synthesis of tri-tetrazine peptide .....	142
5.15. Nanoparticle silica coating.....	145
5.16. Nanoparticle functionalization .....	148
5.17. Photorelease assays.....	154
5.18. <i>In vitro</i> experiments .....	162
5.19. Lanthanide nanoparticles imaging.....	163
<b>6. References .....</b>	<b>166</b>
<b>7. Curriculum vitae.....</b>	<b>181</b>





# 1. Introduction

## 1.1. Context

Cancer is a major health issue worldwide and is the second cause of death in industrialized countries after cardiovascular diseases. <sup>1</sup> The World Health Organization estimated in their GLOBOCAN report that in 2020, more than 19 million new patients suffered from some form of cancer, and that this disease accounted for almost 10 million deaths (*cf. Figure 1*). <sup>2</sup> These numbers are expected to almost double by 2040, which can be explained by the increase in lifetime expectancy and by risks associated with our lifestyle (obesity, sun overexposure, alcohol and cigarette consumption, etc.). In 2020, lung cancer has been reported as the number two in number of new diagnosed cases (2.2 million) and number one in related deaths (1.8 million). Despite affecting mostly only the female population, the number of new breast cancer cases was higher to those of lung cancer, and it represents the first cause for cancer-related deaths in female patients. The third most diagnosed cancer and second in number of deaths, both sexes included, was colorectal cancer with 1.9 million new cases and 0.9 million deaths.

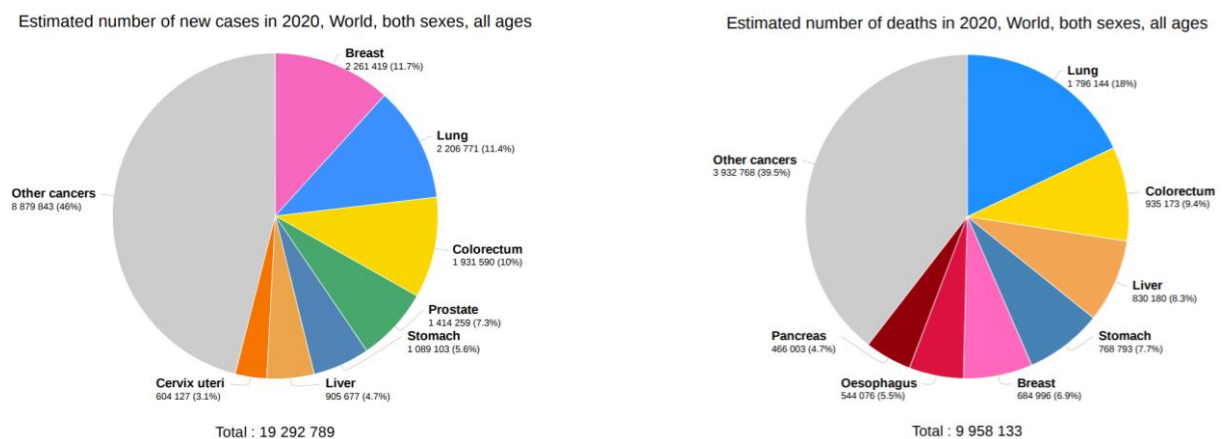


**Figure 1:** Estimated number of total cancer-related new cases and deaths in 2020. “Reprinted (adapted) from Global cancer statistics 2020: GLOBOCAN estimates of incidence and mortality worldwide for 36 cancers in 185 countries. CA: A Cancer Journal for Clinicians. Copyright (2020).”

It is known that the appearance and growth of malignancies is a long process and that telltale symptoms usually only appear when the cancer has reached a more advanced state. Therefore, sensitive and reliable diagnosis methodologies, at early stages of tumor development, are crucial to increase patient survival and remission rates. <sup>3</sup> In addition to early diagnosis, improvements in the therapeutic strategies must be achieved to reduce the side effects of treatments and increase their efficiency. <sup>4</sup>

## 1.2. Cancer Diagnosis and treatment

Nowadays, cancer diagnosis often begins with the detection of specific biomarkers in bodily fluids (blood, serum, and urine).<sup>5</sup> A variety of imaging techniques are then used to attempt observation of the malignant cells, and finally cancer suspicion is confirmed by the removal and analysis of potential tumor tissue through surgical biopsy.<sup>6</sup> Standard imaging techniques include non-invasive (magnetic resonance imaging (MRI), computed tomography (CT), and ultrasound imaging (US)) and invasive methods (positron emission tomography (PET), and single-photon emission computed tomography (SPECT)).<sup>7</sup>

MRI produces contrast in tissues by measuring the relaxation process of  $^1\text{H}$  atoms in different microenvironments when exposed to a radio frequency pulse in a static magnetic field, and often requires injection of contrast agents to achieve an improved resolution. MRI is useful for anatomical imaging of soft tissue due to its deep tissue penetration and high spatial resolution.<sup>8</sup>

In CT scanning, several pictures are taken by X-ray irradiation at different angles to construct a three-dimensional image of the targeted area. CT, exhibiting high spatial resolution with short acquisition times, is mostly used for diagnosing the head, lung, and abdominal regions.<sup>9</sup>

US imaging involves reflecting high frequency broadband sound waves with deep penetration ability on tissues, in order to generate real-time two-dimensional images of the body.<sup>10</sup>

PET and SPECT both require the injection of a radionuclide in the patient to generate a three-dimensional image by detection of the emitted  $\gamma$ -rays. SPECT detects directly emitted  $\gamma$ -rays, whereas PET is based on the radiation emitted by positron decay, and both techniques are heavily used in cancer diagnosis due to their high sensitivity and deep tissue penetration.<sup>11,12</sup>

All imaging techniques have their own shortcomings which can induce diagnosis mistakes. MRI has low sensitivity, which makes long acquisition times necessary as well as potentially using contrast agents.<sup>13</sup> CT, PET and SPECT are all limited by the radiation exposure of the subject.<sup>14,15</sup> This has led to the emergence of the multimodality field, the concept being to design hybrid systems synergistically combining different imaging techniques in order to overcome their individual drawbacks. This aspect will be covered with more details in section 1.5.

Modern cancer treatment involves either surgery, radiotherapy, or chemotherapy, or a combination of these modalities. Surgery consists in excising the tumor from the patient, which is only done if the malignant tissues are limited to a single area. Radiotherapy uses ionizing X-rays, applied by an external beam or internal radiation source, to kill cancer cells or slow their growth by damaging their genetic material.<sup>16</sup> Chemotherapy is based on the administration of highly cytotoxic drugs to induce cancer cells death. These pharmaceuticals include for example alkylating agents which act directly on the cell's DNA (e.g. cisplatin, chlorambucil), antimetabolites which disturb cell metabolism and protein synthesis (e.g. methotrexate, 5-fluorouracil), and antitumor antibiotics which prevent cell reproduction (e.g. doxorubicin, dactinomycin).<sup>17</sup> All these therapeutic compounds suffer from the same limitation, their poor selectivity. This, combined with their high toxicity is responsible for heavy off-target effects which may lead to severe and even lethal conditions.<sup>18</sup> An innovative treatment option that has been investigated is cancer immunotherapy, the goal being to reprogram the patient's immune system to be able to recognize and fight off malignancies: this can be typically achieved for instance with monoclonal antibodies designed to bind specifically cancer cells.<sup>19</sup> This approach allows for much more targeted

treatments, but are still devoid of side effects, as an overactivity of the immune system can lead to severe and unpredictable adverse reactions.<sup>20</sup>

Another potential way to overcome these limitations which has attracted interest in the past decades is the theranostic approach: i.e. the development of single agents combining therapeutic and diagnostic capabilities.<sup>21</sup> The design of systems which combine cancer targeting, multimodal imaging, and drug delivery could offer the option to image and monitor the diseased tissue, delivery kinetics, and drug efficacy with the hope of gaining the ability to adapt the therapy with unprecedented control. In particular, the tunable size and the versatility of the surface properties of nanoparticles have turned nanoprobe into the perfect candidates for potential multimodal theranostic tools (*cf. Figure 2*).

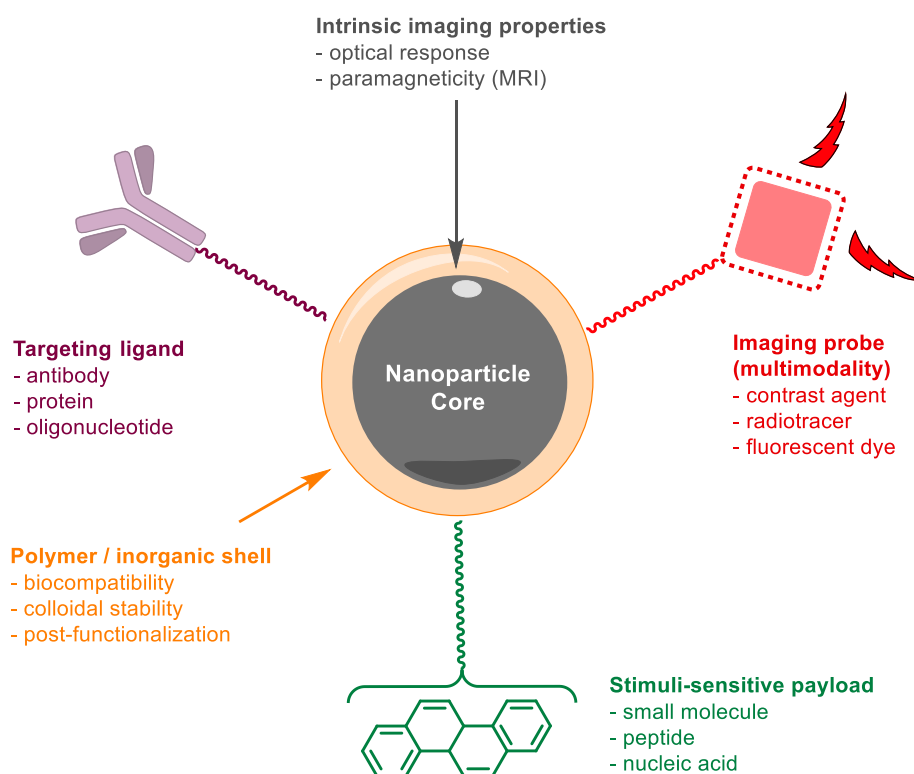


**Figure 2:** Schematic representation of a theranostic multimodal nanoprobe

### 1.3. Nanoparticles in oncology

Nanoparticles (NP) have emerged as promising systems for applications in oncology due to their unique properties. These characteristics include a small size ranging usually from 1 to 100 nm, a high surface area to volume ratio, and an ease of surface functionalization allowing for targeting, imaging, and therapeutic ability: this makes them potentially ideal tools for theranostic applications.<sup>22</sup> The broad variety of NP materials available allow for tuning of these unique physicochemical properties, such as size, shape, and surface charge, necessary in overcoming the numerous barriers present in biological systems.<sup>23</sup> One typical obstacle to NP delivery to a targeted site is the sequestration by the reticuloendothelial system (RES) and the clearance by the immune system, in which size and surface characteristics of the NP play an important role. It has been reported that smaller NPs (< 200 nm) tend to evade the RES more easily, and that surface hydrophilicity achieved by coating with certain polymers (e.g. dextrans and PEGs) is also beneficial as this limits the opsonization phenomenon (i.e. the coating of a foreign body by non-specific proteins in biological media leading to immune detection).<sup>24</sup> Fine tuning of the physicochemical properties of NP materials is necessary. For instance, in the case of size, bigger NPs have the advantage of exhibiting higher accumulation at the tumor site.<sup>25</sup>

Nanotheranostics provide several improvements over traditional cancer therapy, such as increased specificity resulting in reduced off-target effects, and the ability to overcome multidrug resistance (MDR). NPs can achieve specificity through two main mechanisms: passive and active targeting.<sup>26</sup> Passive targeting functions through the enhanced permeability and retention (EPR) effect (*cf. Figure 3*)<sup>27</sup>: NPs tend to accumulate at solid tumor sites because cancer cells require intensive oxygenation due to their fast growth, which stimulates the formation of abnormal vascular structure.

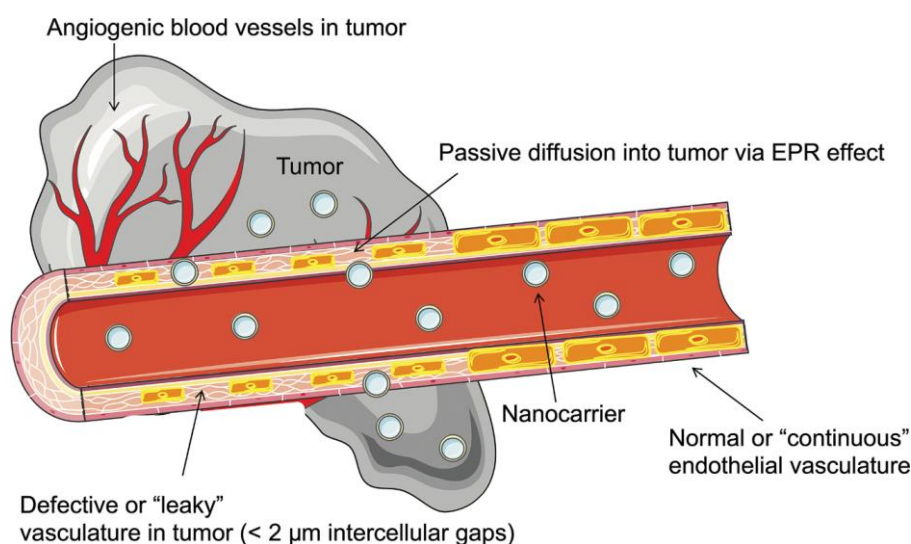


**Figure 3:** Schematic representation of the EPR effect. “Reprinted (adapted) from Stimuli-responsive liposomes for drug delivery. Nanomedicine and Nanobiotechnology. Copyright (2017). Wiley.<sup>28</sup>”

The EPR effect is, however, controversial as recent studies have shown this model to be oversimplified as the tumor uptake was estimated to only be about 0.7 % of the NP injected dose.<sup>29</sup> Active targeting, on the other hand, involves surface functionalization of the NPs with ligands specific to biomarkers expressed by cancer cells or their microenvironment, this approach being

only limited by the ability to identify promising biomarkers and produce corresponding molecules with high affinity and selectivity.<sup>30</sup> Another favorable property of NPs is their ability to overcome MDR of cancer cells and tumoral tissues, which stands as a major challenge in cancer treatment and is often responsible for tumor recurrence. MDR is a complex phenomenon involving various mechanisms, one of the major ones being the increased efflux pumps in the membranes of tumor cells, causing clearance of the therapeutic compounds.<sup>31</sup> Conjugation of the drug to NP carriers can circumvent this issue by causing internalization of the drug through endocytosis, bypassing the efflux pumps.<sup>32</sup>

NPs used in biomedicine can be divided into two main categories, organic and inorganic NPs (*cf. Figure 4*). Organic NPs englobe micelles and liposomes (formed from single or double lipid layers), as well as polymeric nanogels and dendrimers (highly organized polymeric structures).<sup>33</sup> Their main advantages reside in their high biocompatibility and the lack of necessary surface treatment. However, they exhibit several drawbacks, including rapid clearance by the immune system, relatively low internalization in tumors, premature release of therapeutic cargo, and limited chemical structure reproducibility.<sup>34–36</sup> Inorganic NPs have the potential to overcome these limitations, and often also exhibit intrinsic imaging properties and extended lifetime, which make them highly promising in the field of nanomedicine.<sup>37</sup> Most commonly investigated inorganic NPs are composed of silica, metals, metal oxides, rare earth elements, and quantum dots.<sup>38</sup> Nonetheless, they are not without shortcomings, spurring mainly from their low biocompatibility when compared to organic NPs. This issue is generally addressed by coating their surface with a variety of biocompatible materials (e.g polymer or silica shells).<sup>39</sup>

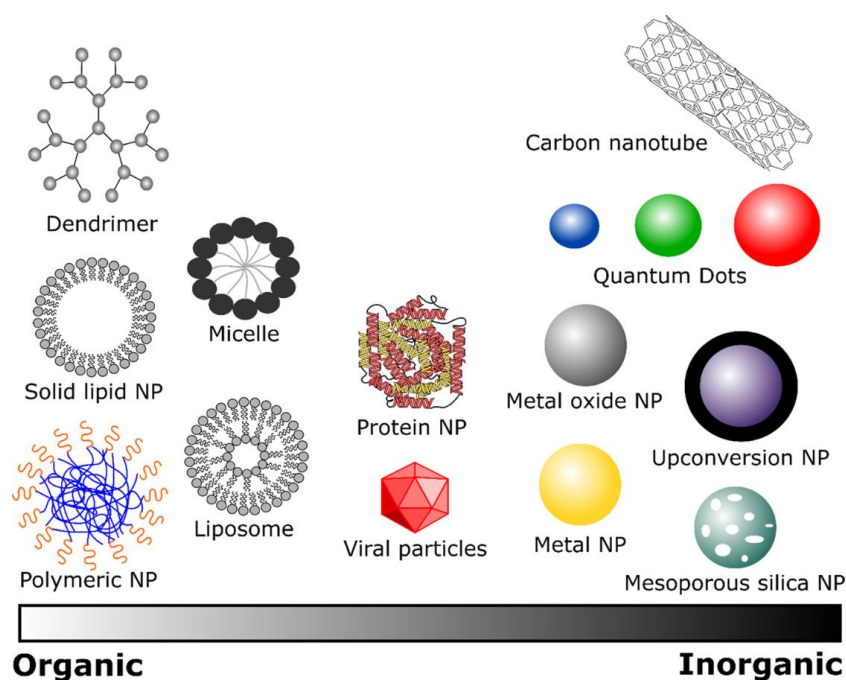


**Figure 4:** Various examples of common organic and inorganic nanoparticles. “Reprinted (adapted) from Nanotechnology in the diagnosis and treatment of lung cancer. Pharmacology and Therapeutics. Copyright (2019). Elsevier.<sup>40</sup>”

### 1.3.1. Inorganic nanoparticles

This section will focus on describing the most intensively investigated inorganic NP materials, including mesoporous silica nanoparticles (MSNs), quantum dots (QDs), gold nanoparticles (AuNPs), superparamagnetic iron oxide nanoparticles (SPIONs), and upconversion nanoparticles (UCNPs).

MSNs are generally synthesized from tetraethyl orthosilicate or trimethoxy silane derivatives through various techniques, including sol-gel, template directed method or using microwave assistance.<sup>41,42</sup> They exhibit good biocompatibility, stability, tunable pore size, and are known for their ability to release caged compounds in a controlled manner.<sup>43</sup> MSNs have found interesting applications in the encapsulation of hydrophobic chemotherapeutics such as doxorubicin, released from their pores to increase drug concentration at the target site.<sup>44</sup> Despite the large number of literature reports on MSNs as drug carriers, only a limited set of MSN-based therapeutics gained the FDA approval for clinical trials.<sup>45</sup> Silica materials are also used for the coating of other inorganic NPs. MSNs exhibit a number of limitations for their translation into clinical use: i) their circulation in the body is limited by their hemolysis of red blood cells<sup>46</sup>; and ii) compared to other inorganic NPs, they do not possess any intrinsic imaging ability. The introduction of imaging properties can be achieved by modification of MSNs through the addition of various chemical handles such as amino groups for post-functionalization.<sup>47</sup> MSNs modified with gadolinium complexes were reported to act as efficient MRI contrast agents.<sup>48</sup>

QDs are small semi-conductor nanocrystals composed of II-VI or II-V elements, synthesized by deposition of surface capping layers on a crystal core.<sup>49</sup> Their electrons have the ability to absorb light in order to reach an excited state, then leading to vibrational relaxation to their ground state emitting one-photon fluorescence.<sup>50</sup> The broad absorption spectrum of QDs is amenable for biological applications, since this allows for excitation of multiple QDs with different emissions at the same time.<sup>51</sup> They show a high photostability over repeated absorption/emission cycles, and tunable optical properties. However, their tendency to release toxic heavy metal ions in physiological conditions when not properly coated, has limited their *in vitro* and *in vivo* applications.<sup>52</sup> A recent report describes the coating of cadmium QDs with chitosan to improve biocompatibility and stability, which then served as a drug delivery system for cytotoxic sesamol for efficient cancer treatment.<sup>53</sup>

AuNPs are produced by reduction of a commercially available gold source, yielding highly biocompatible NPs with a variety of sizes and shapes.<sup>54</sup> Upon laser irradiation, these NPs exhibit surface plasmon resonance (SPR), phenomenon responsible for the scattering of light through electron resonance.<sup>55</sup> This ability can be tuned depending on the size and shape of the nanomaterial, and the plasmonic resonance thus shifted from visible to NIR region for various imaging applications.<sup>56</sup> Another important application of AuNPs is in photothermal therapy (PTT), which relies on the generation of local heat from the NPs upon light irradiation to kill cancer cells.<sup>57</sup> Chen et al. recently developed a furin-instructed intracellular AuNP aggregation strategy and designed a furin-responsive AuNP platform for effective PTT of tumor, both *in vitro* and *in vivo*, thanks to the increase of photothermal effect caused by the aggregation of AuNPs at the targeted site.<sup>58</sup>

SPIONs are biodegradable and biocompatible magnetic NPs made of maghemite ( $\gamma\text{Fe}_2\text{O}_3$ ), usually by co-precipitation of Fe(II) and Fe(III) ions at basic pH.<sup>59</sup> Their small size (< 20 nm) gives them superparamagnetic properties. In the absence of a magnetic field, their overall internal magnetization is zero, but this magnetic momentum attains very high values once exposed to a

magnetic field. SPIONs were therefore intensively studied as MRI contrast agents and can be guided inside tissues with a magnet. As most inorganic NPs they often require coating (with for instance polymers<sup>60</sup> or silica<sup>61</sup>) to increase their biocompatibility and stability. SPIONs are most commonly investigated as MRI contrast agents ( $T_1$  and  $T_2$ ), and represent one of the only class of inorganic nanomaterials which has seen formulations approved by the FDA<sup>62</sup>, but they are also heavily investigated as a basis for drug delivery systems.<sup>63</sup>

UCNPs are based on inorganic nanocrystals of  $\text{NaYF}_4$ ,  $\text{NaGdF}_4$ , or  $\text{YAlO}_3$  doped with lanthanide ions (e.g.  $\text{Yb}^{3+}$  or  $\text{Er}^{3+}$ ).<sup>64</sup> The most commonly reported methods of synthesis for these materials include coprecipitation and solvothermal synthesis, with the latter being more suitable for shape and size control.<sup>65,66</sup> These NPs present non-linear optical properties: they can absorb two or more photons of low energy (generally in the NIR region) to reach excited states, leading to a sharp UV emission, while being resistant to photobleaching.<sup>67</sup> More intense emissions have been reported for materials composed of a core-shell structure.<sup>68</sup> UCNPs have found applications in bioimaging taking advantage of the deeper tissue penetration of NIR wavelengths<sup>69</sup>, but also as multimodal imaging probes for MRI or CT owing to their doping in heavy elements.<sup>70,71</sup> They have also been reported for photodynamic therapy after conjugation to photo sensitizers, exhibiting therapeutic efficiency through the generation of reactive oxygen species (ROS) upon NIR laser irradiation.<sup>72</sup>



### 1.3.2. Harmonic nanoparticles

A novel class of materials has emerged as promising nanomedical tools, called harmonic nanoparticles (HNPs).<sup>73</sup> These NPs are based on a variety of metal oxides (e.g. LiNbO<sub>3</sub>, BiFeO<sub>3</sub>, ZnO) which display a non-centrosymmetric crystalline structure (*cf. Figure 5, A*). Various synthetic procedures were reported depending on the NP composition. For instance, preparation of niobate-based HNPs was described by hydrothermal<sup>74</sup> or solvothermal<sup>75</sup> methods. The particular three-dimensional structure of these materials is responsible for their unique non-linear optical properties. HNPs are able to combine two or more incident photons coinciding in time and space and emit a single photon whose energy is equal to the sum of the energies of the incident coinciding photons (*cf. Figure 5, B*).<sup>76</sup> Harmonic signal generation is not exclusive to this class of materials, and several endogenous agents in biological tissue are able to emit such signals, including collagen (two-photon, second harmonic generation = SHG), proteins and lipids (three-photon, third harmonic generation = THG). However, HNPs are specifically capable of emitting both second and third harmonic signals at sufficient intensity to be detectable. The colocalization of these harmonic signals allow for imaging of HNPs in tissue with high sensitivity and resolution.<sup>77</sup> This property is similar to the one displayed by UCNPs (though it differs by not generating excited transition states in the illuminated material) and has the same potential biomedical applications. Of particular interest, HNPs are not limited to a specific excitation wavelength dictated by the material; incident irradiation with any frequency can be used. In addition, HNPs do not suffer from photobleaching, and thus exhibit a high photostability in time.<sup>78-80</sup> However, the harmonic response of these nanocrystals requires excitation by pulsed laser systems, such as Ti:Sapphire based lasers. Studies performed in our group on bismuth ferrite (BFO) HNPs showed their low cytotoxicity, which is a major asset for their use in biological media. A moderate hemolytic effect of bare BFO NPs was detected, but could be countered by coating with biocompatible materials such as polymers or silica.<sup>81</sup>

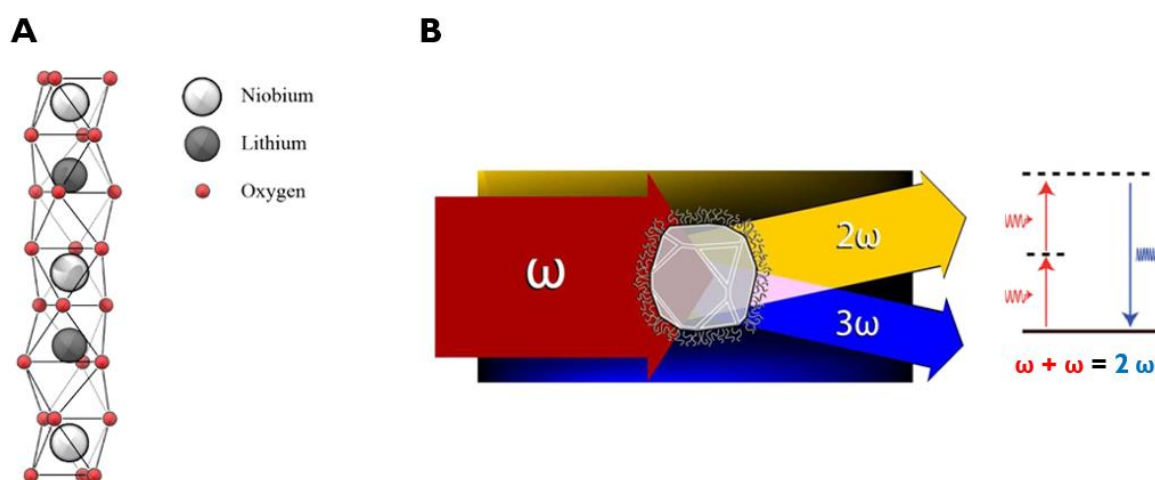


**Figure 5:** **A.** Non-centrosymmetric structure of LiNbO<sub>3</sub>; **B.** Schematic representation of harmonic generation. "Reprinted (adapted) from Nonlinear nanomedicine: harmonic nanoparticles toward targeted diagnosis and therapy. Molecular Pharmaceutics. Copyright (2013). ACS Publications.<sup>73</sup>"

**Table 1:** Summary of the principal advantages and limitations of each type of inorganic NPs described in the previous sections.

<b>Type of inorganic NP</b>	<b>Advantages</b>	<b>Drawbacks</b>
<b>MSNs</b>	High biocompatibility, ease of synthesis and functionalization, stability	No intrinsic imaging property
<b>QDs</b>	Luminescent, stable and tunable optical properties	High toxicity
<b>AuNPs</b>	High biocompatibility, well established synthesis, NIR applicable, PTT	Fast clearance from the body, low brightness
<b>SPIONs</b>	Magnetic properties for MRI, well established synthesis	Low colloidal stability, slight toxicity
<b>UCNPs</b>	Sharp luminescence, high brightness, NIR applicable	Low biocompatibility, challenging synthesis
<b>HNPs</b>	High photostability, tunable excitation and emission, high spatial resolution	Femtosecond pulsed laser system required, challenging synthesis

Owing to their many advantages, HNPs were selected as core materials in this project for the development of a diagnostic and therapeutic NP system.

### 1.3.3. Nanoparticle surface functionalization

This section will detail two main aspects of inorganic NP functionalization: their coating to improve their colloidal properties, and the introduction at their surface of various chemical handles to enable their functionalization with diagnostic and/or therapeutic components.

As previously mentioned, the use of inorganic NPs in physiological environment requires surface coating to avoid clearance by the immune system thus improving their circulation time, and limit aggregation due to their hydrophobic surface. Several methodologies, based on the NP properties and nature of coating materials<sup>82</sup>, can be implemented to achieve surface modification through non-covalent or covalent interactions. Non-covalent coatings are easily achieved, but are strongly affected by changes in pH and ionic strength.<sup>83</sup> On the other hand, covalent functionalization provides more flexible and robust systems. Furthermore, covalently conjugated systems are characterized by enhanced biodistribution and stability.<sup>82</sup>

Different types of covalent surface coatings include biomolecules, polymers, or silica. Commonly used proteins for inorganic NPs coating are albumin<sup>84</sup>, streptavidin and avidin.<sup>85</sup> In the case of polymers, poly(ethylene glycol) (PEG) stands as the most commonly used material. Other options include polylactic acid (PLA), polyethyleneimine (PEI), or carbohydrates like dextran and chitosan (*cf. Figure 6, A*).<sup>86</sup> PEG based coatings were reported to shield the surface of NPs from opsonization, aggregation, and phagocytosis, resulting in a “stealth effect”, enabling the reduction of immunogenicity and prolonging blood-circulation times.<sup>87,88</sup> Due to their good biocompatibility, versatility and ease of post-functionalization, polymers are widely used for inorganic nanomaterials coating.

Surface silanization of inorganic NPs is a common alternative to polymeric coating, as silica is known to be stable in aqueous media, biocompatible and optically transparent, thus avoiding loss of optical efficiency when applied to the coating of optically active NPs.<sup>89</sup> An aqueous suspension of hydroxyl-bearing NPs in the presence of silica precursors (such as tetraethyl orthosilicate or triethoxy-silane derivatives<sup>90</sup>) leads to surface silica condensation through the Stöber process (*cf. Figure 6, B*).<sup>91,92</sup>

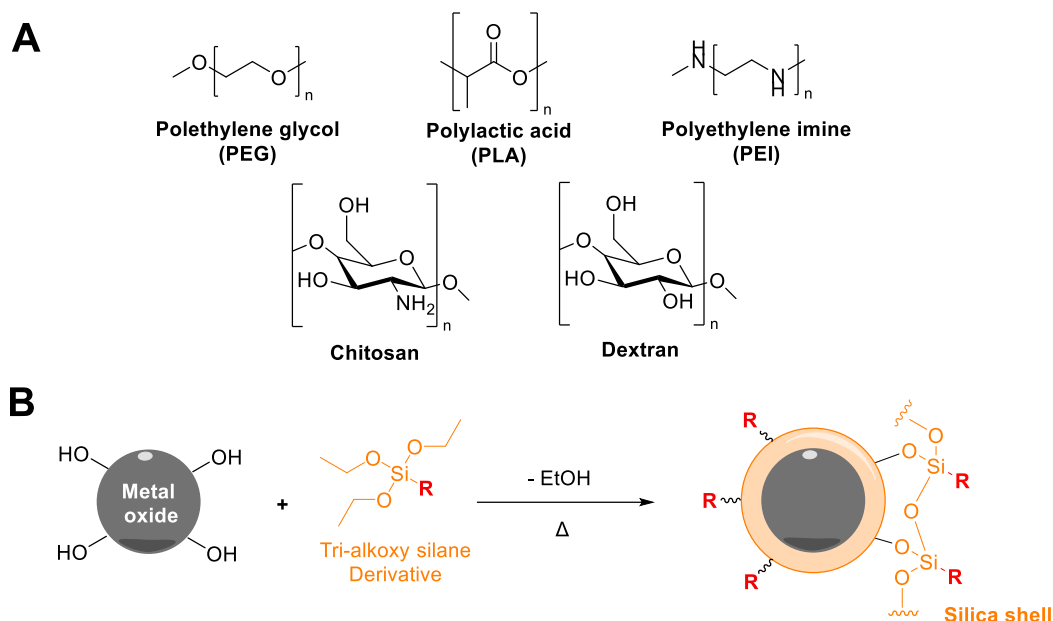


**Figure 6:** A. Examples of coating polymers; B. Schematic representation of nanoparticle silica coating.

Several methodologies, such as mechanical stirring, heating, and a combination of both, have been investigated for the silanization of nanocarriers.<sup>93–95</sup> Water-in-oil (W/O) microemulsions (MEs) (also known as reverse microemulsions), which consist of water droplets dispersed in an oil phase, were reported as promising candidates to act as nanoreactors for the silica coating of NPs.<sup>96–100</sup> MEs are thermodynamically stable dispersions of two immiscible fluids that are stabilized by the self-assembly of surfactant molecules at their interface.<sup>101</sup> As opposed to emulsions, in MEs both the micelle content and the surfactant molecules are constantly exchanged, promoting spatially confined chemical reactions that are involved in the NP coating. One of the key strengths of the use of reverse MEs is the better control over silica nucleation, which is limited to the nanodroplet core<sup>102</sup>, allowing the formation of a uniform silica shell onto individual NPs.

On top of the increase in biocompatibility and stability, another important aspect of NP coating is the ability to introduce surface reactive moieties for post-functionalization (*cf. Figure 7*). Coated NPs are often designed to exhibit amino or carboxyl groups at their surface, onto which payloads can be easily coupled by amide bond formation using various coupling agents, such as carbodiimides.<sup>103</sup> Usage of surface thiol groups is also extensively reported for functionalization by thiol-Michael addition using, for instance, maleimide groups as Michael acceptor.<sup>104</sup> Despite their chemical efficiency, these functionalization strategies may lack selectivity or stability of the formed linkage. Bioorthogonal chemistry encompasses different reactions which are particularly well suited for the conjugation of biomolecules to NPs, due to their high selectivity, efficient kinetics, and the inertness of the formed linkages. These include the Staudinger ligation<sup>105</sup>, the tetrazine ligation<sup>106</sup>, and the strain-promoted azide-alkyne cycloaddition (SPAAC).<sup>107</sup> The SPAAC in particular is widely employed for biological applications. This [3+2] cycloaddition involves the use of a strained cyclic alkyne, reacting with azide groups to form a triazole in the absence of a normally necessary Cu(I) catalyst, thereby avoiding the cytotoxicity of copper.<sup>108</sup>

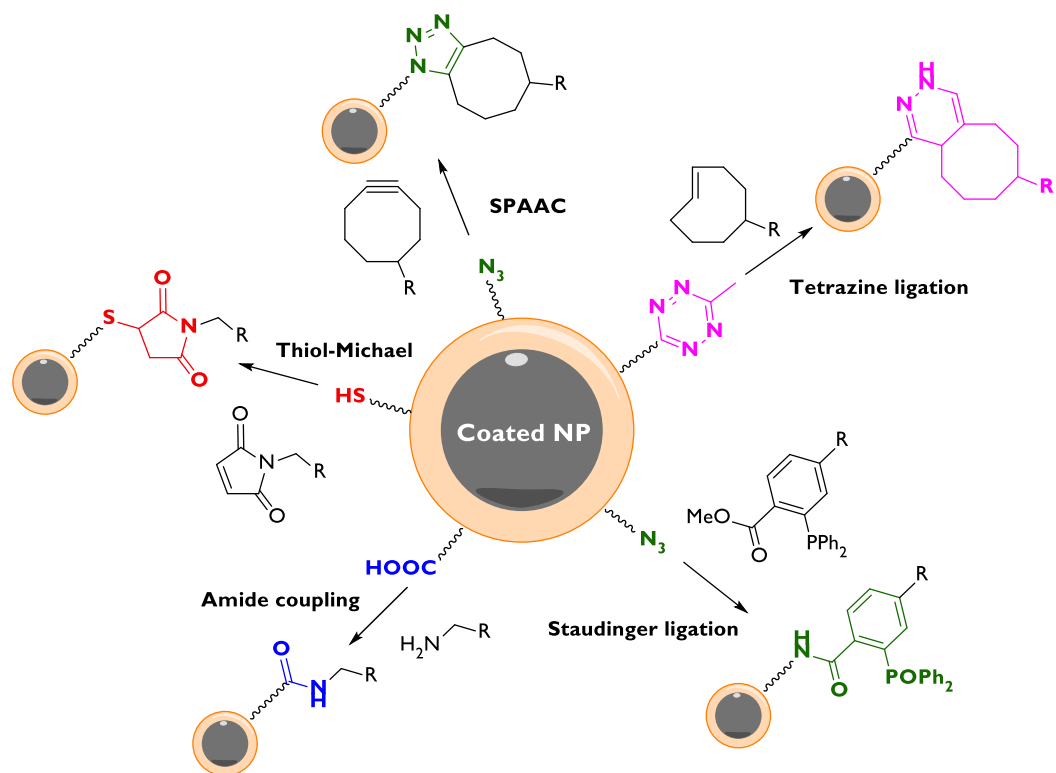


**Figure 7:** Overview of common chemical reactions for nanoparticle conjugation

## 1.4. Light-triggered drug release

The ability to release therapeutics in a selective and controlled manner is expected in the development of efficient theranostic NP platforms, in order to reduce drug side effects and promote high accumulation of therapeutic molecules in the targeted diseased area.<sup>109</sup> Such approach is based on the temporary inactivation and caging of molecular/biomolecular cargos at the NP surface or within the NP structure. Upon application of a stimulus, the cargo is uncaged and its pharmaceutical activity is restored. The efficiency of stimuli-sensitive NP carriers depends on their ability to avoid release outside of the defined conditions, their loading capacity, and their specificity to the targeted site.<sup>110</sup> The stimuli employed to trigger the release of the cargo can either be endogenous or exogenous (*cf. Figure 8*). Endogenous activation strategies provide biologically controlled release by exploiting specific physiochemical characteristics of the targeted environment, such as pH change, redox conditions, or enzymatic cleavage.<sup>111</sup> Exogenous approaches, on the other hand, rely on an external remote stimulus to provide a spatiotemporal and dosage control over the therapy, which include light, ultrasounds, ionizing radiation, and magnetic field.<sup>112</sup>

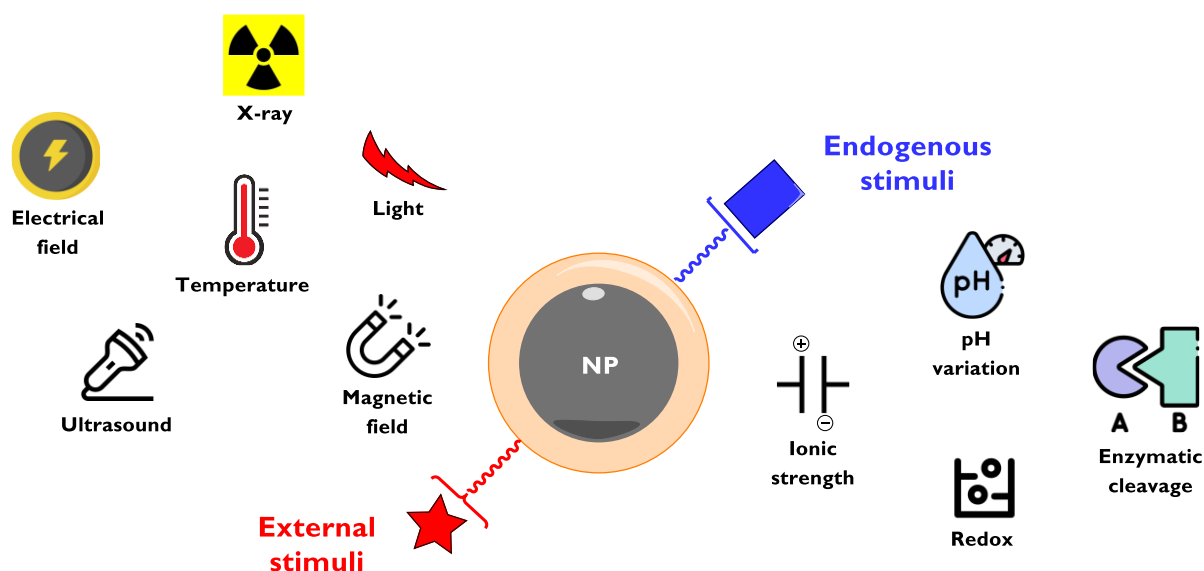


**Figure 8:** Stimuli triggers for release of different therapeutics.

### 1.4.1. Photosensitive systems

Several advantages are associated with the use of light as external uncaging stimulus for controlled drug release, including safety, ease of manipulation and precise spatiotemporal localization.<sup>113</sup> Light irradiation is non-invasive, can be tuned in terms of incident intensity to moderate potential side-effects and usually results in a limited number of formed byproducts.<sup>114</sup> Photosensitive NP carriers rely on: i) the inactivation of the therapeutic cargos through covalent conjugation to a photolabile protecting group (PPG) masking their biologically active site; and ii) immobilization of the caged cargos to the NP material. Upon irradiation at a specific wavelength,

the PPG absorbs light and goes through an excited state. Subsequent photoreaction leads to the cleavage of the covalent bond to the cargo and induces its release.<sup>115</sup> Photocleavable groups are based on aromatic rings and usually absorb in the UV domain. Their use as phototriggers for drug delivery requires a number of properties, including fast and clean photoreaction, high quantum yield, thermal stability, good biocompatibility and low toxicity.<sup>116</sup> Their physicochemical features can be modified by tuning their substituents.<sup>117</sup> Commonly used PPGs include molecules based on *ortho*-nitrobenzyl (*o*NB), *para*-hydroxyphenacyl (*p*HP), and coumarinyl-4-methyl (CM) moieties (*cf. Figure 9*).<sup>118-120</sup> *o*NB photosensitive derivatives, though very commonly employed as phototriggers for drug delivery systems, generate upon UV-light illumination, toxic and strongly absorbent photo-degradation products such as *o*-nitrozobenzaldehyde, which may cause serious side effects.<sup>121</sup> The toxicity of byproducts can be reduced by variation on the aromatic ring substituents. Alternatively, strict control over the uncaging process can limit the concentration of toxic degradation products.<sup>116,121</sup> However, several different classes of more recently developed PPGs based on CM and *p*HP cores do not present these issues.

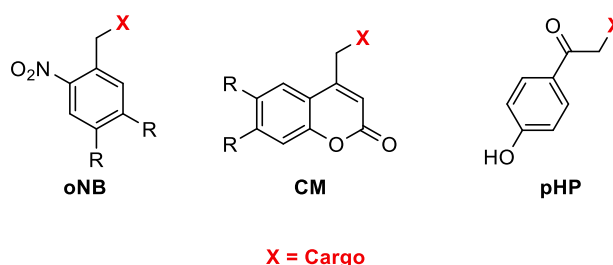


**Figure 9:** Classes of common photocleavable linkers (*ortho*-nitrobenzyl, coumarinyl, *para*-hydroxyphenacyl)

Nucleophilic substitution is usually used to bind therapeutic payloads to photocleavable molecules thanks to amino-, hydroxyl-, carboxylate-, or phosphate groups present on the native active cargo.<sup>122-125</sup> The diversity of strategies and PPG molecules available allows photocaging of virtually any kind of molecule, including but not limited to chemical drugs, proteins, fatty acid derivatives, or RNA and DNA.<sup>126-129</sup>

### 1.4.2. NIR light responsive nanomaterials

Illumination of photocleavable ligands with UV-vis light is usually required for the uncaging of the therapeutic payloads and their release from NP carriers. These wavelengths are, however, not suited for direct clinical use because of two major drawbacks. They exhibit a poor tissue penetration ability due to high scattering on endogenous chromophores, and they can cause cellular damage.<sup>130</sup> One solution which has been extensively investigated is to replace UV-vis light with NIR, which has been shown to be able to penetrate tissue in the cm range and which exhibits decreased cytotoxicity.<sup>131</sup> There are three main mechanisms involved in the uncaging of molecular cargos from NIR-responsive NP carriers: photothermal effect, two-photon absorption (TPA), and upconversion (UC).<sup>132</sup>

In the case of photothermal-based NIR drug delivery systems, the NIR light is absorbed by the caging compound and converted into heat, which then induces the release of the therapeutic compound. Potential materials suitable for photothermal drug delivery include carbon nanotubes, gold nanomaterials, gold NPs and nanorods. These materials benefit from potent light to heat conversion capacity. In the case of gold nanomaterials, this conversion capacity is mediated by the surface plasmon resonance phenomenon. In addition, they are amenable to large-scale production and benefit from high optical absorption coefficient and tunable absorption range.<sup>133</sup> For instance, Yang *et al.* reported a dual responsive (redox and NIR light) drug release system of doxorubicin (DOX) loaded mesoporous silica (MSN) with gold NPs embedded in pores of mesoporous silica. *In vitro* cytotoxicity studies of these nanocarriers showed the synergistic effect of chemo- and photothermal therapy. An enhanced doxorubicin release was observed from these nanocarriers in the presence of GSH (glutathione) and NIR irradiation, illustrating the potential of controlled release systems (*cf. Figure 10, A*).<sup>134</sup>

The second mechanism, TPA, involves the excitation of the system with high-power pulsed femtosecond lasers. Excitation is achieved through the simultaneous absorption by a chromophore of two NIR photons, generally of the same frequency, to reach a singlet excited state with the energy increase being equal to the sum of the incoming photon energies.<sup>135</sup> Lin *et al.* demonstrated that two-photon responsive 7-amino-coumarinyl derivatives could be exploited as a NIR-responsive phototrigger for covalent loading of the anticancer drug chlorambucil in the pores of MSNs. Upon NIR excitation at 800 nm, TPA induced the controlled release of chlorambucil from MSNs and subsequent efficient cancer cell growth inhibition. This exemplifies the possibility to turn traditional PPGs which are responsive to UV light irradiation into NIR-responsive systems for clinical applications (*cf. Figure 10, B*).<sup>136</sup>

Finally, another strategy for circumventing the UV-vis drawbacks involves employing UCNPs to convert incident NIR photons into high energy UV light, which can be used for photo-uncaging of therapeutic payloads bound to the surface of the NPs through common PPGs.<sup>137</sup> For example, Wong *et al.* conjugated PAMAM dendrimer bearing folic acid and *o*NB-DOX photosensitive system to the surface of UCNPs. Upon NIR-light irradiation, UCNPs generated emission bands in the UV region leading to the cleavage of the *o*NB-DOX linkage, and release of up to 90% of the caged DOX within 60 min of irradiation in human cervix carcinoma cells (*cf. Figure 10, C*).<sup>138</sup>



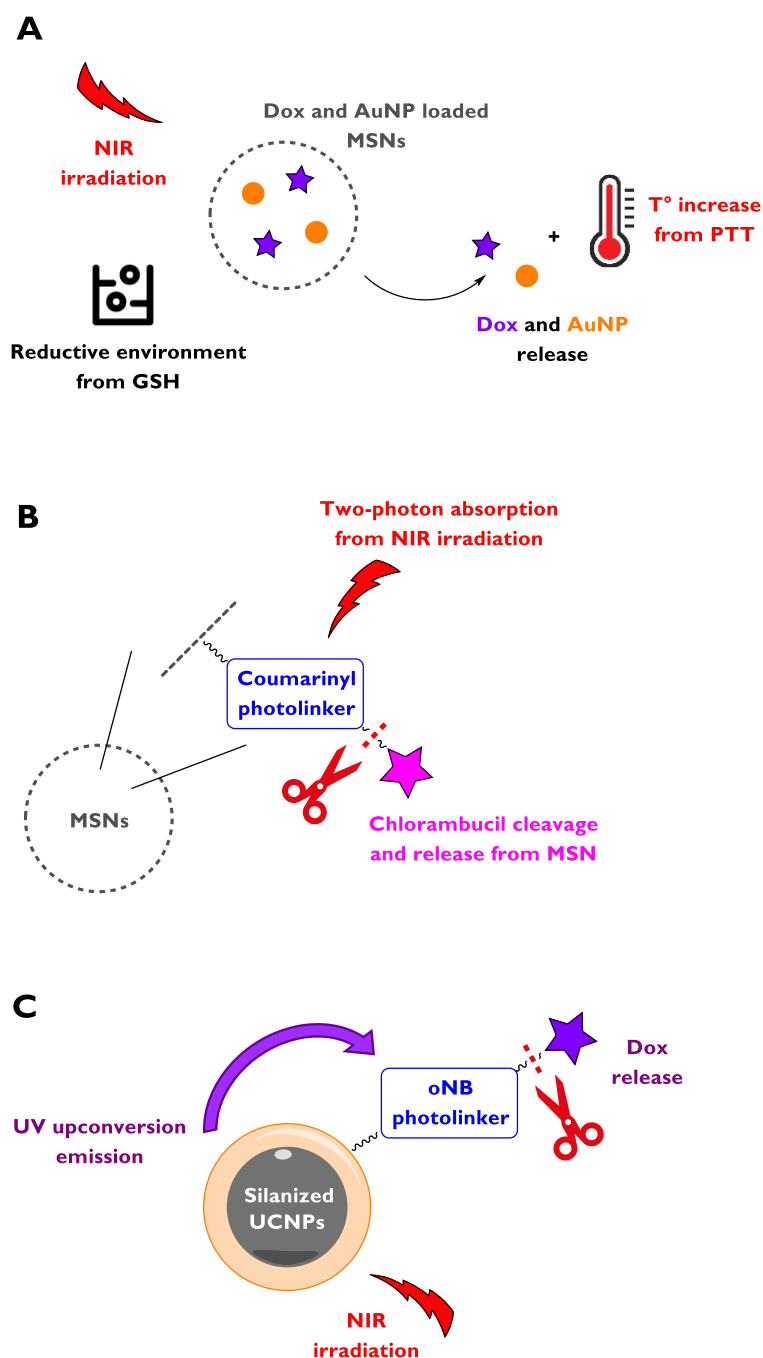


**Figure 10:** Schematic representations of the selected NIR responsive NPs. **A:** Dox release and PTT effect from MSNs upon NIR irradiation and in the presence of a GSH-rich environment. **B:** TPA cleavage of coumarinyl linker upon NIR irradiation, leading to chlorambucil release from MSNs. **C:** NIR irradiation of silanized UCNP leading to UV emission and Dox release from oNB cleavage.

UCNPs exhibit high potency for multimodal imaging and drug release upon NIR irradiation. However, a number of limitations are associated with the use of UCNPs in drug release applications. The wavelengths used for the generation of upconverted luminescence are not flexible. In addition, there is no possibility to use the upconverted signal for decoupled imaging and photo-activation protocols (due to the defined excitation wavelengths). HNPs can overcome those limitations as they lack wavelength constraints (limited only by the capacities of the laser used) which allows the switching between imaging and drug-release modalities by tuning the

wavelength of the laser. Recently, our group presented a system for NIR light-triggered release of molecular cargos induced by the second harmonic emission from BFO HNPs covalently conjugated to a photocaging tether based on coumarin (CM) and L-tryptophan (Trp) as a model molecular cargo. This system showed, for the first time, the possibility to use the harmonic emission of HNPs for the uncaging of surface-conjugated molecular cargos.<sup>139</sup> An important aspect of this project will be to continue the previous investigations of our group in designing a light-triggered drug delivery system based on HNPs.

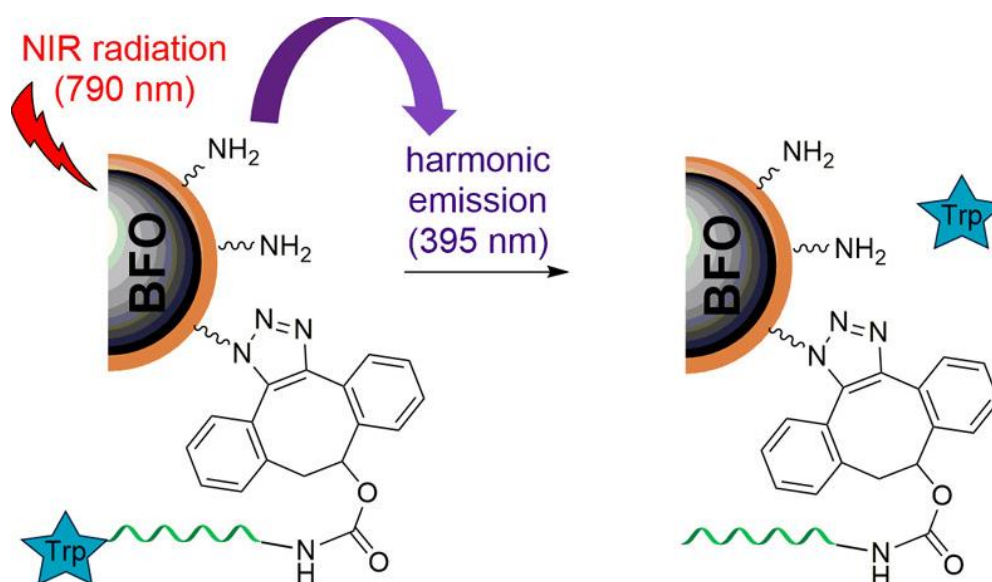


**Figure 11:** Controlled uncaging of Trp molecular cargo triggered by the harmonic emission of functionalized BFO NPs. "Reprinted (adapted) from Two-Photon-Triggered Photorelease of Caged Compounds from Multifunctional Harmonic Nanoparticle. ACS applied Materials & interfaces. Copyright (2019). ACS Publications.<sup>139</sup>"

## 1.5. Multimodal imaging

All single imaging modalities used for diagnosis exhibit limitations with respect to spatial resolution, sensitivity, or tissue penetration depth (*cf. Figure 12*). MRI and X-ray CT are both non-invasive techniques which afford high spatial resolution, and are thus suitable to retrieve anatomical and physiological information. However MRI suffer from a relatively low sensitivity,<sup>140</sup> due to the limited intensity of the magnetic field than can be safely used in a patient. For CT scans, which process multiple X-ray measurements, the radiation dose must be carefully controlled to avoid the harmful effects arising from overexposure to X-ray irradiation. PET and SPECT allow for a very high sensitivity yielding specific and accurate functional information, but they are limited by their relatively low spatial resolution, their invasiveness (as they require injection of radionuclide probes), and the safety risks associated with radioactive irradiation of the patient.<sup>141</sup> Optical imaging is non-invasive, harmless, and allows for a high sensitivity and good resolution at the same time. However, the main shortcoming in this case is the limited depth penetration (in the centimeter range) due to photon scattering by biological tissue.<sup>142</sup>

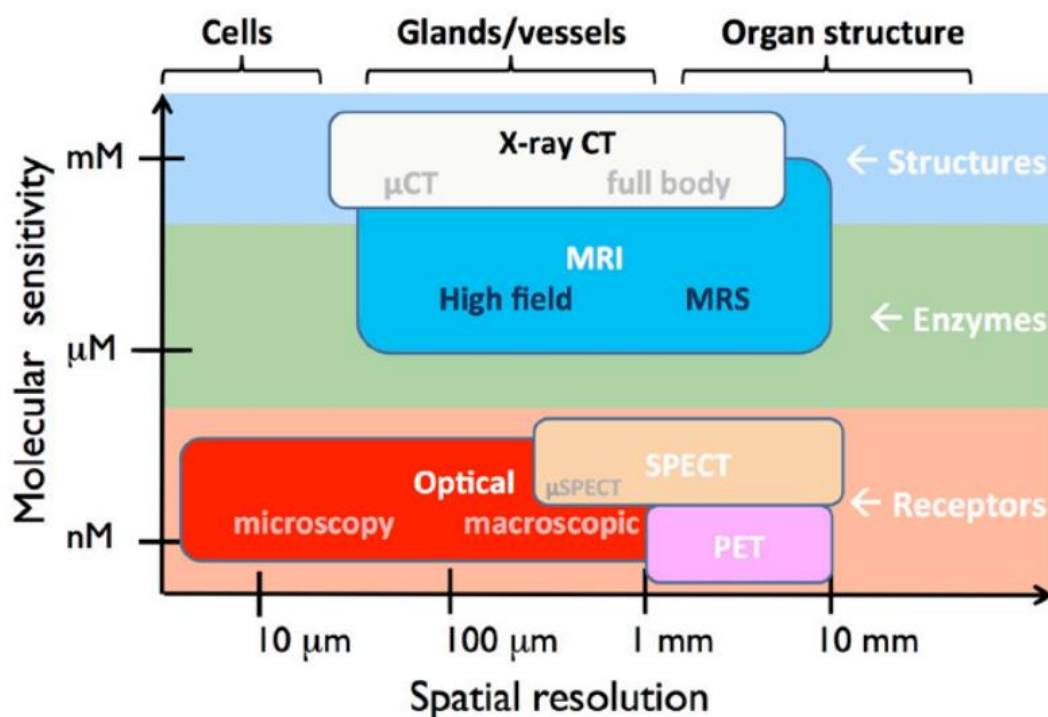


**Figure 12:** Dominant medical imaging modalities with respect to molecular sensitivity and spatial resolution. “Reprinted (adapted) from Quantitative in vivo cell-surface receptor imaging in oncology: kinetic modeling and paired-agent principles from nuclear medicine and optical imaging. Physics in Medicine & Biology. Copyright (2015). IOPscience.<sup>143</sup>”

Because no single imaging technique can provide an optimal combination of characteristics, there has been an increased interest towards multimodal imaging, which combines the advantages of several techniques to obtain more detailed pictures and avoid diagnostic errors. The objective of this approach is to synergistically combine a molecular detection component with an anatomical technique, either by acquiring the images at different times with different machines and then

fusing them together (asynchronous), or by simultaneously acquiring the images with a single device (synchronous).<sup>144</sup> The synchronous acquisition method clearly affords better consistency by eliminating a variety of factors (time of acquisition, position of the patient, machine parameters, etc.), but requires the development of advanced imaging equipment which began with the emergence of PET/CT and SPECT/CT scanners in the 1990s,<sup>145</sup> followed by PET/MRI systems in the 2000s<sup>146</sup> in common clinical use. However, for the multimodal paradigm to progress, on top of the technological progress required, it is also important to develop novel molecular probes acting as contrast agents for a variety of imaging techniques (*cf. Figure 13*). As previously described, NPs appear as appealing theranostic tools due to their surface properties allowing for extensive post-functionalization, and in the same way are potentially ideal for multimodal imaging. In this section, some recent developments in multimodal nanoprobe are presented, illustrating possible strategies than can be employed for combining various imaging modalities on a single nanodevice.

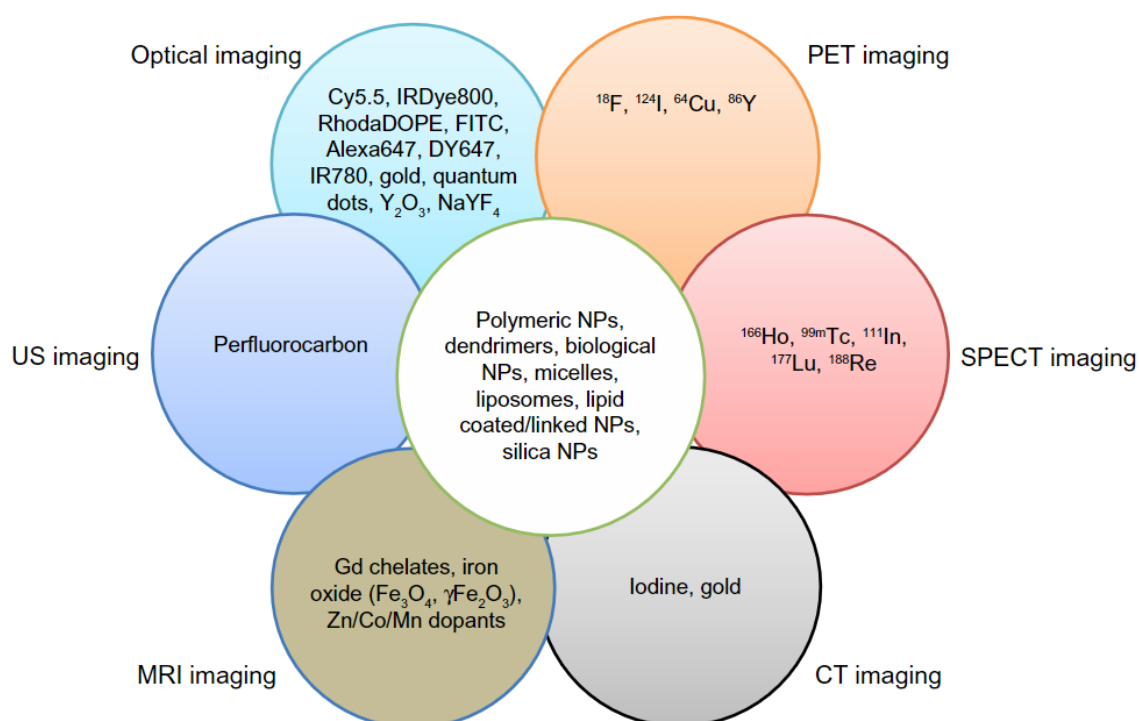


**Figure 13:** Various contrast agents for multimodal imaging. “Reprinted (adapted) from Nanoparticles for multimodal in vivo imaging in nanomedicine. International journal of nanomedicine. Copyright (2014). Taylor & Francis.<sup>147</sup>”

Due to their limited tissue penetration ability, *in vivo* clinical applications of optical imaging in human subjects are restricted. NIR wavelengths exhibit however increased penetration depth and can be used in conjunction with MRI and PET/SPECT to provide important anatomical and physiological information in small animal models. This category of multimodal probes is usually based on gadolinium ions or iron oxide nanomaterials for MRI, <sup>64</sup>Cu or <sup>111</sup>In for nuclear imaging, and synthetic fluorophores, fluorescent semiconductors or upconverting nanomaterials for NIR fluorescence. For instance, Hong *et al.* developed novel red fluorescent ZnO NPs conjugated to <sup>64</sup>Cu and TRC105, a chimeric monoclonal antibody against CD105 (endoglin). The produced bimodal ZnO NPs displayed excellent imaging capability for PET and fluorescence imaging of tumor vasculature (*cf. Figure 14*).<sup>148</sup> Despite the usage being usually restricted to small animals, optical

multimodal approaches can also be exploited for fluorescence guided surgery, which can help to determine tumor margins for patients undergoing surgery. Kircher *et al.* reported a NP probe termed Cy5.5-CLIO for optical/MRI which could be used as both a preoperative MRI contrast agent and as intraoperative optical probe in neurosurgical cases for tumor discrimination.<sup>149</sup>

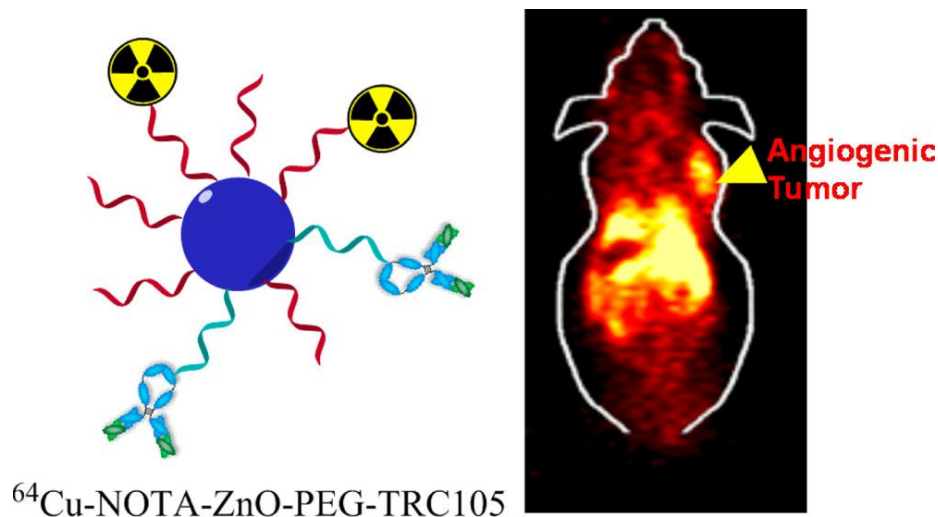


**Figure 14:** Development of multifunctional fluorescent ZnO nanoparticles conjugated with  $^{64}\text{Cu}$  and TRC105. "Reprinted (adapted) from Red Fluorescent Zinc Oxide Nanoparticle: A Novel Platform for Cancer Targeting. ACS applied materials & interfaces. Copyright (2015). ACS Publications.<sup>148</sup>"

Recently, some groups have combined NIR fluorescence with both nuclear and MRI modalities, capable of providing even more information than dual-modality approaches. Hwang *et al.* demonstrated this type of trimodality by designing cobalt-ferrite NPs surrounded by rhodamine within a silica shell, which was further conjugated to an aptamer targeting nucleolin (a cell-membrane protein highly expressed in tumors). The NPs were functionalized with chelating agents and further labeled with  $^{67}\text{Ga}$  citrate for radionuclide imaging. These NPs were then injected into mice to assess their potential for: *in vivo* tumor PET (*cf.* Figure 15, A), *in vivo* MRI (*cf.* Figure 15, B) and *ex vivo* NIR fluorescence of excised tumors (*cf.* Figure 15, C).<sup>150</sup>

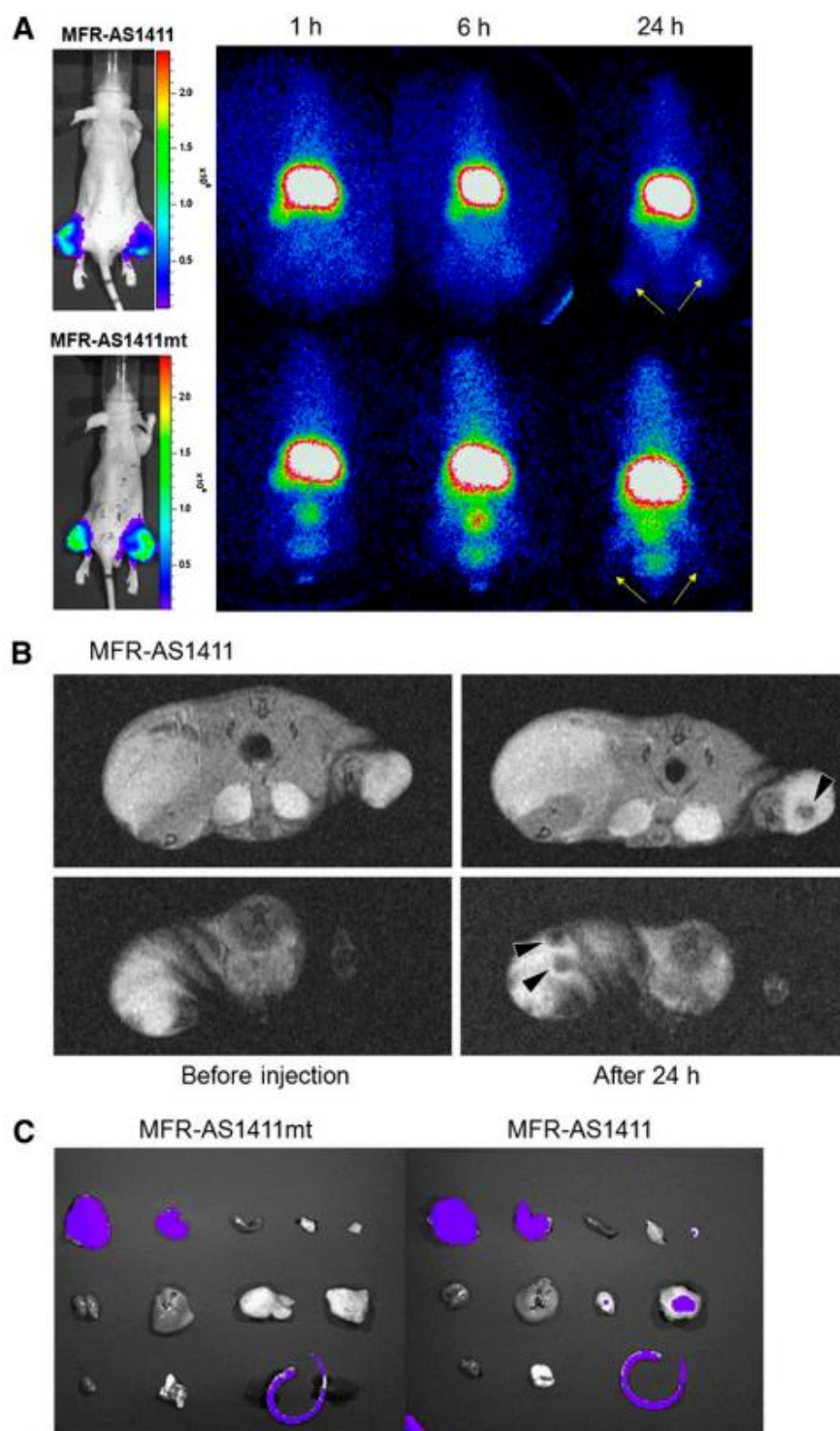


**Figure 15:** *In vivo* multimodal cancer targeting and imaging using trimodal MFR-AS1411 particles. **A:** Particles were intravenously injected into tumor-bearing mice, and radionuclide images were acquired at 1, 6, and 24 h after injection. Scintigraphic images of C6 tumors in mice that received MFRAS1411 showed that C6 tumors had accumulated MFR-AS1411 at 24 h after injection but did not accumulate MFRAS1411mt. Tumor growth patterns were followed using bioluminescence signals acquired from luciferase-expressing C6 cells. **B:** MR images of tumor-bearing mice before and after injection of MFR-AS1411 were acquired. Dark signal intensities at tumor sites were detected in MFR-AS1411-injected mice (arrowhead). **C:** Tumors were isolated and their fluorescence verified using IVIS200 system. Fluorescence signal at tumor site injected with MFRAS1411 was detected, compared with tumors injected with MFR-AS1411mt. Isolated organs in order from upper left to lower right were intestine, liver, spleen, muscle, fat, kidney, stomach, right tumor, left tumor, heart, lung, and tail. "Reprinted (adapted) from A Nucleolin-Targeted Multimodal Nanoparticle Imaging Probe for Tracking Cancer Cells Using an Aptamer. *Journal of Nuclear Medicine*. Copyright (2010). SOC Nuclear Med.<sup>150</sup>"

Another example of trimodal nanodevice was presented by Du *et al.*<sup>151</sup> This system is based on a UCNP core and takes advantage of their unique properties for optical imaging using upconversion and downshifting luminescence. By doping these UCNPs with Lu and Yb which provide high X-ray attenuation, the device can also act as X-ray CT contrast agent. Finally, the NPs were coated with chitosan and decorated with Ag<sub>2</sub>Se nanodots, which are characterized by a high NIR absorption capacity. This property can be used for photoacoustic (PA) imaging, which is a way to combine optical and ultrasound imaging. Ag<sub>2</sub>Se nanodots absorb NIR wavelengths, thereby generating a small heat spike which in turn generates an ultrasound wave by thermoelastic expansion. The ultrasound wave generated can then be detected without getting attenuated while travelling in biological tissue. The NPs were injected in tumor-bearing mice to visualize the malignancy through the three distinct modalities (*cf.* Figure 16).

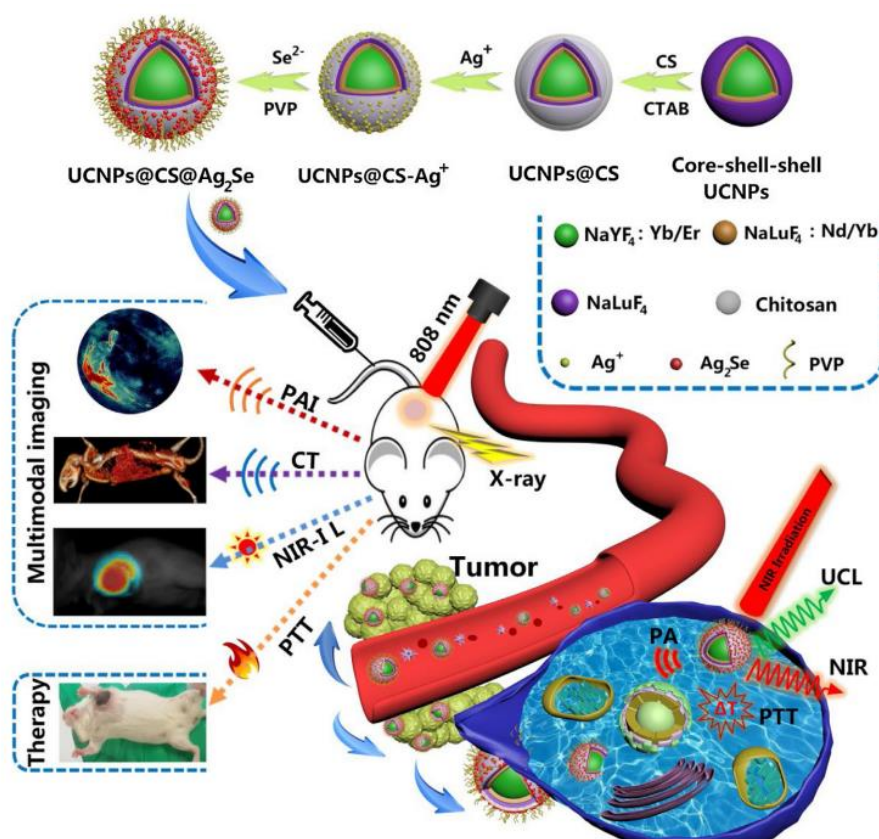


**Figure 16:** Schematic illustration of the fabrication process of UCNPs@CS@Ag<sub>2</sub>Se nanocomposites and UCNPs@CS@Ag<sub>2</sub>Se nanocomposites for multimodal imaging guided PTT of cancer. “Reprinted (adapted) from In situ decorating of ultrasamll Ag<sub>2</sub>Se on upconversion nanoparticles as novel nanotheranostic agent for multimodal imaging-guided cancer photothermal therapy. Applied Materials Today. Copyright (2020).<sup>151</sup>”

The recent advances in surface modification of inorganic NPs with a variety of caged drugs, imaging probes and targeting ligands have paved the way toward the development of theranostic approaches for improved management of cancer patients. In this project, we aimed at combining the favourable properties of HNPs for optical multiphoton imaging with additional modalities, including controlled drug delivery and complementary imaging capacities.

## 2. Presentation of the project

---

The GBF group at EPFL has been working for the past 8 years on the design, preparation, and evaluation of new nanodevices based on HNPs to combine the detection and imaging of tumors at their early stage of development with controlled treatment modalities. In previous work, bismuth ferrite (BFO) and lithium niobate (LNO) HNPs were identified as highly promising bioimaging probes due to their high harmonic efficiency, low cytotoxicity and surface reactivity for chemical functionalization.<sup>77,81,152,153</sup>

The present project focused on the functionalization of LNO HNPs with caged therapeutic compounds and imaging probes for drug delivery and multimodal imaging applications. This PhD study was developed within a collaborative network involving several academic partners (*cf. Figure 17*). The bare HNPs were produced by the Laboratoire des Systèmes et Matériaux pour la Mécatronique (SYMME, Profs Yannick Mugnier and Ronan Le Dantec) at the University Savoie Mont-Blanc (France). Our group was involved in all functionalization strategies and subsequent NP characterization. The assessment of multiphoton imaging capabilities and light-activated drug release efficiency was developed in collaboration with the Nonlinear BioImaging LAB (NBI, Prof. Luigi Bonacina) at the University of Geneva. Finally, *in vitro* evaluations were performed in collaboration with the Department of Biomedical Sciences (DBS, Prof. Dario Diviani, Dr Davide Staedler) at the University of Lausanne.

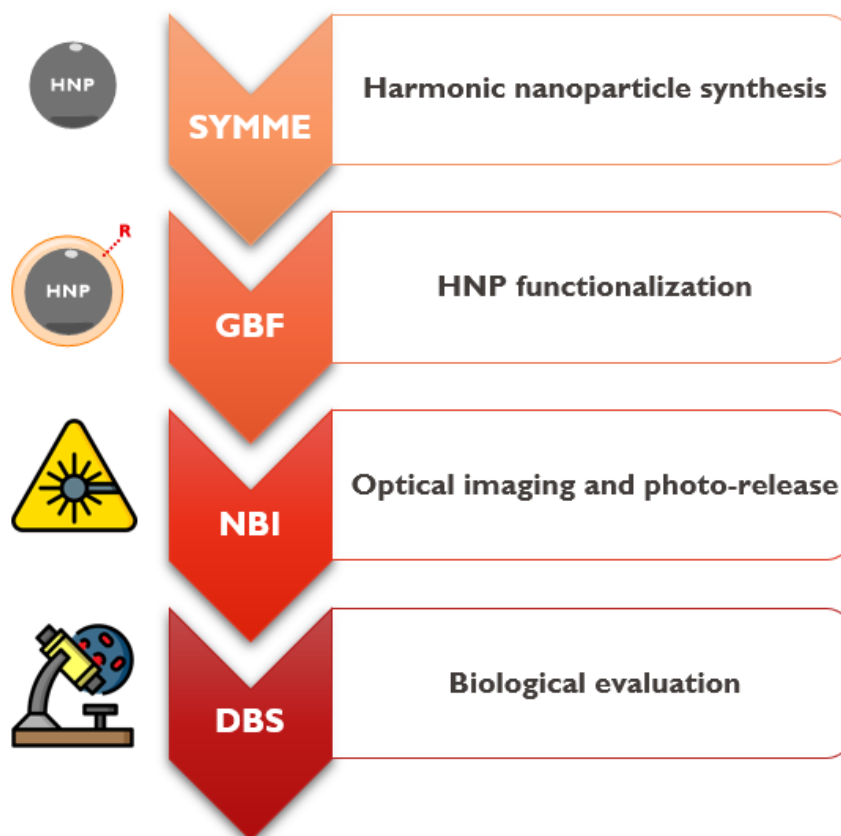


**Figure 17:** Workflow of the collaborative network involved in HNP production, functionalization and evaluation.



The first focus of this work was to develop new methodologies for the silica coating of HNPs, with the goal of achieving monodisperse NP suspensions with improved surface properties and high density of surface reactive moieties for post-functionalization. The HNPs were coated with tetraethoxysilane (TEOS) and (3-aminopropyl)triethoxysilane (APTES) derivatives either through the standard Stöber process, already established in our group, or through a newly developed water-in-oil microemulsion approach (*cf. Figure 18*). The coupling of synthetic branched peptides on coated HNPs was also investigated, for the densification of surface reactive groups and further improvement of NP properties in physiological media.

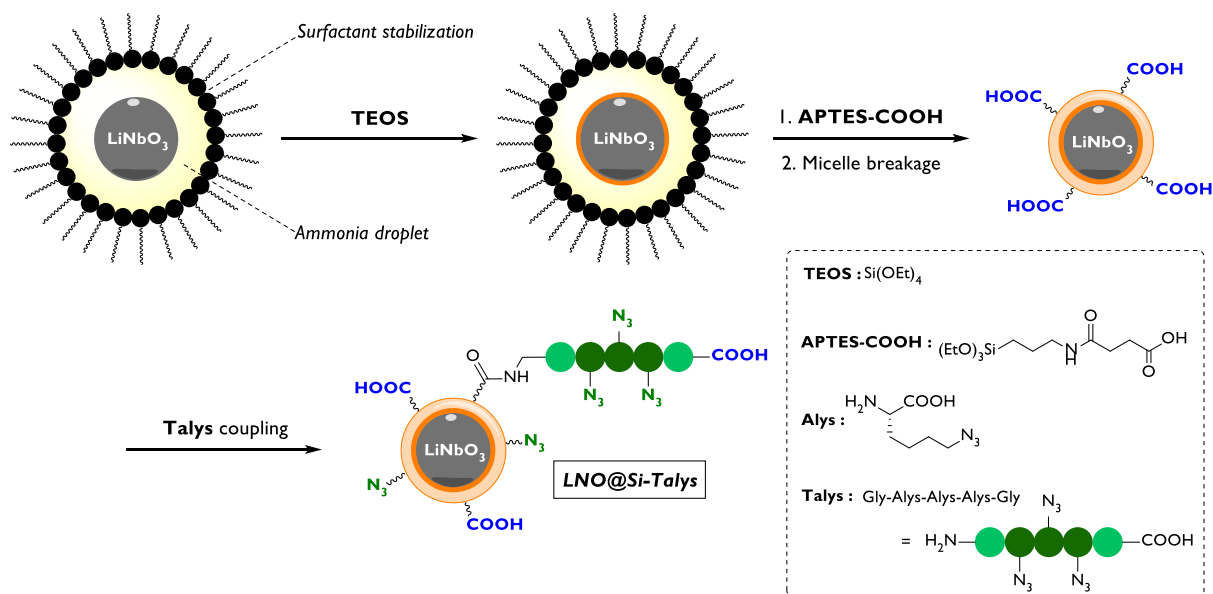


**Figure 18:** Water-in-oil microemulsion coating and peptide functionalization of HNPs.

The second axis of this project involved the functionalization of coated HNPs with a photo-triggered drug delivery system based on a coumarinyl linker previously developed in our group. The therapeutic compound evaluated was a derivative of the drug erlotinib, a FDA approved medication acting as a reversible inhibitor of the epidermal growth factor receptor (EGFR), a transmembrane protein and a tyrosine kinase receptor overexpressed in certain tumors. Erlotinib interacts with the tyrosine residue of EGFR through its aminoquinoline moiety while its alkyne-substituted aromatic ring binds to the ATP receptor, leading to disruption of the replication cycle. Once synthesized, the drug delivery system was conjugated to coated HNPs via SPAAC. The release of the erlotinib derivative from the NPs upon NIR irradiation was evaluated *in vitro* on EGFR overexpressing prostate cancer cells (*cf. Figure 19*).

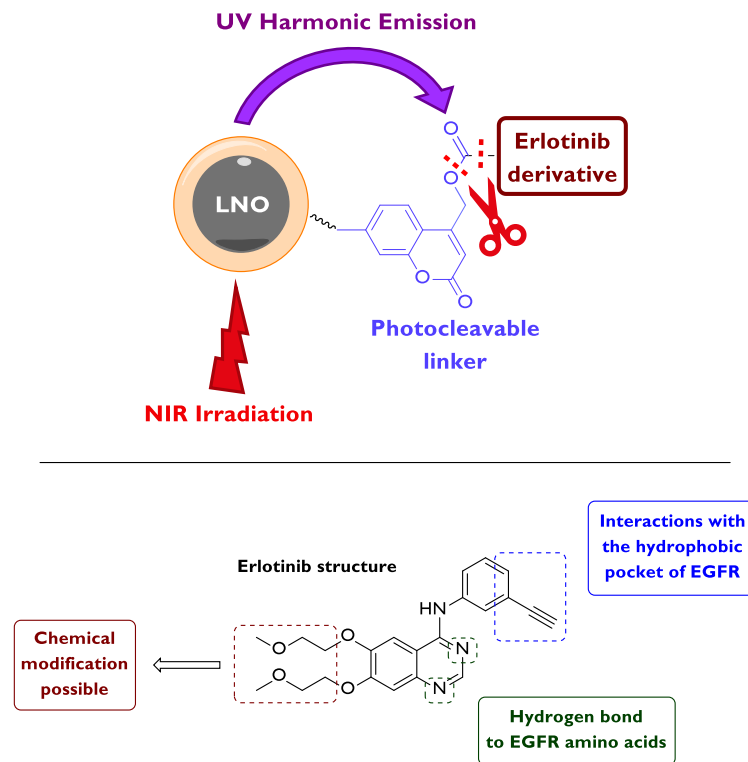


**Figure 19:** Drug release mechanism and erlotinib structure.

The last part of this work involved the synthesis of various lanthanide complexes, which were then conjugated to coated HNPs either by copper-catalysed azide-alkyne cycloaddition (CuAAC) or SPAAC. The multimodal imaging capabilities of the lanthanide-functionalized NPs were then evaluated (*cf. Figure 20*).

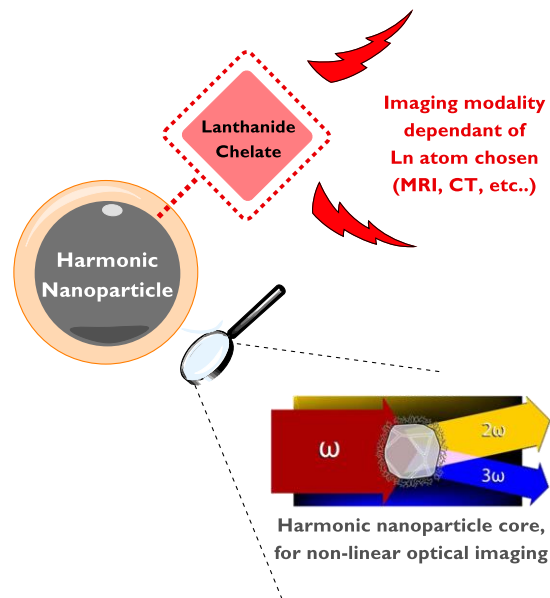


**Figure 20:** Multimodal platform based on lanthanide-functionalized harmonic nanoparticles.



### 3. Results and Discussion

---

#### 3.1. Silica coatings of nanoparticles and introduction of reactive moieties

In the following sections is presented the HNP coating in a silica shell through various approaches, which was disclosed in the publication: Modulating the Surface Properties of Lithium Niobate Nanoparticles by Multifunctional Coatings Using Water-in-Oil Microemulsions. *Nanomaterials*, **2023**, 13(3), p.522. The role of this shell is to passivate the NP surface to reduce their potential inherent cytotoxicity and improve their colloidal properties, while introducing reactive moieties on the surface, which can be used for post-functionalization with various ligands. The main surface reactivity investigated is the introduction of azide groups, which can react with alkynes by CuAAC, or with strained alkynes by SPAAC.

Two different silanization techniques were investigated: either by a standard Stöber process approach assisted by ultrasonication, or by a water-in-oil microemulsion (W/O ME) approach (*cf. Figure 21*). In the case of HNPs coated by W/O ME, NPs were further modified by the introduction of short azide-bearing peptides, in order to increase the colloidal properties while keeping a high amount of surface reactive moieties.

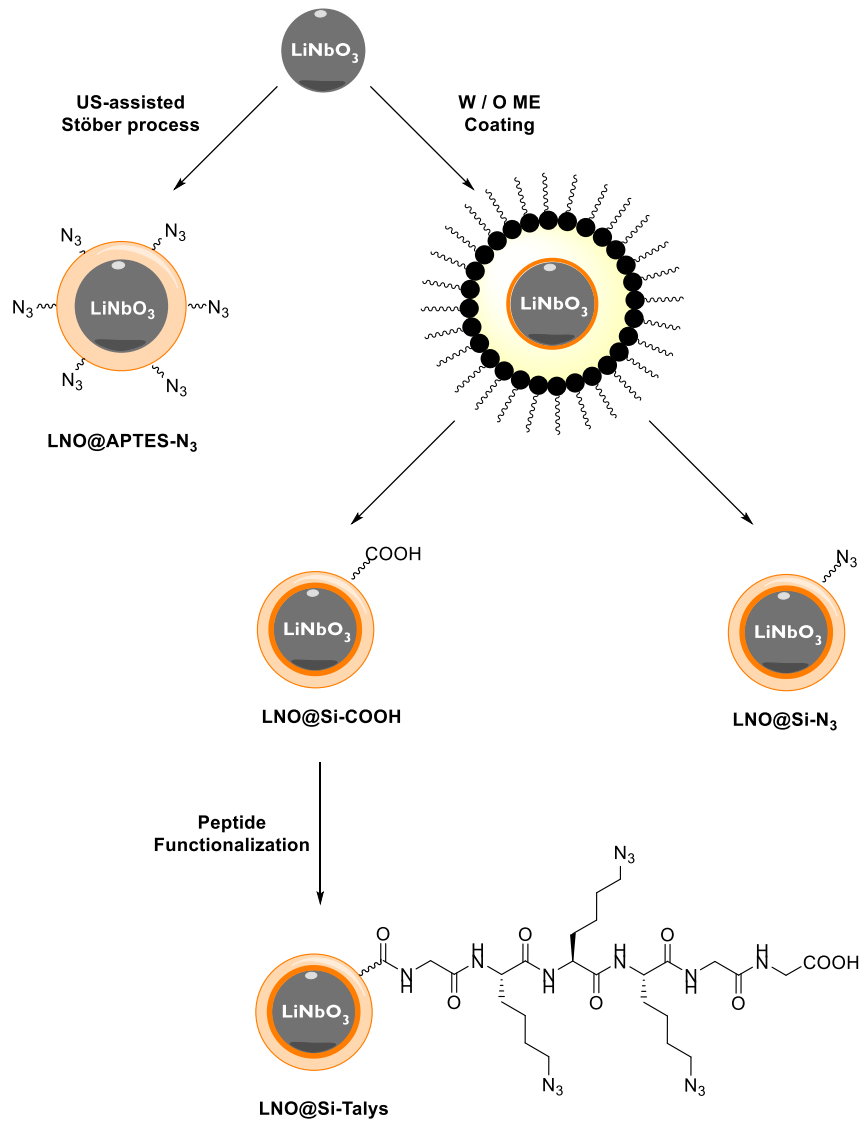
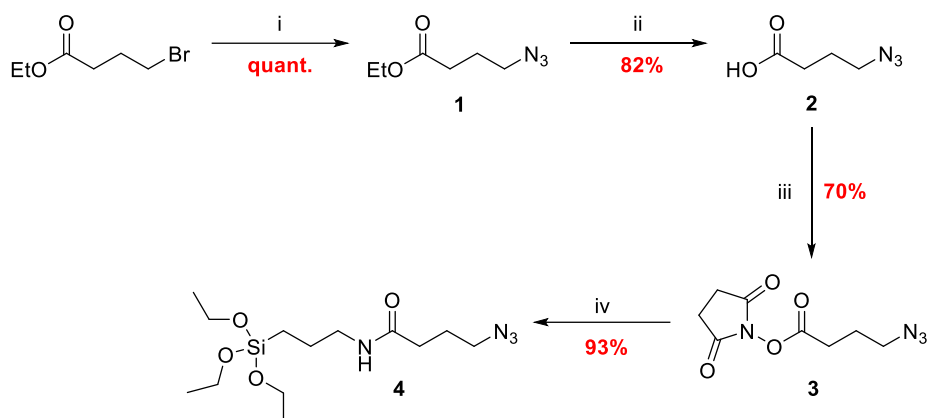


**Figure 21:** Different pathways for the surface silanization and azidation of LNO NPs.

### 3.1.1. Silanization by standard Stöber process

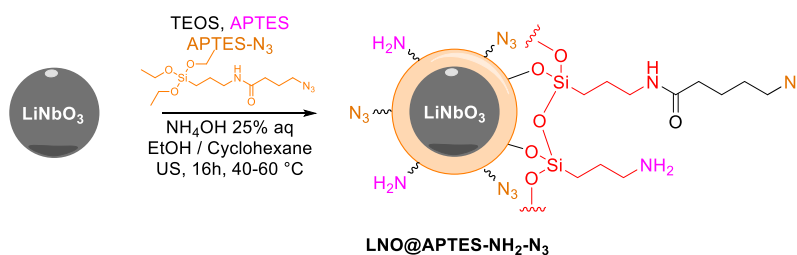
The synthesis of the azide modified silane, **APTES-N<sub>3</sub>**, follows the procedure developed in our group (*cf. Scheme 1*).<sup>154,155</sup> First, substitution of 4-bromobutanoate in the presence of sodium azide was performed to produce **1** in quantitative yield, followed by saponification of the ethyl ester to afford the corresponding carboxylic acid **2** in 82% yield. The carboxylic acid was activated with NHS to afford **3**, followed by coupling to the primary amine of APTES to afford **APTES-N<sub>3</sub>** (**4**) in almost quantitative yield, which was used for surface modification of the HNPs.



**Scheme 1: Synthesis of APTES-N<sub>3</sub>.** i- NaN<sub>3</sub>, MeOH / H<sub>2</sub>O, reflux, 7 h; ii- KOH, MeOH / H<sub>2</sub>O, 0°C to r.t, 6 h; iii- DCC, NHS, DCM, r.t, 4 h; iv- APTES, Et<sub>3</sub>N, DCM, r.t, 5 h.

LNO HNPs were used owing to their high second harmonic generation efficiency,<sup>156</sup> and were produced by our collaborators from SYMME (University of Savoie Mont Blanc, France) at a low hydrolysis rate of alkoxide precursors with a solvothermal route previously described.<sup>157</sup> Briefly, almost spherical and cubic-like LNO nanocrystals were prepared from a commercial double ethoxide precursor (LiNb(OEt)<sub>6</sub>) diluted in its parent alcohol and with 1,4-butanediol as co-solvent. Primary solid species are formed and condensate at room temperature upon water addition and ligand exchange, after which solvothermal reaction for 1 day at 235 °C generate non-centrosymmetric crystals with an average size between 20 to 100 nm. The exact molecular reaction pathway and crystallization mechanisms of LNO nanoparticles under solvothermal conditions were derived by our collaborators through extensive time- and temperature-resolved experiments allowing to track all the transient molecular and solid species. This led to the recently accepted publication by Riperto, F. et al., Nonclassical Nucleation and Crystallization of LiNbO<sub>3</sub> Nanoparticles from the Aqueous Solvothermal Alkoxide Route. *Small* **2023**, in press.

The first silica coating tests were attempted using a procedure previously developed in our group, adapted from the commonly described Stöber process.<sup>154,155</sup> LNO HNPs were suspended in a mixture of ethanol and cyclohexane (1:1), followed by the addition of TEOS, APTES and **APTES-N<sub>3</sub>** (**4**) (2:1:1). Aqueous ammonia 25% was added and the suspension was ultrasonicated for 16 h under argon (temperature starting at 40 °C, increasing up to 60 °C due to the heating caused by sonication). The resulting **LNO@APTES-NH<sub>2</sub>-N<sub>3</sub>** NPs were thoroughly washed to remove the unreacted organic compounds and characterized by DLS measurement of their hydrodynamic diameter and zeta potential. The first results were similar to the ones previously reported for this coating procedure (*cf. Scheme 2*).



**Scheme 2:** LNO coating with TEOS, APTES and APTES-N<sub>3</sub>, initial procedure.

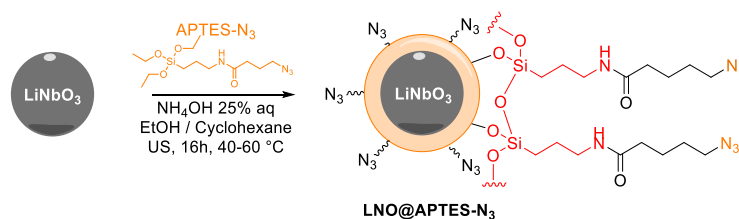
Further tests were attempted on two LNO batches, designated by LNO50 and LNO20 which exhibited respectively a TEM diameter of 50 and 20 nm. Unfortunately, using the general conditions that we previously developed for the silanization of metal oxide HNPs, it was not possible to achieve stable monodisperse colloidal suspension, as evidenced by the large DLS hydrodynamic diameters measured and apparent aggregation of the coated NPs when suspended in aqueous medium (*cf. Table 2*).

**Table 2:** DLS characterization of LNO50@APTES-NH<sub>2</sub>-N<sub>3</sub> and LNO20@APTES-NH<sub>2</sub>-N<sub>3</sub>.

Nanoparticles	Hydrodynamic diameter [nm]	Zeta Potential [mV]
LNO50 uncoated	138.3 ± 0.8	-50.1 ± 3.5
LNO50@APTES-NH <sub>2</sub> -N <sub>3</sub>	1708 ± 39.9	-11.7 ± 1.3
LNO20 uncoated	124.9 ± 2.6	-40.6 ± 1.7
LNO20@APTES-NH <sub>2</sub> -N <sub>3</sub>	1726 ± 100.8	-28.3 ± 1.9

Mean hydrodynamic diameter ( $d$ , intensity distribution) and surface charge ( $ZP$ ) were measured in distilled H<sub>2</sub>O at 22°C.

This prompted a screening of the coating conditions to determine the cause of this lack of repeatability and poor colloidal stability. After investigation, results seemed to indicate that the issue was arising from the surface properties of the new LNO batches, which appeared to vary from the previous batches produced. A simplified protocol was implemented, by removing APTES and TEOS, and by increasing the amount of APTES-N<sub>3</sub> in suspension to compensate (*cf. Scheme 3*).



**Scheme 3:** LNO coating with APTES-N<sub>3</sub>, modified procedure.

Coating with the modified protocol showed a clear improvement in terms of colloidal stability in aqueous medium (*cf.* Table 3). Upon silanization, **LNO@APTES-N<sub>3</sub>** showed a significant increase in size but without obvious signs of aggregation (Polydispersity Index or PDI  $\sim 0.2$ ). In addition, the removal of APTES from the coating procedure led to higher reproducibility in terms of zeta potential measurements due to the absence of primary amines on the surface. The more negative surface charge of the coated HNPs is beneficial by increasing the electrostatic repulsion between NPs, and by potentially reducing their toxicity since negatively charged NPs are reported to be generally safer than more positive ones.<sup>158</sup>

**Table 3:** DLS characterization of **LNO@APTES-N<sub>3</sub>**.

Nanoparticles	Hydrodynamic diameter [nm]	Zeta potential [mV]	PDI
Bare LNO	$77.8 \pm 10.3$	$-47.1 \pm 0.9$	0.232
<b>LNO@APTES-N<sub>3</sub></b>	$146.3 \pm 42.9$	$-42.8 \pm 2.6$	0.208

Mean hydrodynamic diameter ( $d$ , number distribution) and surface charge ( $ZP$ ) were measured in PBS (pH 7.4) at 22°C.

Scanning transmission electron microscopy (STEM) images of the coated NPs with energy dispersive X-ray (EDX) elemental composition analysis showed the presence of a homogeneous silica shell around the LNO core, which appeared to be around 10 nm thick (*cf.* Figure 1). These images also show that the hydrodynamic diameter measured in DLS is larger than the size of the core NPs, which ranged from 50 to 100 nm in diameter.

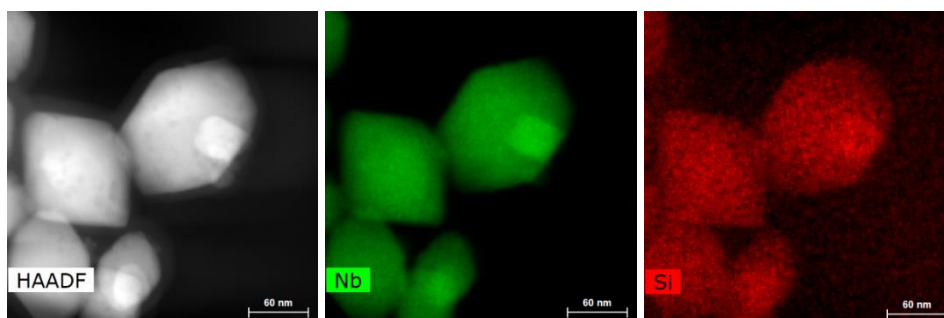


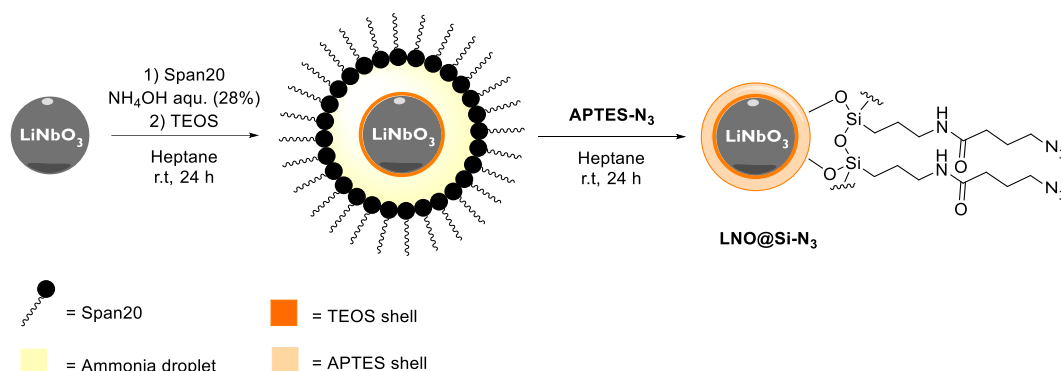
**Figure 22:** Representative STEM images with EDX elemental analysis of **LNO@APTES-N<sub>3</sub>**. **Left:** dark field STEM image, **Middle:** Nb EDX map, **Right:** Si EDX map.

In summary, LNO NPs were coated with an azide-bearing APTES derivative using a modified ultrasonication-assisted Stöber process, with an improved colloidal stability of the coated NPs. Nonetheless, the silica shell around the HNP core is relatively thin and less robust as it lacks the density provided by the cross-linking between silane units which occurs when TEOS is included. Improvement of this coating protocol will be discussed in the next section, with the main goal of being able to introduce TEOS in the silica shell while maintaining a good colloidal stability and a high density of surface azide groups.



### 3.1.2. Coating by water-in-oil microemulsion

The use of reverse MEs was investigated in order to achieve a high control over the size and monodispersity of the resulting colloidal suspension of silica-coated LNO NPs. A two-step procedure was applied, involving the addition of TEOS for polycondensation at the NP surface through the Stöber process, followed by addition of the azide-bearing APTES derivative (*cf. Scheme 4*).



**Scheme 4:** Silanization of LNO NPs using reverse W/O MEs.

In W/O MEs, small aqueous droplets dispersed in oil phase act as “nanoreactors” which accommodate a single NP for subsequent silanization. The method allows to monitor the droplet size for better control over the thickness of the silica layer achieved through the thorough adjustment and tuning of parameters such as amounts of surfactants, oil phase, aqueous phase and silica precursors.

The stability and the efficiency of the reverse ME method strongly depend on the selection of the surfactant and ratios of applied reagents. Screening of surfactants (Tween 80, Brij 35, AOT and Span 20) revealed that only Span 20 led to stable droplets over the time of the coating procedure. The use of co-surfactants, such as EtOH or octan-2-ol, led to a significant increase in the droplet size. The optimal volume ratio of oil to aqueous ammonia was empirically found to be 15 mL : 50  $\mu$ L (heptane : ammonia). Furthermore, the use of a more concentrated ammonia solution (28% aq) allowed to increase the thickness of the silica coating layer. Coating procedures were performed at r.t. to avoid evaporation of ammonia, due to its low boiling point. The silanization protocol lasted for 48 h and a slight increase of the size of the droplets was observed over the course of the reaction. However, only the initial size of the droplets needs to be finely tuned to accommodate the size of bare LNO NPs.

The reverse ME method should avoid the formation of multi-core coated NPs or core-free silica NPs by matching the number of uncoated NPs ( $N_{\text{NPs}}$ ) with the number of stabilized droplets ( $N_{\text{droplets}}$ ), so that one droplet would accommodate a single LNO HNP.  $N_{\text{NPs}}$  and  $N_{\text{droplets}}$  were defined as follows:

$$N_{\text{NPs}} = \frac{m_{\text{NPs}}}{m_{1\text{ NP}}} = \frac{m_{\text{NPs}}}{d \times \frac{4}{3} \times \pi \times r_{\text{NP}}^3}$$

where  $m_{1\text{ NP}}$  represents the mass of one NP,  $m_{\text{NPs}}$  represents the total mass of NPs added in the reaction,  $d$  stands for the LNO density ( $d = 4.65 \text{ g/cm}^3$ ), and  $r_{\text{NP}}$  is the radius of the bare LNO NP (measured by DLS).

$$N_{\text{droplets}} = \frac{V_{\text{aqueous phase}}}{V_{1\text{ droplet}}} = \frac{V_{\text{aqueous phase}}}{\frac{4}{3} \times \pi \times r^3}$$

where  $V_{\text{aqueous phase}}$  is the volume of aqueous ammonia added in the reaction and  $r$  is the radius of one droplet (measured by the DLS size distribution in number during the procedure, i.e., before addition of LNO NPs).

The radius of the ammonia droplets was measured at 85 nm after 3 h of stabilization, but their size was observed to increase over time. After 7 h, their radius reached 100 nm and went up to 130 nm after 20 h. If this last value is taken for the radius of the droplets (half way through the silanization procedure), and considering that bare LNO NPs have an average radius of about 50 nm (measured by DLS), the amount of NP required to match the number of ammonia droplets corresponds to 10 mg for the conditions described above.

Several reaction parameters were screened to optimize the coating conditions and to achieve monodispersity of the resulting **LNO@Si-N<sub>3</sub>** NP suspension. After stabilization of the NP / ME mixture for 3 h, TEOS was added and left to react for 24 h. Addition of **APTES-N<sub>3</sub>** was done after dissolution in EtOH at a concentration of 300 mg/mL, to facilitate handling and ease its transfer to the aqueous droplets due to EtOH acting as a co-surfactant. The resulting **LNO@Si-N<sub>3</sub>** NPs were analysed by DLS (*cf. Table 4*) in EtOH and PBS 0.1x. In EtOH, a significant increase in size was observed compared to bare LNO NPs, and monodispersity of the suspension was preserved (PDI = 0.07). In buffered aqueous solution, **LNO@Si-N<sub>3</sub>** NPs showed signs of agglomeration (large hydrodynamic diameter and PDI ~ 0.3) which was attributed to the high density of hydrophobic chains introduced at the NP surface.

**Table 4:** DLS characterization of **LNO@Si-N<sub>3</sub>** NPs.

Nanoparticles	Bare LNO	LNO@Si-N <sub>3</sub>
Hydrodynamic diameter <sup>a</sup> [nm]	120.1 ± 1.8	233.2 ± 0.5
PDI <sup>a</sup>	0.03	0.07
Hydrodynamic diameter <sup>b</sup> [nm]	78.2 ± 29.6	864.2 ± 37.6
PDI <sup>b</sup>	0.28	0.29
Zeta potential, pH 7.4 <sup>b</sup> [mV]	-34.8 ± 1.4	-27.6 ± 4.1
Zeta potential, pH 3.0 <sup>c</sup> [mV]	-33.8 ± 0.4	-9.0 ± 1.5

<sup>a</sup>EtOH. <sup>b</sup>PBS 0.1x (pH 7.4). <sup>c</sup>PBS 0.1x (pH 3.0).

Fourier transform infrared spectroscopy (FTIR) was used to assess the efficiency of the coating method and confirm the presence of the silica layer, as well as N<sub>3</sub> moieties at the NP surface

(Figure 23). All spectra were normalized with respect to the O-Nb-O asymmetric and symmetric bands (720 and 650  $\text{cm}^{-1}$ , respectively). **LNO@Si-N<sub>3</sub>** NPs presented peaks related to the linear stretching of the O-Si-O bond at 1080  $\text{cm}^{-1}$  and a band characteristic of the Si-CH<sub>2</sub> symmetric bending at 1200  $\text{cm}^{-1}$ , indicating the formation of the silica coating layer. NPs displayed especially an intense band for the characteristic N=N=N stretch ( $\sim$ 2100  $\text{cm}^{-1}$ ). The presence of these intense peaks gave evidence for the efficiency of the silanization procedure and confirmed the presence of surface reactive azido moieties for downstream functionalization.

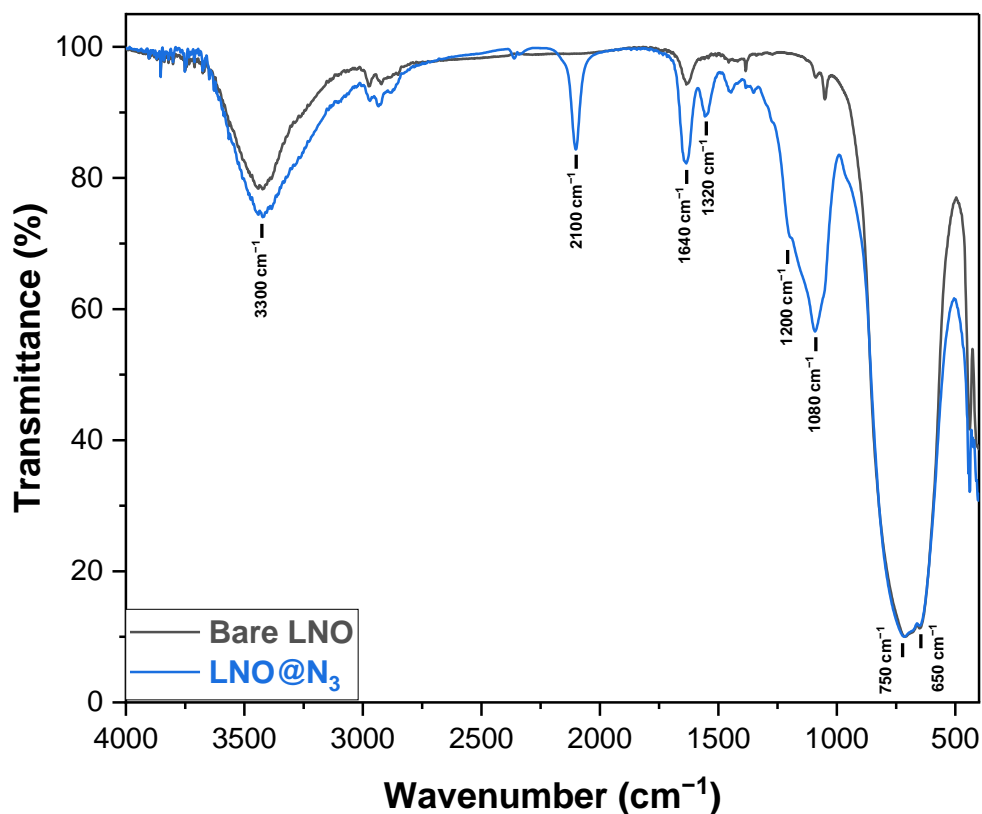


**Figure 23:** FTIR spectra of bare LNO (black), and **LNO@Si-N<sub>3</sub>** (blue), NPs normalized with respect to the O-Nb-O bands.

The morphology of **LNO@Si-N<sub>3</sub>** NPs was further investigated by STEM and EDX elemental mapping (*cf.* Figure 24). The silica coating was not homogeneous, revealing the formation of silica clusters in some regions of the NP surface and very thin silica layer on part of the inorganic cores. The hydrophobic character of the **APTES-N<sub>3</sub>** silanization reagent was suspected to be the cause of the poor quality of the resulting silica coating.

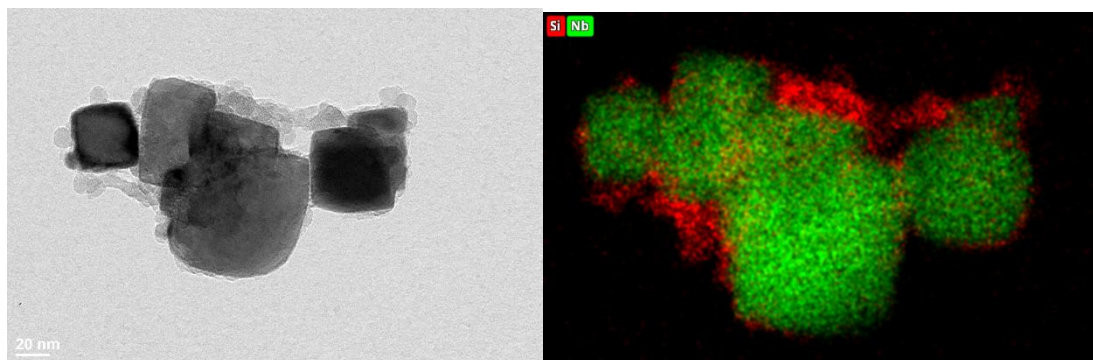


**Figure 24:** Representative STEM images with EDX elemental analysis of **LNO@Si-N<sub>3</sub>**. **Left:** Bright field STEM image, **Right:** Merge of Si and Nb EDX maps, Scale bar: 20 nm.

In summary, a W/O ME method was successfully developed to coat LNO NPs in a silica shell composed of TEOS and APTES-N<sub>3</sub>, displaying high monodispersity in organic medium and a high density of surface azido groups. However, **LNO@Si-N<sub>3</sub>** displayed poor colloidal stability in aqueous medium, which is not suitable for potential biological applications, and STEM analysis showed that the silica coating was not homogeneous around the LNO core. The strategy developed to improve upon this W/O ME silanization method is discussed in the following section, aiming at improving the colloidal properties of the coated NPs, especially in an aqueous medium.

### 3.1.3. Surface peptide functionalization

An alternative strategy was investigated for the introduction of azido groups while ensuring monodisperse NP suspension in aqueous medium (PDI < 0.2). First, LNO NPs were coated through the W/O ME method with a silanization reagent displaying terminal carboxylic acid (**APTES-COOH**). The aim here was to introduce a more hydrophilic chain on the NP surface to reduce aggregation in water. Conjugation of the resulting **LNO@Si-COOH** NPs with a branched peptide containing multiple azide-bearing side chains was then envisaged to provide the simultaneous presence of azido and carboxylate surface orthogonal functionalities and to improve the hydrophilic character of the functionalized NPs for enhanced colloidal stability in aqueous medium. The peptide structure design was based on repeating azide-modified lysine units (azidolysine = **Alys**). As the number of **Alys** units could be easily modified, the length of the peptide backbone could be tuned to exhibit various azide to carboxylate ratios. The peptide herein described (tri-azidolysine = **Talys**, *cf. Figure 25*) contains three **Alys** units, and was capped with one glycine unit at each end to reduce the steric hindrance on the amine and carboxylic acid groups, thus increasing their reactivity.

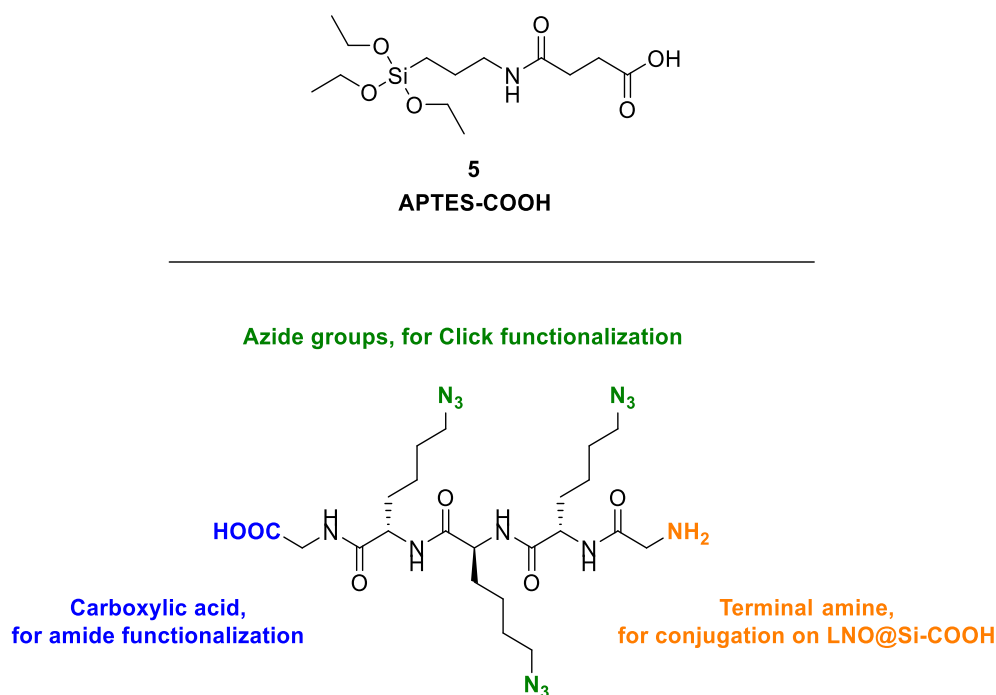
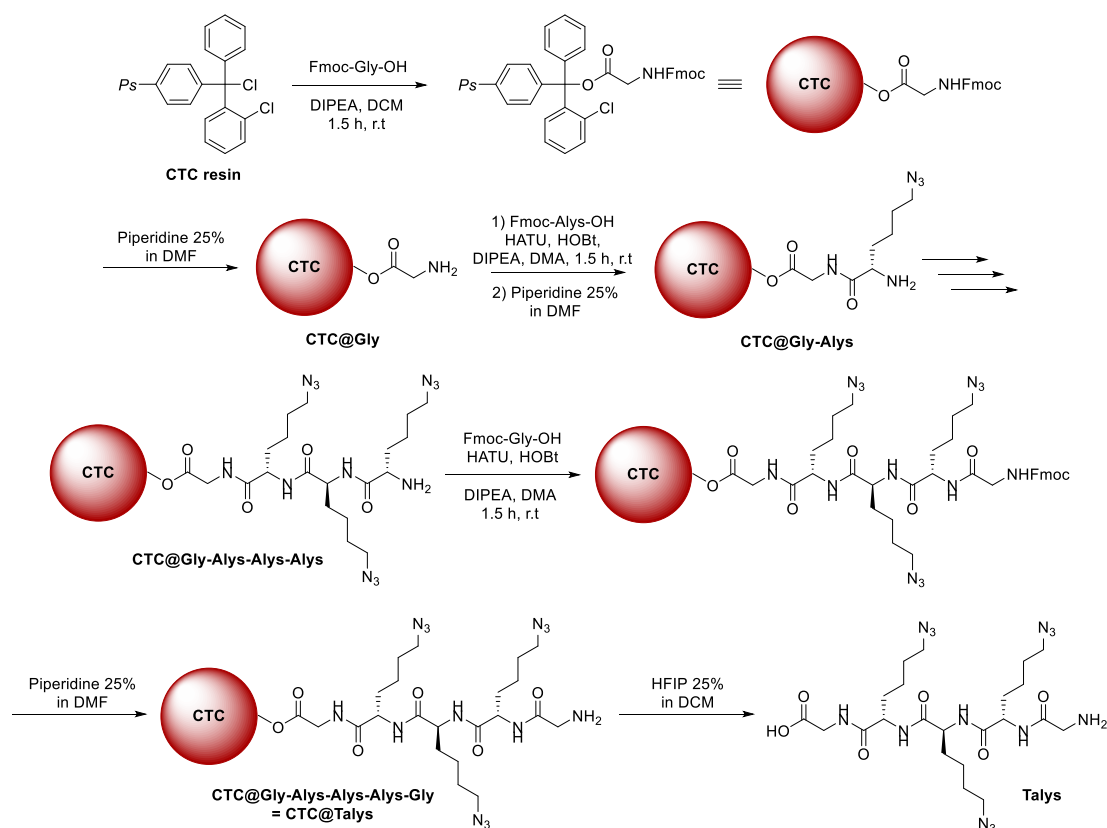


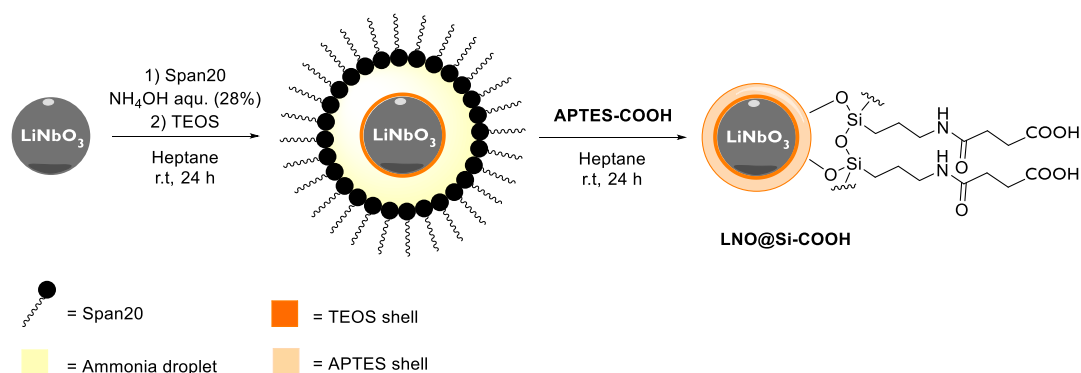
**Figure 25:** Structure of **APTES-COOH** and of the designed **Talys** peptide (tri-azidolysine, Gly-Alys-Alys-Alys-Gly).

**Talys** was produced by solid phase peptide synthesis (SPPS, *cf. Scheme 5*), using Fmoc protected amino acids as building units. Fmoc-protected glycine was loaded onto 2-chlorotrityl chloride (CTC) resin, followed by deprotection of the terminal amine with piperidine 25% in DMF. Fmoc-protected **Alys** was then successively coupled and deprotected three times on CTC@Gly. Finally, the last glycine unit was added through coupling and Fmoc deprotection, after which **Talys** was cleaved from the resin using HFIP 25% in DCM, and purified by preparative HPLC.



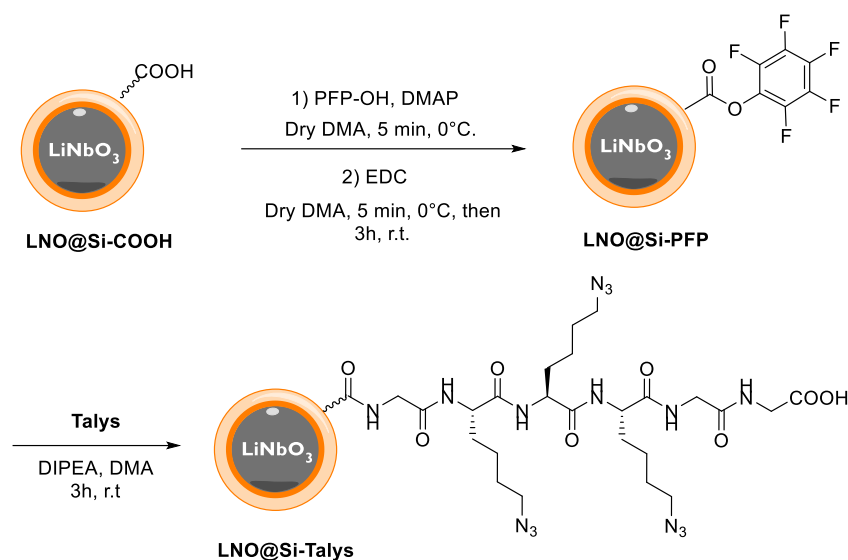
Scheme 5: Preparation of Talys by SPPS.

**LNO@Si-COOH** NPs were produced by W/O ME coating using the conditions described in 1.1.2, replacing **APTES-N<sub>3</sub>** with **APTES-COOH** (*cf. Scheme 6*).



Scheme 6: Preparation of LNO@Si-COOH.

**Talys** was grafted to **LNO@Si-COOH** by amide bond coupling (*cf. Scheme 7*). The selected conditions started with the activation of surface carboxylic acid groups using pentafluorophenol (PFP-OH) in the presence of EDC and DMAP, generating the PFP ester. The excess of coupling agents was discarded by centrifugation, and the activated **LNO@Si-PFP** NPs were treated with **Talys** and DIPEA to afford **LNO@Si-Talys** NPs which were characterized by DLS.



**Scheme 7:** Synthesis of **LNO@Si-Talys** NPs.

The silanization procedure afforded **LNO@Si-COOH** NPs with a high monodispersity (PDI < 0.1) of the resulting colloidal suspension in PBS buffer (*cf.* Table 5). The presence of surface hydrophilic groups also resulted in large pH-dependent variations of the surface charge (on average from -43 mV at pH 7.4 to -12 mV at pH 3.0), consistent with the presence of carboxylates at the NP surface. As evidenced by measurement of their size and PDI, **LNO@Si-Talys** NPs exhibited an impressive ability to suspend in both organic (EtOH) and aqueous media (PBS), resulting in the formation of homogeneous colloidal suspensions (PDI of 0.10 and 0.06 in EtOH and PBS 0.1x, respectively) (*cf.* Table 4). The slight increase in size and very similar zeta potentials compared to **LNO@Si-COOH** NPs are consistent with surface conjugation to a small peptide.

**Table 5.** DLS characterization of **LNO@Talys** NPs.

Nanoparticles	<b>LNO@Si-COOH</b>	<b>LNO@Si-Talys</b>
<b>Hydrodynamic diameter<sup>a</sup></b> [nm]	Not measured	184.5 ± 8.8
<b>PDI<sup>a</sup></b>	Not measured	0.10
<b>Hydrodynamic diameter<sup>b</sup></b> [nm]	152.1 ± 3.6	169.5 ± 2.5
<b>PDI<sup>b</sup></b>	0.09	0.06
<b>Zeta potential, pH 7.4<sup>b</sup></b> [mV]	-44.8 ± 1.1	-35.8 ± 0.4
<b>Zeta potential, pH 3.0<sup>c</sup></b> [mV]	-11.4 ± 2.3	-10.6 ± 2.3

<sup>a</sup>EtOH. <sup>b</sup>PBS 0.1x (pH 7.4). <sup>c</sup>PBS 0.1x (pH 3.0).

**LNO@Si-Talys** NPs were further characterized by FTIR (*cf. Figure 26*) which gave evidence for the introduction of azido groups, corresponding to their characteristic band at  $2100\text{ cm}^{-1}$  (though smaller in intensity as compared to **LNO@Si-N<sub>3</sub>** NPs). The signals attributed to the silanization ( $1640$ ,  $1200$  and  $1080\text{ cm}^{-1}$ ) are also mostly identical between **LNO@Si-COOH** and **LNO@Si-Talys** NPs, indicating that the coupling procedure was not detrimental to the integrity of the silica shell.

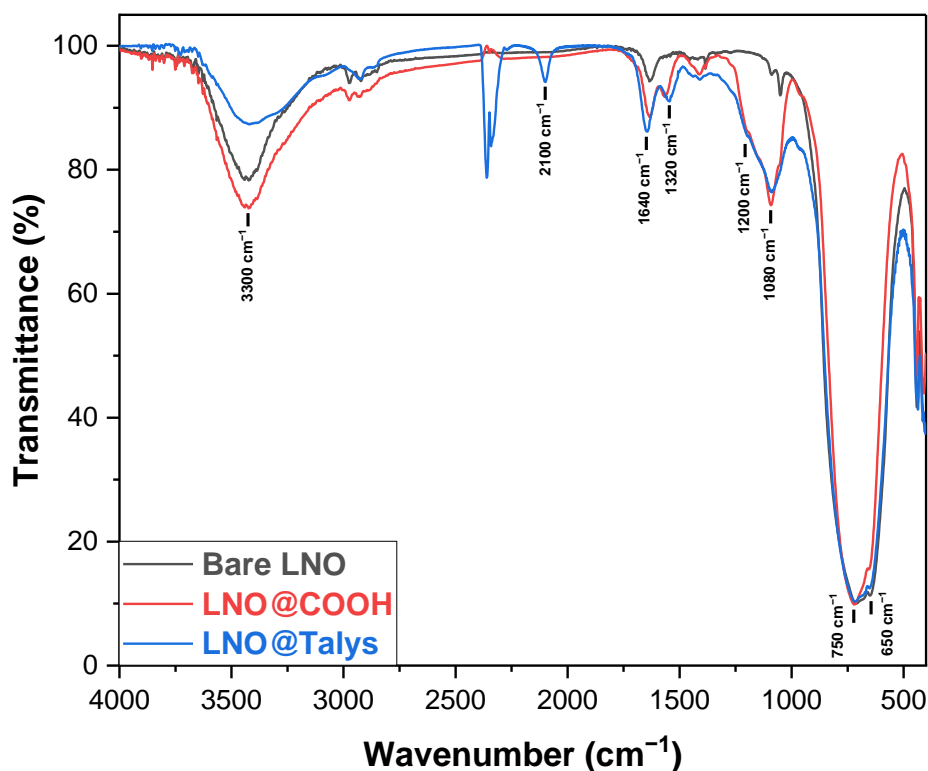


**Figure 26:** FTIR spectra of bare LNO NPs (black), **LNO@Si-COOH** NPs (red), and **LNO@Si-Talys** NPs (blue), normalized with respect to the Nb signal.

The morphology of **LNO@Si-Talys** NPs was also assessed by STEM and EDX elemental mapping analysis, illustrating that a dense and homogeneous silica shell was formed around the crystalline core during silanization, with a significant improvement of the silica layer homogeneity as compared to **LNO@Si-N<sub>3</sub>** NPs (*cf. Figure 27*, average thickness of the coating layer was measured at 10 nm).

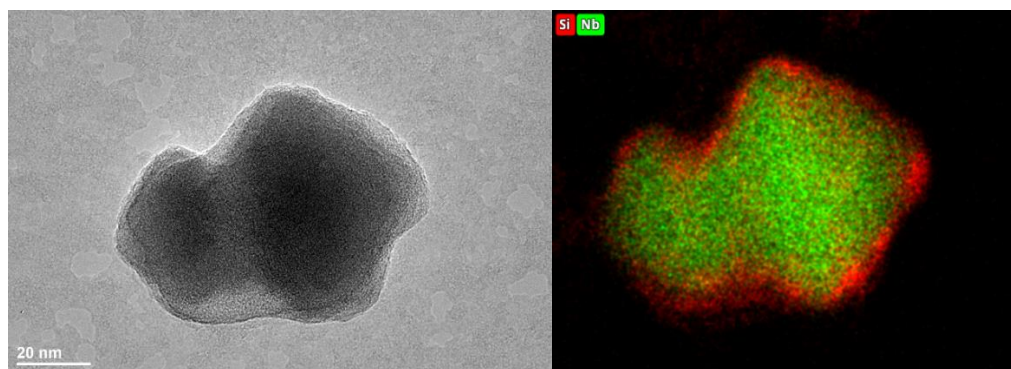
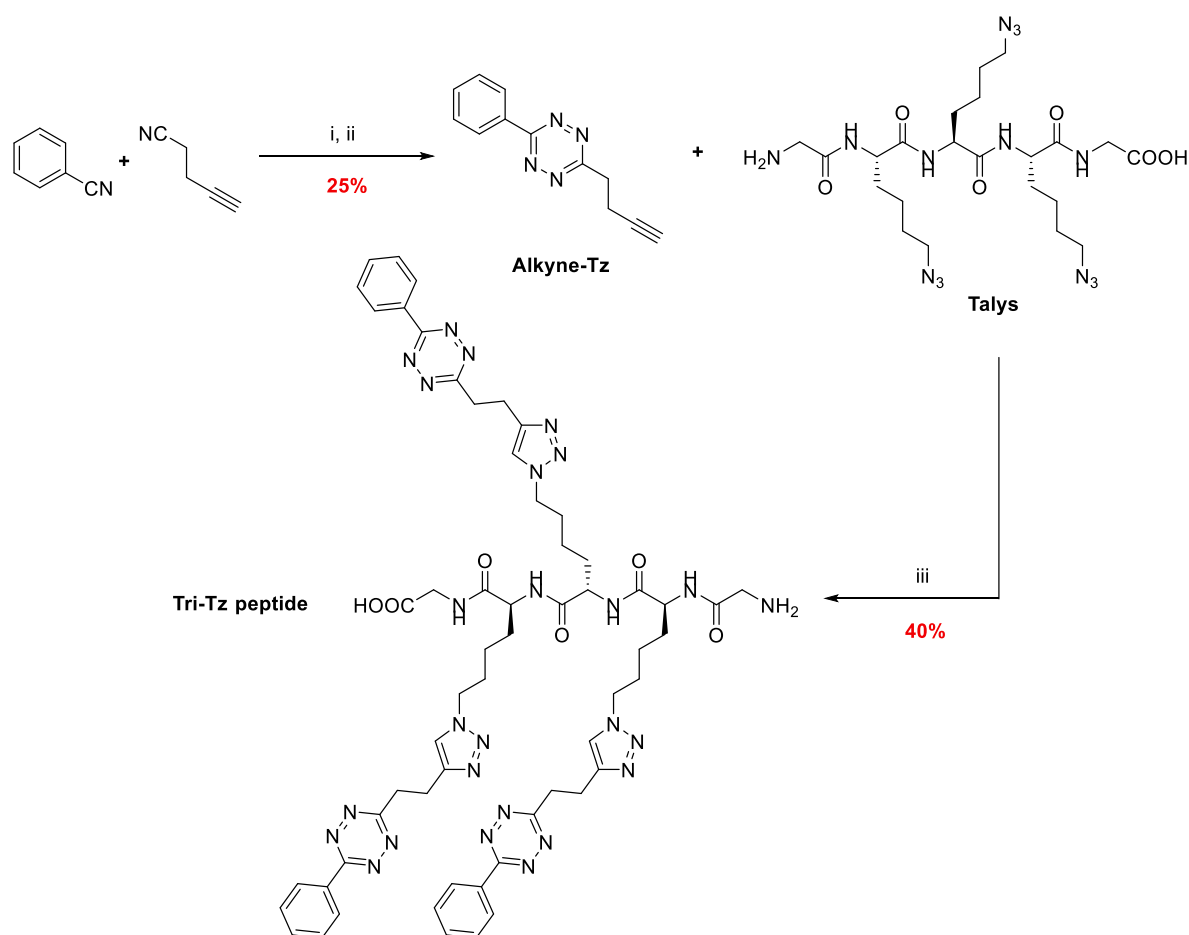


**Figure 27:** Representative STEM images with EDX elemental analysis of **LNO@Si-Talys**. **Left:** Bright field STEM image, **Right:** Merge of Si and Nb EDX maps, Scale bar: 20 nm.



In summary, through the modification of the silanization reagent for the *W / O* ME assisted coating step and subsequent surface coupling to a short peptide bearing multiple azide moieties, the resulting **LNO@Si-Talys** NPs displayed remarkable colloidal properties in both organic and aqueous media, and presented orthogonal surface reactive groups for downstream functionalization.

Other peptide derivatives were envisaged for surface modification of **LNO@Si-COOH** NPs in order to enlarge the possibilities for post-functionalization strategies using click reactions. In the long term, the ability to introduce different orthogonal reactive moieties on the NP surface could allow for simultaneous multi-functionalization with various ligands, which could pave the way for the efficient preparation of complex theranostic nanoplatforms. One such new functionalization strategy which was investigated was through the tetrazine ligation, involving the reaction between a tetrazine group and a strained alkene by inverse electron demand Diels Alder cycloaddition, followed by an irreversible retro Diels Alder reaction. In this scope, the **Talys** peptide was modified with an alkyne-bearing tetrazine small molecule (**alkyne-Tz**) by CuAAC, in order to substitute its azido groups with Tz (*cf. Scheme 8*).



**Scheme 8: Talys modification with Tz.** i- mercaptopropionic acid, hydrazine monohydrate, neat, 50 °C, 24 h; ii- NaNO<sub>2</sub>, HCl, H<sub>2</sub>O, r.t, 1 h; iii- CuSO<sub>4</sub>, NaAsc, THPTA, THF/H<sub>2</sub>O 1:1, r.t, 2 h.

This **Tri-Tz** peptide was successfully prepared in moderate yield, but due to time constraints, we did not explore the capabilities of these Tz containing derivatives for post-conjugation reactions. However, we believe that Tz moieties might offer faster kinetics for surface conjugation by click reaction as compared to azido groups.<sup>159,160</sup>

### 3.2. Stimuli responsive nanocarriers

The following chapters cover the conjugation of an analogue of the anticancer drug erlotinib to a coumarinyl photocleavable linker. The coumarin-drug conjugate was further derivatized with a strained cyclooctyne moiety in order to be functionalized on the surface of azide-bearing silica coated nanoparticles by SPAAC. The efficiency of erlotinib derivative uncaging triggered by the SHG emission of the LNO core (UV) upon NIR irradiation was evaluated *in vitro* on a cancer cell line overexpressing the epidermal growth factor receptor (*cf. Figure 7*). The results presented in this section were disclosed in the publication Photoresponsive Nanocarriers Based on Lithium Niobate Nanoparticles for Harmonic Imaging and On-Demand Release of Anticancer Chemotherapeutics. *ACS Nanoscience Au*, **2022**, 2(4), pp.355-366.

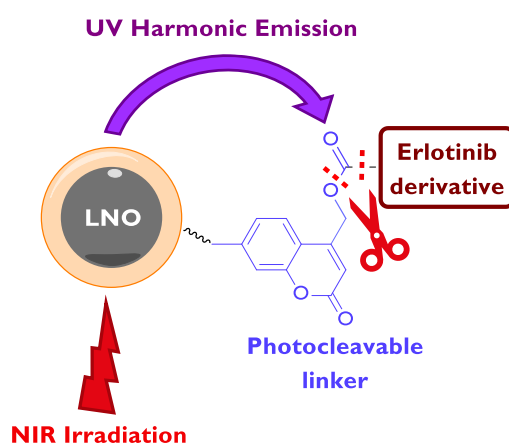
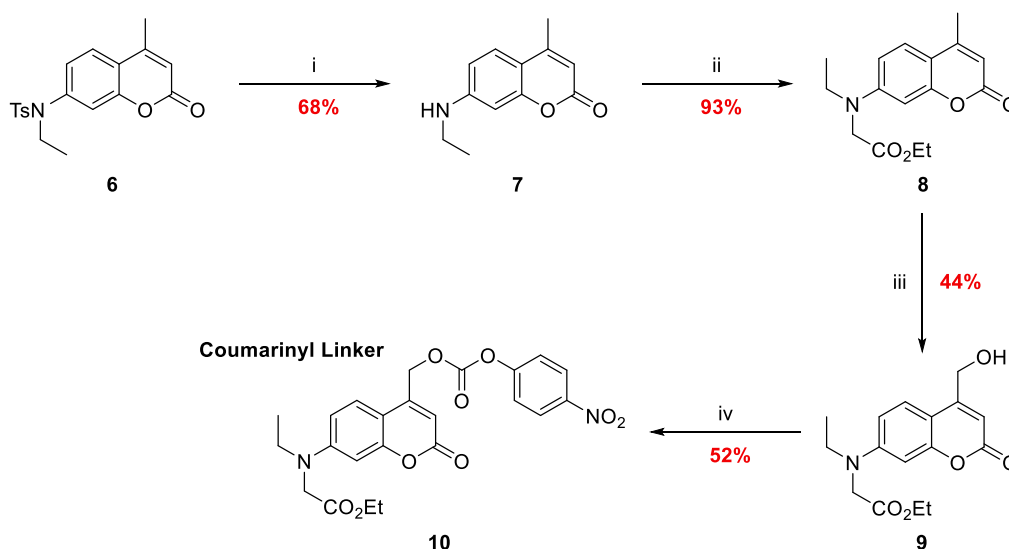


**Figure 7:** Schematic representation of the mechanism of drug photo-release from caged LNO NPs.

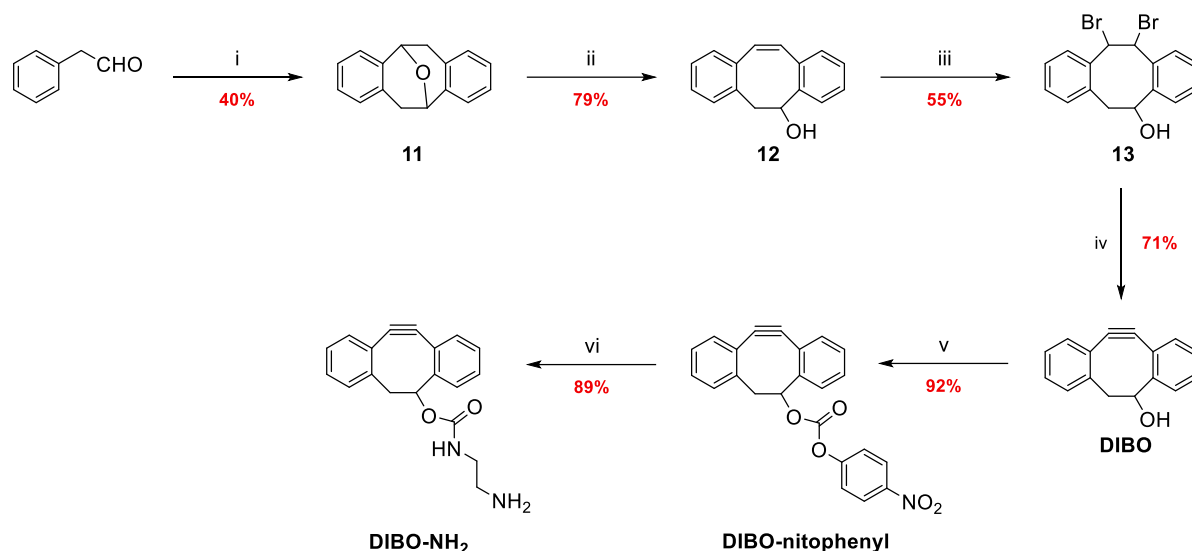
### 3.2.1. Synthesis of the drug delivery system

The coumarinyl linker was synthesized according to the procedure reported in the thesis of Dr. Jérémy Vuilleumier (*cf. Scheme 9*).<sup>155</sup> The tosyl group of intermediate **6** (previously synthesized in our group starting from 3-aminophenol) was removed with sulfuric acid and the resulting secondary amine was alkylated with ethyl bromoacetate to afford **8** in 63% yield (2 steps). Riley oxidation followed by NaBH<sub>4</sub> reduction afforded the photocleavable linker **9**, which was activated as a 4-nitrophenyl carbonate (**10**).



**Scheme 8: Synthesis of CM derivative.** i- H<sub>2</sub>SO<sub>4</sub>, 0°C, 1 h; ii- ethyl bromoacetate, K<sub>2</sub>CO<sub>3</sub>, TBAB, NaI, ACN, reflux, 46 h; iii- SeO<sub>2</sub>; *p*-xylene, reflux 24 h; then NaBH<sub>4</sub>, MeOH, r.t, 3 h; iv- 4-nitrophenyl chloroformate, DIPEA, DCM, r.t, 16 h.

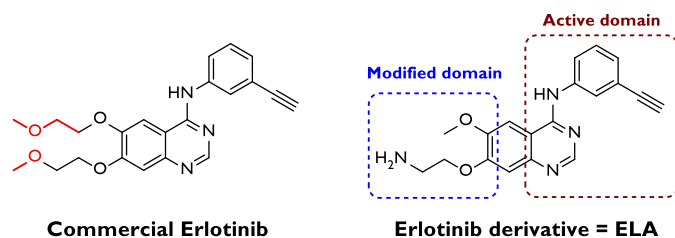
The synthesis of the strained cyclooctyne, a derivative of DIBO, was performed according to a pathway previously developed in our group (*cf. Scheme 9*).<sup>154,155</sup> Phenylacetaldehyde was dimerized in the presence of trimethylsilyl iodide to afford intermediate **11** in moderate yield. Under basic condition, elimination and subsequent ether bridge opening led to the alcohol **12** in moderate yield. Bromination of the cyclooctene and LDA-assisted elimination afforded **DIBO** in 39% (2 steps). Using this protocol, batches up to 500 mg were produced. Activation with *p*-nitrophenyl chloroformate and condensation with ethylenediamine afforded **DIBO-NH<sub>2</sub>** in good yield, which was used for the coupling with the coumarinyl linker and the erlotinib derivative.



**Scheme 9: Synthesis of DIBO derivatives.** i- Me<sub>3</sub>SiI, DCM, 5°C, 7 days; ii- BuLi, THF, r.t, 4 h; iii- Br<sub>2</sub>, CHCl<sub>3</sub>, r.t, 2 h; iv- LDA, THF, r.t, 1 h; v- 4-nitrophenyl chloroformate, pyridine, DCM, r.t, 16 h; vi- ethylenediamine, Et<sub>3</sub>N, DCM, r.t, 2 h.

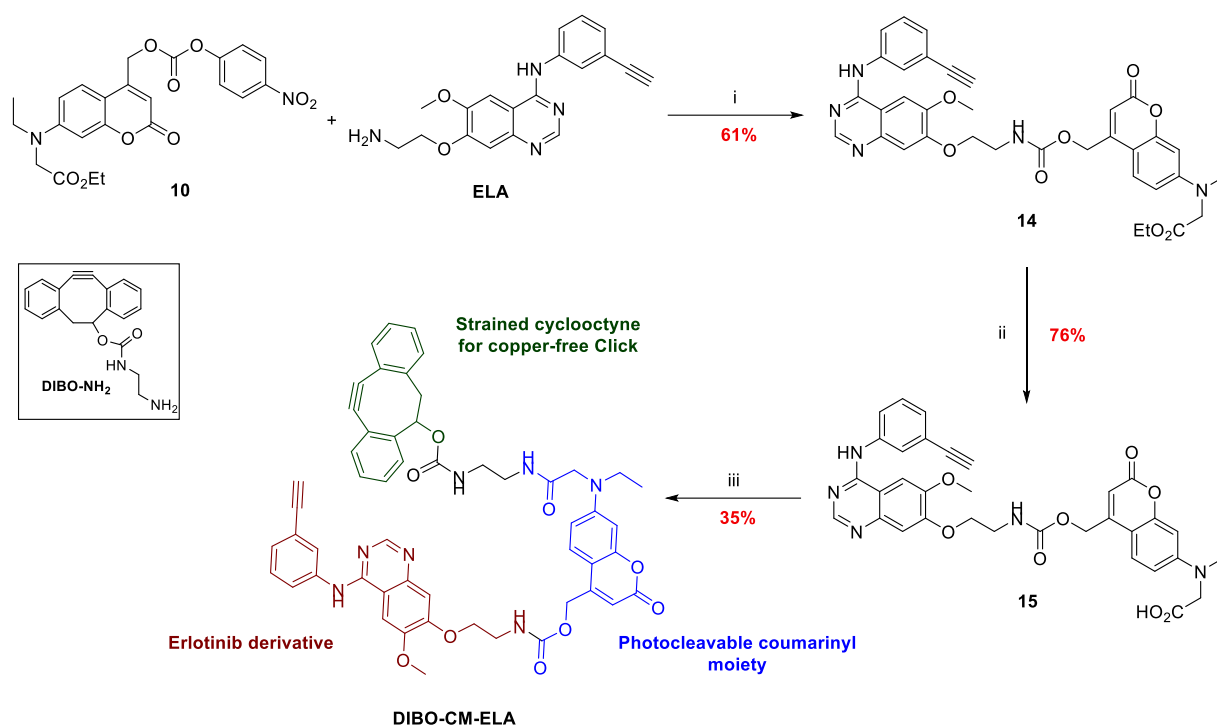
In this project, erlotinib was chosen as the cancer chemotherapeutic to be released from the NPs. Erlotinib acts as tyrosine kinase inhibitor, and is used in the treatment of EGFR-overexpressing tumours by blocking the adenosine triphosphate site of the receptor.<sup>161</sup> Since mutations in the EGFR are occurring in different cancer types, including non-small-cell lung cancer, glioblastoma and epithelial cancer<sup>162</sup>, this treatment approach can target a variety of malignancies. This treatment strategy was selected as the release of inhibitors of tyrosine kinases from nanoplatfroms have been much less studied in the literature than more common therapeutics, such as for instance doxorubicin, and they can still benefit from the advantages procured by an NP-based drug delivery system, since compounds like erlotinib suffer from low bioavailability and patient acquired resistance after repeated treatments.<sup>163</sup>

In order to allow for covalent conjugation to coated LNO NPs, the design of an erlotinib analogue (**ELA**) was previously developed in our group to maintain the active domain involved in EGFR recognition while installing a reactive side chain (*cf. Scheme 10*). Starting from vanillin, **ELA** was synthesized in 11 steps.<sup>155</sup>



**Scheme 10:** Chemical structures of erlotinib and **ELA** analogue.

The primary amine of **ELA** was conjugated to the coumarinyl linker by formation of a carbamate (**17**) in moderate yield. Saponification of the ethyl ester followed by coupling with **DIBO-NH<sub>2</sub>** provided the drug delivery system (DDS) **DIBO-CM-ELA** in 35% yield (*cf. Scheme 11*).

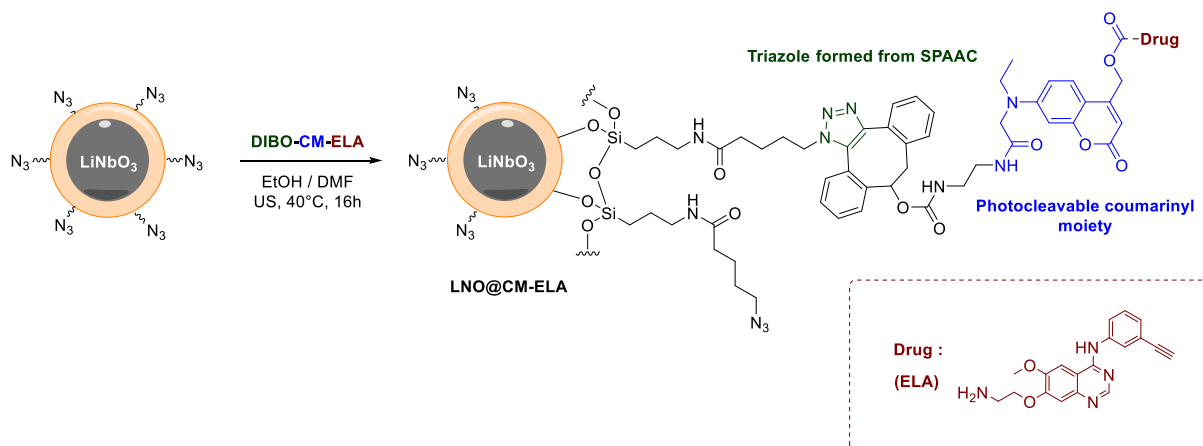


**Scheme 11: Synthesis of DIBO-CM-ELA:** i- DIPEA, DMF, r.t., 16 h; ii- LiOH, MeOH / H<sub>2</sub>O (5:1), r.t., 6 h; iii- *DIBO-NH<sub>2</sub>*, HOBT, DMAP, EDCI, DIPEA, DMF, r.t., 24 h.

In summary, a DDS based on a coumarinyl photocleavable linker capable of releasing the erlotinib derivative **ELA** and displaying a strained cyclooctyne moiety for SPAAC conjugation was successfully synthesized. The functionalization of this DDS on silanized LNO NPs presenting azide surface moieties is described in the next section.

### 3.2.2. Nanoparticle functionalization with the drug delivery system

**DIBO-CM-ELA** was conjugated to **LNO@APTES-N<sub>3</sub>** NPs (silanization described in section 3.1.1) by SPAAC reaction which avoids the use of external reagents, thus facilitating the purification of the final NP conjugates (*cf. Scheme 12*).



**Scheme 12:** Functionalization of **LNO@APTES-N<sub>3</sub>** with **DIBO-CM-ELA**.

**LNO@CM-ELA** NPs were characterized by DLS in PBS, revealing a slight increase in size (from  $146.3 \pm 42.9$  nm for **LNO@APTES-N<sub>3</sub>** to  $179.2 \pm 4.4$  nm) and a PDI value of 0.1, indicating monodispersity and a good colloidal stability in aqueous medium.

The amount of **DIBO-CM-ELA** grafted on the NP surface was estimated indirectly, by measuring the remaining concentration of **DIBO-CM-ELA** in the supernatant at the end of the functionalization procedure. This measurement was done by UV-vis absorption, comparing the values measured in the supernatant to the absorption of **DIBO-CM-ELA** standards prepared at set concentrations (see Experimental 5.17). The surface loading of the erlotinib derivative **ELA** was thereby estimated at 27 nmol/mg of NPs.

The photocleavage and subsequent release of **ELA** from the surface of functionalized LNO NPs was first assessed under direct UV irradiation at 366 nm in PBS (*cf. Figure 28*, black curve, see Experimental 5.17 for detailed calculation and progress curve). Analysis of the medium by ultrahigh-performance liquid chromatography-mass spectrometry (UHPLC-MS) at successive time points indicated that the unique released component was **ELA** (assessed by its coelution with the standard after 2.0 min and accurate mass, see Experimental 5.17 for quantification protocols and calibration curve). Then, the ability of the second harmonic emission of **LNO@CM-ELA** NPs to trigger the uncaging of the cytotoxic cargo was investigated using the unfocused beam from an amplified Ti:sapphire pulsed laser system. In a first setting, we used an amplified laser system delivering femtosecond pulse train at 1 kHz repetition rate (setup 1, see Experimental 5.17). The choice of an amplified laser system at low repetition rate allows to maintain a comparatively large peak intensity (necessary for exerting nonlinear interaction) on a large sample area, which facilitates the subsequent reliable quantification of **ELA** release by UHPLC-MS. The low repetition rate is also advantageous for limiting heat accumulation effect and sample photodamage.<sup>164</sup> After 15 min irradiation at 790 nm in PBS, the release of **ELA** reached 41% (*cf. Figure 28*, red curve). This irradiation induced a SHG emission at 395 nm from the HNPs, matching with the absorption

of amino-coumarin dyes reported around 380 nm.<sup>165</sup> The progress curves were fitted using a monoexponential function and the initial rate ( $k_0$ ) at 5 min was calculated to be 271 nM.min<sup>-1</sup> (see Experimental 5.17 for detailed calculation and progress curve). As expected, under NIR irradiation the observed release rate was slower as compared to direct UV treatment as the efficiency of SHG to generate the cleaving wavelength has to be considered.

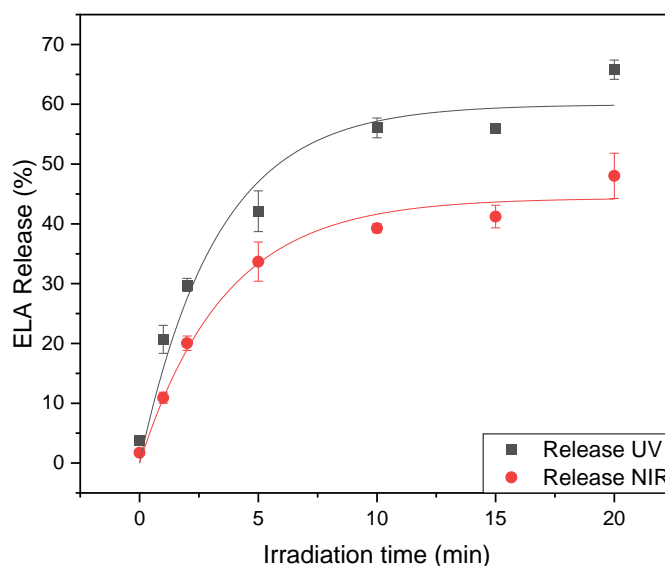


**Figure 28:** Release of **ELA** from **LNO@CM-ELA** NPs (150  $\mu\text{g}/\text{mL}$  in PBS) upon UV (366 nm) and NIR (790 nm) irradiation. The curves were fitted by a monoexponential function.

In order to verify the dependence of SHG wavelength on the release, given that setup 1 works at fixed wavelength, the irradiation was repeated on a tunable MHz laser (setup 2, see Experimental 5.17). Because of the inherent characteristics of this source, different peak intensity and irradiation surfaces had to be used. To *partially* compensate for these discrepancies, longer irradiation times were applied and the sample was continuously moved during the irradiation as detailed in the experimental section. The irradiation treatment was applied at three excitation wavelengths (800, 1000, and 1100 nm) for 1 h. Although the results by UHPLC-MS are less quantitatively reliable under these irradiation conditions, **ELA** release could only be observed upon 800 nm irradiation (corresponding to SHG emission within the absorption spectrum of CM, *cf.* Figure 29).



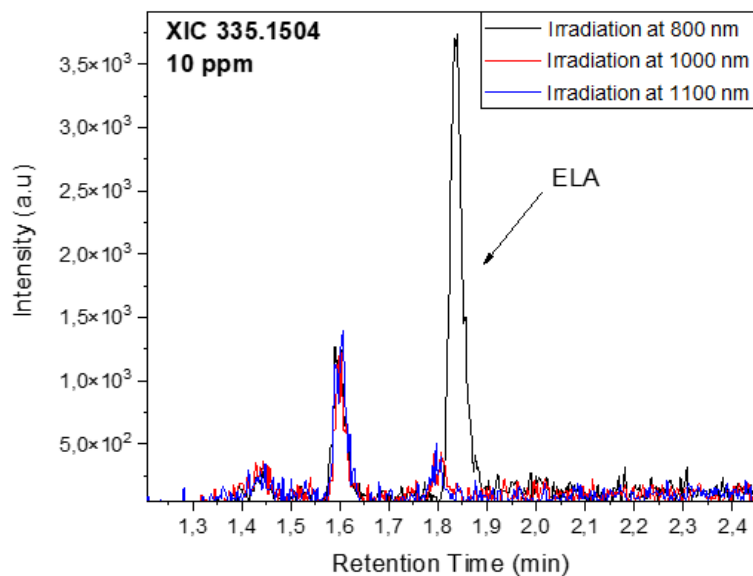


**Figure 29:** XIC (335.1504 MEW  $\pm$  50 ppm) of the samples collected from the irradiation of **LNO@CM-ELA** NPs at 800 nm (black curve), 1000 nm (red curve) and 1100 nm (blue curve).

Different control experiments were performed to verify that the **ELA** release resulted from the photocleavage of the carbamate bond of **DIBO-CM-ELA**, primarily induced by the SHG from the HNP core. A variation of **DIBO-CM-ELA**, **DIBO-ELA**, was synthesized to exhibit a direct covalent bond between **DIBO** and **ELA**, without photocleavable linker (*cf.* Figure 30). Upon conjugation to **LNO@APTES-N<sub>3</sub>** (following the same procedure as described earlier in this section), **LNO@ELA** NPs served as a negative control which should not be able to release the compound upon any irradiation.

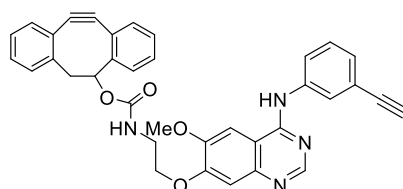


**Figure 30:** Structure of **DIBO-ELA**.

The results of these control experiments are summarized below (*cf.* Table 6). Following silanization and post-conjugation of **DIBO-CM-ELA** and **DIBO-ELA**, the resulting functionalized HNPs presented **ELA** loading values of 30 and 38 nmol/mg for **LNO@CM-ELA** and **LNO@ELA** NPs, respectively. First, these **LNO** derivatives were irradiated for 15 min at 790 nm, leading to 70.1% and 7.4% release of the cargo, respectively. Then, the release of **ELA** was quantified from **LNO@CM-ELA** NPs, kept in the dark for 15 min. at 22°C (6.6% release), or heated at 50 °C up to 30 min (8% release). Under NIR irradiation, the temperature increase induced by exposure to the laser excitation was estimated well below this value. The release from **DIBO-CM-ELA** NPs, non-conjugated to the surface of LNO NPs was also evaluated. The cargo release resulting from direct two-photon absorption of the photocleavable coumarinyl linker contributed to 37% of the release with respect to conjugated **LNO-CM-ELA** NPs. This value is not surprisingly higher than what previously observed for BFO NPs,<sup>8</sup> as LNO has a smaller nonlinear optical efficiency,<sup>9</sup> which is

compensated by enhanced size and morphology dispersion properties leading to more robust functionalization strategies.

**Table 6:** ELA release control studies (setup 1). The NPs concentration was kept at 150 µg/mL in PBS in all experiments.

Sample	Conditions	ELA release (nM)	Release SD (nM)	% of release
<b>LNO@CM-ELA</b> NPs	790 nm irradiation 15 min	631.1	4.4	70.1
<b>LNO@ELA</b> NPs	790 nm irradiation 15 min	66.8	6.9	7.4
<b>DIBO-CM-ELA</b> <sup>a</sup>	790 nm irradiation 15 min	161.6 ( <i>231</i> )	14.6	18.0 ( <i>26</i> )
<b>LNO@CM-ELA</b> NPs	No irradiation, 22°C	59.6	5.8	6.6
<b>LNO@CM-ELA</b> NPs	No irradiation 50 °C, 30 min	71.8	7.0	8.0

<sup>a</sup>This control was performed at a different laser average power (4.1 instead of 4.9 W, same beam geometry and pulse duration). The values corrected taking into account squared intensity dependence are in italic.

In summary, the DDS synthesized was used to prepare **LNO@CM-ELA** HNPs, capable of releasing the erlotinib derivative **ELA** upon NIR irradiation. The drug loading and release efficiency were quantified, and the series of control experiments demonstrated that only the full system (equipped with the photocleavable linker) could induce the release of **ELA** at a concentration prone to exert a cytotoxic effect upon the proper NIR irradiation, and that any temperature increase caused by the irradiation did not contribute to the drug uncaging. These results prompted the investigation of the system's ability to trigger a cytotoxic effect on cancerous cells under similar conditions, which will be described in the next section.

### 3.2.3. *In vitro* tests

With the help of our collaborators from the NBI Lab (UniGe, Geneva) and the DBS (CHUV, Lausanne), a series of *in vitro* tests on DU-145 human androgen dependent prostate cancer cells overexpressing the EGFR were performed, to evaluate the ability of **LNO@CM-ELA** NPs to induce a therapeutic effect upon NIR irradiation.

The nonlinear optical properties of **LNO@CM-ELA** NPs were evaluated upon NIR excitation between 800 and 1000 nm (*cf. Figure 10*). The spectra at each wavelength are associated with the emission of the object indicated by the dashed outline in the representative image obtained upon 1000 nm excitation. In the lower row are presented a series of nonlinear microscopy images of DU-145 cells treated by **LNO@CM-ELA** NPs (50  $\mu\text{g}/\text{mL}$ ). Upon excitation at 800 nm, the SHG is visible in the 400 nm channel and the DAPI fluorescence from the nuclei in the channel centered at 495 nm. Using the 1250 nm excitation, the system is capable of acquiring both the THG at 416 nm and the SHG at 625 nm (1/2 and 1/3 of the excitation wavelength, respectively). The comparison between the three harmonic responses highlights HNP excitation tunability beyond the NIR range. The labelling of cells is quite sparse as HNPs appear as isolated aggregates, but overall sufficient for recognizing cell morphologies.

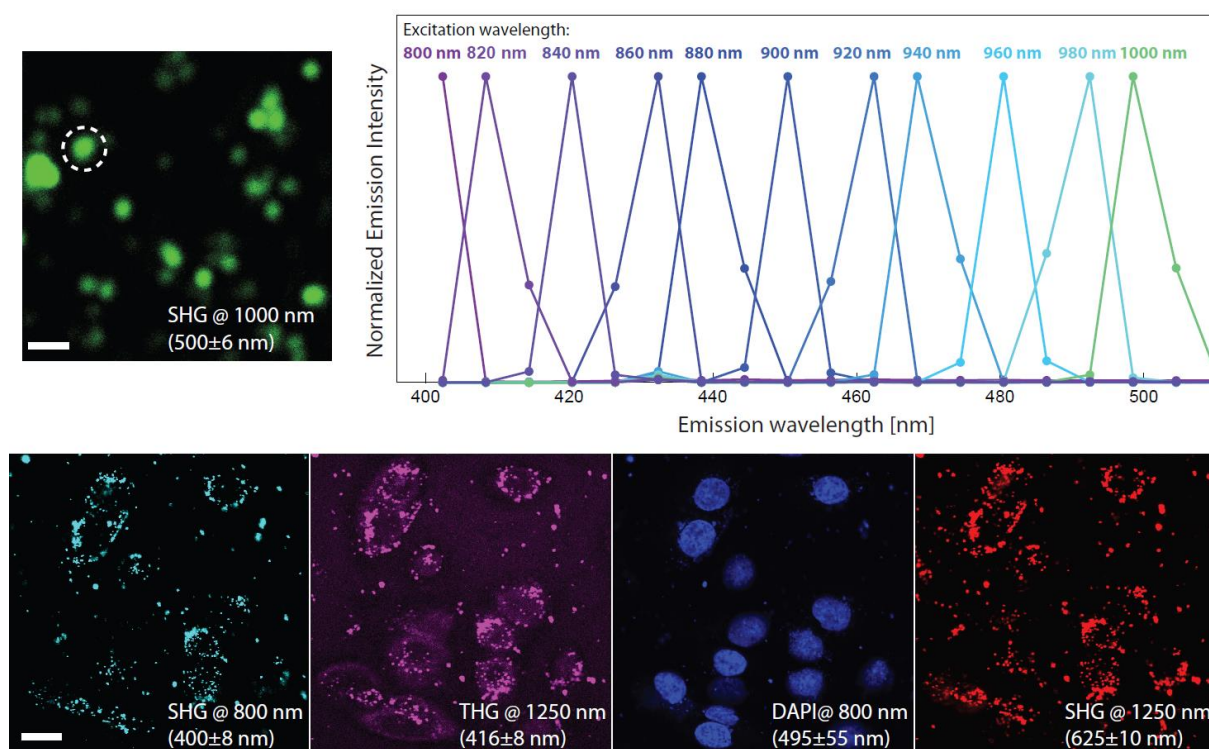


**Figure 10: Upper row. Left.** SHG image excited at 1000 nm of **LNO@CM-ELA** NPs deposited on a substrate. Scale bar 2  $\mu\text{m}$ . **Right.** Normalized spectra of the SHG emissions upon excitation spanning from 800 to 1000 nm obtained by integrating the signal of the object indicated by the dashed outline. **Lower row.** Nonlinear microscopy images of DU145 cells (fixed) treated with **LNO@CM-ELA** NPs (50  $\mu\text{g}/\text{mL}$ ). The labels indicate the signal attribution (THG, SHG, DAPI fluorescence), the excitation wavelength (@800, @1250 nm), and the acquisition spectral range. Scale bar: 20  $\mu\text{m}$ .

Before testing the properties of **LNO@CM-ELA** NPs *in vitro*, the erlotinib derivative **ELA** was first evaluated for its cytotoxic effect in comparison with the parent commercial drug. DU-145 cells were incubated with commercial erlotinib or **ELA** for 72 h using concentrations ranging from 0.5 to 10  $\mu\text{M}$  following the protocol described in the experimental section. The impact on cell viability was assessed using the MTT colorimetric assay. Results indicated that the two compounds displayed a similar cytotoxicity profile as they were able to induce 40-57 % growth inhibition at 1  $\mu\text{M}$  and 88-90 % at 10  $\mu\text{M}$ , measured 72 hours post-treatment (*cf. Figure 11*). These results suggest that the erlotinib derivative **ELA** conserves the ability to inhibit the growth of EGFR-overexpressing cancer cells.

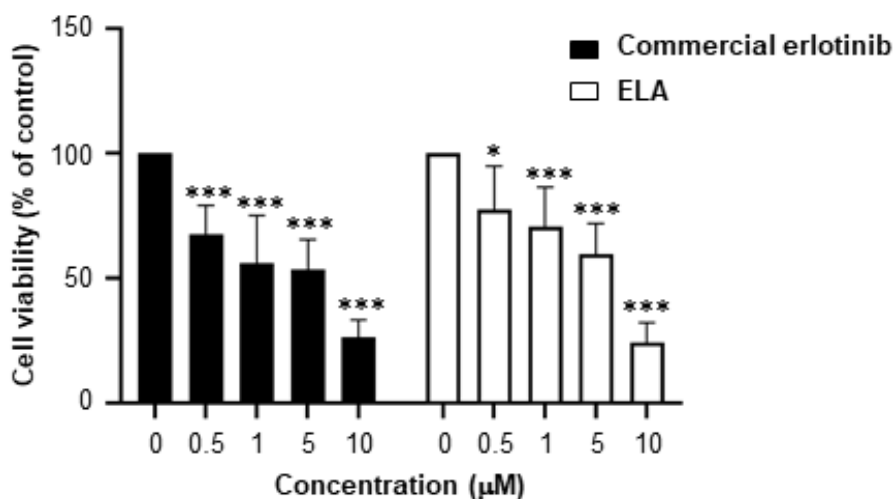


**Figure 11:** Evaluation of the cytotoxic effect of **ELA** and commercial erlotinib on DU145 cells. DU145 cells were incubated with increasing concentrations of **ELA** or commercial erlotinib for 72 h. Cell viability was assessed using the MTT colorimetric assay. Results are expressed as the mean  $\pm$  SD of two independent experiments. Statistical differences were calculated by two-way ANOVA. \*  $p < 0.05$ , \*\*  $p < 0.01$ , \*\*\*  $p < 0.001$  compared to the control.

In order to assess the therapeutic effect of the drug delivery upon NIR irradiation, DU-145 cells were incubated with **LNO@CM-ELA** NPs for 24 h and subsequently irradiated at 790 nm for 15 min. Cell viability was evaluated 72 h after the light exposure treatment (*cf. Figure 12*). Irradiation of DU-145 cells exposed to **LNO@CM-ELA** NPs resulted in 66% cell growth inhibition, an effect comparable to the effect induced by 0.98  $\mu\text{M}$  **ELA** (*cf. Figure 11*). The cell viability observed was slightly lower in the case of treatment with **LNO@CM-ELA** NPs as compared to incubation with **ELA**. This observation is consistent with the calculated concentration of **ELA** released from **LNO@CM-ELA** NPs at a concentration of 150  $\mu\text{g}/\text{mL}$ , which was estimated to reach 1.6  $\mu\text{M}$ . Importantly, no detrimental effect was observed for non-irradiated cells or for irradiated cells incubated with **LNO@APTES-N<sub>3</sub>** NPs. This result suggests that **LNO@APTES-N<sub>3</sub>** and **LNO@CM-ELA** NPs do not exert intrinsic cytotoxic properties, and that the release of **ELA** upon NIR irradiation from loaded HNPs can efficiently inhibit the growth of EGFR-overexpressing prostate cancer cells.

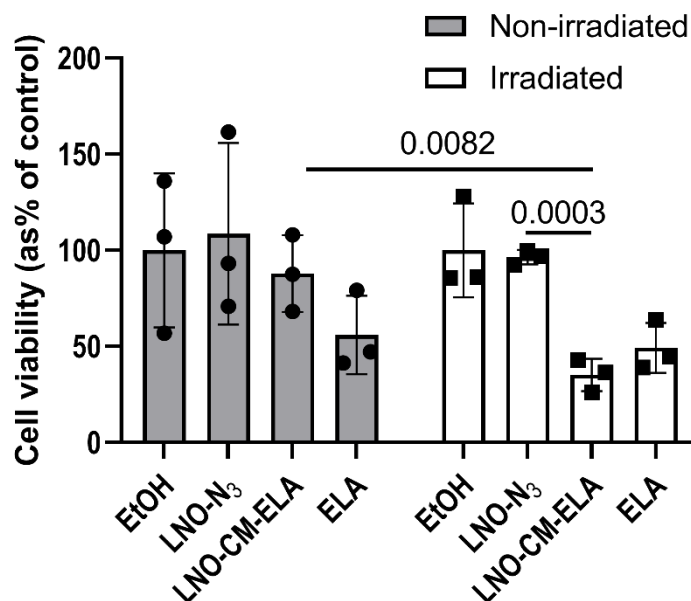


**Figure 12:** Effect of the NIR-triggered release of ELA on the viability of DU145 cells. Cells were incubated with **LNO@APTES-N<sub>3</sub>** NPs (150  $\mu\text{g}/\text{mL}$ ), **LNO@CM-ELA** NPs (150  $\mu\text{g}/\text{mL}$ ) or ELA (0.98  $\mu\text{M}$ ) for 24 h, followed by 15 min femtosecond laser pulsed irradiation at 790 nm. Cell viability was evaluated by MTT assay 72 h after exposure to the laser source (gray bars). The same protocol was performed, in parallel, without laser exposure (black bars). Results are expressed as the mean  $\pm$  SD of three independent experiments. Differences between irradiated and non-irradiated samples and between cells exposed to **LNO@APTES-N<sub>3</sub>** and **LNO@CM-ELA** NPs were statistically analyzed by a two-way ANOVA test: \*\*  $p < 0.01$ ; \*\*\*  $p < 0.001$ .

In summary, the potential to visualize the functionalized HNPs by nonlinear optical imaging in cells was shown, and their ability to trigger the photo-release of a tyrosine kinase inhibitor upon NIR irradiation to induce a therapeutic effect on a cancerous cell line was demonstrated. These results show that HNPs can stand as promising nanoplatfoms, capable of decoupled drug delivery and harmonic imaging visualization.

### 3.3. Lanthanide functionalization towards multimodal HNPs

In these final sections is presented the functionalization of silanized LNO NPs with an imaging probe, based on a lanthanide chelating ligand whose design was reported previously in our group (*cf. Figure 13*).<sup>154</sup> This ligand was initially designed for gadolinium (III) ions to be used as an MRI contrast agent, which requires a free coordination site for water molecules to be able to bind to, and which was modified to contain an alkyne group without interfering with the properties of the chelate for post-functionalization on coated NPs. The objective was to assess if this ligand could be used to complex other lanthanide ions in order to reach different imaging modalities, mainly luminescence and X-ray computed tomography, and also to attempt at improving the design of the ligand so that conjugation by SPAAC would be possible. Part of the work presented herein was disclosed in the publication *Gd<sup>3+</sup>-Functionalized Lithium Niobate Nanoparticles for Dual Multiphoton and Magnetic Resonance Bioimaging. ACS Applied Nano Materials, 2022, 5(2), pp.2912-2922.*

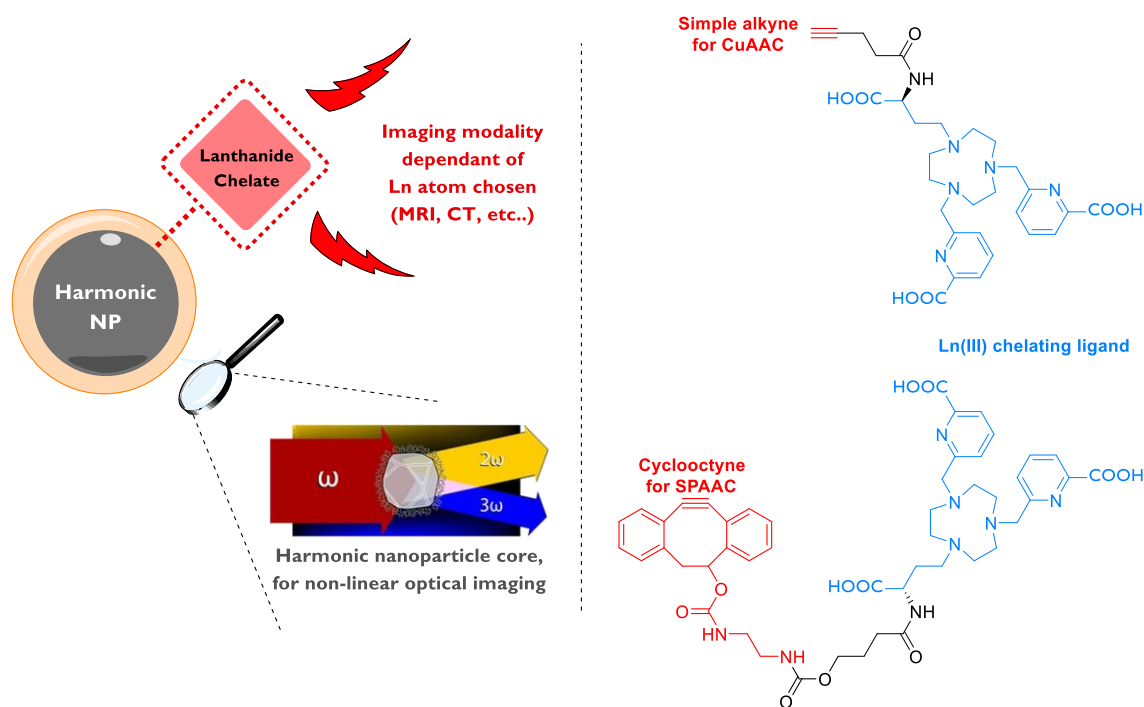
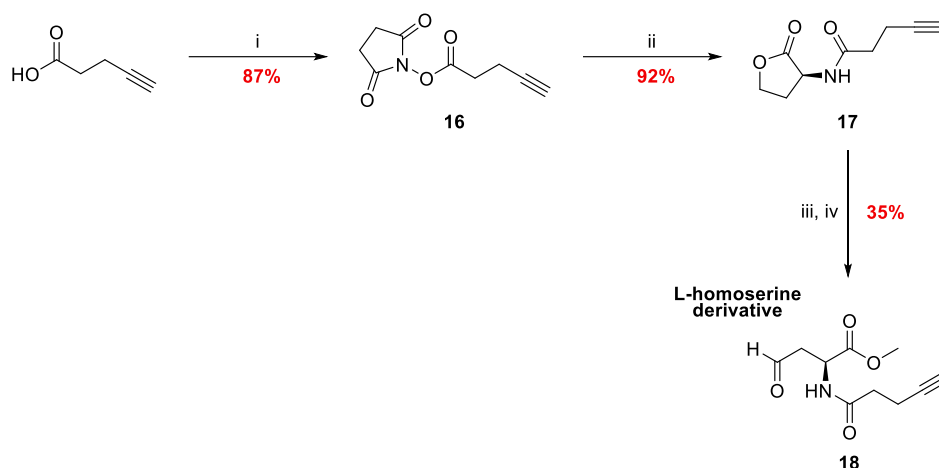


**Figure 13:** Design of multimodal harmonic NPs by lanthanide functionalization.

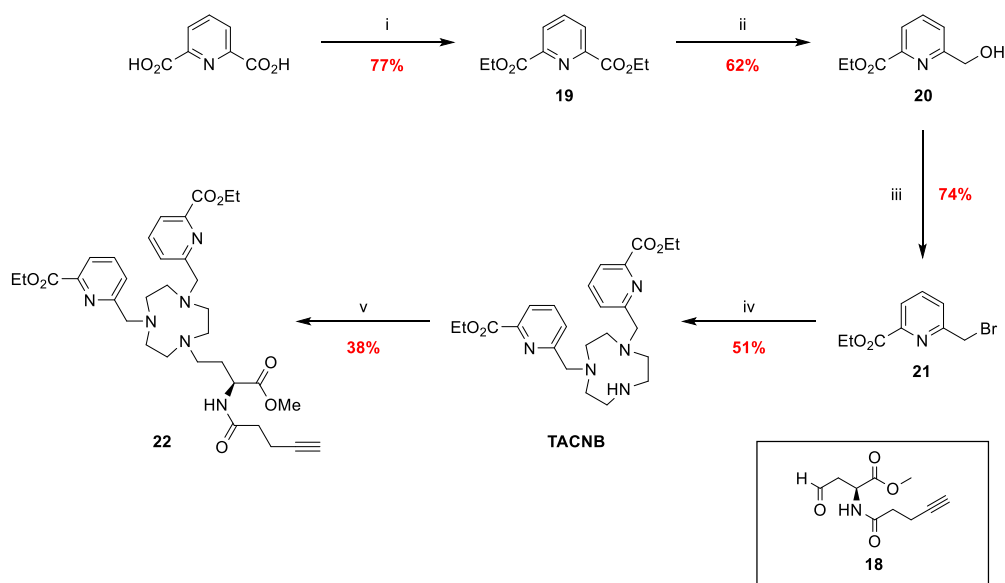
### 3.3.1. Synthesis of alkyne-lanthanide complexes and HNP functionalization

The synthesis of the ligand was adapted from the pathway previously presented in our group.<sup>154</sup> First the alkyne bearing side chain was produced starting from pent-4-ynoic acid, which was activated with NHS to afford **16**, followed by coupling of the NHS ester with (S)-(-)- $\alpha$ -amino- $\gamma$ -butyrolactone hydrobromide to generate **17** in high yield. Ring opening and esterification of the lactone in methanol under acidic conditions formed the intermediate alcohol, which was then subsequently oxidised into the aldehyde by Swern oxidation to afford the L-homoserine derivative **18** in 28% overall yield (*cf. Scheme 13*).



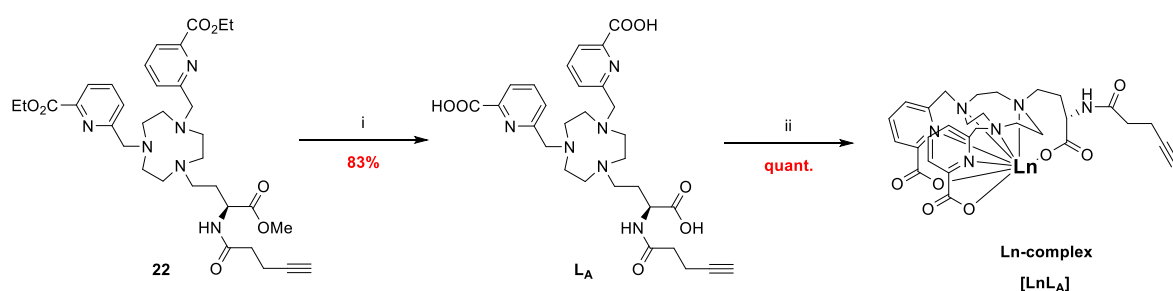
**Scheme 13: Synthesis of L-homoserine derivative.** i- NHS, DCC, THF, r.t, 2 h; ii- (S)-(-)- $\alpha$ -amino- $\gamma$ -butyrolactone hydrobromide, Et<sub>3</sub>N, DCM, r.t, 2 h; iii- H<sub>2</sub>SO<sub>4</sub>, MeOH, 24 h, r.t; iv- (COCl)<sub>2</sub>, DMSO, Et<sub>3</sub>N, DCM 0 °C, 2 h.

The synthesis of the substituted TACN ring started with the esterification of dipicolinic acid to form the diester **19**, followed by mono-reduction in the presence of NaBH<sub>4</sub> to generate alcohol **20** in moderate yield. The hydroxyl group was substituted with a bromine by Appel reaction to produce the bromopicolinate **21**, which was then added onto the TACN ring by controlled nucleophilic substitution, leaving a free secondary amine position and affording **TACNB** in moderate yield. Finally, the alkyne bearing side-chain was added to the bi-substituted **TACNB** by reductive amination, to obtain the ligand ester precursor **22** in 38% yield (*cf. Scheme 14*).



**Scheme 14: Synthesis of the ligand ester precursor.** i-  $\text{H}_2\text{SO}_4$  conc. EtOH, reflux, 16 h; ii-  $\text{NaBH}_4$ , EtOH, reflux, 16 h; iii-  $\text{CBr}_4$ ,  $\text{PPH}_3$ , DCM, rt, 3 h; iv- TACN  $\cdot$  3 HCl, DIPEA, ACN, reflux, 16 h; v- *L*-homoserine derivative,  $\text{NaBH}_3\text{CN}$ , DCE/ACN, rt, 16 h.

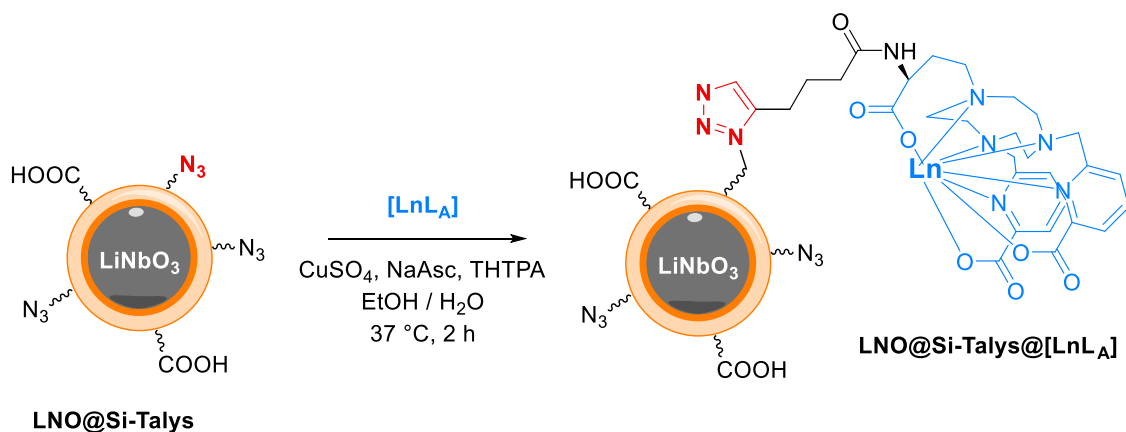
The formation of Ln(III) chelates was optimized to achieve both high yield and purity of the final complexes. The three esters of the ligand precursor were hydrolysed in the presence of lithium hydroxide and the tri-carboxylic acid form was isolated and purified by dialysis against distilled water to afford the ligand  $\text{L}_A$  in good yield. The ligand was then used for the complexation of various lanthanide ions upon treatment with their trichloride salts, including La, Eu, Gd, Tb and Yb ions. Purification by dialysis against distilled water afforded the lanthanide complexes  $[\text{LnL}_A]$  in quantitative yields (*cf. Scheme 15*).



**Scheme 15: Lanthanide complexation.** i-  $\text{LiOH}$ ,  $\text{MeOH}/\text{H}_2\text{O}$ , r.t 4 h; ii-  $\text{LnCl}_3$ ,  $\text{H}_2\text{O}$ ,  $37^\circ\text{C}$ , 16 h.

The lanthanide complexes of Eu, Gd and Yb were used to functionalize **LNO@Si-Talys** NPs (silanization described in 1.1.3). The functionalization proceeded by CuAAC, in the presence of the Cu(I) stabilizing ligand tris(3-hydroxypropyltriazolylmethyl)amine (THPTA)<sup>166</sup> (*cf. Scheme 16*). The functionalized **LNO@Si-Talys@ $[\text{LnL}_A]$**  were characterized by DLS. However, they all displayed significant signs of aggregation in aqueous conditions and suboptimal colloidal stability (hydrodynamic sizes  $> 1000$  nm, PDI  $> 0.3$ ). For preliminary study of the luminescence properties of the Eu and Yb conjugates (see section 3.3.3), suspensions in DMSO improved the quality of the colloidal suspensions.



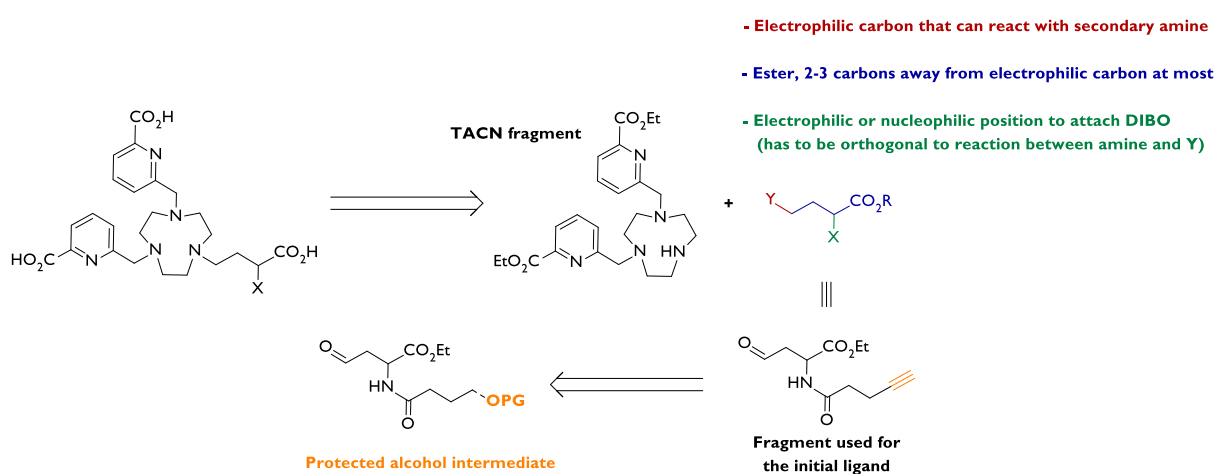


**Scheme 16:** Conjugation of the alkyne-lanthanide complex on **LNO@Si-Talys**.

In summary, the lanthanide ligand **L<sub>A</sub>** was synthesized and successfully applied to chelate various lanthanide ions, ranging from the lightest (La) to the heaviest (Yb) which proves its versatility. The silanized HNPs functionalized with various **[LnL<sub>A</sub>]** complexes displayed however poor colloidal properties in aqueous medium, which hinders potential biological applications and thus requires optimization. The following section attempts at providing a solution through the modification of the ligand, so that it can be conjugated to the HNP surface by SPAAC instead of CuAAC.

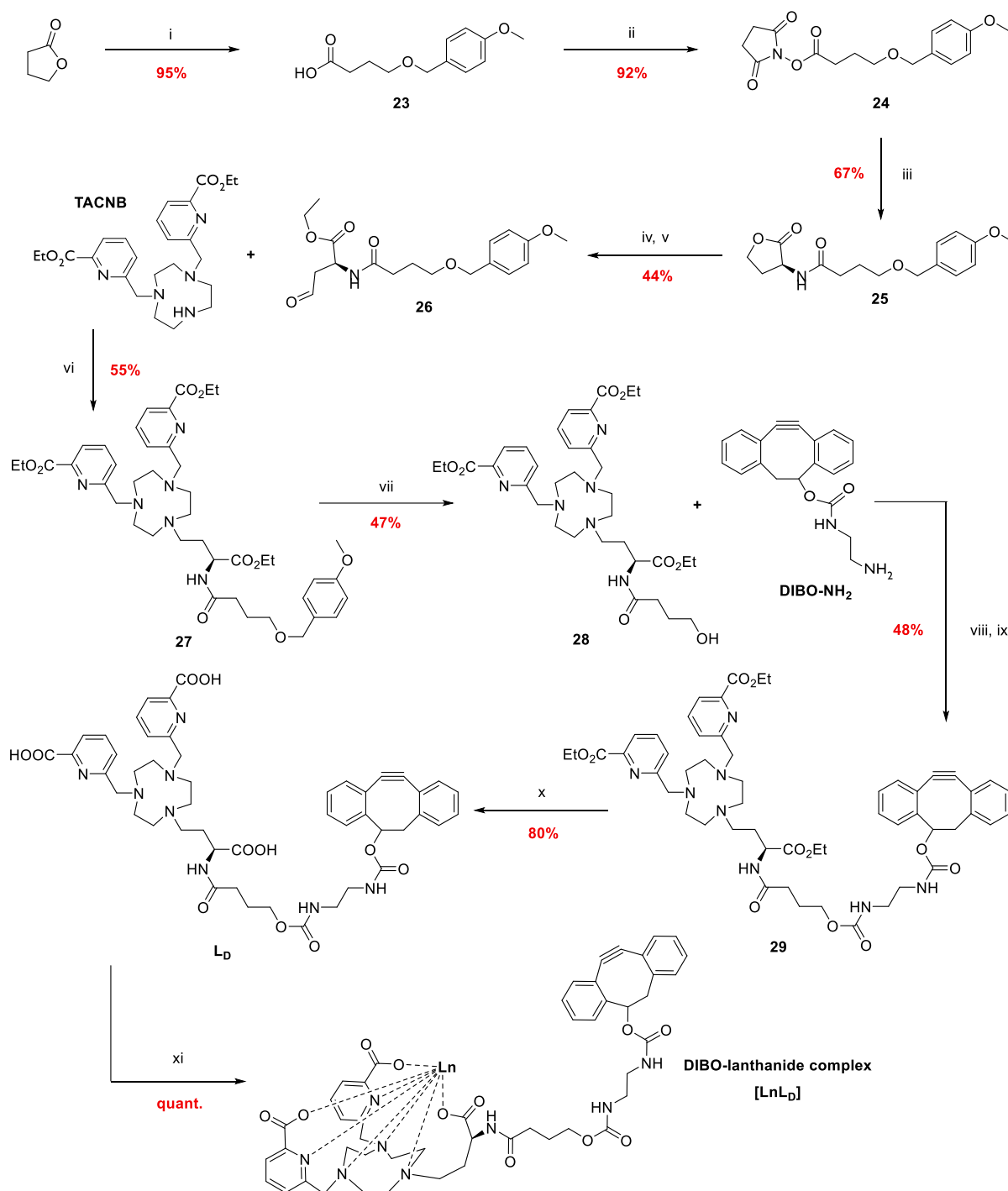
### 3.3.2. Synthesis of cyclooctyne-lanthanide complexes and HNP functionalization

In the previous conjugation strategy, based on CuAAC click reaction, we suspected that the reagents involved in the mechanism ((Cu(I) and (II), sodium ascorbate, THPTA) may be responsible for the poor colloidal stability of the resulting conjugates, in particular through degradation of the silica shell and competitive coordination at the various carboxyl moieties. Thereby, the design of a modified ligand exhibiting a strained cyclooctyne instead of a simple alkyne could help by requiring milder conjugation conditions. Since the complexation properties of the ligand seemed very promising, the modification should not alter its ability to chelate lanthanide ions. A new synthetic pathway was thus designed by altering the L-homoserine alkyne derivative used in the previous synthesis, by going through a protected alcohol intermediate (*cf.* Scheme 17).



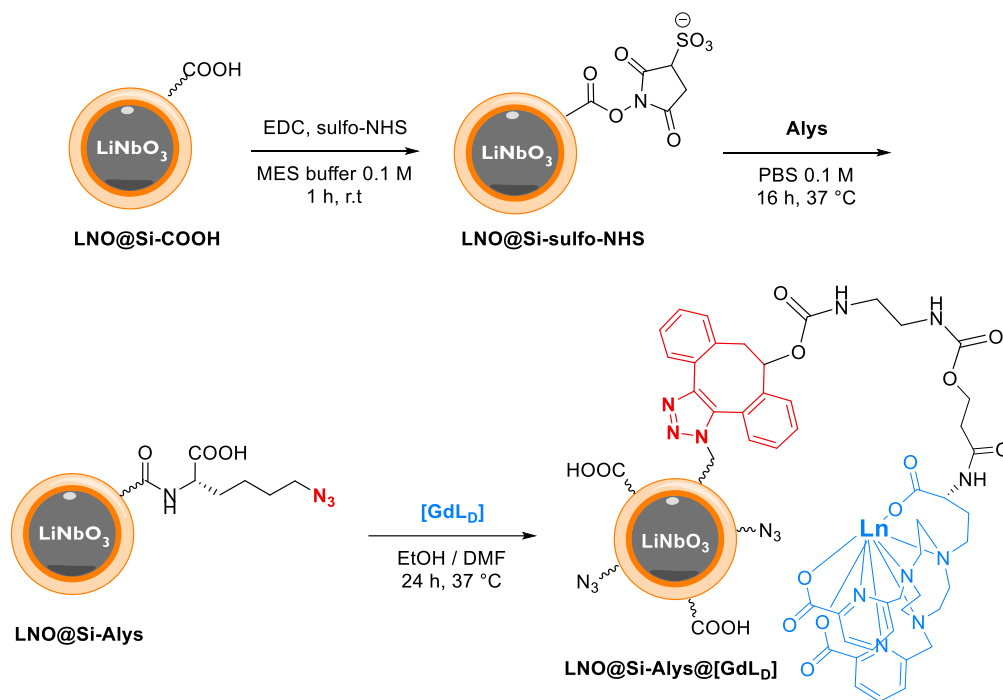
**Scheme 17:** Rational behind the new ligand synthetic pathway.

First, the lactone ring of  $\gamma$ -butyrolactone was opened with a strong base to generate the alcohol, which was protected in a one-pot reaction with *p*-methoxybenzylbromide (PMBBr) to generate **23** in almost quantitative yield. The NHS-ester **24** was formed by activation of the carboxyl group with DCC / NHS, which could then be coupled to the primary amine of (*S*)-(-)- $\alpha$ -amino- $\gamma$ -butyrolactone, producing **25** in high yield. Acid-catalysed ring opening was used to form an unstable alcohol intermediate, which could then be oxidized to the aldehyde **26** in medium overall yield by Swern reaction. The aldehyde was coupled to the secondary amine of TACNB by reductive amination in the presence of  $\text{NaBH}(\text{OAc})_3$  to generate **27**, from which the alcohol could be deprotected with 2,3-dichloro-5,6-dicyano-1,4-benzoquinone (DDQ) by a radical mechanism, yielding **28**. The as-formed alcohol was activated with a nitrophenyl group, which could then react with DIBO-NH<sub>2</sub> by nucleophilic substitution to form compound **29** in medium yield. The cyclooctyne-ligand L<sub>D</sub> was finally obtained by saponification with LiOH in high yield. Following the same procedure as described in the previous section, L<sub>D</sub> was used to chelate a variety of lanthanide ions (including Eu, Gd and Yb), leading to the formation of the corresponding [LnL<sub>D</sub>] complexes (*cf.* Scheme 18).



**Scheme 18: Synthesis of the [LnL<sub>D</sub>] complexes:** i- PMBBR, KOH, toluene, reflux, 4 days; ii- NHS, DCC, THF, r.t, 3 h; iii- (S)-(-)- $\alpha$ -amino- $\gamma$ -butyrolactone hydrobromide, Et<sub>3</sub>N, DCM, r.t, 2 h; iv- H<sub>2</sub>SO<sub>4</sub>, EtOH, r.t, 24 h; v- (COCl)<sub>2</sub>, DMSO, Et<sub>3</sub>N, DCM 0 °C, 2 h; vi- AcOH, NaBH(OAc)<sub>3</sub>, DCE, r.t, 16 h; vii- DDQ, DCM/PBS 4:1, r.t, 3 h; viii- 4-nitrophenyl chloroformate, pyridine, DCM, r.t, 16 h; ix- DIPEA, DMF, r.t, 16 h; x- LiOH, EtOH/H<sub>2</sub>O, r.t 4 h; xi- LnCl<sub>3</sub>, H<sub>2</sub>O, 37 °C, 16 h.

First investigations of dual imaging capabilities were performed with the Gd(III) chelate **GdL<sub>D</sub>**. **LNO@Si-COOH** NPs produced through the W/O method were further conjugated to **Alys** (single azidolysine unit) through EDC / sulfo-NHS coupling to afford **LNO@Si-Alys** NPs (*cf. Scheme 19*). Post-functionalization with **[GdL<sub>D</sub>]** chelate by SPAAC allowed for conjugation under mild conditions (37°C, absence of additional reagents) and simplified the purification procedure as only the unreacted chelate needed to be separated from the conjugated NPs.



**Scheme 19:** Preparation of **LNO@Si-Alys@[GdL<sub>b</sub>]** NPs.

The NPs were characterized by DLS across the functionalization steps (*cf. Table 7*). The mean NP size in PBS increased after the W/O ME coating and **Alys** grafting, and remained constant after **[GdL<sub>b</sub>]** conjugation, while the PDI remained below 0.2. This indicated systematic monodispersity and good colloidal stability in aqueous medium for the NPs across the different functionalization steps. The large difference in ZP measured at pH 7.4 and pH 3.0 for coated and conjugated NPs further suggested the presence of negatively charged carboxylates on the NP surface.

**Table 7:** DLS characterization of **LNO@Si-Alys@[GdL<sub>b</sub>]**.

Nanoparticles	Hydrodynamic diameter (number mean) [nm]	PdI	Zeta potential pH 7.4 [mV]	Zeta potential pH 3.0 [mV]
Bare LNO	127.7 ± 3.8	0.06	-48.8 ± 1.1	-36.7 ± 0.3
LNO@Si-COOH	179.9 ± 16.2	0.10	-44.0 ± 0.9	-27.5 ± 0.4
LNO@Si-Alys	209.4 ± 4.3	0.05	-36.9 ± 1.2	-4.2 ± 0.6
LNO@Si-Alys@[GdL <sub>b</sub> ]	236.6 ± 14.6	0.14	-40.9 ± 0.5	-13.0 ± 0.4

Mean hydrodynamic diameter ( $d$ , number distribution) and surface charge (ZP) were measured in PBS (pH 7.4 and 3.0) at 22°C.

Additional STEM and EDX mapping analyses gave evidence for a dense silica shell around the Nb core, which correlates with the observed increase in size measured by DLS (*cf. Figure 31*).

Furthermore, the Gd EDX map exhibited a sparse yet homogeneous elemental distribution around the Nb core, pointing towards the efficient covalent grafting of **[GdL<sub>D</sub>]** to the LNO HNPs.

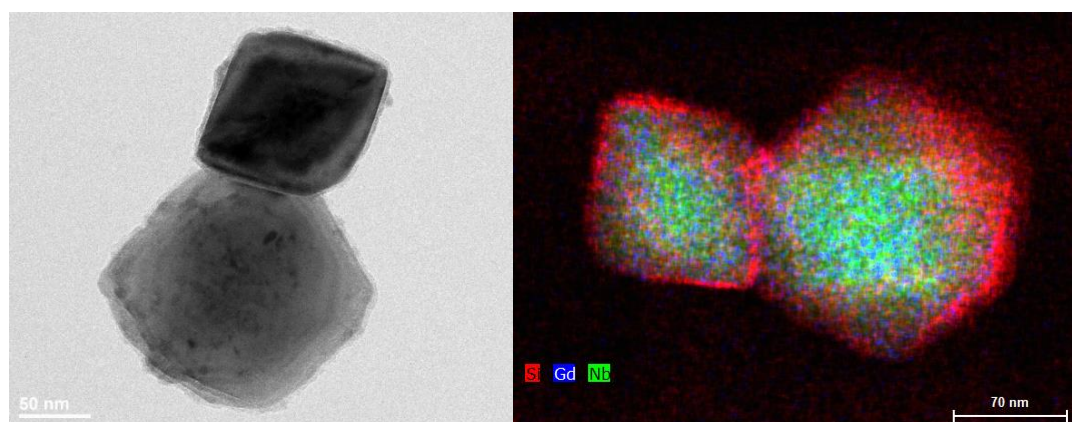


**Figure 31:** LNO@Si-Alys@[GdL<sub>D</sub>] STEM and EDX characterization. **Left:** Bright field STEM image, scale bar: 50 nm. **Right:** merged EDX map of Si, Gd, Nb, scale bar: 70 nm.

In summary, a new synthetic pathway for a strained cyclooctyne-bearing lanthanide ligand was successfully developed, and the ligand was used to chelate Ln ions, including Eu, Gd and Yb, illustrating that the versatility of the ligand was not lost upon modification. Functionalization of the Gd complex on coated LNO NPs resulted in the formation of **LNO@Si-Alys@[GdL<sub>D</sub>]** NPs, which presented improved colloidal properties in aqueous medium.

### 3.3.3. Assessment of dual imaging capabilities

In this last section, preliminary studies were performed to evaluate the potential of the various lanthanide-functionalized LNO NPs to act as multimodal imaging platforms.

#### Luminescence of LNO@Si-Talys@[LnL<sub>A</sub>]

Despite their poor colloidal properties in aqueous medium, preliminary luminescence experiments were performed on the [LnL<sub>A</sub>] complexes and the LNO@Si-Talys@[LnL<sub>A</sub>] to evaluate if those could be used as luminescent lanthanide probes (*cf. Figure 32 and 33*). The measurements were performed in DMSO to limit the aggregation effect of the functionalized LNOs.

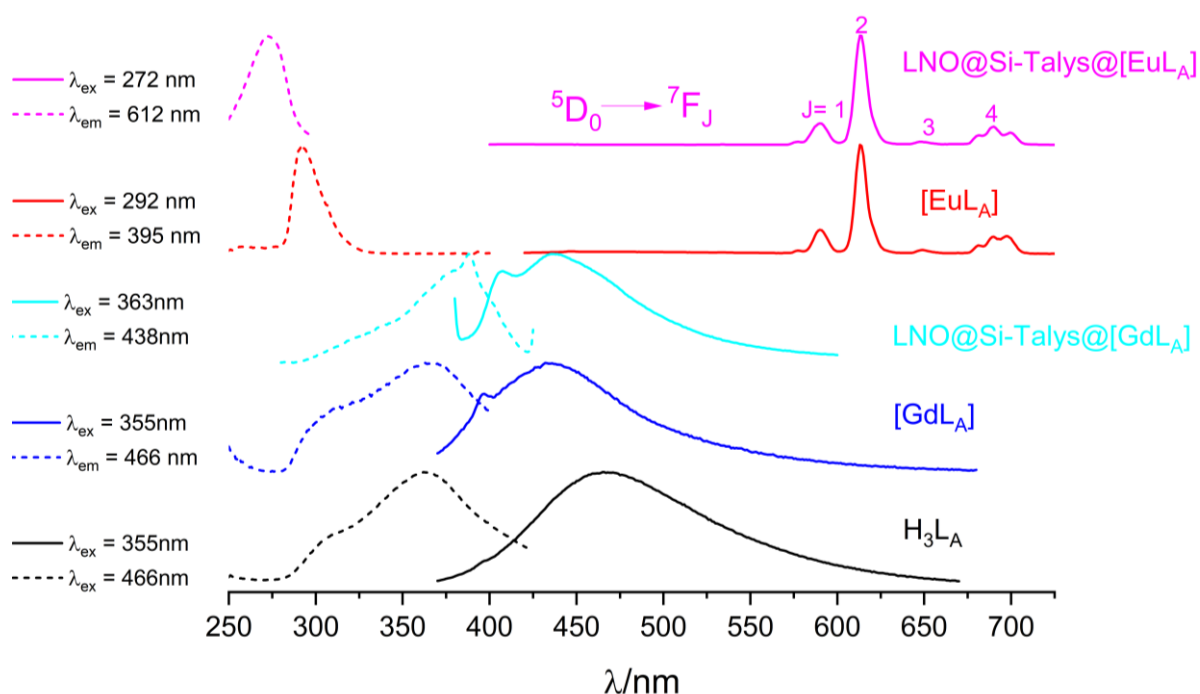


**Figure 32:** Normalized emission and excitation spectra of the different complexes and Ln-NP conjugates, at room temperature.

The un-complexed ligand H<sub>3</sub>L<sub>A</sub> and the [GdL<sub>A</sub>] complex displayed one main excitation band centered at 362 nm with a shoulder at 305 nm. Upon grafting on the NPs, a bathochromic shift of about 8 nm was observed with LNO@Si-Talys@[GdL<sub>A</sub>]. Upon excitation into the maximum of the excitation band, emission from the singlet  $1\pi\pi^*$  state and/or the  $3\pi\pi^*$  state was seen as a one-component band with maxima at 466 nm for H<sub>3</sub>L<sub>A</sub> and as a two-component band with maxima at 397 and 432 nm for [GdL<sub>A</sub>]. The emission was slightly red-shifted by 7 nm with LNO@Si-Talys@[GdL<sub>A</sub>]. Further experiments in phosphorescence mode will be done to assign the contribution of the triplet and the singlet states. The band was blue shifted with maxima at 292 and 272 nm for [EuL<sub>A</sub>] and LNO@Si-Talys@[EuL<sub>A</sub>], respectively. At room temperature, the  $1\pi\pi^*$  and  $3\pi\pi^*$  emission disappeared for both compounds which evidenced an efficient ligand to metal energy transfer. The emission of the [EuL<sub>A</sub>] complex and the functionalized NPs upon excitation

at 292 and 272, respectively, mainly displayed the characteristic metal-centered emission lines from the  $\text{Eu}(^5\text{D}_0)$  excited states upon ligand excitation. The  $^5\text{D}_0 \rightarrow ^7\text{F}_0$  transition appeared as a very faint band;  $^5\text{D}_0 \rightarrow ^7\text{F}_j$  transitions displayed two, two and four main components for  $J = 1, 2,$  and  $4$ . This emission spectrum may be interpreted as arising from a main species with a single chemical environment, possibly a pseudo  $D_3$  symmetry around the metal cation. This should be further confirmed by experiments performed at low temperature which will give more resolved spectra. The emission transitions and intensities of **LNO@Si-Talys@[EuL<sub>A</sub>]** remained the same as compared to **[EuL<sub>A</sub>]** which pointed to the same symmetry around the Eu(III) center, whatever the complex was free or grafted. The presence of one main species present in solution was further confirmed by the fact the emission decays were both mono-exponential, pointing to 1.23 and 0.92 ms. The lifetimes of **LNO@Si-Talys@[EuL<sub>A</sub>]** was slightly shorter compared to **[EuL<sub>A</sub>]**, pointing to deactivation pathways taking place on the surface of the NPs. Preliminary results gave quantum yields of **[EuL<sub>A</sub>]** at  $14\% \pm 0.3$  while it was less than 2% for **LNO@Si-Talys@[EuL<sub>A</sub>]** NPs.

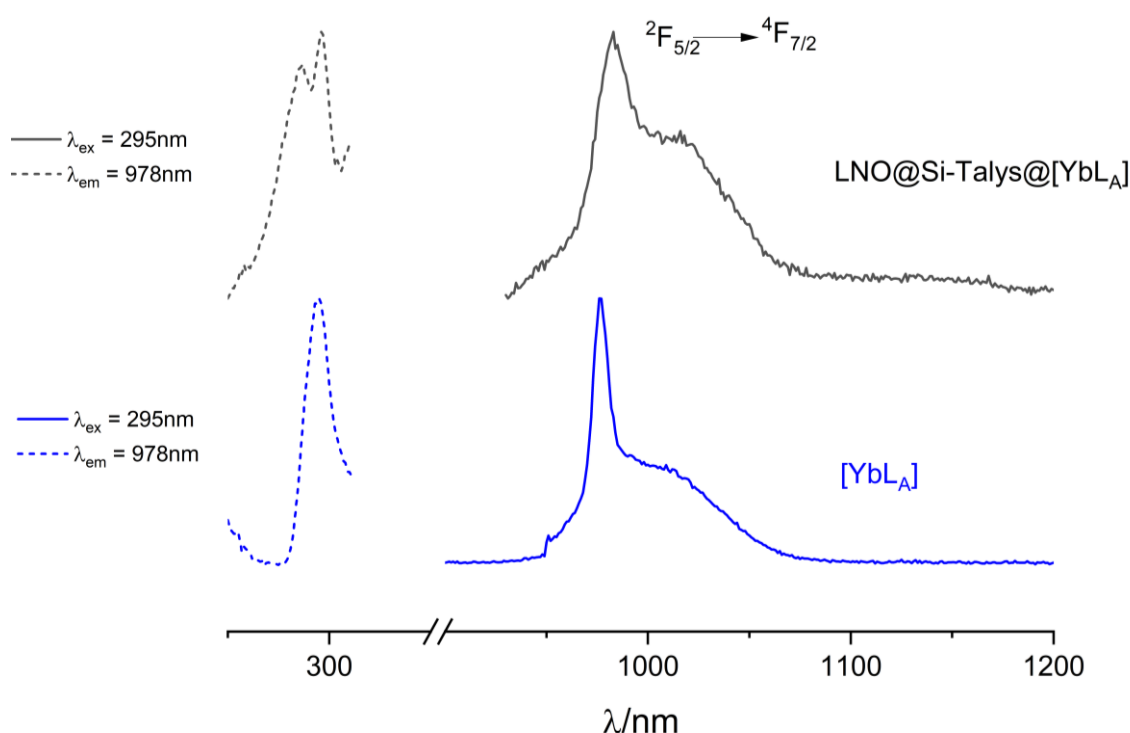


**Figure 33:** Normalized emission and excitation spectra of **[YbL<sub>A</sub>]** and **LNO@Si-Talys@[YbL<sub>A</sub>]** NPs, at room temperature.

In the case of the Yb complex and functionalized LNOs, the characteristic emission of Yb (III) in the NIR region at 900-1100 nm could be observed, for both **[YbL<sub>A</sub>]** and **LNO@Si-Talys@[YbL<sub>A</sub>]** compounds, corresponding to the  $^2\text{F}_{5/2} \rightarrow ^2\text{F}_{7/2}$  transition. Although the intensity of the emission was lower for the NPs, it was easily observed at room temperature. These data also confirmed that the complexation and surface conjugation was successful in the case of Yb ions, and showed how multiple emission wavelengths can be achieved through variation of the lanthanide species. Another interesting perspective for the **LNO@Si-Talys@[YbL<sub>A</sub>]** resides in the fact that Yb (III) complexes are reported to behave as efficient X-ray CT contrast agents, which could pave the way for an additional imaging modality for the designed nanoplatforms.

### Nonlinear optical response of $\text{LNO@Si-Alys@[GdL}_D]$ and potential as MRI probe

With the help of our collaborators from CHUV and UNIGE, DU145 cancer cells were incubated with  $\text{LNO@Si-Alys@[GdL}_D]$  ( $50 \mu\text{g/mL}$ ), and the nonlinear optical response of the functionalized LNOs was evaluated upon NIR irradiation (*cf. Figure 34*). Upon 800 nm excitation (upper row), the SHG signal was observed in the 400 nm channel while the DAPI signal corresponding to cell nuclei was observed in the 595 nm channel. Colocalization of both signals demonstrated the efficient internalization of  $\text{LNO@Si-Alys@[GdL}_D]$  into the cell cytoplasm. Upon 1250 nm excitation (lower row), the SHG and THG signals were simultaneously acquired in the 625 nm and 416 nm channels, respectively. The detection of SHG at two excitation wavelengths highlights the emission tunability as well as the possibility to use both NIR-I and NIR-II excitations, while the simultaneous detection of SHG and THG shows the multi-order response of the LNO core, confirming that the functionalization steps did not impact the LNO's optical properties. The high internalization allowed in some cases to distinguish the cell outline with the NP optical response (bottom cells). Overall, this demonstrates the potential of  $\text{LNO@Si-Alys@[GdL}_D]$  to label cancer cells *in vitro*.

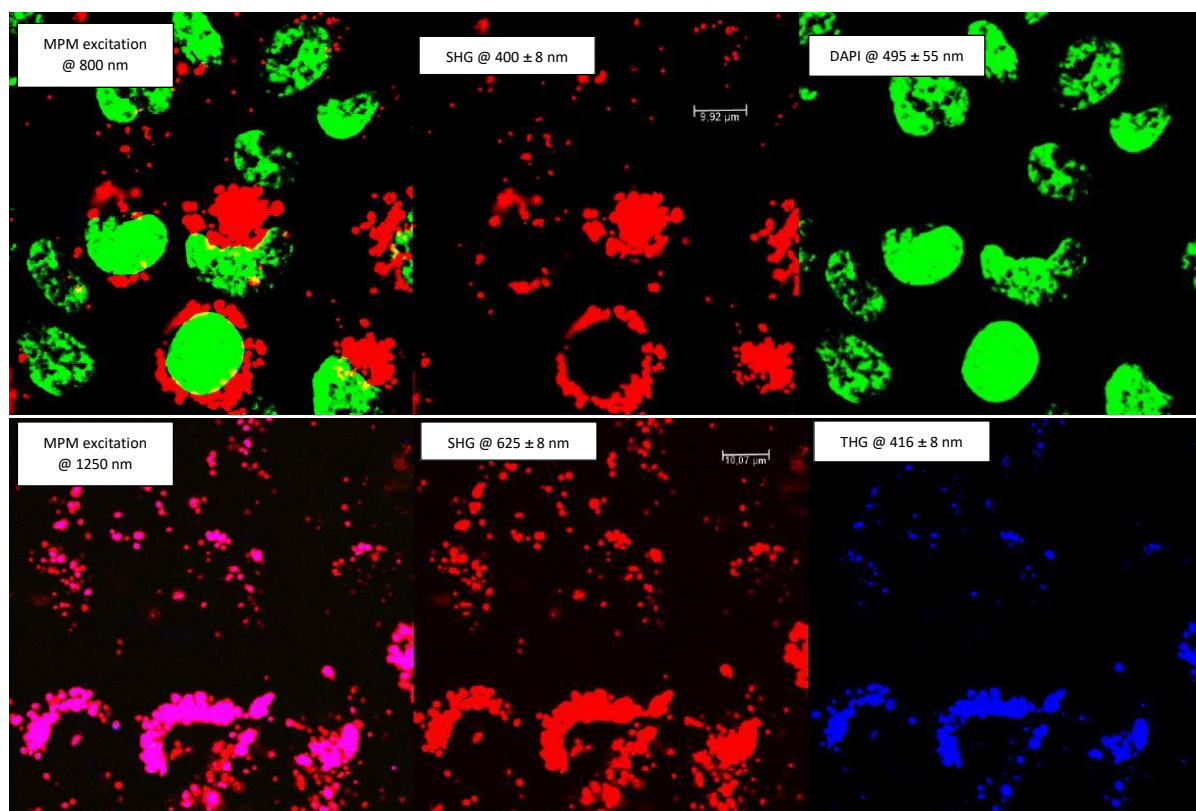


**Figure 34:** Nonlinear optical microscopy images of fixed DU145 cells after treatment  $\text{LNO@Si-Alys@[GdL}_D]$  ( $50 \mu\text{g/mL}$ ). Each panel indicates the signal attribution (SHG, THG, DAPI), the emission wavelength and the acquisition spectral range. **Upper row.** Colocalization (left) of SHG emission (middle) and DAPI emission (right) upon 800 nm excitation. **Lower row.** Colocalization (left) of SHG emission (middle) and THG emission (right) upon 1250 nm excitation. Scale bar:  $10 \mu\text{m}$ .

To further assess the ability of  $\text{LNO@Si-Alys@[GdL}_D]$  to act as MRI contrast agent, the proton longitudinal and transverse relaxation rates  $R_1$  and  $R_2$  were measured at physiological temperature ( $37^\circ\text{C}$ ) using a 60 MHz (1.4 T) Bruker Minispec spectrometer. An agarose gel-based phantom was prepared with 11 NMR tubes (5 mm in diameter) containing  $\text{LNO@Si-Alys@[GdL}_D]$  at concentrations ranging from 0 to  $1.0 \text{ mg/mL}$  (*cf. Table 8, Figure 35a*). The contrast properties



of **LNO@Si-Alys@[GdL<sub>D</sub>]** were evaluated at 9.4 T and 14.1 T for the T<sub>1</sub>/T<sub>2</sub> relaxation times and for the MR images, as clinical MRI scanners for whole-body applications operate at magnetic field strengths higher than 1.5 T. These experiments were carried out at the ISIC NMR platform (ISIC-NMRP) and the Biomedical Imaging Research Center (CIBM).

**Table 8:** Composition of the agarose gel-based phantom.

Sample	1	2	3	4	5	6	7	8	9	10	11
<b>LNO@Si-Alys@[GdL<sub>D</sub>]</b> [mg/mL]	1.00	0.75	0.50	0.25	0.20	0.15	0.10	0.05	0.01	0.005	0.00

The T<sub>1</sub> spin-lattice relaxation time and the T<sub>2</sub> spin-spin relaxation time were simultaneously measured on a single phantom on a 9.4 T NMR spectrometer (*cf. Figure 35b, c*). A concentration-dependent decrease in the T<sub>1</sub> spin-lattice relaxation time, corresponding to an increase in R<sub>1</sub> relaxation rate was observed. This suggests a signal-increasing effect on tumour imaging with increasing **LNO@Si-Alys@[GdL<sub>D</sub>]** amounts. On the contrary, a concentration-dependent increase in the T<sub>2</sub> spin-spin relaxation time corresponding to a decrease in R<sub>2</sub> relaxation rate was observed, suggesting a signal-increasing effect as well on tumour imaging with increasing NP amounts.

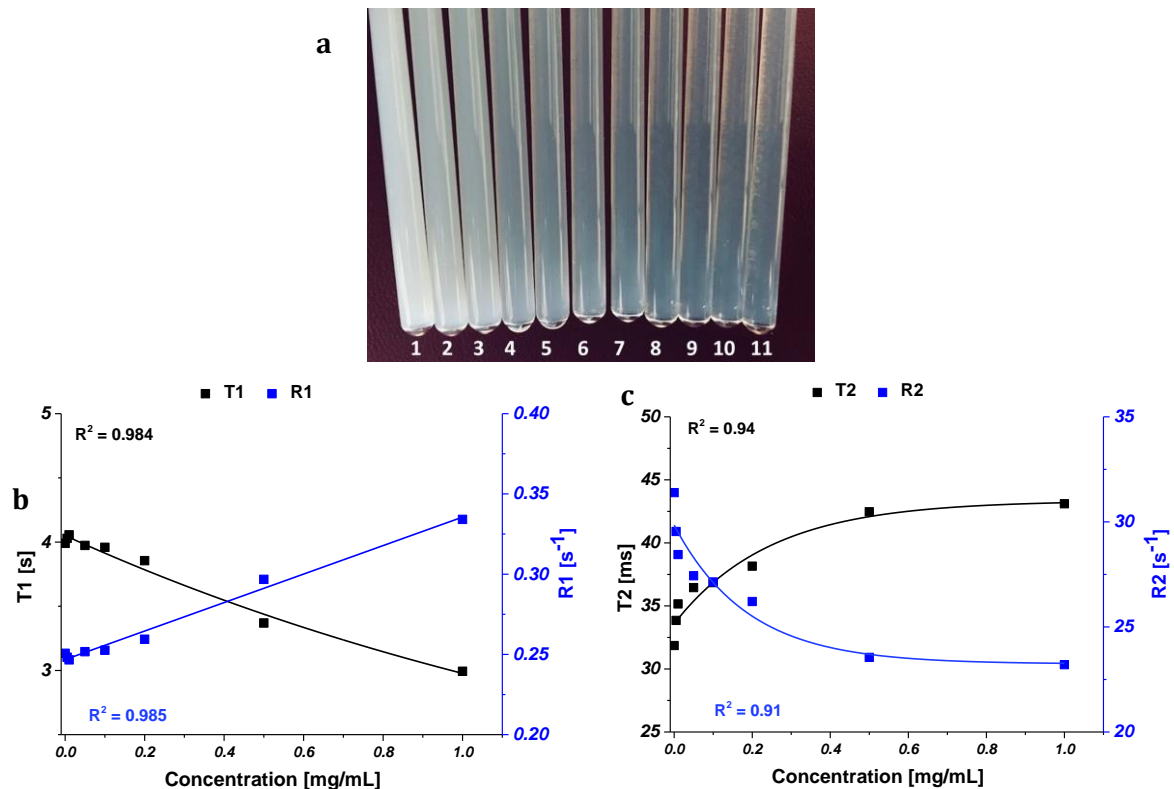


**Figure 35:** Relaxation measurement for **LNO@Si-Alys@[GdL<sub>D</sub>]** NPs at concentrations of 0-1.0 mg/mL at 9.4 T. (a) Agarose gel-based phantom. (b) T<sub>1</sub> relaxation time and R<sub>1</sub> relaxation rate curves. (c) T<sub>2</sub> relaxation time and R<sub>2</sub> relaxation rate curves.

The phantom  $T_1$ -weighted and  $T_2$ -weighted 2D images were recorded using a gradient-echo sequence/FLASH on a 14.1 T MRI instrument (*cf. Figure 36a, b*), which showed no significant trend in signal change with respect to NP concentration. Both the quantitative  $T_1$  mapping (*cf. Figure 36c, e*) and  $T_2$  mapping (*cf. Figure 36d, f*) revealed only statistically weak Pearson correlation ( $P > 0.01$ ) between the relaxation time and the corresponding contrast. Together with recently reported MR contrast with a similar construct<sup>167</sup> as well as the Gd EDX map, this suggests that the functionalized NPs displayed only a low amount of Gd(III) chelates, giving rise to dim MR signal despite the observed concentration-dependent relaxation time variations.

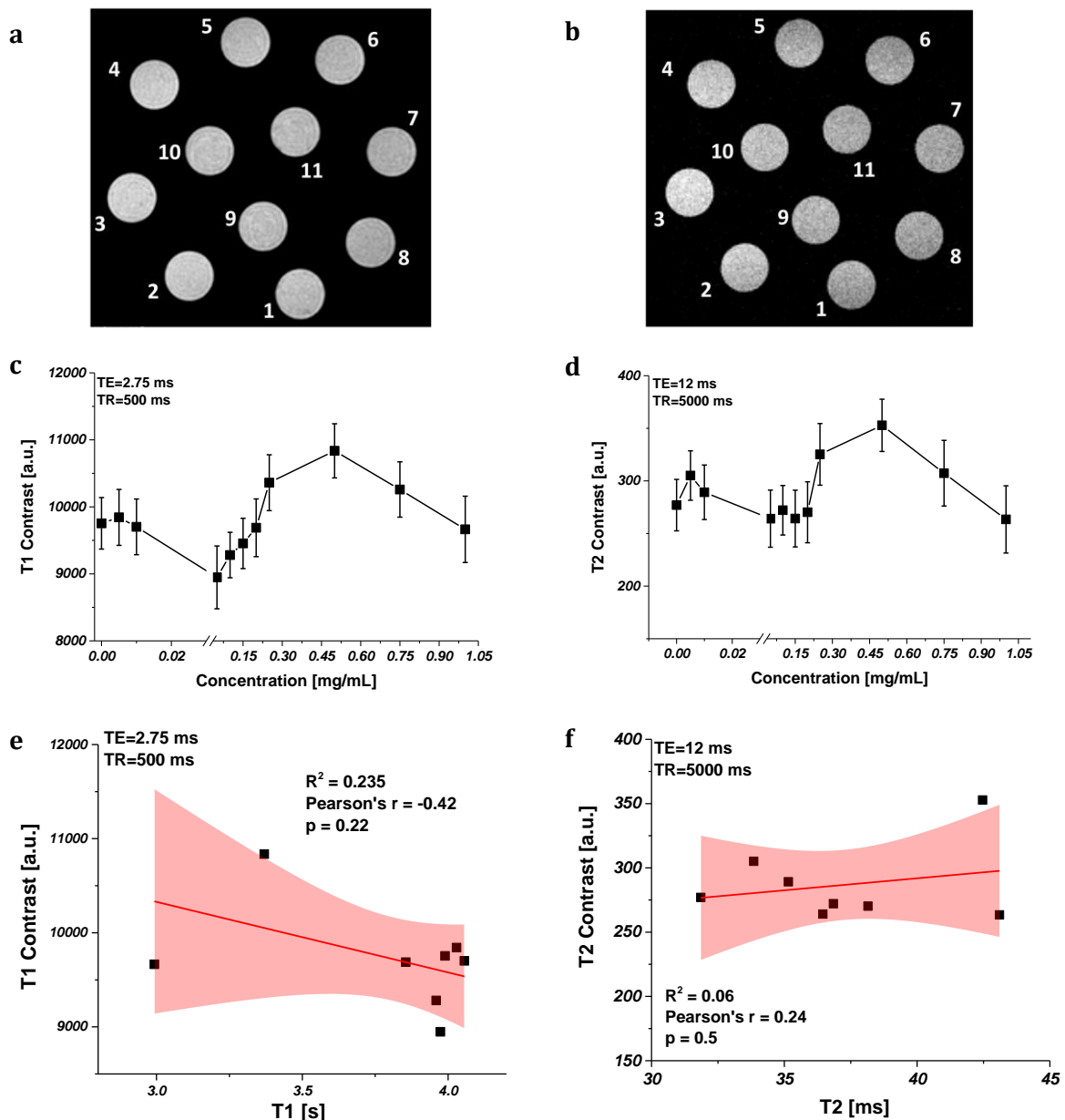


**Figure 36:** MR phantom images and contrast evaluation at 14.1 T. (a) 2D  $T_1$ -weighted and (b)  $T_2$ -weighted phantom images. (c,d) Contrast quantification curves. (e) Pearson correlation between the  $T_1$  relaxation time and the  $T_1$ -weighted contrast enhancement and (f) Pearson correlation between the  $T_2$  relaxation time and the  $T_2$ -weighted contrast enhancement with respect to increasing LNO@Si-Allys@[GdL<sub>D</sub>] concentration.

Altogether, these results strongly suggest that if the density of Gd chelates can be increased on the NP surface, **LNO@Si-Alys@[GdL<sub>D</sub>]** can be further developed as a nonlinear optical/MRI dual modal imaging probe for cancer bioimaging *in vitro*. The first option that we envisaged to increase the density of Gd ions was the use of **LNO@Si-Talys** NPs as starting point for click conjugation to **[GdL<sub>D</sub>]**, taking advantage of the increased number of surface azido groups. With such approach, the resulting **LNO@Si-Talys@[GdL<sub>D</sub>]** NPs displayed again poor colloidal stability in water, similarly to what was observed for **LNO@Si-Talys@[LnL<sub>A</sub>]** (hydrodynamic sizes > 1000 nm, PDI > 0.3). However, the phantom experiments were repeated on this sample, and showed much clearer trends in signal change with respect to NP concentration (Pearson correlation < 0.01, *cf. Figure 37*). T<sub>1</sub> contrast appeared to increase with NP concentration up to 0.25 mg/mL, after which it tended to plateau, whereas T<sub>2</sub> contrast stagnated at low concentrations and decreased with increasing concentration starting from 0.25 mg/mL. These observations agreed with what was previously published in our group, and seem to indicate that a significantly higher amount of Gd was grafted on the NP surface in the case of **LNO@Si-Talys**, at the cost of a poorer dispersibility in water.

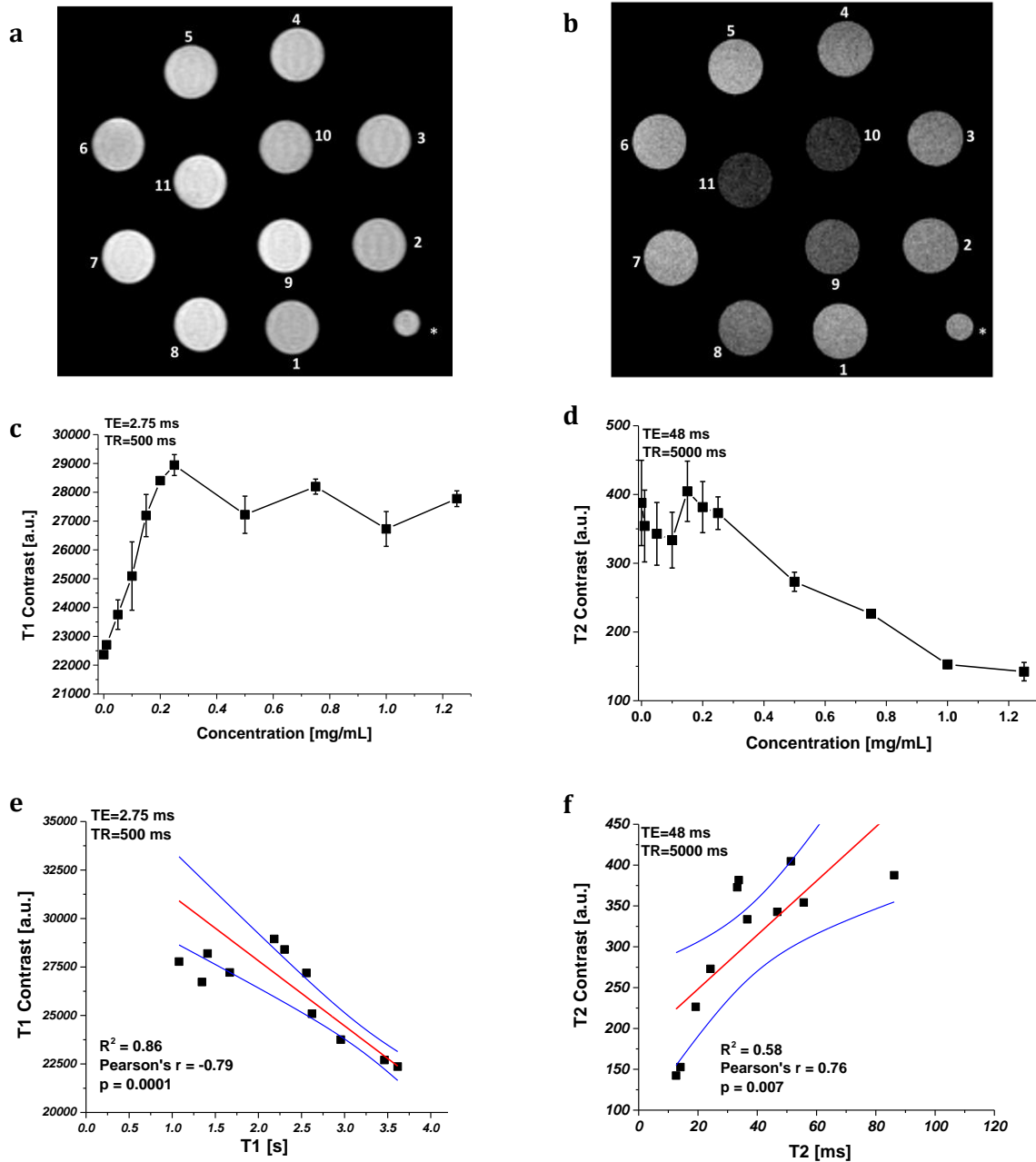


**Figure 37:** MR phantom images and contrast evaluation at 14.1 T. (a) 2D T<sub>1</sub>-weighted and (b) T<sub>2</sub>-weighted phantom images. (c,d) Contrast quantification curves. (e) Pearson correlation between the T<sub>1</sub> relaxation time and the T<sub>1</sub>-weighted contrast enhancement and (f) Pearson correlation between the T<sub>2</sub> relaxation time and the T<sub>2</sub>-weighted contrast enhancement with respect to increasing LNO@Si-Talys@[GdL<sub>D</sub>] concentration.

These data suggest that playing on the composition of the coating layer (tunable density of surface reactive group) and on the nature of the click conjugation reaction holds the potential for optimizing the properties of the dual imaging NPs.

In summary, though these results are preliminary and do not constitute a full study, they clearly show the potential of **LNO@Si@[LnL]** platforms to act as multimodal imaging probes applicable for nonlinear and luminescent optical imaging, while also reaching modalities more suitable for deep tissue imaging such as MRI or X-ray CT.



## 4. Conclusion and outlooks

---

As cancer continues to represent a major health problem worldwide, current treatments still face many challenges to decisively increase patient life expectancies. These challenges are mainly twofold: the lack of specificity of treatments, leading to severe side effects hampering survival rates, and the difficulty in detecting cancerous lesions at an early stage. A potential solution arises in the development of novel precision medicine strategies, involving the design of complex theranostic platforms, capable of both selective therapy and efficient diagnosis of tumors.

In this context, inorganic NPs emerged as a promising basis to design such multi-functional platforms. They can act as carriers, and their unique surface properties allow their conjugation to a variety of ligands for both therapeutic and imaging scopes. Moreover, the intrinsic imaging capabilities of inorganic NPs make them of particular interest for the development of multimodal imaging systems, which have the potential of overcoming the limitations of standard diagnosis approaches.

The aim of this thesis was to develop robust functionalization strategies of HNPs by silanization and further grafting of short peptides. This surface modification had the objective of increasing the colloidal properties and biocompatibility of this material while introducing reactive handles amenable for post-functionalization by click chemistry, paving the way for the design of a novel theranostic nanosystem. These NPs were then conjugated with a drug delivery system, taking advantage of their intrinsic optical properties to trigger the release of an erlotinib-based chemotherapeutic upon NIR irradiation. In addition, these coated HNPs were functionalized with lanthanide chelates to supplement their multi-harmonic emission with other imaging modalities, including luminescence, MR and X-ray responsiveness.

Silica coating of HNPs was achieved through reaction with alkoxy silane derivatives by Stöber process. The standard ultrasonication-assisted was improved by going towards a reverse water-in-oil microemulsion approach, which produced monodisperse NPs in a reproducible manner. A short peptide, **Talys**, was then synthesized to exhibit multiple azide-bearing side chains and conjugated to the silanized HNPs. The resulting **LNO@Si-Talys** NPs exhibited promising colloidal properties in both organic and aqueous media, while displaying a high density of surface azido groups for efficient click modification.

For the development of therapeutic HNPs, a drug delivery system was synthesized by covalently linking an erlotinib derivative to a cyclooctyne through a coumarinyl photocleavable linker (**DIBO-CM-ELA**). This DDS could then be conjugated to azide-bearing silanized HNPs by SPAAC. The capacity of these **LNO@CM-ELA** NPs to inhibit the growth of cancerous cells overexpressing EGFR was demonstrated *in vitro*, through the release of the **ELA** therapeutic compound upon NIR irradiation.

Finally, alkyne (**LA**) or cyclooctyne (**LB**) bearing chelating ligands were synthesized and used to form a panel of lanthanide (III) complexes, ranging from lanthanum to ytterbium. These complexes were then grafted onto silanized HNPs and their imaging properties assessed through preliminary studies. The lanthanide-NP systems showed luminescent emissions and MRI contrasting capabilities depending on the lanthanide atom chosen, without compromising their inherent multi-harmonic emission capabilities. These represent promising results for the use of functionalized HNPs as biomedical multimodal probes.

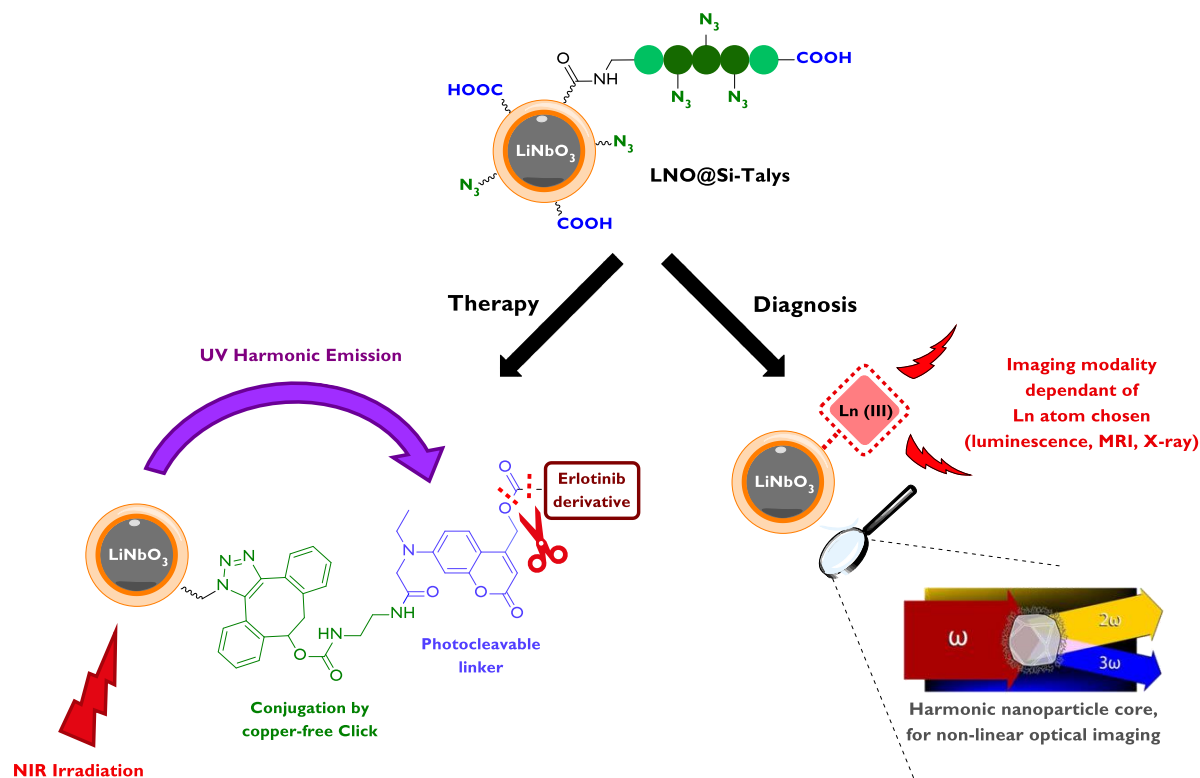


**Figure 38:** Schematic representation of the thesis project.

For the continuation of this project, several avenues remain worth investigating for the improvement of the system:

- The development of new peptides with different functionalities could allow the NP functionalization through strategies other than CuAAC or SPAAC, such as the work that was started on tetrazine-bearing peptides. Furthermore, the cytotoxicity and cell internalization capacity of HNPs functionalized with peptides should be studied in more detail, to ensure the biocompatibility of these materials.
- Since the functionalization with the drug delivery system happened at the beginning of this thesis project chronologically, the DDS could not be assessed on Talys-bearing HNPs. It would be interesting to see how the optimizations on the coating procedure would impact the therapeutic system *in vitro*.
- Efforts should be made to improve the HNP functionalization with lanthanide complexes for potential biomedical applications. This could be achieved by finding a good compromise between lanthanide grafting efficiency and colloidal stability of the final system. Again, the investigation of different conjugation strategies than azide-alkyne cycloadditions could represent a promising avenue of research.
- This was not the scope of this project, but in the future introduction of targeting ligands (such as antibodies or aptamers) on the HNP surface will certainly be crucial to the design of a selective theranostic platform, and represents an exciting perspective.
- The combination of multiple functionalities (therapy, diagnosis, targeting) on a single NP platform still represents the ultimate objective on this project. The use of peptide scaffolds, facilitating the introduction of diverse and orthogonal reactive moieties, could prove instrumental in this task.



In conclusion, a new methodology was implemented for the silanization and surface modification of HNPs through the introduction of short synthetic peptides. Functional HNPs could be modified with both therapeutic and imaging modalities, advancing towards the development of a theranostic nanoplatform. The therapeutic system was the first *in vitro* confirmation of cell growth inhibition through the photo-release of tyrosine kinase inhibitor, and the preliminary tests performed on lanthanide-conjugated HNPs illustrated their potential as a multimodal imaging platform for cancer diagnosis.



## 5. Experimental

---

### 5.1. General Information

Reagents and solvents were purchased from commercial sources (Aldrich, Acros, Merck, Fluka and VWR international) and preserved under argon. Air and humidity sensitive compounds were stored in a desiccator or glove-box if required. Commercial reagents were used without further purification unless otherwise noted. All reactions were performed in flame dried glassware under an inert atmosphere of argon when necessary. Evaporation and concentration *in vacuo* were conducted using Rotavapor devices from Büchi. All products were dried under medium vacuum ( $10^{-2}$  bar) before analytical characterization. Dialysis purifications were performed against distilled H<sub>2</sub>O at room temperature (water changed every 3 h), with dialysis membranes from Roth (dialysis tubes Float-A-Lyzer G2 CE, 10 mL, exclusion limit 100-500 Da, dry packed treated with glycerine; unless otherwise mentioned). Samples were lyophilised in a VaCo 5 Zirbus technology freeze dryer (0.3 mbar, -80 °C).

**Thin Layer Chromatography (TLC):** Reactions were monitored using Merck Kieselgel 60F254 aluminium or glass backed plates. TLC's were visualized by UV fluorescence (254 nm) then one of the following reagent: KMnO<sub>4</sub>, molybdenate, ninhydrine, pancaldi, p-anisaldehyde, vanillin.

**Flash Column Chromatography (FC):** SiO<sub>2</sub> 60A (230-400 mesh, particle size 40-63 µm) and Al<sub>2</sub>O<sub>3</sub> 60A (50-200 mesh, basic Brockmann I) were obtained from Fluka.

**NMR <sup>1</sup>H- and <sup>13</sup>C-NMR spectra:** NMR spectra were recorded on Bruker Avance III-400, Bruker Avance-400 or Bruker DRX-400 spectrometers at room temperature, <sup>1</sup>H frequency is at 400.13 MHz, <sup>13</sup>C frequency is at 100.62 MHz. Chemical shifts (δ) were reported in parts per million (ppm) relative to residual solvent peaks rounded to the nearest 0.01 ppm for proton and 0.1 ppm for carbon (ref : CHCl<sub>3</sub> [<sup>1</sup>H: 7.26 ppm, <sup>13</sup>C: 77.2 ppm], MeOH [<sup>1</sup>H: 3.31 ppm, <sup>13</sup>C 49.0 ppm], ACN [<sup>1</sup>H: 1.94 ppm, <sup>13</sup>C: 1.3 ppm], DMSO [<sup>1</sup>H: 2.50 ppm, <sup>13</sup>C: 39.5 ppm]). Coupling constants (J) were reported in Hz to the nearest 0.1 Hz. Peak multiplicity was indicated as follows s (singlet), d (doublet), t (triplet), q (quartet), m (multiplet) and br (broad). Attribution of peaks was done using the multiplicities and integrals of the peaks.

**Accurate Mass:** The qualitative accurate masses were measured by ESI-TOF using the Xevo G2-S QTOF (Waters) and nanoESI-FT-MS using the Elite™ Hybrid Ion Trap-Orbitrap (ThermoFisher) Mass Spectrometer. Quantitative MS analyses were performed on the 6530 Accurate-Mass Q-TOF LC/MS mass spectrometer coupled to the 1290 Infinity UHPLC system (Agilent Technologies, USA). The separation was achieved using an ACQUITY UPLC® BEH C18 1.7µm column, 2.1 mm x 50 mm (Waters) heated at 30°C using water and acetonitrile as mobile phases.

**Dynamic Light Scattering (DLS) and Zeta potential:** measurements made with Malvern NanoZ instrument.

**IR spectra:** recorded on a Nicolet 6700 FT-IR Spectrophotometer from Thermo Fisher Scientific with KBr pellets. The spectra are reported in cm<sup>-1</sup>.

**UV-vis absorption:** Measurements performed with BioTek Synergy 2 multi-mode reader instrument between 200 to 700 nm with increment of one nm in a 96-well plate (Corning® UV-Transparent microplate).

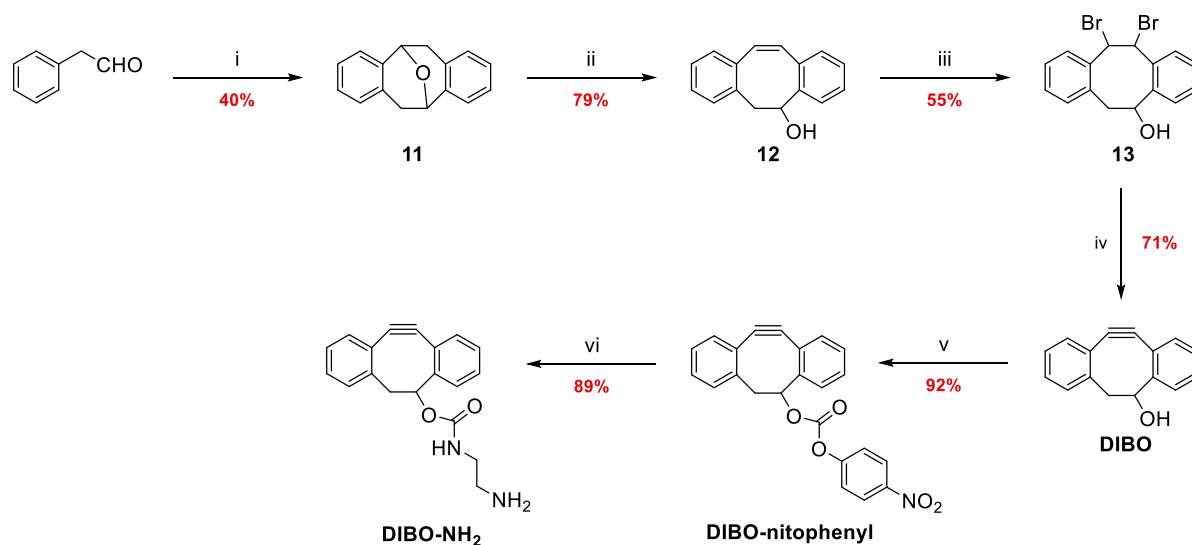
**Sonicator:** Elmasonic P 120 H; Branson 1800 Ultraonic Cleaner sonicator.

**Centrifugator:** HERAEUS Biofuge 13 centrifuge; Beckman Coulter Allegra X-30 centrifuge.

**STEM:** Scanning transmission electron microscopy (STEM) and energy-dispersive X-ray spectroscopy (EDX) were performed at the Interdisciplinary Centre for Electron Microscopy (CIME, EPFL, Lausanne, Switzerland) on a FEI Tecnai Osiris (200 kV).

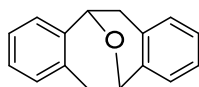
**Luminescence:** Spectra acquired on a Fluorolog spectrofluorometer with Time-Related Single-Photon Counting (TCSPC).

## 5.2. Synthesis of cyclooctyne derivatives



**Scheme 20: Synthesis of DIBO derivatives.** i-  $\text{Me}_3\text{SiI}$ , DCM,  $5^\circ\text{C}$ , 7 days; ii-  $\text{BuLi}$ , THF, r.t., 4 h; iii-  $\text{Br}_2$ ,  $\text{CHCl}_3$ , r.t., 2 h; iv-  $\text{LDA}$ , THF, r.t., 1 h; v- 4-nitrophenyl chloroformate, pyridine, DCM, r.t., 16 h; vi- ethylenediamine,  $\text{Et}_3\text{N}$ , DCM, r.t., 2 h.

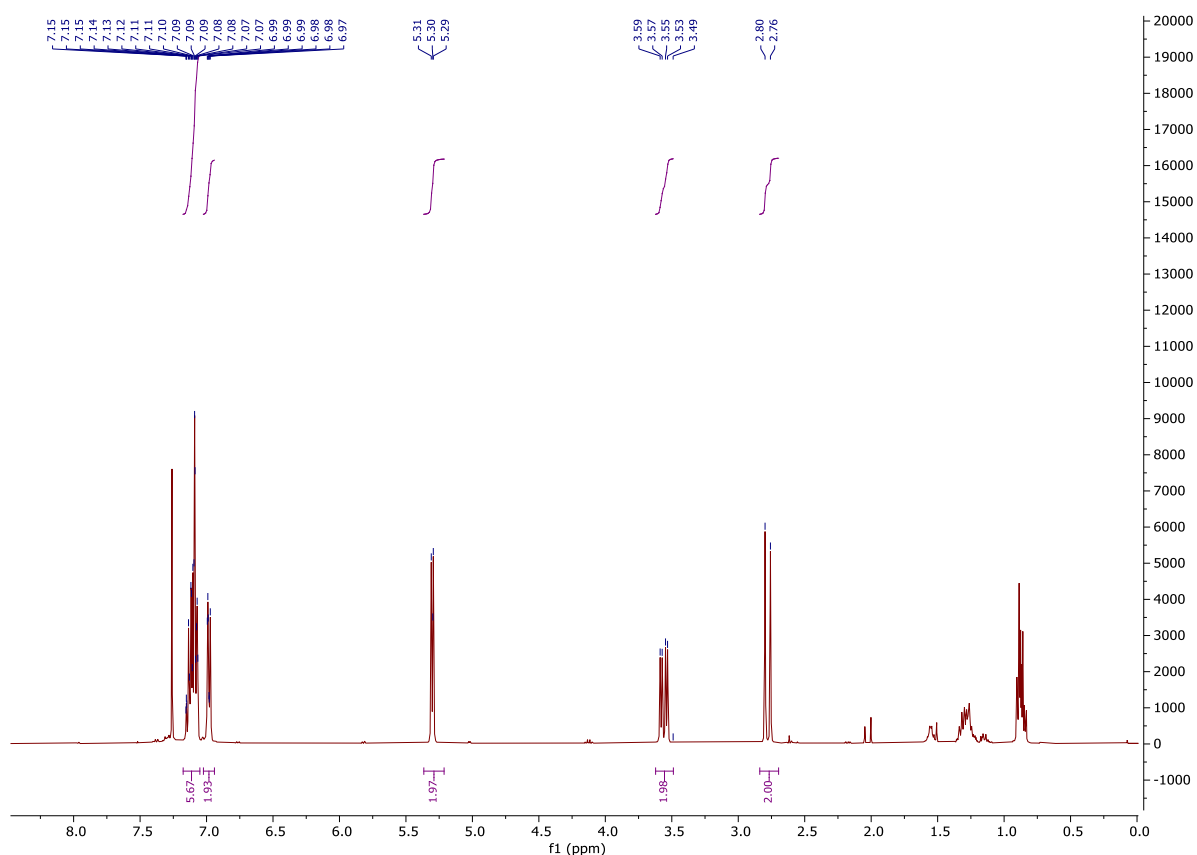
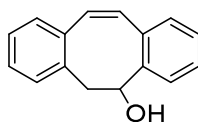
### 5,6,11,12-Tetrahydro-5,11-epoxydibenzo[*a,e*][8]annulene (11)



2-Phenylacetaldehyde (9.7 mL, 83.2 mmol, 1.0 eq) was dissolved in dry DCM (45 mL) and the solution was cooled to  $0^\circ\text{C}$ . Trimethylsilyl iodide (12.1 mL, 84.9 mmol, 1.02 eq) was added dropwise and the reaction mixture was stirred at  $5^\circ\text{C}$  for 7 days under argon atmosphere. A sat. aqueous solution of  $\text{Na}_2\text{S}_2\text{O}_3$  (30 mL) and DCM (20 mL) were added and the reaction mixture was stirred until the iodine colour vanished. The aqueous layer was extracted with DCM (2 X 25 mL) and the combined organic layers were dried over  $\text{MgSO}_4$ , filtered and concentrated under reduced pressure. The crude mixture was purified by FC eluting with a mixture of PE / EtOAc (50:1 to 1:1) to afford the product (3.6 g, 16.2 mmol, 40% yield) as a light brown solid.

$^1\text{H NMR}$  (400 MHz, Chloroform-*d*):  $\delta$  7.17 – 7.04 (m, 6H, 6 X Ar-*H*), 6.99 (m, 2H, 2 X Ar-*H*), 5.30 (d,  $J = 6.0$  Hz, 2H, 2 X CH), 3.56 (dd,  $J = 16.2, 6.1$  Hz, 2H, 2 X HC-*H*), 2.78 (d,  $J = 16.2$  Hz, 2H, 2 X HC-*H*).

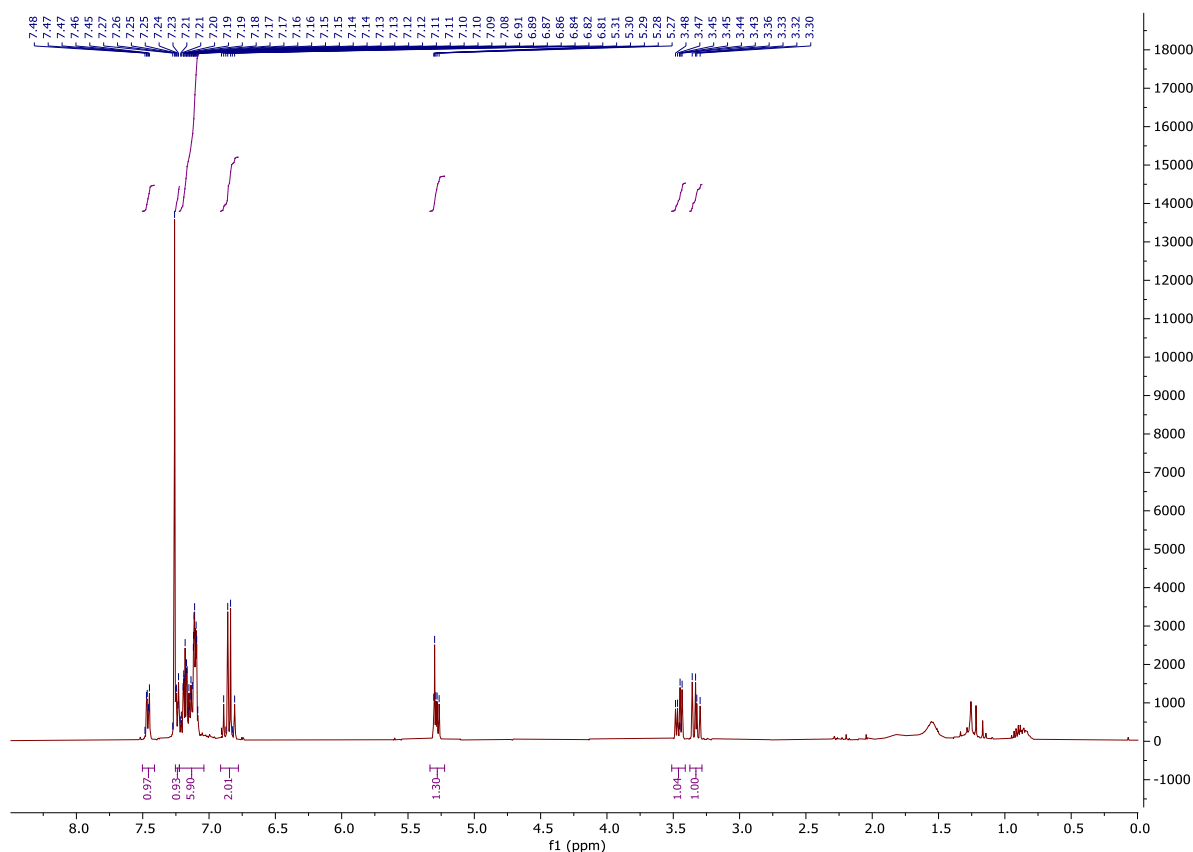
The analytical data were in accordance with previously reported data.<sup>154,155</sup>

<sup>1</sup>H NMR spectrum:**(Z)-5,6-Dihydrodibenzo[*a,e*][8]annulen-5-ol (12)**

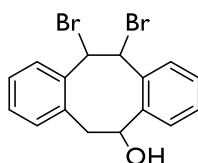
A 2.6 M solution of *n*-BuLi (6.7 mL, 18 mmol, 2.0 eq.) in toluene was added dropwise to a solution of 5,6,11,12-tetrahydro-5,11-epoxydibenzo[*a,e*][8]annulene (2.0 g, 9.0 mmol, 1.0 eq) in dry THF (100 mL). The reaction mixture was stirred at r.t for 4 h under argon atmosphere. The mixture was quenched by addition of H<sub>2</sub>O (10 mL) and THF was removed under reduced pressure. The aqueous layer was extracted with DCM (3 X 15 mL) and the combined organic layers were washed with brine (1 X 25 mL), dried over MgSO<sub>4</sub>, filtered and concentrated under reduced pressure. The crude mixture was purified by FC eluting with a mixture of PE / EtOAc (5:1). The product (1.6 g, 7.1 mmol, 79% yield) was obtained as a white solid.

**<sup>1</sup>H NMR** (400 MHz, Chloroform-*d*): δ 7.46 (m, 1H, Ar-*H*), 7.24 (m, 1H, Ar-*H*), 7.25 – 7.10 (m, 6H, 6 X Ar-*H*), 6.93 – 6.79 (m, 2H, RHC=CHR), 5.28 (m, 1H, CH), 3.46 (dd, *J* = 13.8, 6.1 Hz, 1H, HC-*H*), 3.33 (dd, *J* = 13.8, 10.0 Hz, 1H, HC-*H*).

The analytical data were in accordance with previously reported data.<sup>154,155</sup>

<sup>1</sup>H NMR spectrum:

### 11,12-Dibromo-5,6,11,12-tetrahydrobenzo[*a,e*][8]annulen-5-ol (13)



Bromine was added dropwise (0.23 mL, 4.5 mmol, 1.0 eq) to a solution of (*Z*)-5,6-dihydrodibenzo[*a,e*][8]annulen-5-ol (1.0 g, 4.5 mmol, 1.0 eq) in CHCl<sub>3</sub> (13.5 mL). The reaction mixture was stirred at r.t for 2 h. The mixture was quenched by addition of sat. aqueous solution of Na<sub>2</sub>S<sub>2</sub>O<sub>3</sub> (30 mL). The aqueous layer was extracted with CHCl<sub>3</sub> (3 X 30 mL) and the combined organic layers were washed with brine (1 X 30 mL), dried over MgSO<sub>4</sub>, filtered and concentrated under reduced pressure. The crude mixture was purified by FC eluting with a mixture of PE / DCM (2:1). The product (0.90 g, 2.4 mmol, 55% yield) was obtained as a yellow oil.

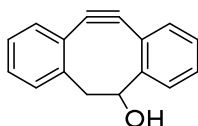
<sup>1</sup>H NMR (400 MHz, Chloroform-*d*, major diastereoisomer): δ 7.51 (dt, *J* = 7.9, 1.3 Hz, 1H, Ar-*H*), 7.23 (s, 1H, Ar-*H*), 6.97 – 6.75 (m, 5H, 5 X Ar-*H*), 6.70 (dt, *J* = 7.5, 1.3 Hz, 1H, Ar-*H*), 5.65 (d, 1H, R<sub>2</sub>BrC-*H*), 5.59 (d, 1H, R<sub>2</sub>BrC-*H*), 5.29 (dd, *J* = 3.7, 2.5 Hz, 1H, CH), 3.58 (ddd, *J* = 16.2, 2.4, 1.2 Hz, 1H, HC-*H*), 2.93 (dd, *J* = 16.1, 3.8 Hz, 1H, HC-*H*).

The analytical data were in accordance with previously reported data.<sup>154,155</sup>





## Dibenzocyclooctyne: DIBO

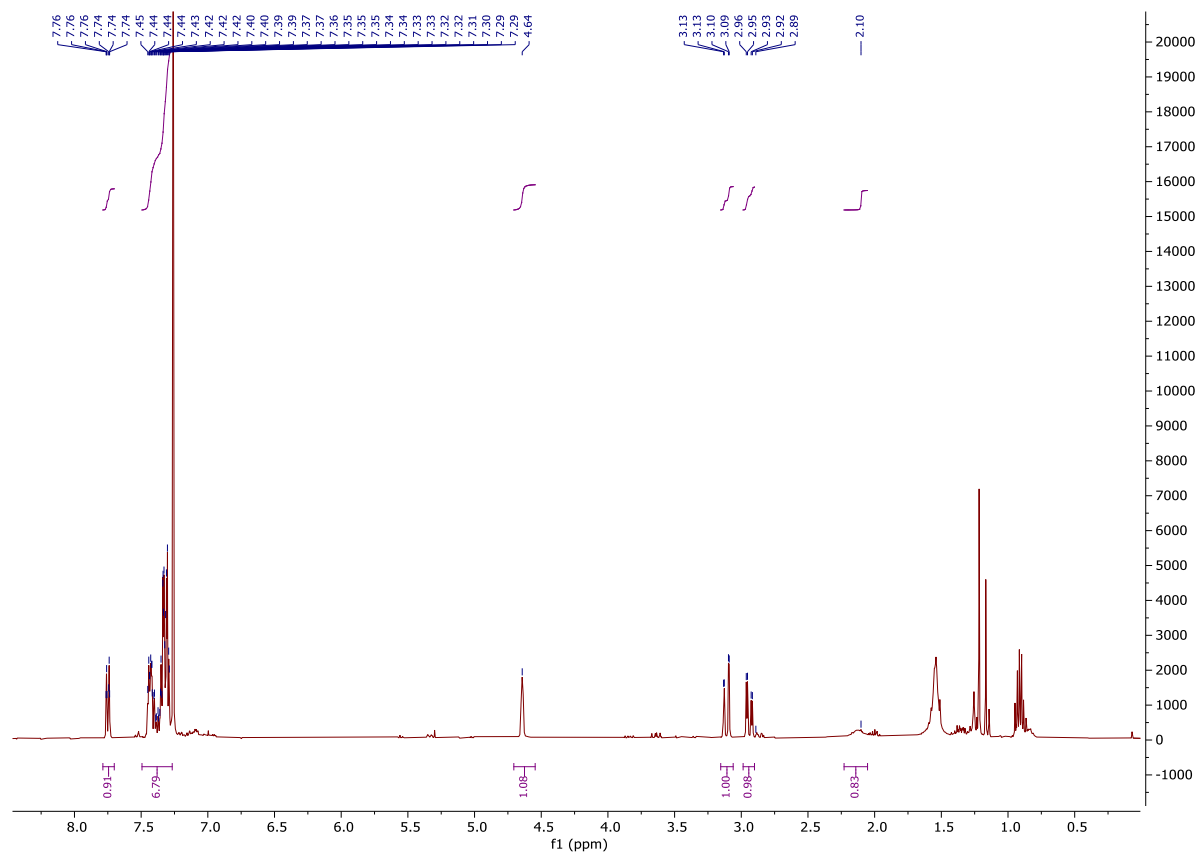


Freshly prepared 0.8 M solution of LDA (10.2 mL, 8.1 mmol, 5.8 eq) in dry THF was added dropwise at 0°C to a solution of 11,12-dibromo-5,6,11,12-tetrahydrodibenzo[*a,e*][8]annulen-5-ol (0.52 g, 1.4 mmol, 1.0 eq) in dry THF (17 mL). The reaction mixture was allowed to warm up to r.t and was stirred for 1 h under argon atmosphere. The mixture was quenched by addition of H<sub>2</sub>O (10 mL) and THF was evaporated under reduced pressure. The aqueous layer was extracted with DCM (3 X 10 mL) and the combined organic layers were washed with H<sub>2</sub>O (1 X 10 mL), brine (1 X 10 mL), dried over MgSO<sub>4</sub>, filtered and concentrated under reduced pressure. The crude mixture was purified by FC eluting with a mixture of PE / DCM (1:3). The product (0.21 g, 1.0 mmol, 71% yield) was obtained as a white solid.

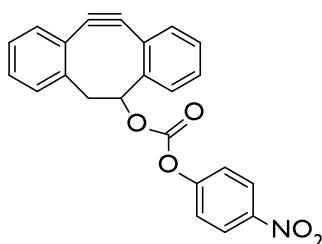
**<sup>1</sup>H NMR** (400 MHz, Chloroform-*d*): δ 7.75 (dd, *J* = 7.8 Hz, 1H, Ar-*H*), 7.48 – 7.27 (m, 7H, 7 X Ar-*H*), 4.64 (s, 1H, CH), 3.11 (dd, *J* = 14.7, 2.2 Hz, 1H, HC-*H*), 2.94 (dd, *J* = 14.7, 3.8 Hz, 1H, HC-*H*), 2.10 (s, 1H, OH).

The analytical data were in accordance with previously reported data.<sup>154,155</sup>

<sup>1</sup>H NMR spectrum:



## DIBO-nitrophenyl

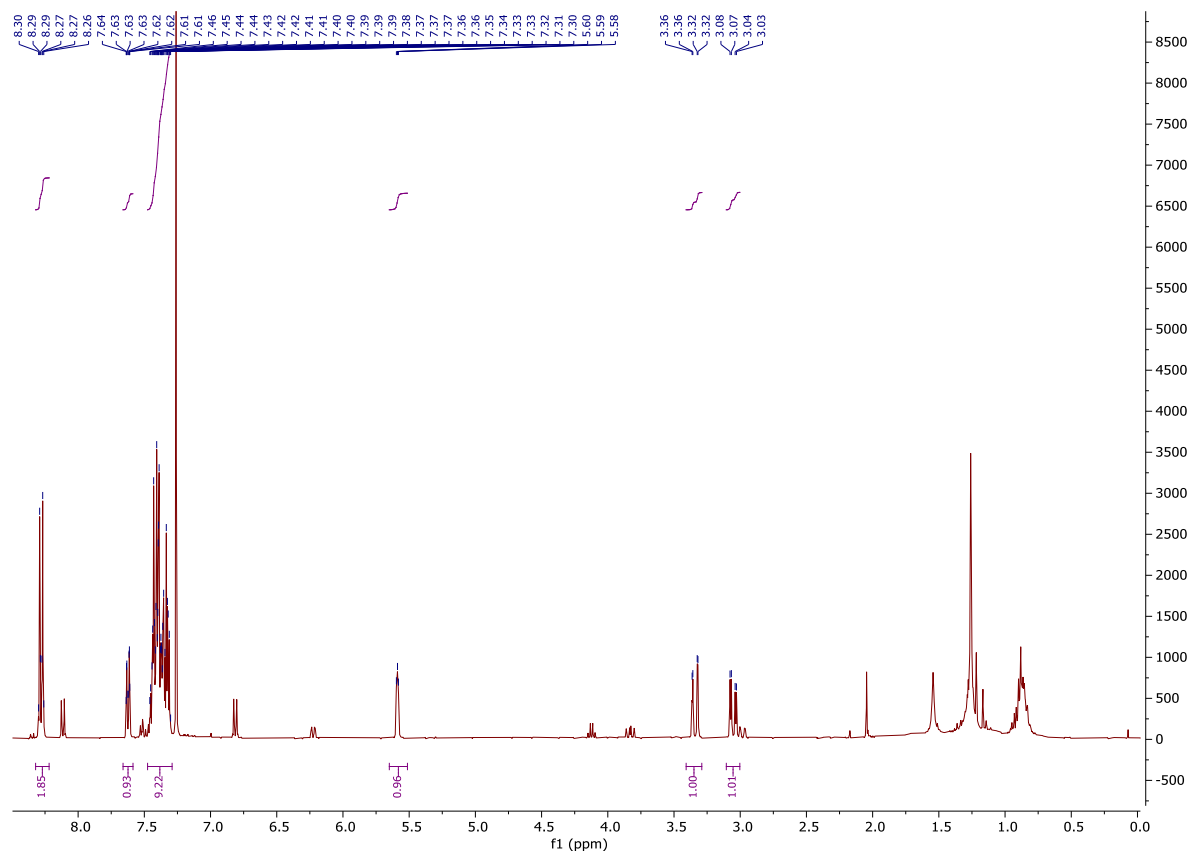


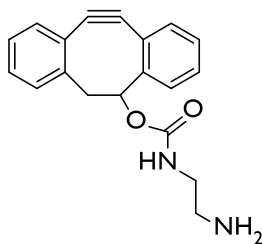
DIBO (125 mg, 0.58 mmol, 1.0 eq) and 4-nitrophenyl chloroformate (230 mg, 1.2 mmol, 2.0 eq) were dissolved in DCM (20 mL). Pyridine (0.23 mL, 2.9 mmol, 5.0 eq) was added and the reaction mixture was stirred at r.t for 16 h. The mixture was washed with brine (2 X 5 mL) and the organic layer was dried over  $\text{MgSO}_4$ , filtered and concentrated under reduced pressure. The crude mixture was purified by FC eluting with a mixture of PE / EtOAc (5:1). The product (205 mg, 0.52 mmol, 92% yield) was obtained as a white solid.

$^1\text{H NMR}$  (400 MHz, Chloroform-*d*):  $\delta$  8.28 (m, 2H, 2 X Ar-*H*), 7.62 (dq,  $J = 7.8, 1.0$  Hz, 1H, DIBO-*H*), 7.47 – 7.29 (m, 9H, 7 X DIBO-*H* and 2 X Ar-*H*), 5.59 (t,  $J = 3.0$  Hz, 1H,  $\text{CH}_{\text{DIBO}}$ ), 3.34 (dd,  $J = 15.4, 2.2$  Hz, 1H, H- $\text{CH}_{\text{DIBO}}$ ), 3.05 (dd,  $J = 15.3, 4.0$  Hz, 1H, H- $\text{CH}_{\text{DIBO}}$ ).

The analytical data were in accordance with previously reported data.<sup>154,155</sup>

$^1\text{H NMR}$  spectrum:



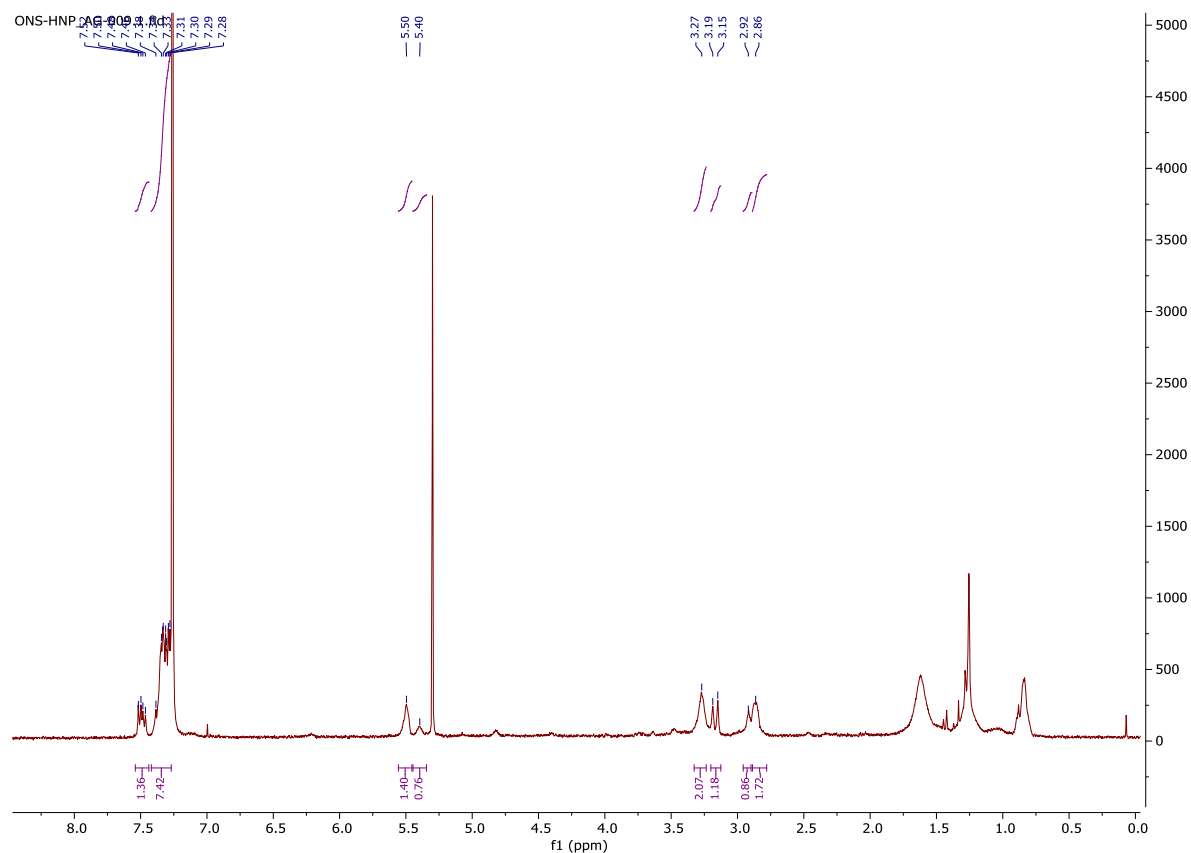
DIBO-NH<sub>2</sub>

A solution of DIBO-nitrophenyl (0.10 g, 0.26 mmol, 1.0 eq) in dry DCM (1 mL) was added dropwise to a solution of ethylenediamine (0.09 mL, 1.3 mmol, 5.0 eq) and Et<sub>3</sub>N (0.11 mL, 0.78 mmol, 3.0 eq) in dry DCM (7 mL). The reaction mixture was stirred at r.t for 2 h under argon atmosphere and the solvent was removed under reduced pressure. The crude mixture was purified by FC eluting with a mixture of DCM / MeOH (5:1). The product (70 mg, 0.23 mmol, 89% yield) was obtained as a slightly yellow oil.

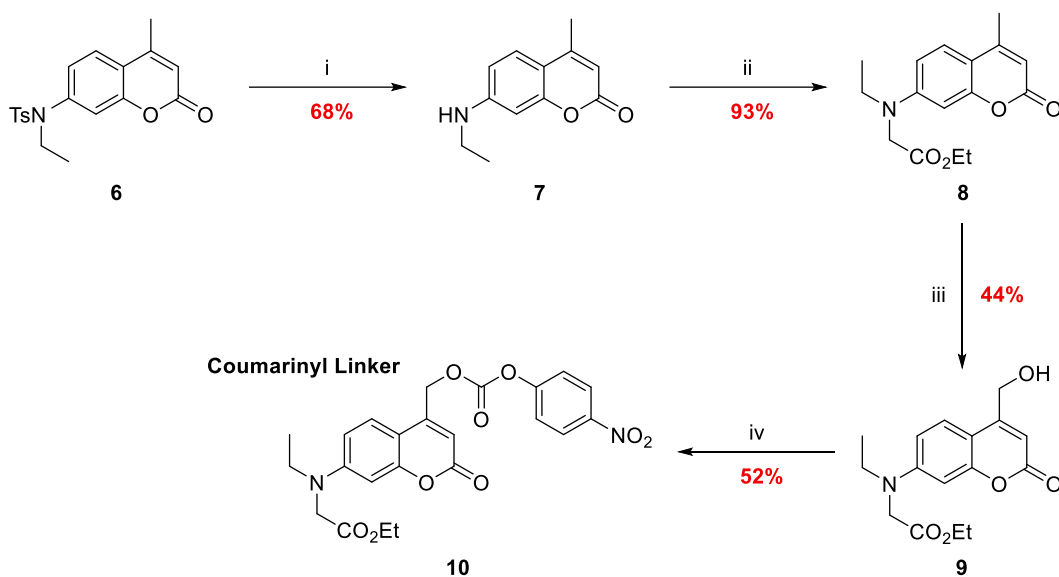
**<sup>1</sup>H NMR** (400 MHz, Chloroform-*d*): δ 7.49 (dd, *J* = 13.5, 7.7 Hz, 1H, Ar-*H*), 7.41 – 7.24 (m, 7H, 7 X Ar-*H*), 5.50 (s, 1H, CH), 5.40 (s, 1H, NH), 3.27 (s, 2H, RNH-CH<sub>2</sub>-CH<sub>2</sub>-NH<sub>2</sub>), 3.17 (d, *J* = 15.0, 1H, HC-*H*), 2.92 (s, 1H, HC-*H*), 2.86 (s, 2H, CH<sub>2</sub>-NH<sub>2</sub>).

The analytical data were in accordance with previously reported data. <sup>154,155</sup>

<sup>1</sup>H NMR spectrum:

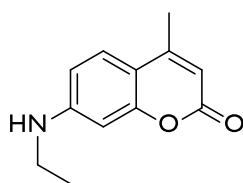


### 5.3. Synthesis of coumarinyl linker



**Scheme 21: Synthesis of CM derivative.** i-  $\text{H}_2\text{SO}_4$ ,  $0^\circ\text{C}$ , 1 h; ii- ethyl bromoacetate,  $\text{K}_2\text{CO}_3$ , TBAB, NaI, ACN, reflux, 46 h; iii-  $\text{SeO}_2$ ; *p*-xylene, reflux 24 h; then  $\text{NaBH}_4$ , MeOH, r.t, 3 h; iv- 4-nitrophenyl chloroformate, DIPEA, DCM, r.t, 16 h.

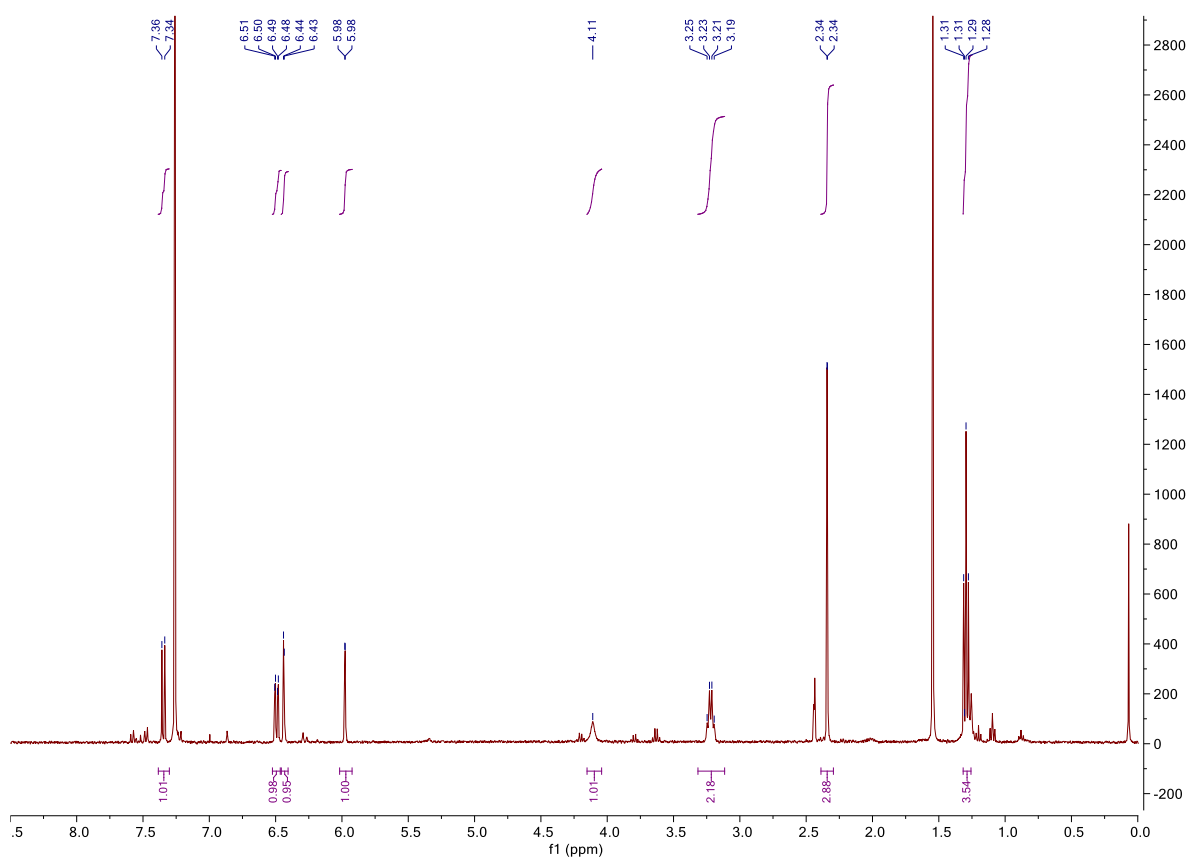
#### 7-(Ethylamino)-4-methyl-2*H*-chromen-2-one (7)



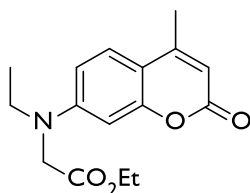
4-Methyl-*N*-(4-methyl-2-oxo-2*H*-chromen-7-yl)benzenesulfonamide (2.2 g, 6.2 mmol, 1.0 eq) was added to conc. sulfuric acid (10 mL) and the reaction mixture was stirred at  $0^\circ\text{C}$  for 1 h. The reaction mixture was poured into  $\text{H}_2\text{O}$  (40 mL) and neutralized with sat. aqueous  $\text{NaHCO}_3$  (300 mL). The aqueous layer was extracted with DCM (3 X 400 mL). The combined organic layers were dried over  $\text{MgSO}_4$ , filtered and concentrated under reduced pressure. The crude mixture was purified via FC eluting with a mixture of EtOAc / PE (6:4) to afford the product (0.82 g, 4.0 mmol, 68% yield) as a yellow solid.

$^1\text{H NMR}$  (400 MHz, Chloroform-*d*):  $\delta$  7.35 (d,  $J = 8.6$  Hz, 1H, coumarin-*H*), 6.49 (dd,  $J = 8.6, 2.4$  Hz, 1H, coumarin-*H*), 6.44 (d,  $J = 2.3$  Hz, 1H, coumarin-*H*), 5.98 (d,  $J = 1.5$  Hz, 1H, coumarin-*H*), 4.11 (s, 1H, N-*H*), 3.22 (q,  $J = 7.1$ , 2H,  $\text{CH}_2$  ester), 2.34 (d,  $J = 1.2$  Hz, 3H,  $\text{CH}_3$  coumarin), 1.29 (t,  $J = 7.2$  Hz, 3H,  $\text{CH}_3$  ester).

The analytical data were in accordance with previously reported data.<sup>155</sup>

<sup>1</sup>H NMR spectrum:

**Ethyl *N*-ethyl-*N*-(4-methyl-2-oxo-2*H*-chromen-7-yl)glycinate (8)**



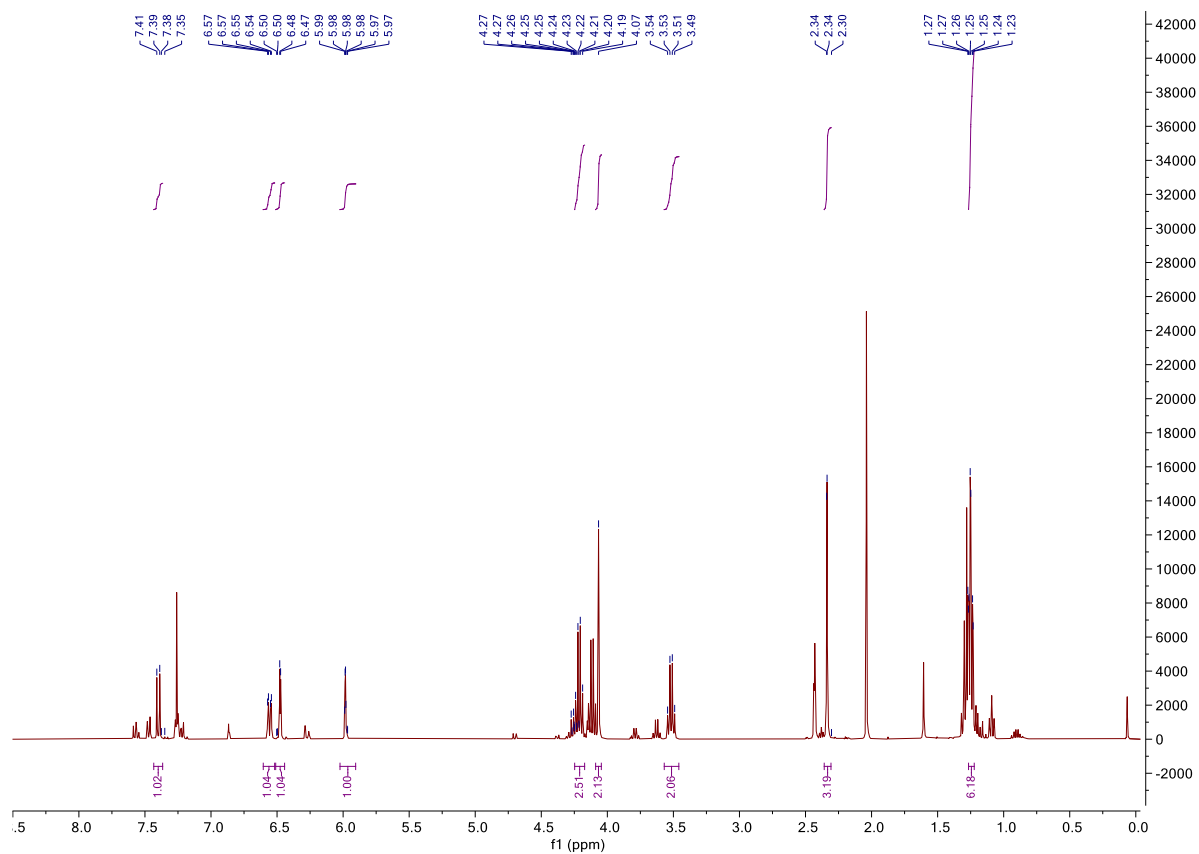
7-(Ethylamino)-4-methyl-2*H*-chromen-2-one (0.8 g, 3.9 mmol, 1.0 eq), K<sub>2</sub>CO<sub>3</sub> (1.6 g, 11.8 mmol, 3.0 eq), NaI (0.12 g, 0.78 mmol, 0.2 eq) and tetrabutylammonium bromide (0.26 g, 0.74 mmol, 0.2 eq) were dissolved in acetonitrile (40 mL). Ethyl bromoacetate (4 mL, 39.2 mmol, 10.0 eq) was added and the mixture was refluxed for 48 h. The reaction mixture was cooled down to r.t, filtered and the solvent was removed under reduced pressure. The residue was dissolved in EtOAc (80 mL) and washed with H<sub>2</sub>O (3 X 80 mL). The organic layer was dried over MgSO<sub>4</sub>, filtered and concentrated under reduced pressure. The residue was purified via FC eluting with a mixture of EtOAc / PE (6:4) to afford the product (1.1 g, 3.7 mmol, 93% yield) as a yellow solid.

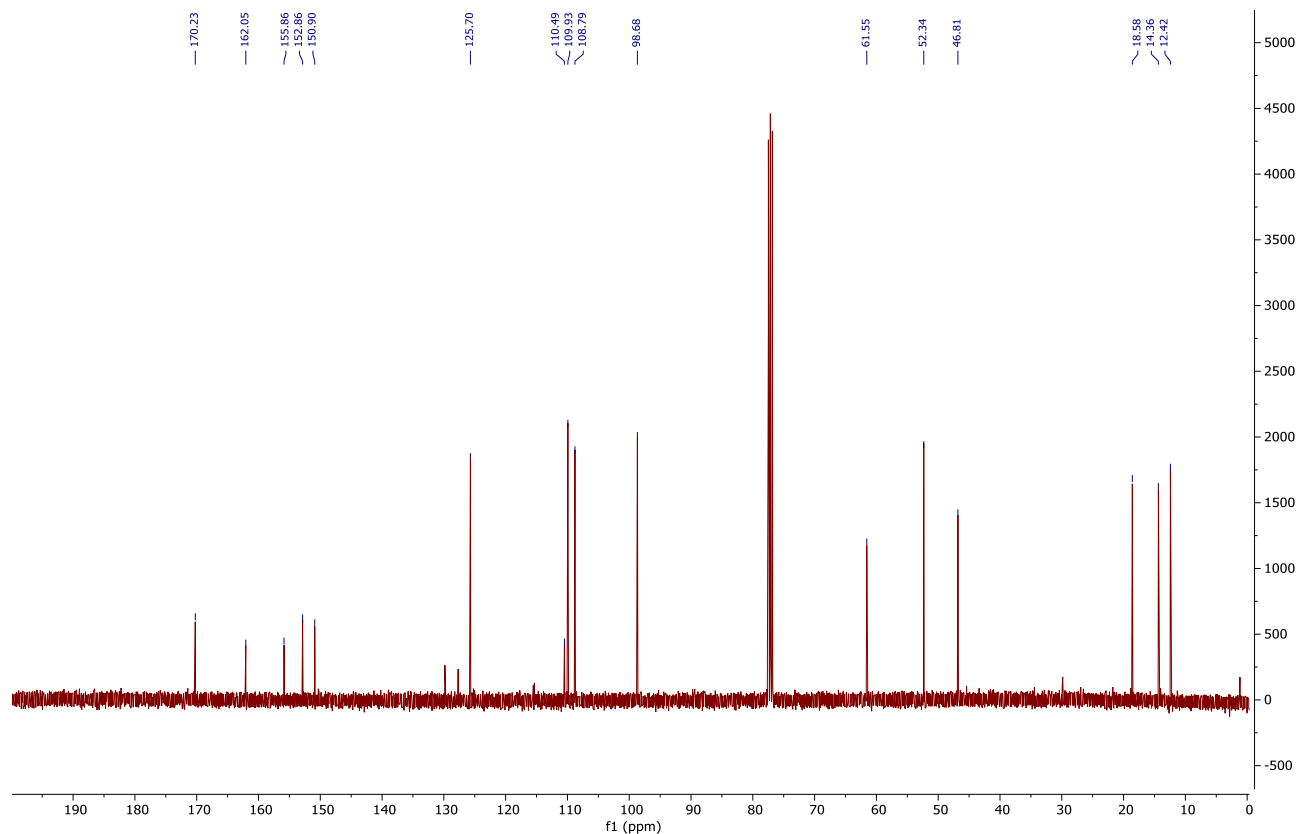
**<sup>1</sup>H NMR** (400 MHz, Chloroform-*d*): δ 7.40 (d, *J* = 8.9 Hz, 1H, coumarin-*H*), 6.56 (dd, *J* = 8.9, 2.6 Hz, 1H, coumarin-*H*), 6.48 (d, *J* = 2.6 Hz, 1H, coumarin-*H*), 5.98 (q, *J* = 1.5 Hz, 1H, coumarin-*H*), 4.21 (q, *J* = 7.1 Hz, 2H, CH<sub>2</sub> ester), 4.07 (s, 2H, RN-CH<sub>2</sub>-CO<sub>2</sub>Et), 3.52 (q, *J* = 7.1 Hz, 2H, R<sub>2</sub>N-CH<sub>2</sub>-CH<sub>3</sub>), 2.34 (d, *J* = 1.1 Hz, 3H, CH<sub>3</sub> coumarin), 1.25 (m, 6H, R<sub>2</sub>N-CH<sub>2</sub>-CH<sub>3</sub> and CH<sub>3</sub> ester).

$^{13}\text{C}$  NMR (101 MHz, Chloroform-*d*):  $\delta$  170.2 ( $\text{C}_\text{O}$ ), 162.1 ( $\text{C}_\text{CM}$ ), 155.9 ( $\text{C}_\text{CM}$ ), 152.9 ( $\text{C}_\text{CM}$ ), 150.9 ( $\text{C}_\text{CM}$ ), 125.7 ( $\text{CH}_\text{CM}$ ), 110.5 ( $\text{C}_\text{CM}$ ), 109.9 ( $\text{CH}_\text{CM}$ ), 108.8 ( $\text{CH}_\text{CM}$ ), 98.7 ( $\text{CH}_\text{CM}$ ), 61.6 ( $\text{CH}_2$ ), 52.3 ( $\text{CH}_2$ ), 46.8 ( $\text{CH}_2$ ), 18.6 ( $\text{CH}_3$ ), 14.4 ( $\text{CH}_3$ ), 12.4 ( $\text{CH}_3$ ) ppm.

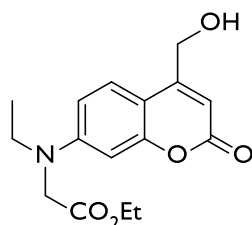
The analytical data were in accordance with previously reported data.<sup>155</sup>

$^1\text{H}$  and  $^{13}\text{C}$  NMR spectra:





**Ethyl *N*-ethyl-*N*-(4-(hydroxymethyl)-2-oxo-2*H*-chromen-7-yl)glycinate (9)**



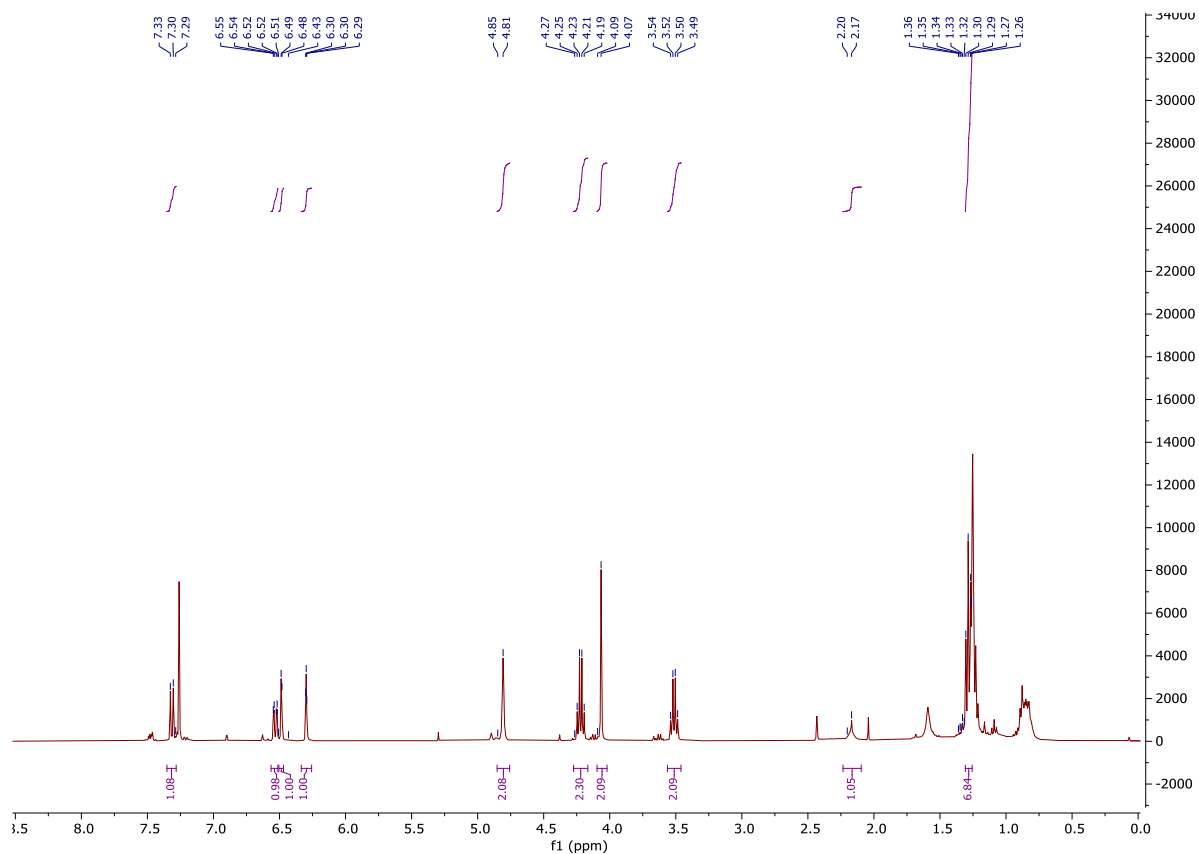
Ethyl *N*-ethyl-*N*-(4-methyl-2-oxo-2*H*-chromen-7-yl)glycinate (1.29 g, 4.46 mmol, 1.0 eq) and  $\text{SeO}_2$  (0.99 g, 8.92, 2.0 eq) were dissolved in *p*-xylene (40 mL). The reaction mixture was refluxed with vigorous stirring under argon atmosphere for 24 h. The reaction mixture was cooled to r.t, filtered through paper filter and concentrated under reduced pressure. The crude was dissolved in methanol (30 mL) and  $\text{NaBH}_4$  (0.34 g, 8.92 mmol, 2.0 eq) was added. The reaction mixture was stirred at r.t for 3 h and the suspension was neutralized with 1M aqueous HCl (10 mL) and  $\text{H}_2\text{O}$  (100 mL). The mixture was extracted with DCM (3 X 150 mL) and the combined organic layers were dried over  $\text{MgSO}_4$ , filtered and concentrated under reduced pressure. The crude mixture was purified via FC eluting with a mixture of EtOAc / PE (3:7 to 6:4). The product (0.6 g, 2.0 mmol, 44% yield) was obtained as a yellow solid.

**$^1\text{H}$  NMR** (400 MHz, Chloroform-*d*):  $\delta$  7.32 (d,  $J = 8.9$  Hz, 1H, coumarin-*H*), 6.53 (dd,  $J = 8.9, 2.6$  Hz, 1H, coumarin-*H*), 6.48 (d,  $J = 2.6$  Hz, 1H, coumarin-*H*), 6.30 (s, 1H, coumarin-*H*), 4.81 (s, 2H,  $\text{CH}_2$  coumarin), 4.22 (q,  $J = 7.1$ Hz, 2H,  $\text{CH}_2$  ester), 4.07 (s, 2H,  $\text{R}_2\text{N}-\text{CH}_2-\text{CO}_2\text{Et}$ ), 3.51 (q,  $J = 7.1$  Hz, 2H,  $\text{RNH}-\text{CH}_2-\text{CH}_3$ ), 2.17 (s, 1H, RO-*H*), 1.28 (m, 3H,  $\text{CH}_3$  ester), 1.27 (m, 3H,  $\text{R}_2\text{N}-\text{CH}_2-\text{CH}_3$ ).

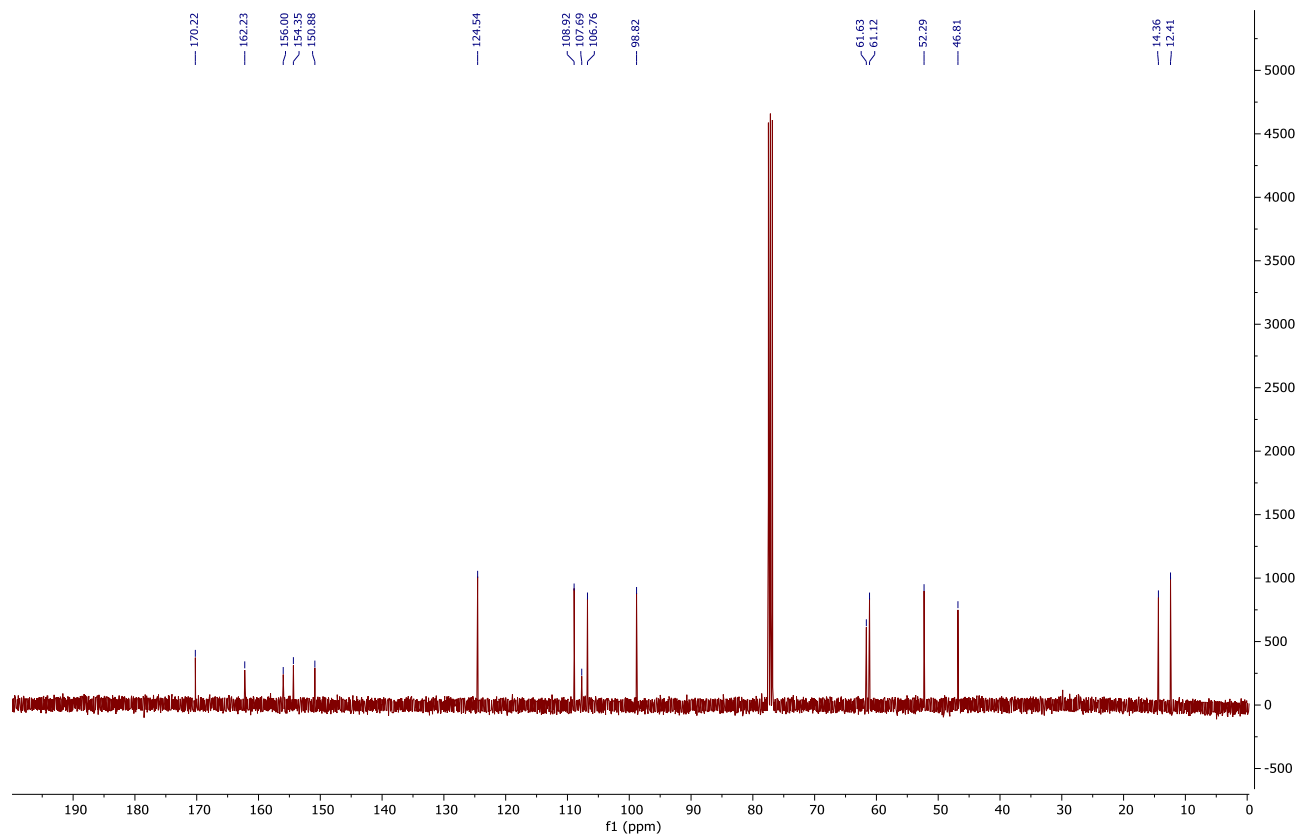
$^{13}\text{C}$  NMR (101 MHz, Chloroform-*d*):  $\delta$  170.1 ( $\text{C}_\text{O}$ ), 162.1 ( $\text{C}_\text{CM}$ ), 155.9 ( $\text{C}_\text{CM}$ ), 154.2 ( $\text{C}_\text{CM}$ ), 150.7 ( $\text{C}_\text{CM}$ ), 124.4 ( $\text{CH}_\text{CM}$ ), 108.8 ( $\text{CH}_\text{CM}$ ), 107.5 ( $\text{C}_\text{CM}$ ), 106.6 ( $\text{CH}_\text{CM}$ ), 98.7 ( $\text{CH}_\text{CM}$ ), 61.5 ( $\text{CH}_2$ ), 61.0 ( $\text{CH}_2$ ), 52.1 ( $\text{CH}_2$ ), 46.7 ( $\text{CH}_2$ ), 14.2 ( $\text{CH}_3$ ), 12.3 ( $\text{CH}_3$ ) ppm.

The analytical data were in accordance with previously reported data.<sup>155</sup>

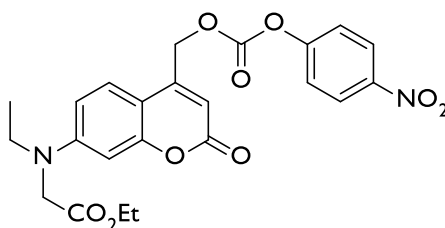
$^1\text{H}$  and  $^{13}\text{C}$  NMR spectra:







**Ethyl-*N*-ethyl-*N*-(4-(((4-nitrophenoxy)carbonyloxy)methyl)-2-oxo-2*H*-chromen-7-yl)glycinate: Coumarinyl linker (10)**



Ethyl *N*-ethyl-*N*-(4-(hydroxymethyl)-2-oxo-2*H*-chromen-7-yl)glycinate (0.30 g, 0.99 mmol, 1.0 eq) and 4-nitrophenyl chloroformate (297 mg, 1.47 mmol, 1.5 eq) were dissolved in dry DCM (7 mL) under argon atmosphere and dark conditions. DIPEA (0.60 mL, 3.96 mmol, 4.0 eq) was added and the reaction mixture was stirred at r.t for 24 h. The solvent was removed under reduced pressure and the crude was purified via column chromatography eluting with a mixture of EtOAc / PE (7:3 to 5:5). The product (241 mg, 0.52 mmol, 52% yield) was obtained as a yellow oil.

**<sup>1</sup>H NMR** (400 MHz, Chloroform-*d*): δ 8.31 (m, 2H, Ar-*H*), 7.42 (m, 2H, Ar-*H*), 7.35 (d, *J* = 9.0 Hz, 1H, coumarin-*H*), 6.60 (dd, *J* = 9.0, 2.6 Hz, 1H, coumarin-*H*), 6.52 (d, *J* = 2.6 Hz, 1H, coumarin-*H*), 6.29 (s, 1H, coumarin-*H*), 5.41 (s, 2H, CH<sub>2</sub> coumarin), 4.23 (q, *J* = 7.1 Hz, 2H, CH<sub>2</sub> ester), 4.10 (s, 2H, R<sub>2</sub>N-CH<sub>2</sub>-CO<sub>2</sub>Et), 3.54 (q, *J* = 7.1 Hz, 2H, R<sub>2</sub>N-CH<sub>2</sub>-CH<sub>3</sub>), 1.28 (m, 3H, CH<sub>3</sub> ester), 1.27 (m, 3H, R<sub>2</sub>N-CH<sub>2</sub>-CH<sub>3</sub>).

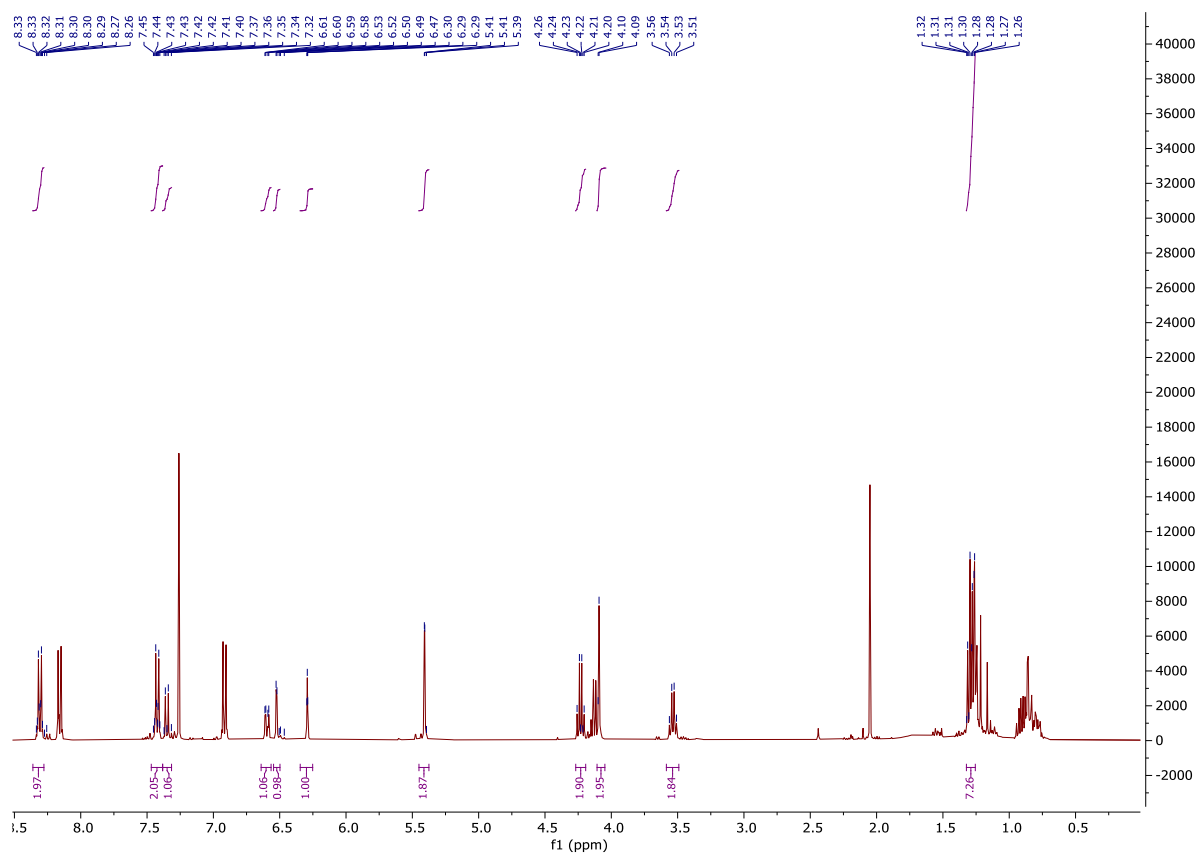
**<sup>13</sup>C NMR** (101 MHz, Chloroform-*d*): δ 170.0 (CO), 161.4 (C<sub>CM</sub>), 156.2 (C<sub>CM</sub>), 155.3 (C<sub>Ar</sub>), 152.3 (C<sub>CM</sub>), 151.3 (C<sub>CM</sub>), 147.7 (C<sub>Ar</sub>), 125.6 (CH<sub>Ar</sub>), 124.5 (CH<sub>CM</sub>), 121.9 (CH<sub>Ar</sub>), 109.2 (CH<sub>CM</sub>), 108.3 (CH<sub>CM</sub>), 107.0 (C<sub>CM</sub>), 99.0 (CH<sub>CM</sub>), 65.8 (CH<sub>2</sub>), 61.7 (CH<sub>2</sub>), 52.3 (CH<sub>2</sub>), 46.9 (CH<sub>2</sub>), 14.4 (CH<sub>3</sub>), 12.4 (CH<sub>3</sub>) ppm.

**HRMS (nanochip-ESI/LTQ-Orbitrap) m/z:**  $[M + Na]^+$  Calcd for  $C_{23}H_{22}N_2NaO_9^+$  493.1218; Found 493.1207.

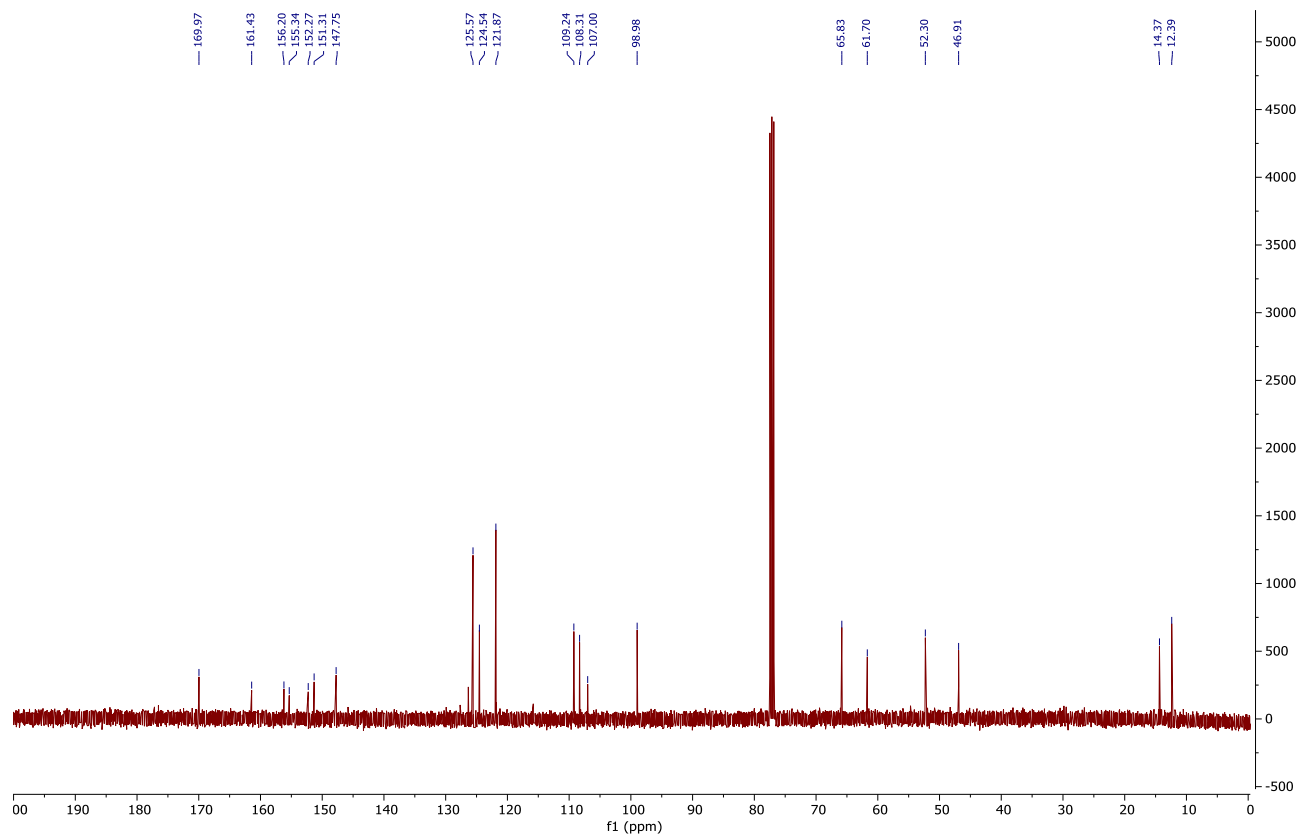
**IR (neat,  $cm^{-1}$ ):** 2960, 1730, 1610, 1520, 1410, 1280, 1185, 1165, 1065, 860.

The analytical data were in accordance with previously reported data.<sup>155</sup>

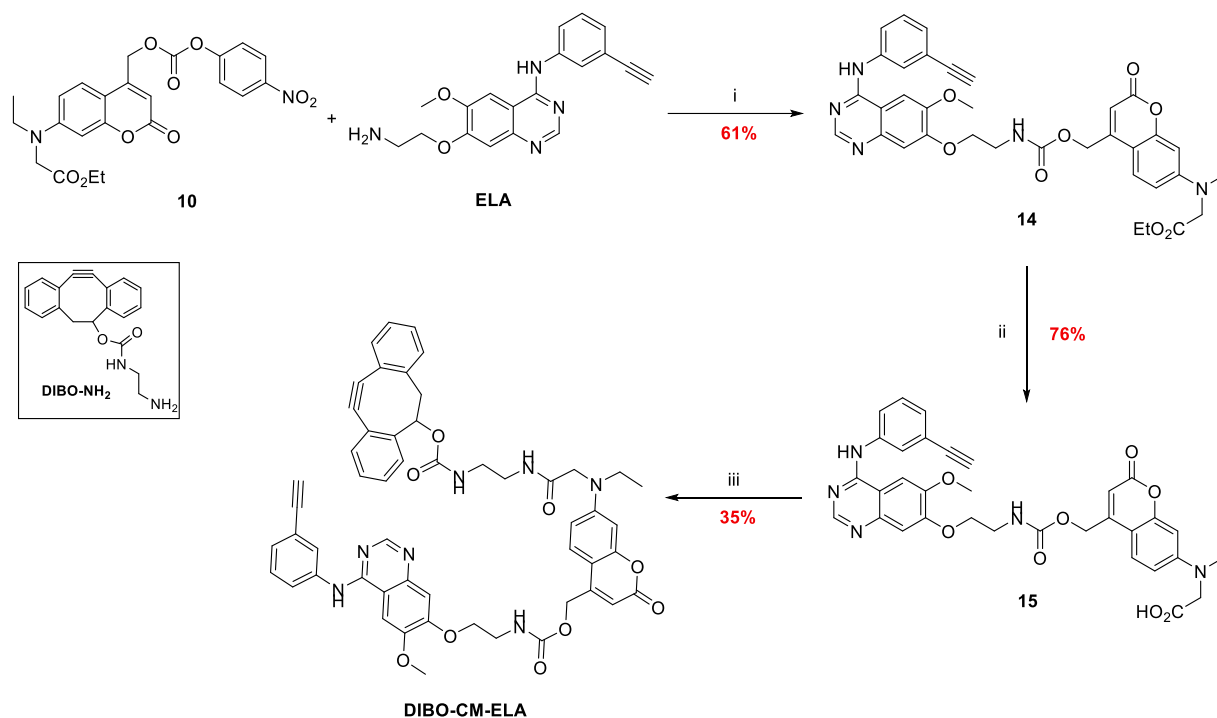
$^1H$  and  $^{13}C$  NMR spectra:



# Experimental

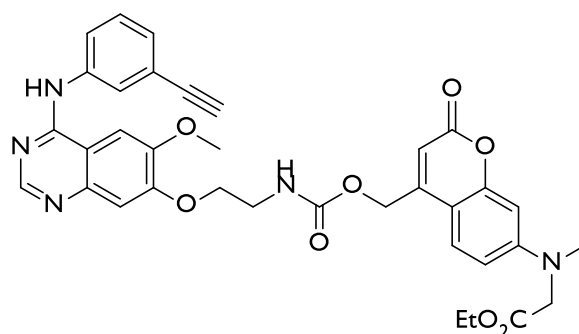


### 5.4. Synthesis of erlotinib delivery system



**Scheme 22: Synthesis of DIBO-CM-erlo.** i- DIPEA, DMF, r.t, 16 h; ii- LiOH, MeOH / H<sub>2</sub>O (5:1), r.t., 6 h; iii- *DIBO-NH<sub>2</sub>*, HOBT, DMAP, EDCI, DIPEA, DMF, r.t, 24 h.

#### Ethyl-*N*-ethyl-*N*-(4-(((2-((4-((3-ethynylphenyl)amino)-6-methoxyquinazolin-7-yl)oxy)ethyl)carbamoyl)oxy)methyl)-2-oxo-2*H*-chromen-7-yl)glycinate (**14**)



The coumarinyl linker (100.0 mg, 0.21 mmol, 1.0 eq) and **ELA** (71.2 mg, 0.21 mmol, 1.0 eq) were dissolved in dry DMF (10 mL). DIPEA (0.15 mL, 0.85 mmol, 4.0 eq) was added and the reaction mixture was stirred at r.t for 16 h under argon atmosphere and dark conditions. The solvent was removed under reduced pressure and the crude was purified via FC eluting with a mixture of PE / EtOAc (5:5 to 0:1) to afford the product (86 mg, 0.13 mmol, 61% yield) as a yellow solid.

<sup>1</sup>H NMR (400 MHz, DMSO-*d*<sub>6</sub>): δ 9.51 (s, 1H, *NH*<sub>erlotinib</sub>), 8.50 (s, 1H, *CH*<sub>Ar</sub>), 7.99 (t, *J* = 1.9 Hz, 1H, *CH*<sub>Ar</sub>), 7.90 (m, 2H, *CH*<sub>Ar</sub>), 7.81 (t, *J* = 5.6 Hz, 1H, *NH*<sub>carbamate</sub>), 7.48 (d, *J* = 9.0 Hz, 1H, coumarin-*H*), 7.41 (t, *J* = 7.8 Hz, 1H, *CH*<sub>Ar</sub>), 7.22 (m, 2H, *CH*<sub>Ar</sub>), 6.64 (dd, *J* = 9.1, 2.6 Hz, 1H, coumarin-*H*), 6.53 (d, *J* = 2.5 Hz, 1H, coumarin-*H*), 6.05 (s, 1H, coumarin-*H*), 5.25 (s, 2H, *CH*<sub>2</sub><sub>coumarin</sub>), 4.28 (s, 2H, *R*<sub>2</sub>*N-CH*<sub>2</sub>-*CO*<sub>2</sub>Et), 4.23 (t, *J* =

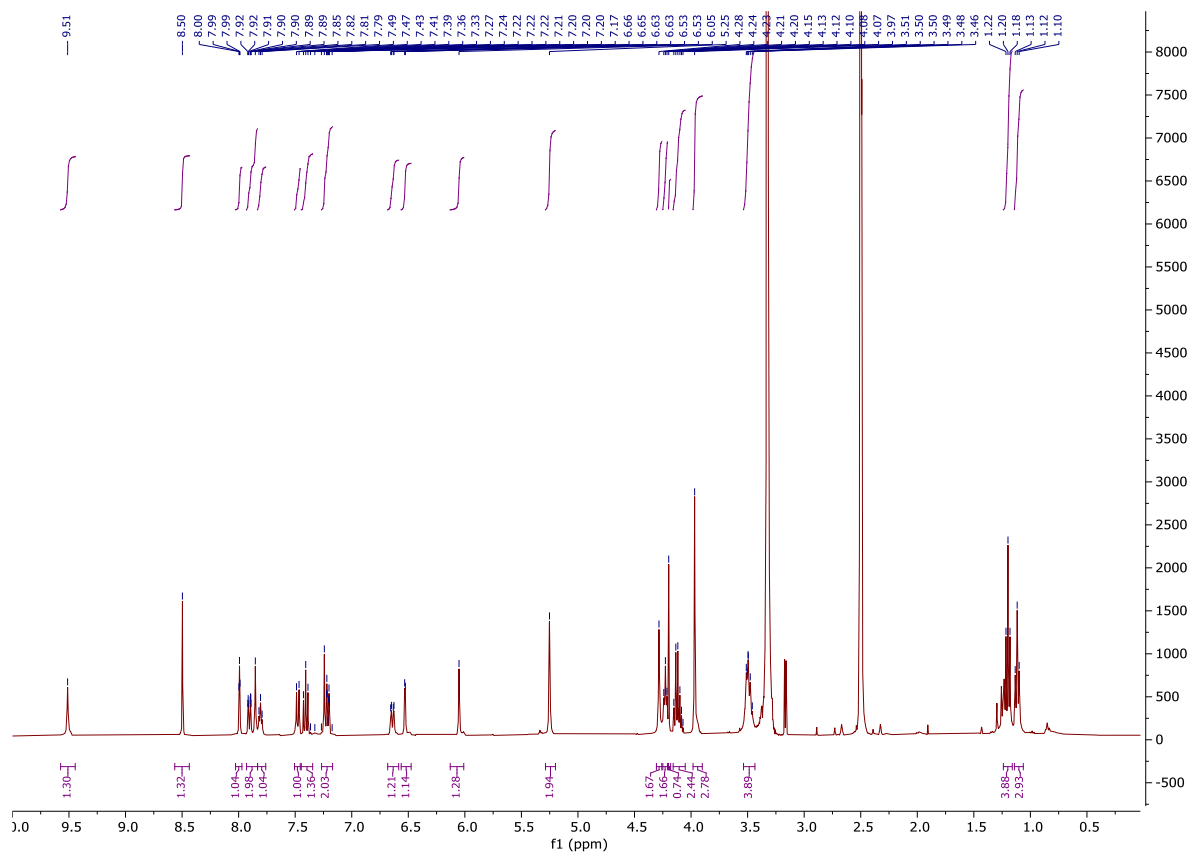
5.5 Hz, 2H,  $\text{RCO}_2\text{NH-CH}_2\text{-CH}_2\text{-OAr}$ ), 4.20 (s, 1H,  $\text{HC}\equiv\text{C-Ar}$ ), 4.13 (m, 2H,  $\text{CH}_2$  ester), 3.97 (s, 3H,  $\text{CH}_3\text{-OAr}$ ), 3.49 (m, 4H,  $\text{RRN-CH}_2\text{-CH}_3$  and  $\text{RCO}_2\text{NH-CH}_2\text{-CH}_2\text{-OAr}$ ), 1.20 (t,  $J = 7.1$  Hz, 3H,  $\text{R}_2\text{N-CH}_2\text{-CH}_3$ ), 1.12 (t,  $J = 7.0$  Hz, 3H,  $\text{CH}_3$  ester).

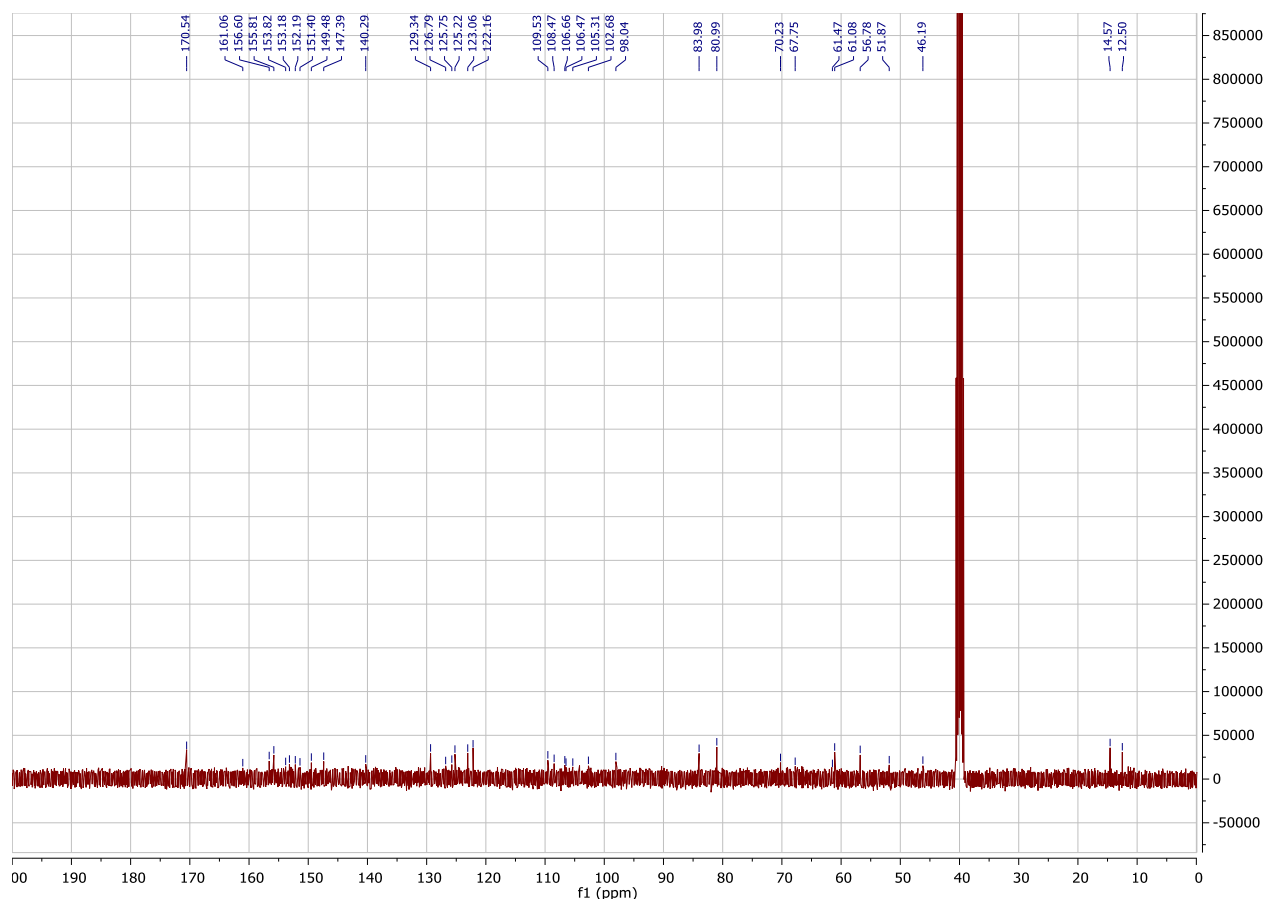
$^{13}\text{C NMR}$  (101 MHz,  $\text{DMSO-}d_6$ ):  $\delta$  170.5 ( $\text{CO}_2\text{Et}$ ), 161.1 ( $\text{CO}_{\text{CM}}$ ), 156.6 ( $\text{C}_{\text{ELA}}$ ), 155.8 ( $\text{C}_{\text{CM}}$ ), 153.8 ( $\text{C}_{\text{erlo}}$ ), 153.2 ( $\text{CH}_{\text{ELA}}$ ), 152.2 ( $\text{CO}_{\text{carbamate}}$ ), 151.4 ( $\text{C}_{\text{CM}}$ ), 149.5 ( $\text{C}_{\text{ELA}}$ ), 147.4 ( $\text{C}_{\text{ELA}}$ ), 140.3 ( $\text{C}_{\text{ELA}}$ ), 129.3 ( $\text{CH}_{\text{ELA}}$ ), 126.8 ( $\text{CH}_{\text{ELA}}$ ), 125.7 ( $\text{CH}_{\text{CM}}$ ), 125.2 ( $\text{CH}_{\text{ELA}}$ ), 123.1 ( $\text{CH}_{\text{ELA}}$ ), 122.2, 109.5 ( $\text{CH}_{\text{CM}}$ ), 108.5 ( $\text{CH}_{\text{ELA}}$ ), 106.7 ( $\text{CH}_{\text{CM}}$ ), 106.5 ( $\text{C}_{\text{CM}}$ ), 105.3 ( $\text{C}_{\text{ELA}}$ ), 102.7 ( $\text{CH}_{\text{ELA}}$ ), 98.0 ( $\text{CH}_{\text{CM}}$ ), 84.0 ( $\text{C}_{\text{alkyne}}$ ), 81.0 ( $\text{CH}_{\text{alkyne}}$ ), 67.6 ( $\text{CH}_2$  ELA), 61.5 ( $\text{CH}_2$  CM), 61.1 ( $\text{CH}_2$  CM), 56.8 ( $\text{CH}_3$  ELA), 51.9 ( $\text{CH}_2$  CM), 46.2 ( $\text{CH}_2$  CM), 40.2 ( $\text{CH}_2$  ELA), 14.6 ( $\text{CH}_3$  CM), 12.5 ( $\text{CH}_3$  CM). Two carbons are not resolved.

**IR (neat,  $\text{cm}^{-1}$ ):** 3345, 1960, 1620, 1700, 1155, 835, 770, 715.

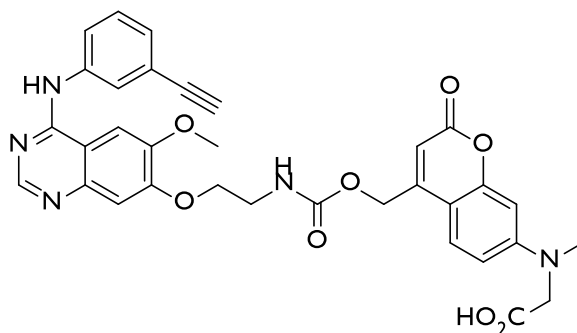
The analytical data were in accordance with previously reported data.<sup>155</sup>

$^1\text{H}$  and  $^{13}\text{C}$  NMR spectra:





***N*-Ethyl-*N*-(4-(((2-((4-((3-ethynylphenyl)amino)-6-methoxyquinazolin-7-yl)oxy)ethyl)carbamoyl)oxy)methyl)-2-oxo-2*H*-chromen-7-yl)glycine (15)**

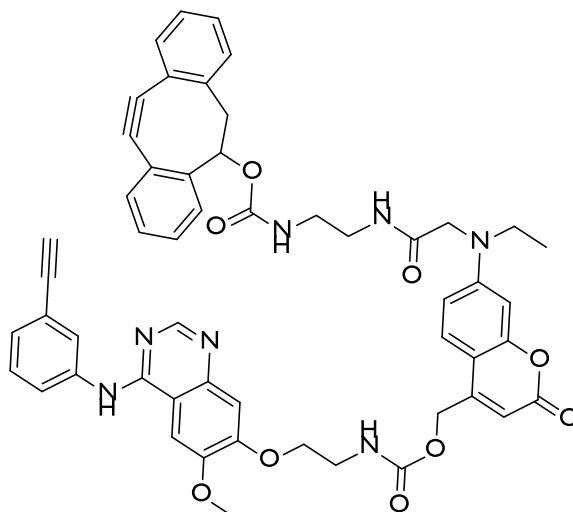


Ethyl-*N*-ethyl-*N*-(4-(((2-((4-((3-ethynylphenyl)amino)-6-methoxyquinazolin-7-yl)oxy)ethyl)carbamoyl)oxy)methyl)-2-oxo-2*H*-chromen-7-yl)glycinate (1409 mg, 0.21 mmol, 1.0 eq) was dissolved in a mixture of LiOH (100 mg, 4.2 mmol, 20.0 eq) in MeOH / H<sub>2</sub>O / DMF (8 mL, 5:1:1) and the reaction mixture was stirred at r.t. for 6 h under dark conditions. The solvent was removed and the reaction mixture was diluted with H<sub>2</sub>O (50 mL) and 1M hydrochloric acid (8 mL). The aqueous layer was extracted with EtOAc (3 X 60 mL) and the combined organic layers were dried over MgSO<sub>4</sub>, filtered and concentrated under reduced pressure. The residue was purified via FC eluting with a mixture of DCM / MeOH (9:1). The product (102 mg, 0.16 mmol, 89% yield) was obtained as a light yellow solid.

**HRMS (ESI/QTOF) m/z:** [M + H]<sup>+</sup> Calcd for C<sub>34</sub>H<sub>32</sub>N<sub>5</sub>O<sub>8</sub><sup>+</sup> 638.2245; Found 638.2252.

The analytical data were in accordance with previously reported data.<sup>155</sup>

### DIBO-CM-ELA



*N*-Ethyl-*N*-(4-(((2-(((4-((3-ethynylphenyl)amino)-6-methoxyquinazolin-7-yl)oxy)ethyl)carbamoyl)oxy)methyl)-2-oxo-2*H*-chromen-7-yl)glycine (25.0 mg, 39.2  $\mu$ mol, 1.0 eq), DIBO-NH<sub>2</sub> (13.2 mg, 43.1  $\mu$ mol, 1.1 eq), DMAP (2.4 mg, 19.6  $\mu$ mol, 0.5 eq), HOBT (21.2 mg, 0.16 mmol, 4.0 eq), and EDCI (30.1 mg, 0.16 mmol, 4.0 eq) were dissolved in dry DMF (2.5 mL). DIPEA (27  $\mu$ L, 0.16 mmol, 4.0 eq) was added and the reaction mixture was stirred at r.t. for 24 h under argon atmosphere and dark conditions. The solvent was removed under reduced pressure and the crude was purified by preparative TLC eluting with a mixture of DCM / MeOH (18:1). The product (12.9 mg, 13.8  $\mu$ mol, 35% yield) was obtained as yellowish solid.

<sup>1</sup>H NMR (400 MHz, DMSO-*d*<sub>6</sub>):  $\delta$  9.54 (s, 1H, NH<sub>erlotinib</sub>), 9.45 (d, *J* = 7.9 Hz, 1H, NH<sub>amide</sub>), 8.50 (d, *J* = 5.4 Hz, 1H, CH<sub>Ar</sub>(2)), 7.99 (d, *J* = 12.5 Hz, 1H, CH<sub>Ar</sub>(2')), 7.94 – 7.86 (m, 2H, CH<sub>Ar</sub>(5) and CH<sub>Ar</sub>(6')), 7.81 (d, *J* = 8.4 Hz, 1H, CH<sub>Ar-cyclooctyne</sub>), 7.60 (dt, *J* = 11.5, 5.7 Hz, 1H, NH<sub>carbamate</sub>), 7.56 – 7.49 (m, 1H, coumarin-*H* and CH<sub>Ar-cyclooctyne</sub>), 7.47 – 7.27 (m, 7H, CH<sub>Ar</sub>(5') and 6 X CH<sub>Ar-cyclooctyne</sub>), 7.26 – 7.18 (m, 2H, CH<sub>Ar</sub>(4') and CH<sub>Ar</sub>(8)), 6.56 (dd, *J* = 21.0, 8.6 Hz, 1H, coumarin-*H*), 6.51 – 6.40 (m, 1H, coumarin-*H*), 6.04 (d, *J* = 3.1 Hz, 1H, coumarin-*H*), 5.27 (m, 2H, NH<sub>carbamate</sub> and CH<sub>DIBO</sub>), 5.23 (s, 2H, CH<sub>2</sub> coumarin), 4.39 (t, *J* = 5.6 Hz, 1H, RCO<sub>2</sub>NH-CH<sub>2</sub>-CH<sub>2</sub>-OAr), 4.23 (t, *J* = 5.9 Hz, 1H, RCO<sub>2</sub>NH-CH<sub>2</sub>-CH<sub>2</sub>-OAr), 4.20 (d, *J* = 5.1 Hz, 1H, CH<sub>alkyne</sub>), 3.97 (s, 3H, CH<sub>3</sub>-O), 3.96 – 3.84 (m, 4H, R<sub>2</sub>N-CH<sub>2</sub>-CONHR and RCO<sub>2</sub>NH-CH<sub>2</sub>-CH<sub>2</sub>-OAr), 3.58 – 3.47 (m, 2H, R<sub>2</sub>N-CH<sub>2</sub>-CH<sub>3</sub>), 3.17 (q, *J* = 6.3, 5.6 Hz, 3H, RCONH-CH<sub>2</sub>-CH<sub>2</sub>-NHCO<sub>2</sub>R and H-CH<sub>DIBO</sub>), 3.06 (q, *J* = 7.6, 6.8 Hz, 2H, RCONH-CH<sub>2</sub>-CH<sub>2</sub>-NHCO<sub>2</sub>R), 2.75 (dd, *J* = 15.0, 4.4 Hz, 1H, H-CH<sub>DIBO</sub>), 1.06 (t, *J* = 7.0 Hz, 1H, R<sub>2</sub>N-CH<sub>2</sub>-CH<sub>3</sub>).

<sup>13</sup>C NMR (101 MHz, DMSO-*d*<sub>6</sub>):  $\delta$  171.2 (CO<sub>amide</sub>), 169.4 (CO<sub>amide</sub>), 159.8 (CO<sub>CM</sub>), 156.6 (C<sub>ELA</sub>), 155.8 (C<sub>CM</sub>), 155.8 (C<sub>ELA</sub>), 155.8, 153.2 (C<sub>ELA</sub>), 152.1 (CH<sub>ELA</sub>), 151.3 (C<sub>CM</sub>), 149.5 (C<sub>DIBO</sub>), 142.8 (C<sub>ELA</sub>), 146.1 (C<sub>ELA</sub>), 140.3 (C<sub>ELA</sub>), 129.3 (CH<sub>ELA</sub>), 128.9 (CH<sub>DIBO</sub>), 127.8 (CH<sub>DIBO</sub>), 127.8 (CH<sub>DIBO</sub>), 126.5 (CH<sub>ELA</sub>), 126.2 (CH<sub>DIBO</sub>), 125.2 (CH<sub>ELA</sub>), 124.3 (CH<sub>CM</sub>), 123.9 (CH<sub>DIBO</sub>), 123.4 (C<sub>DIBO</sub>), 123.0 (CH<sub>ELA</sub>), 122.2 (CH<sub>DIBO</sub>), 120.8 (C<sub>DIBO</sub>), 119.0 (C<sub>DIBO</sub>), 113.0 (CH<sub>DIBO</sub>), 109.5 (CH<sub>CM</sub>), 108.5 (CH<sub>ELA</sub>), 107.1 (C<sub>CM</sub>), 105.6 (CH<sub>CM</sub>), 102.6 (CH<sub>ELA</sub>), 98.0 (CH<sub>CM</sub>), 92.0 (C<sub>DIBO</sub>), 84.0 (C<sub>ELA</sub>), 81.0 (CH<sub>alkyne</sub>), 75.9 (CH<sub>DIBO</sub>), 68.8 (CH<sub>2</sub>

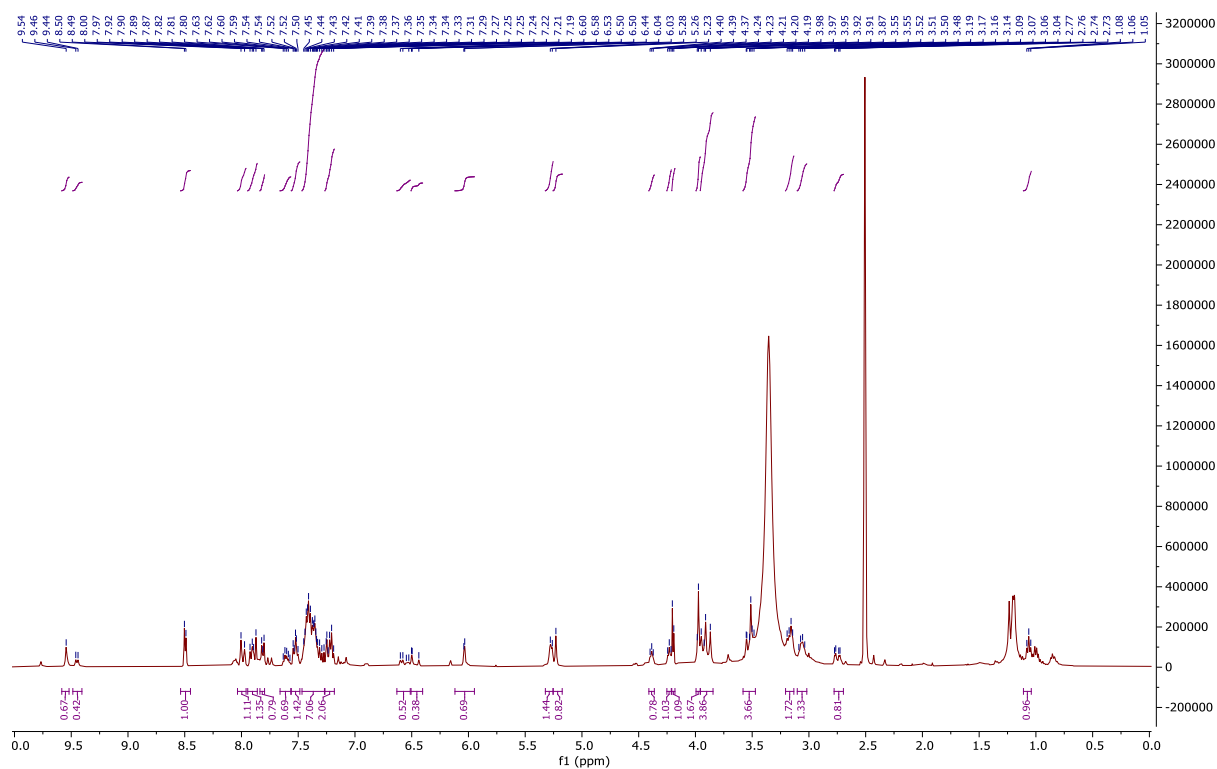
ELA), 61.9 (CH<sub>2</sub>CM), 56.6 (CH<sub>3</sub> ELA), 53.5 (CH<sub>2</sub> CM), 46.1 (CH<sub>2</sub> CM), 45.9 (CH<sub>2</sub> DIBO), 40.9 (CH<sub>2</sub> ELA), 40.7 (CH<sub>2</sub> DIBO), 39.1 (CH<sub>2</sub> DIBO), 12.1 (CH<sub>3</sub> CM). Five carbons were not resolved.

**HRMS (ESI/QTOF):** *m/z* calcd for C<sub>34</sub>H<sub>32</sub>N<sub>5</sub>O<sub>8</sub><sup>+</sup> ([M + H]<sup>+</sup>): 926.3508; Found 926.3509.

**IR (neat, cm<sup>-1</sup>):** 2955, 2920, 1705, 1655, 1620, 1575, 1530, 1425, 1260, 1085, 1020, 795, 770.

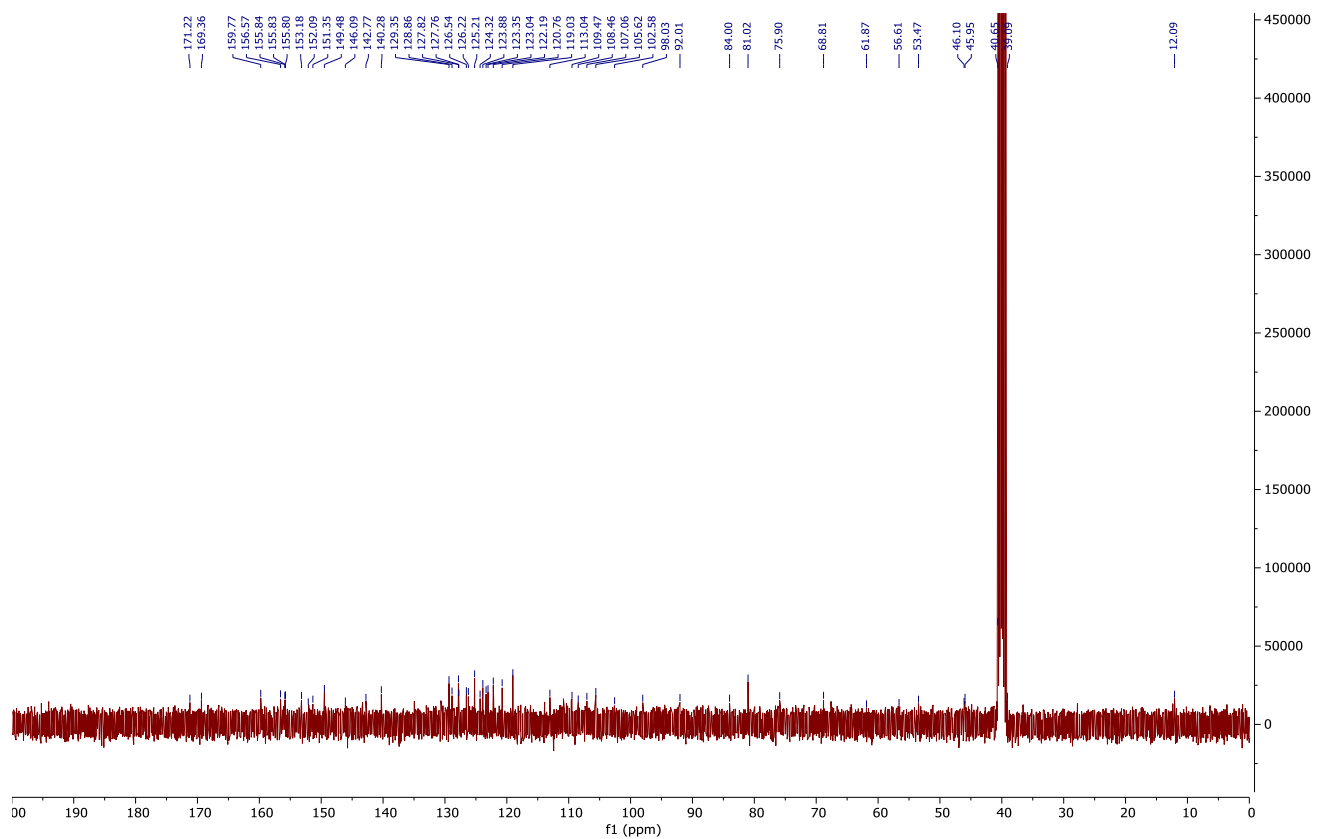
The analytical data were in accordance with previously reported data.<sup>155</sup>

<sup>1</sup>H and <sup>13</sup>C NMR spectra:

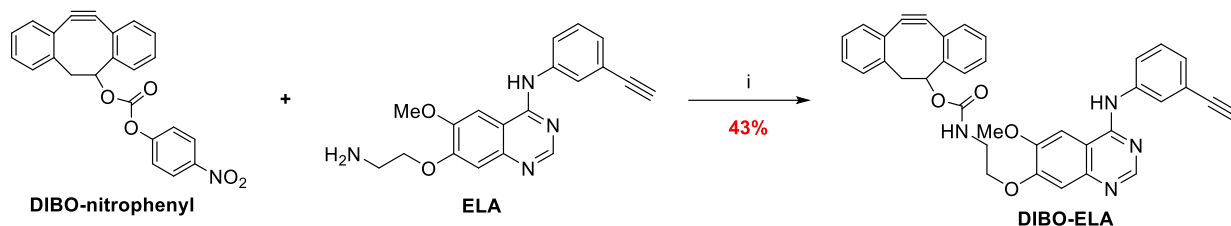




# Experimental



### 5.5. Synthesis of DIBO-ELA control



**Scheme 23: Synthesis of DIBO-ELA.** i- DIPEA, DMF, r.t, 16 h.

**ELA** (25 mg, 0.05 mmol, 1.0 eq) and **DIBO-nitrophenyl** (20 mg, 0.05 mmol, 1.0 eq) were dissolved in dry DMF (2 mL). DIPEA (44  $\mu$ L, 0.25 mmol, 5 eq) was added and the reaction mixture was stirred at r.t. for 16h under argon. The solvent was removed under reduced pressure and the crude was purified by FC eluting with DCM / MeOH (30:1) to afford the **DIBO-ELA** as a white solid (13 mg, 0.022 mmol, 43%).

**$^1\text{H NMR}$**  (400 Hz, Chloroform- $d$ ):  $\delta$  8.50 (s, 1H,  $\text{H}_{\text{Ar, ELA}}$ ), 7.89 (d,  $J = 6.4$  Hz, 1H,  $\text{H}_{\text{Ar, ELA}}$ ), 7.80 (d,  $J = 7.4$  Hz, 1H,  $\text{NH}_{\text{ELA}}$ ), 7.48 (d,  $J = 7.3$  Hz, 1H,  $\text{H}_{\text{Ar, DIBO}}$ ), 7.41 – 7.19 (m, 11H, 7x  $\text{H}_{\text{Ar, DIBO}}$ , 4 x  $\text{H}_{\text{Ar, ELA}}$ ), 5.65 (t,  $J = 6.0$  Hz, 1H,  $\text{H}_{\text{Ar, ELA}}$ ), 5.51 (s, 1H,  $\text{NH}_{\text{carbamate}}$ ), 4.22 – 4.09 (m, 2H,  $\text{CH}_2$ ), 4.02 (s, 3H,  $\text{CH}_3$ ), 3.93 (s, 1H,  $\text{CH}_{\text{DIBO}}$ ), 3.69 (d,  $J = 5.7$  Hz, 2H,  $\text{CH}_2$ ), 3.17 (d,  $J = 14.9$  Hz, 1H,  $\text{CH}_{\text{DIBO}}$ ), 2.98 – 2.82 (m, 1H,  $\text{CH}_{\text{DIBO}}$ ).

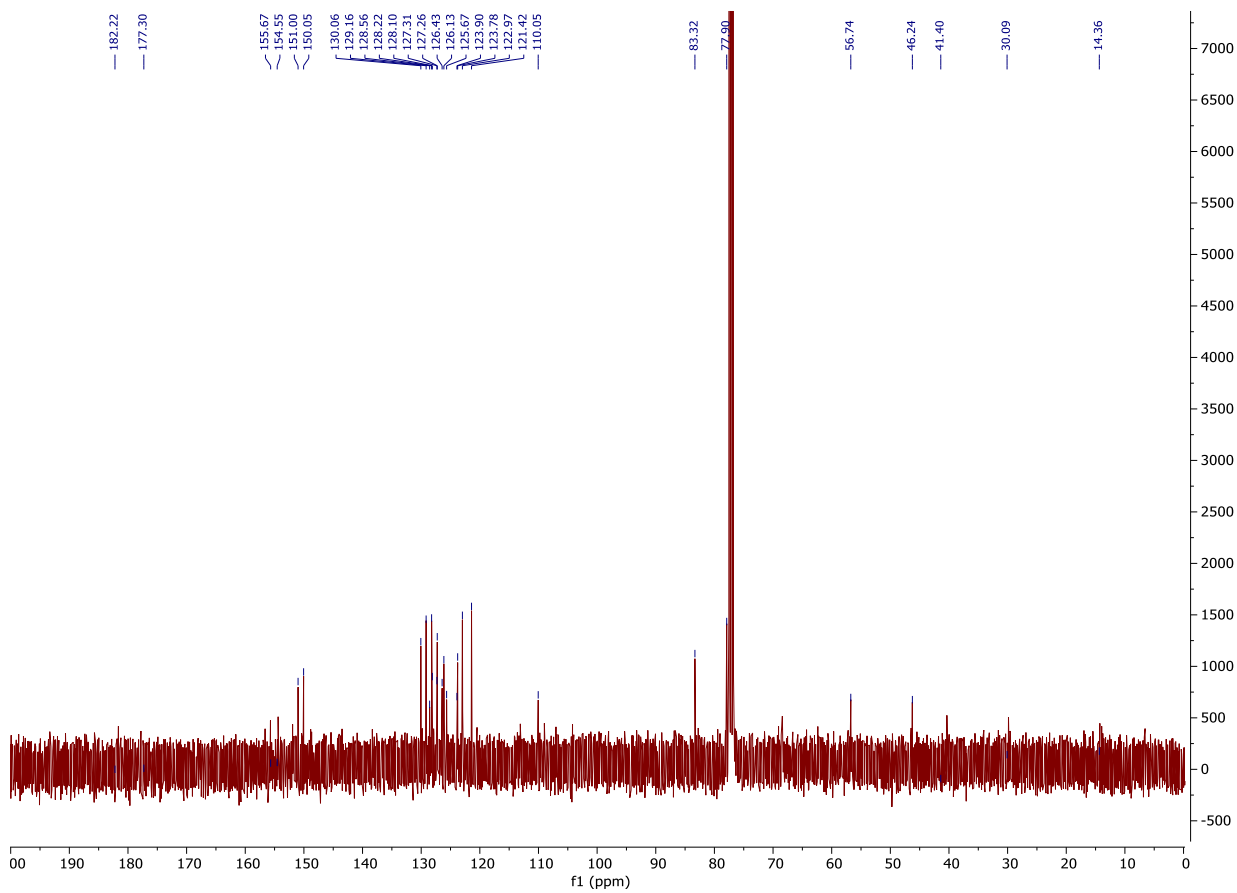
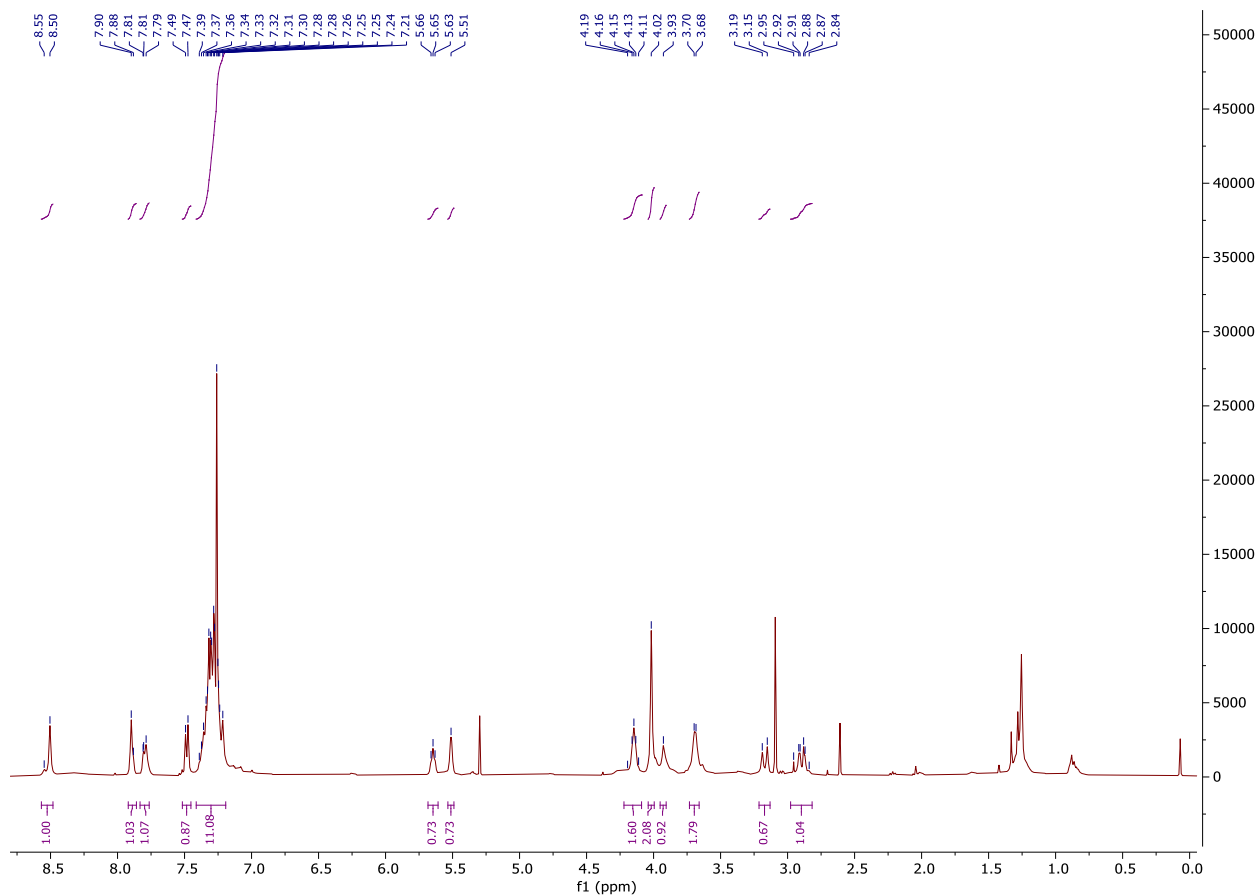
**$^{13}\text{C NMR}$**  (101 Hz, Chloroform- $d$ ): 182.2 ( $\text{C}_{\text{Ar}}$ ), 177.3 ( $\text{C}_{\text{Ar}}$ ), 155.7 ( $\text{C}_{\text{carbamate}}$ ), 154.6 ( $\text{C}_{\text{Ar}}$ ), 151.0 ( $\text{C}_{\text{Ar}}$ ), 150.1 ( $\text{C}_{\text{Ar}}$ ), 130.1 ( $\text{C}_{\text{Ar}}$ ), 129.2 ( $\text{C}_{\text{Ar}}$ ), 128.6 ( $\text{CH}_{\text{Ar}}$ ), 128.2 ( $\text{CH}_{\text{Ar}}$ ), 128.1 ( $\text{CH}_{\text{Ar}}$ ), 127.3 ( $\text{CH}_{\text{Ar}}$ ), 127.2 ( $\text{CH}_{\text{Ar}}$ ), 126.4 ( $\text{CH}_{\text{Ar}}$ ), 126.1 ( $\text{CH}_{\text{Ar}}$ ), 125.7 ( $\text{CH}_{\text{Ar}}$ ), 123.9 ( $\text{C}_{\text{Ar}}$ ), 123.8 ( $\text{C}_{\text{Ar}}$ ), 123.0 ( $\text{C}_{\text{Ar}}$ ), 121.4 ( $\text{C}_{\text{Ar}}$ ), 110.1 ( $\text{C}_{\text{Ar}}$ ), 83.3 ( $\text{C}_{\text{alkyne}}$ ), 77.9 ( $\text{CH}_{\text{alkyne}}$ ), 56.7 ( $\text{CH}_3$ ), 46.2 ( $\text{CH}_2$ ), 41.4 ( $\text{CH}_2$ ), 30.1 ( $\text{CH}_2$ ), 14.4 ( $\text{CH}_2$ ).

**HRMS** (nanochip-ESI/LTQ-Orbitrap)  $m/z$ :  $[\text{M} + \text{H}]^+$  Calcd for  $\text{C}_{36}\text{H}_{29}\text{N}_4\text{O}_4$  581.2183; Found 581.2189.

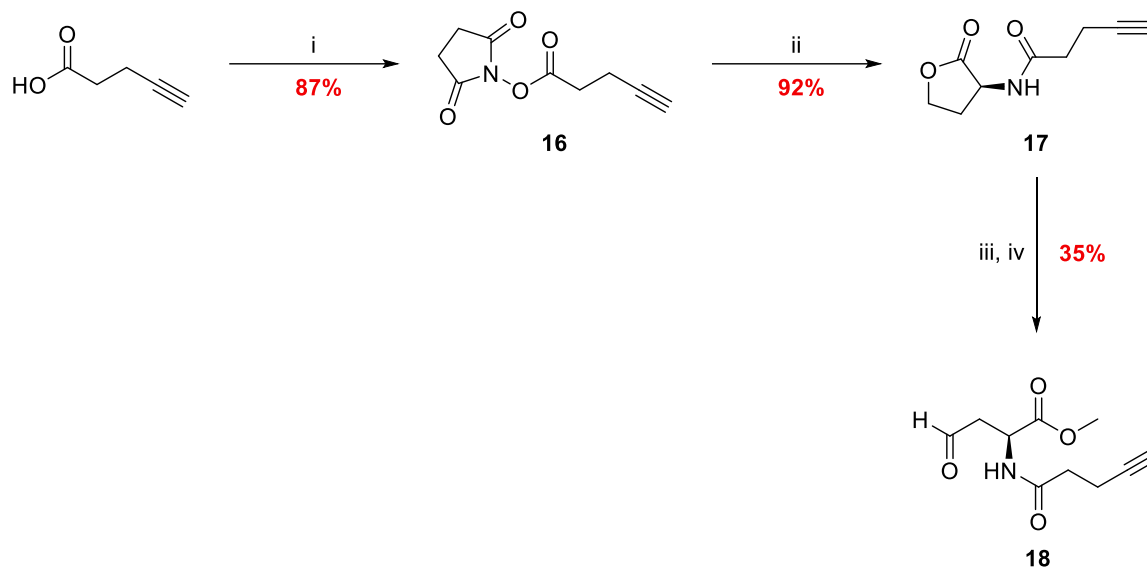
**IR** (neat,  $\text{cm}^{-1}$ ): 2954, 2925, 2854, 1718, 1633, 1569, 1511, 1450, 1279, 1158, 1075, 760.

$^1\text{H}$  and  $^{13}\text{C}$  NMR spectra:

# Experimental

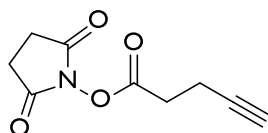


## 5.6. Synthesis of L-homoserine derivative



**Scheme 24: Synthesis of L-homoserine derivative.** i- NHS, DCC, THF, r.t, 2 h; ii- (S)-(-)- $\alpha$ -amino- $\gamma$ -butyrolactone hydrobromide, Et<sub>3</sub>N, DCM, r.t, 2 h; iii- H<sub>2</sub>SO<sub>4</sub>, MeOH, r.t, 24 h; iv- (COCl)<sub>2</sub>, DMSO, Et<sub>3</sub>N, DCM 0 °C, 2 h.

### 2,5-dioxopyrrolidin-1-yl pent-4-ynoate (16)

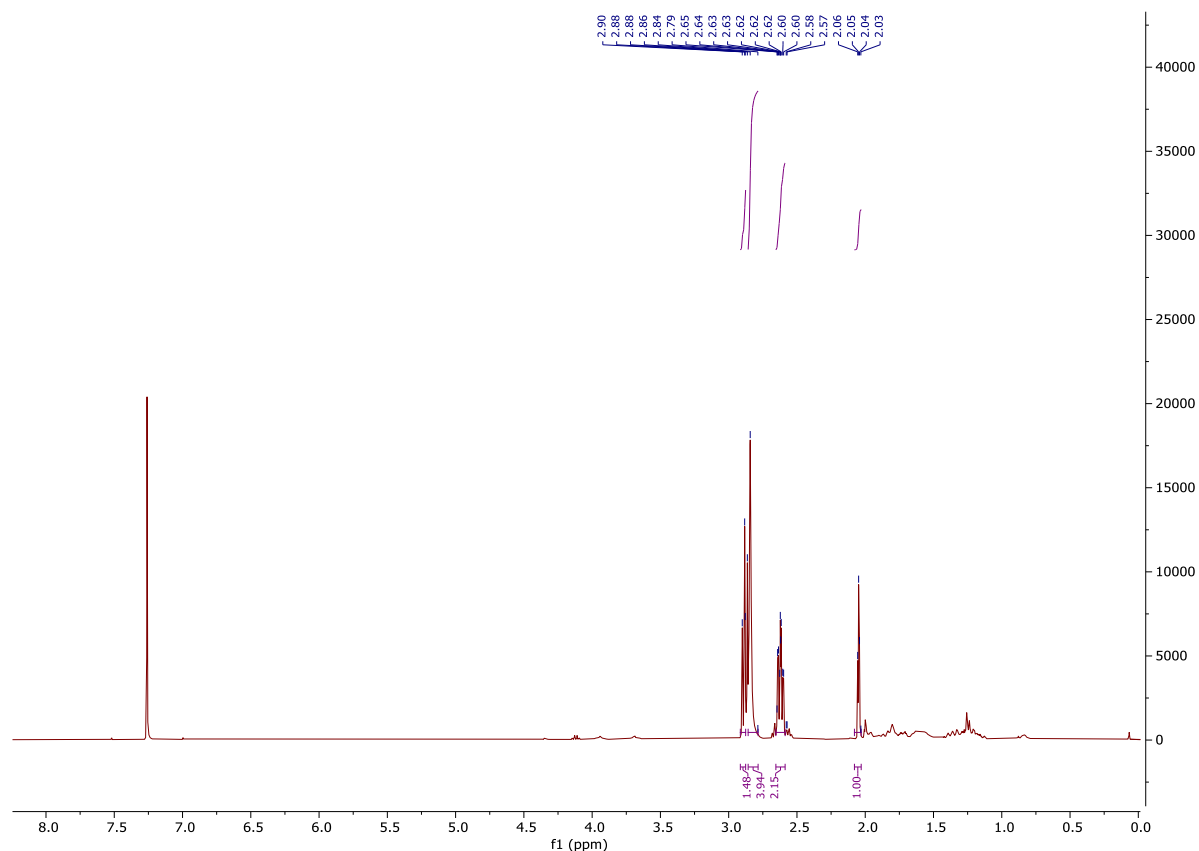


A solution of pent-4-ynoic acid (3.0 g, 30.58 mmol, 1.0 eq) and *N*-hydroxysuccinimide (3.52 g, 30.58 mmol, 1.0 eq) in dry THF (100 mL) was cooled to 0 °C. DCC (6.31 g, 30.58 mmol, 1.0 eq) in dry THF (35 mL) was added dropwise and the mixture was stirred at 0 °C for 45 min. The mixture was warmed up to rt and stirred for 2 h. The mixture was filter and concentrated under reduce pressure. The residue was dissolved in EtOAc (100 mL) and filtered. The organic layer was washed with sat. solution of NaHCO<sub>3</sub> in water (100 mL) and brine (100 mL), dried over MgSO<sub>4</sub>, filtered and concentrated under reduced pressure to afford the product as a white solid (5.20 g, 26.6 mmol, 87%).

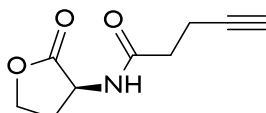
<sup>1</sup>H NMR (400 MHz, Chloroform-d):  $\delta$  2.93 – 2.84 (m, 2H), 2.84 (s, 4H), 2.62 (m, 2H), 2.05 (t, *J* = 2.6 Hz, 1H).

The analytical data were in accordance with previously reported data.<sup>154</sup>

$^1\text{H}$  NMR spectrum:



**(S)-N-(2-oxotetrahydrofuran-3-yl)pent-4-ynamide (17)**

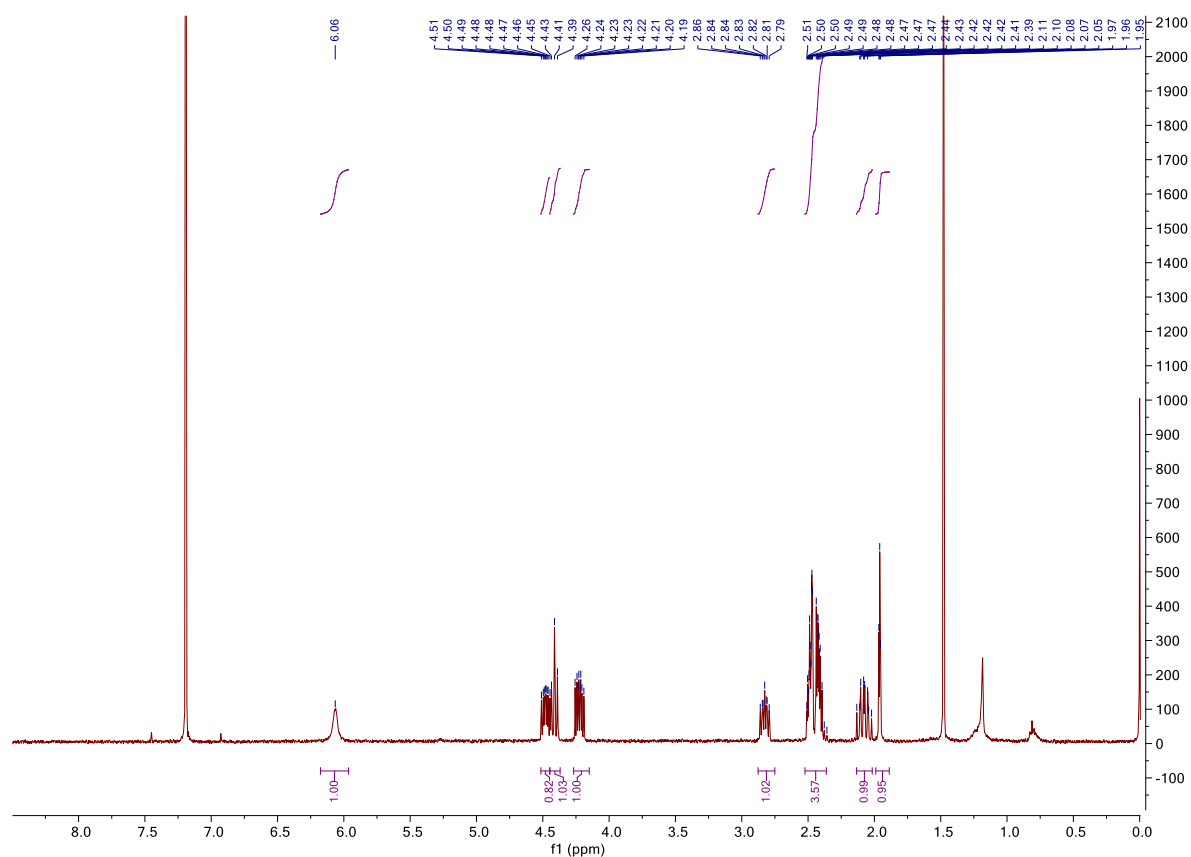


To a solution of (*S*)-(-)- $\alpha$ -amino- $\gamma$ -butyrolactone hydrobromide (3.04 g, 16.72 mmol, 1.1 equiv) and  $\text{Et}_3\text{N}$  (6.3 mL, 45.6 mmol, 3 equiv) in dry DCM (130 mL) 2,5-dioxopyrrolidin-1-yl pent-4-ynoate (3.0 g, 15.2 mmol, 1.0 equiv) was added portion wise and the mixture was stirred at r.t. for 2 h. The mixture was washed with sat. solution of  $\text{NH}_4\text{Cl}$  in water (100 mL) and the aqueous layer was extracted with DCM (8 X 100 mL). The combine organic layers were dried over  $\text{MgSO}_4$ , filtered and concentrated under reduced pressure. The crude was purified by FC eluting with PE/EtOAc (1:3) to afford the product as a white solid (2.56 g, 14.0 mmol 92%).

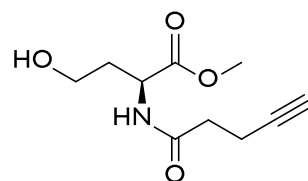
The analytical data were in accordance with previously reported data.<sup>154</sup>

$^1\text{H}$  NMR (400 MHz, Chloroform- $d$ ):  $\delta$  6.06 (s, 1H), 4.48 (m, 1H), 4.41 (m, 1H), 4.22 (ddd,  $J = 11.4, 9.3, 5.8$  Hz, 1H), 2.83 (m, 1H), 2.45 (m, 4H), 2.08 (qd,  $J = 11.8, 8.8$  Hz, 1H), 1.96 (t,  $J = 2.5$  Hz, 1H).

$^1\text{H}$  NMR spectrum:

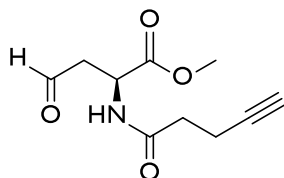


### Methyl pent-4-ynoate-*L*-homoserinate



To a solution of (*S*)-*N*-(2-oxotetrahydrofuran-3-yl)pent-4-ynamide (500 mg, 2.76 mmol, 1.0 eq) in MeOH (3 mL) conc.  $\text{H}_2\text{SO}_4$  (cat., 5 drops) was added and the mixture was stirred at r.t. for 24 h. The mixture was cooled down to 0 °C and the reaction was neutralized by addition of  $\text{NaHCO}_3$ . The mixture was filtered and concentrated under reduced pressure at 25 °C. The crude product was used without further treatment in the next step.

### Methyl (*S*)-4-oxo-2-(pent-4-ynamido)butanoate: *L*-homoserine derivative (18)

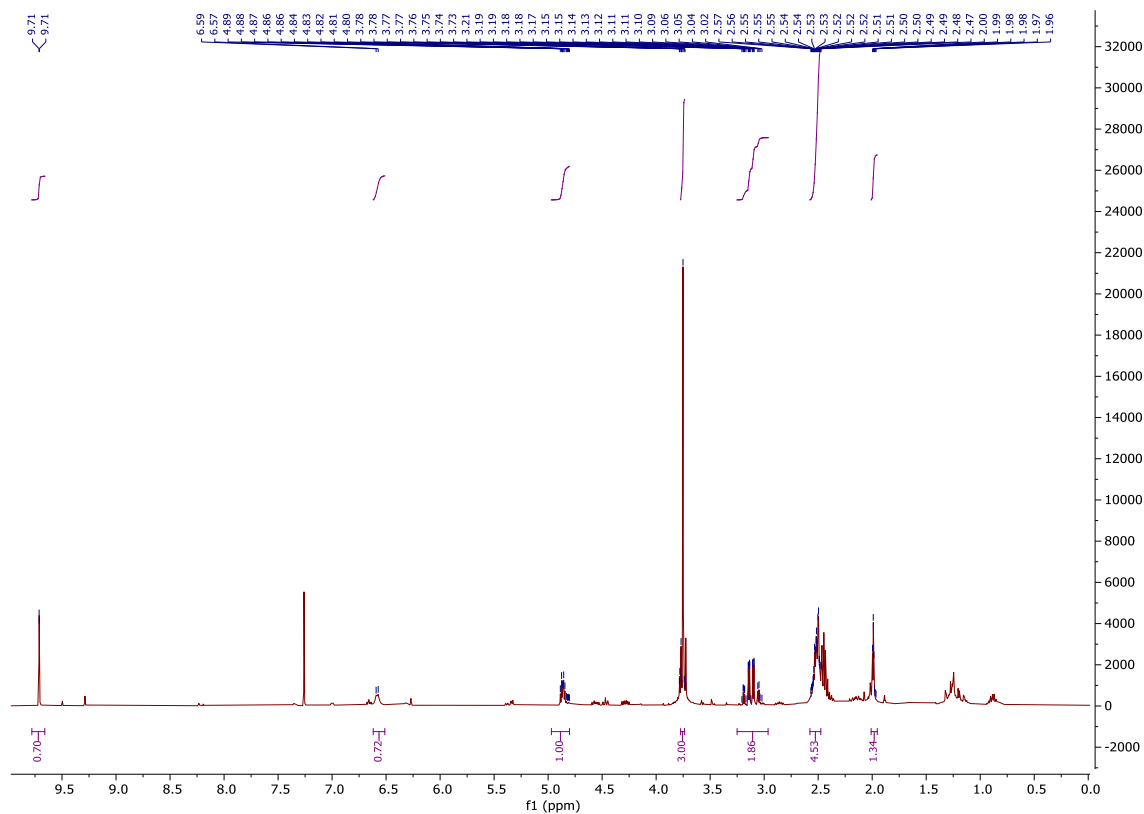


A solution of  $(\text{COCl})_2$  (0.48 mL, 5.52 mmol, 2.0 eq) in dry DCM (16 mL) was cooled to  $-78\text{ }^\circ\text{C}$ . DMSO (0.8 mL, 11.04 mmol, 4.0 eq) in dry DCM (8 mL) was added dropwise and the mixture was stirred at  $-78\text{ }^\circ\text{C}$  for 10 min. Methyl pent-4-ynoate-*L*-homoserinate (600 mg, 2.76 mmol, 1.0 eq) in dry DCM (8 mL) was added dropwise and the mixture was stirred at  $-78\text{ }^\circ\text{C}$  for 30 min.  $\text{Et}_3\text{N}$  (2.3 mL, 16.56 mmol, 6.0 eq) was added dropwise and the mixture was warmed up to  $0\text{ }^\circ\text{C}$  and stirred for 2 h. The reaction was quenched with  $\text{H}_2\text{O}$  (20 mL) and the aqueous layer was extracted with DCM (8 X 20 mL). The combined organic layers were dried over  $\text{MgSO}_4$ , filtered and concentrated under reduced pressure. The crude was purified by FC eluting with PE/EtOAc (1:3) to afford the product as a yellow oil (205 mg, 0.98 mmol 35%).

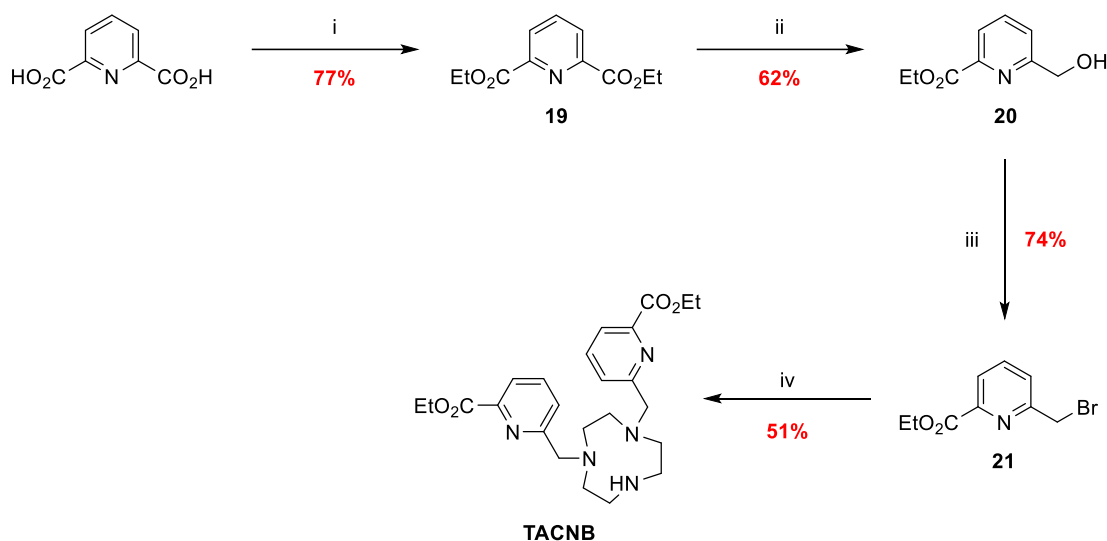
$^1\text{H NMR}$  (400 MHz, Chloroform- $d$ ):  $\delta$  9.71 (s, 1H, CHO-*H*), 6.58 (d,  $J = 7.7\text{ Hz}$ , 1H, *NH*), 4.87 (dt,  $J = 7.8, 4.6\text{ Hz}$ , 1H, *CH*), 3.75 (s, 3H, COO- $\text{CH}_3$ ), 3.12 – 3.04 (m, 2H,  $\text{CH}_2$ ), 2.56 – 2.38 (m, 4H,  $\text{CH}_2$ - $\text{CH}_2$ ), 1.99 (t,  $J = 2.5\text{ Hz}$ , 1H,  $\text{CH}_{\text{alkyne}}$ ).

The analytical data were in accordance with previously reported data.<sup>154</sup>

$^1\text{H NMR}$  spectrum:

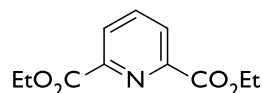


### 5.7. Synthesis of bi-substituted triazacyclononane TACNB



**Scheme 25: Synthesis of the bisubstituted TACN.** i-  $\text{H}_2\text{SO}_4$  conc. EtOH, reflux, 16 h; ii-  $\text{NaBH}_4$ , EtOH, reflux, 16 h; iii-  $\text{CBr}_4$ ,  $\text{PPH}_3$ , DCM, r.t, 3 h; iv- TACN  $\cdot$  3 HCl, DIPEA, ACN, reflux, 16 h.

#### Diethyl pyridine-2,6-dicarboxylate (19)



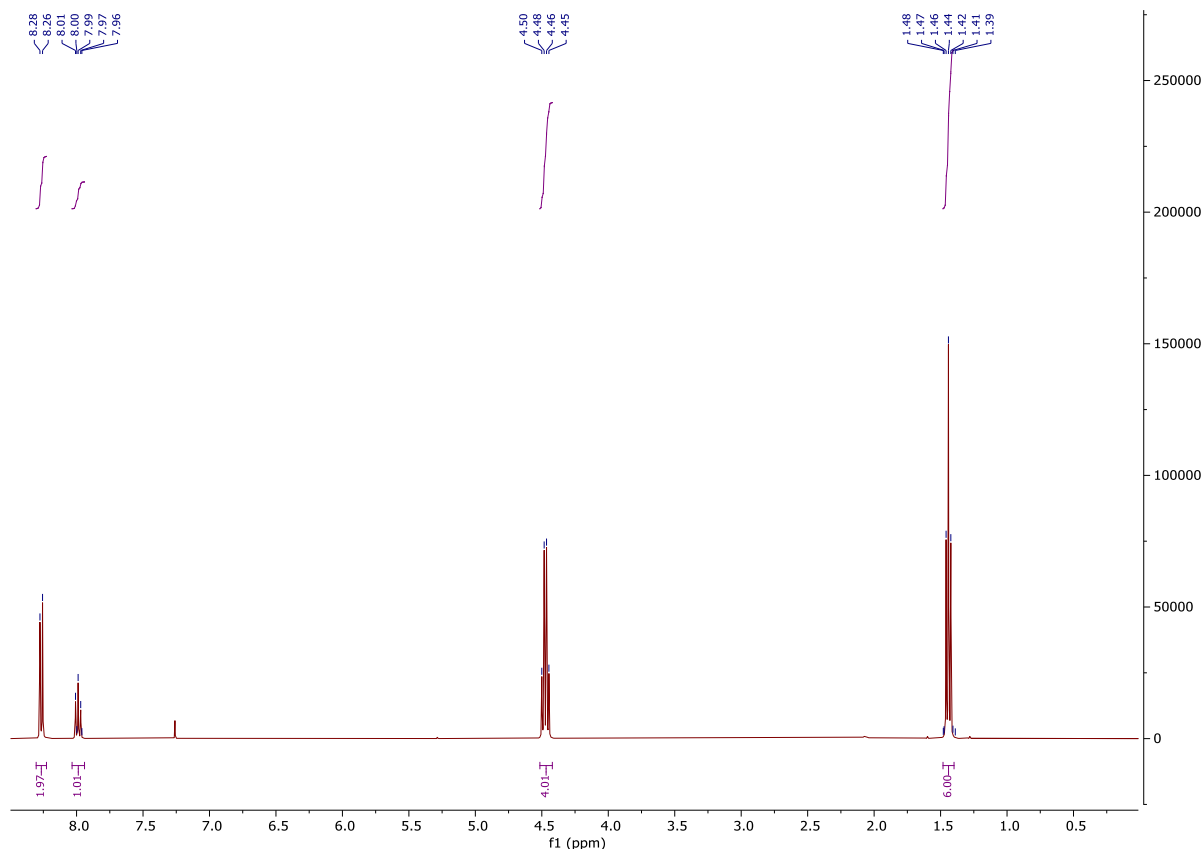
To a solution of pyridine-2,6-dicarboxylic acid (10 g, 59.8 mmol, 1.0 eq) in EtOH (200 mL), conc.  $\text{H}_2\text{SO}_4$  (25.5 mL, 479 mmol, 8 eq) was added dropwise and the mixture was refluxed for 16 h. The mixture was concentrated to half volume and poured into a sat. aqueous solution of  $\text{Na}_2\text{CO}_3$  in water at 0 °C. The aqueous layer was extracted with DCM (5 X 150 mL) and the combined organic layers were dried over  $\text{MgSO}_4$ , filtered and concentrated under reduced pressure to afford the product as a white solid (10.3 g, 45.9 mmol, 77%).

$^1\text{H NMR}$  (400 MHz, Chloroform- $d$ ):  $\delta$  8.27 (d,  $J$  = 7.8 Hz, 2H), 7.99 (t,  $J$  = 7.8 Hz, 1H), 4.47 (q,  $J$  = 7.1 Hz, 4H), 1.44 (t,  $J$  = 7.1 Hz, 6H).

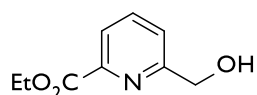
The analytical data were in accordance with previously reported data.<sup>154</sup>

$^1\text{H NMR}$  spectrum:





### Ethyl 6-(hydroxymethyl)picolinate (20)

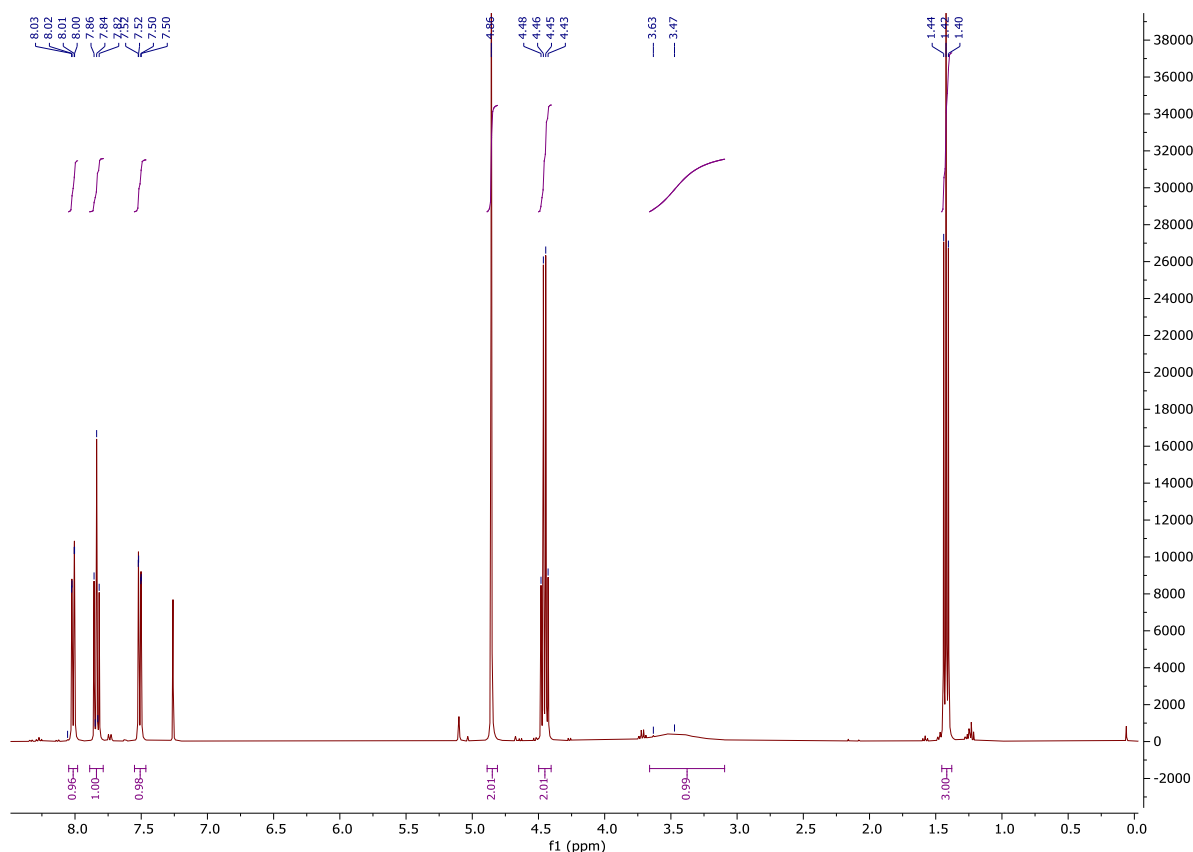


To a solution of diethyl pyridine-2,6-dicarboxylate (2.0 g, 8.96 mmol, 1.0 eq) in EtOH (30 mL), NaBH<sub>4</sub> (272 mg, 7.16 mmol, 0.8 eq) was added portion wise and the mixture was reflux for 16 h. The mixture was neutralized with aqueous 6M HCl (xx mL). H<sub>2</sub>O (20 mL) was added and the aqueous layer was extracted with DCM (5 X 20 mL). The combined organic layers were then washed with H<sub>2</sub>O (20 mL), dried over MgSO<sub>4</sub>, filtered and concentrated under reduced pressure to afford the product as a white solid (1.0 g, 5.6 mmol, 62%).

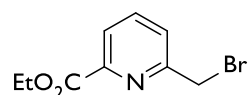
**<sup>1</sup>H NMR** (400 MHz, Chloroform-d): δ 8.01 (dd, *J* = 7.7, 1.0 Hz, 1H), 7.84 (t, *J* = 7.8 Hz, 1H), 7.51 (dd, *J* = 7.8, 1.0 Hz, 1H), 4.86 (s, 2H), 4.45 (q, *J* = 7.1 Hz, 2H), 3.55 (s, 1H), 1.42 (t, *J* = 7.1 Hz, 3H).

The analytical data were in accordance with previously reported data.<sup>154</sup>

<sup>1</sup>H NMR spectrum:



### Ethyl 6-(bromomethyl)picolinate (21)

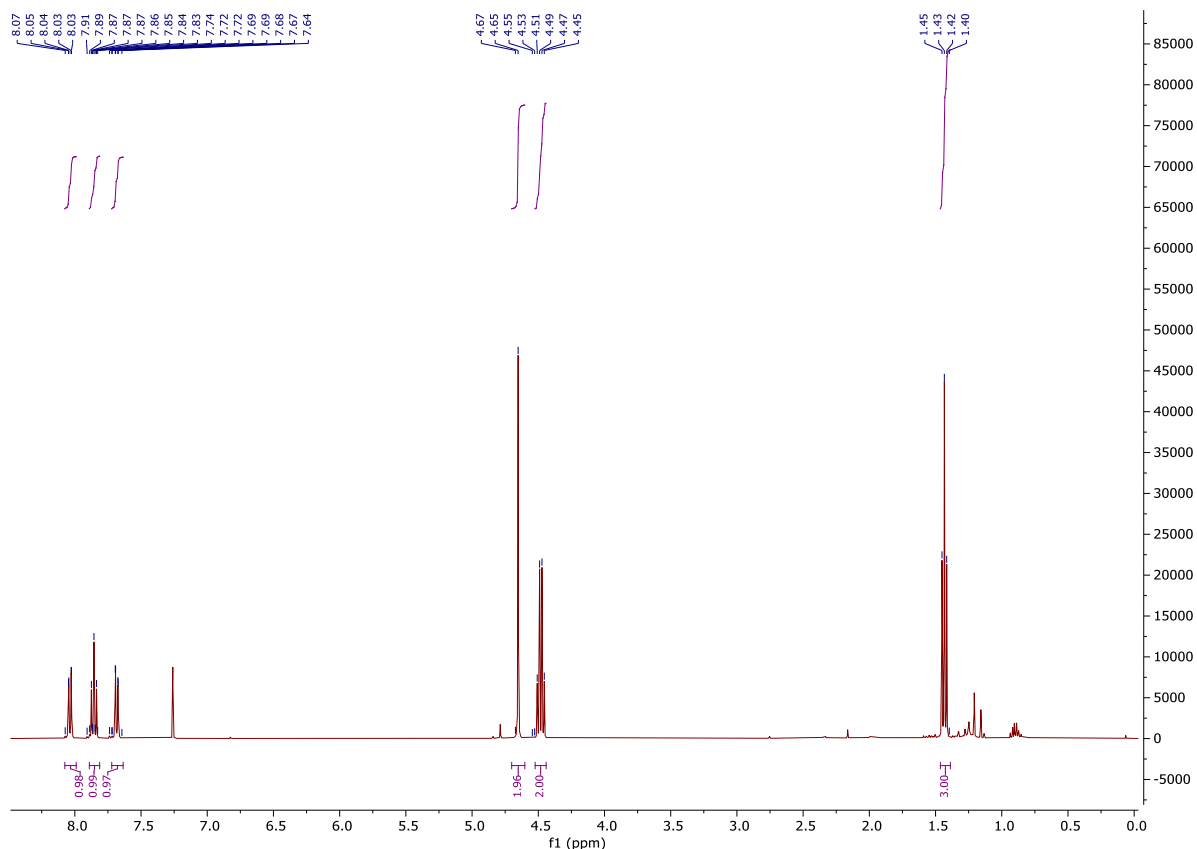


To a solution of ethyl 6-(hydroxymethyl)picolinate (500 mg, 2.76 mmol, 1.0 eq) in dry DCM (7 mL), tetrabromomethane (1.12 g, 3.37 mmol, 1.2 eq) was added. The mixture was cooled to 0 °C and triphenylphosphine (1.16 g, 4.42 mmol, 1.6 eq) in dry DCM (3 mL) was added over 1 h. The mixture was stirred at r.t. for 3 h, and was then concentrated under reduced pressure. The crude was purified by FC eluting with PE/EtOAc (4:1) to afford the product as a yellow oil (497 mg, 2.04 mmol, 74 %).

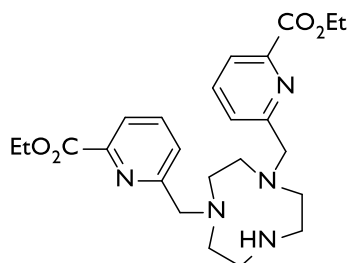
**<sup>1</sup>H NMR** (400 MHz, Chloroform-d):  $\delta$  8.04 (dd,  $J = 7.7, 1.0$  Hz, 1H), 7.86 (t,  $J = 7.8$  Hz, 1H), 7.68 (dd,  $J = 7.8, 1.1$  Hz, 1H), 4.65 (s, 2H), 4.48 (q,  $J = 7.1$  Hz, 2H), 1.43 (t,  $J = 7.1$  Hz, 3H).

The analytical data were in accordance with previously reported data.<sup>154</sup>

<sup>1</sup>H NMR spectrum:



### Diethyl 6,6'-((1,4,7-triazonane-1,4-diyl)bis(methylene))dipicolinate, TACNB

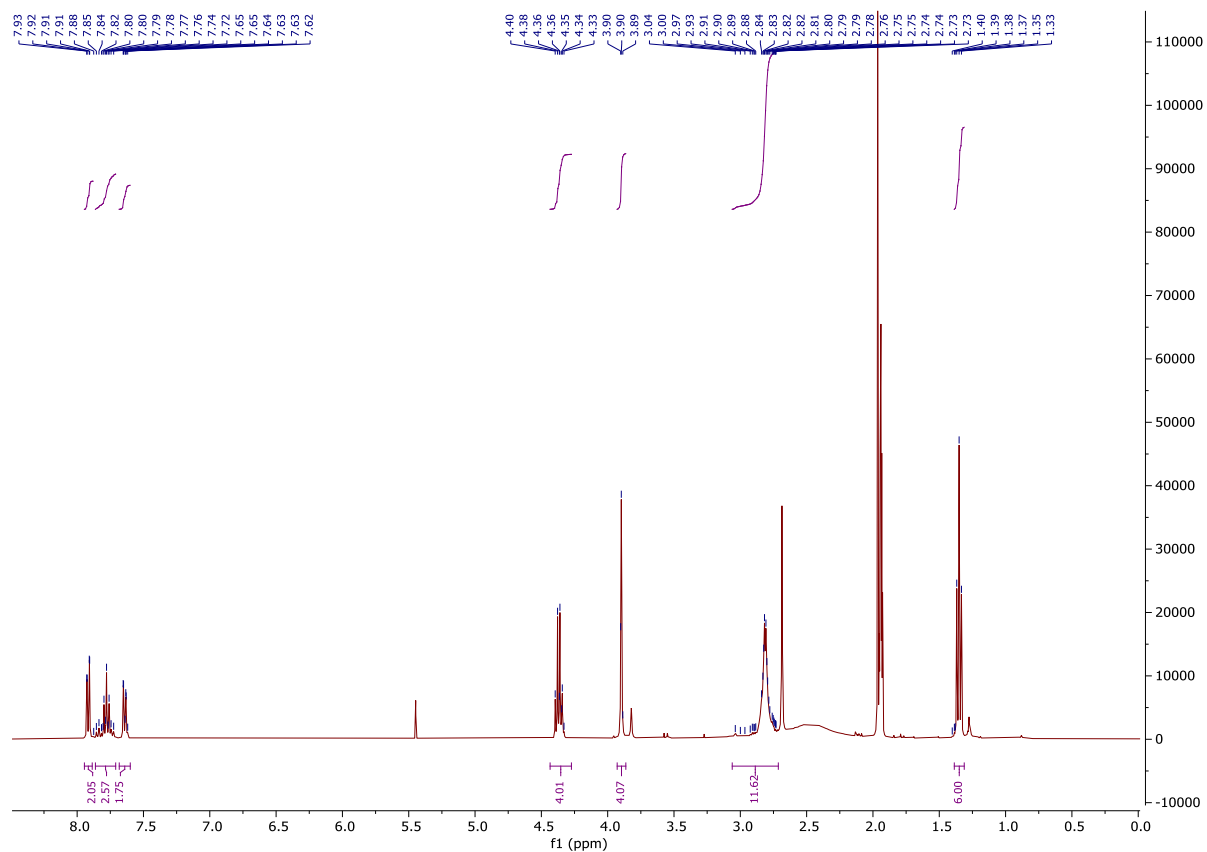


To a solution of ethyl 6-(bromomethyl)picolinate (400 mg, 1.64 mmol, 1.05 eq) in dry ACN (12 mL) TACN.3 HCl (372 mg, 1.56 mmol, 1.0 eq) and DIPEA (0.95 mL, 5.78 mmol, 3.7 eq) were added and the mixture was refluxed for 16 h. The mixture was concentrated under reduce pressure and the residue was dissolved in a minimum amount of DCM and filtered. The filtrate was concentrated under reduced pressure and the crude was purified by FC (Al<sub>2</sub>O<sub>3</sub> basic III (4.9 % water)) eluting with DCM/MeOH (1:0 then 20:1) to afford the product as a brown oil (190 mg, 0.42 mmol, 51 %).

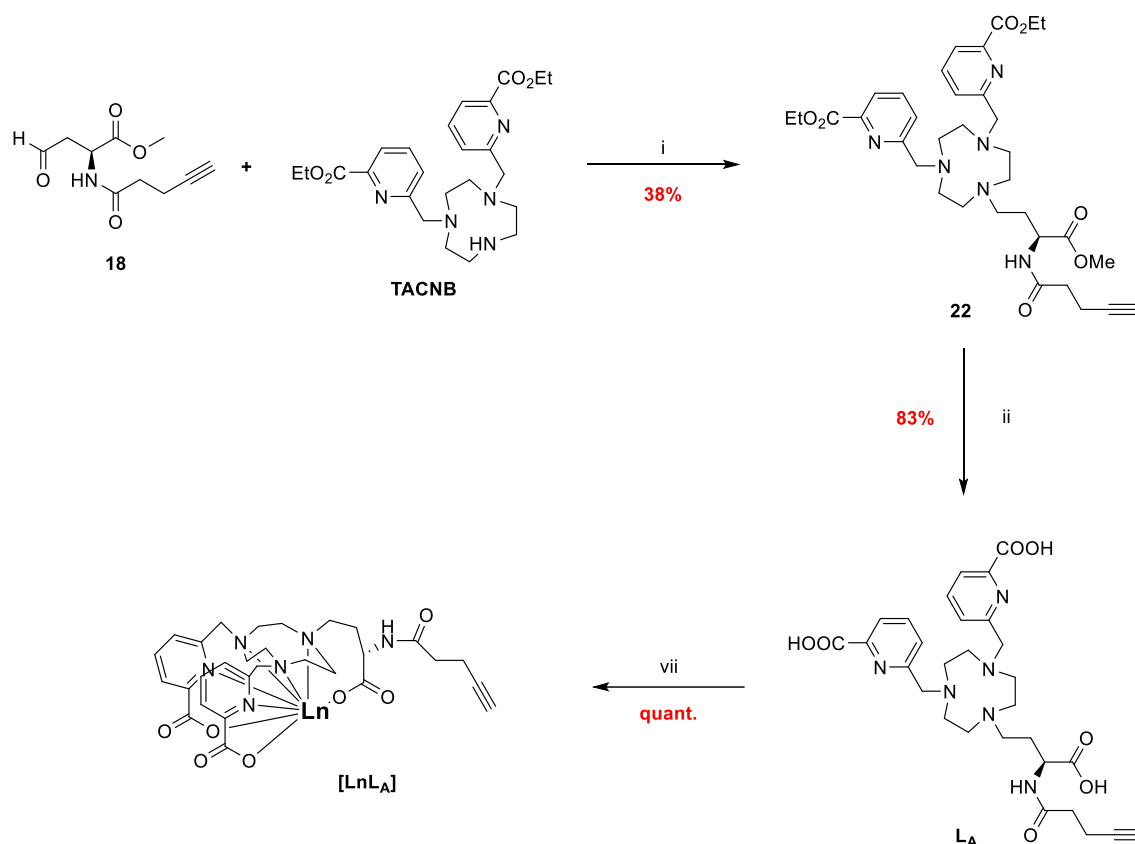
<sup>1</sup>H NMR (400 MHz, Acetonitrile-d<sub>3</sub>): δ 7.92 (dd, *J* = 7.6, 1.1 Hz, 2H), 7.78 (m, 2H), 7.64 (dd, *J* = 7.8, 1.1 Hz, 2H), 4.37 (q, *J* = 7.1 Hz, 4H), 3.90 (s, 4H), 2.81(m, 12H), 1.35 (t, *J* = 7.1 Hz, 6H).

The analytical data were in accordance with previously reported data.<sup>154</sup>

<sup>1</sup>H NMR spectrum:

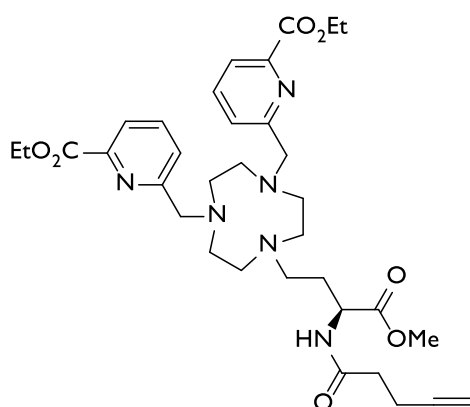


### 5.8. Synthesis of the alkyne lanthanide (III) ligand and Ln complexes



**Scheme 26: Synthesis of the alkyne-Ln-complex.** i- NaBH<sub>3</sub>CN, DCE/ACN, r.t, 16 h; ii- LiOH, MeOH/H<sub>2</sub>O, r.t 4 h; iii- LnCl<sub>3</sub>, H<sub>2</sub>O, 37 °C, 16 h.

#### Diethyl-6,6'-((7-(3-(methoxycarbonyl)-5-oxonon-8-yn-1-yl)-1,4,7-triazonane-1,4-diyl)bis(methylene))(R)-dipicolinate (22)



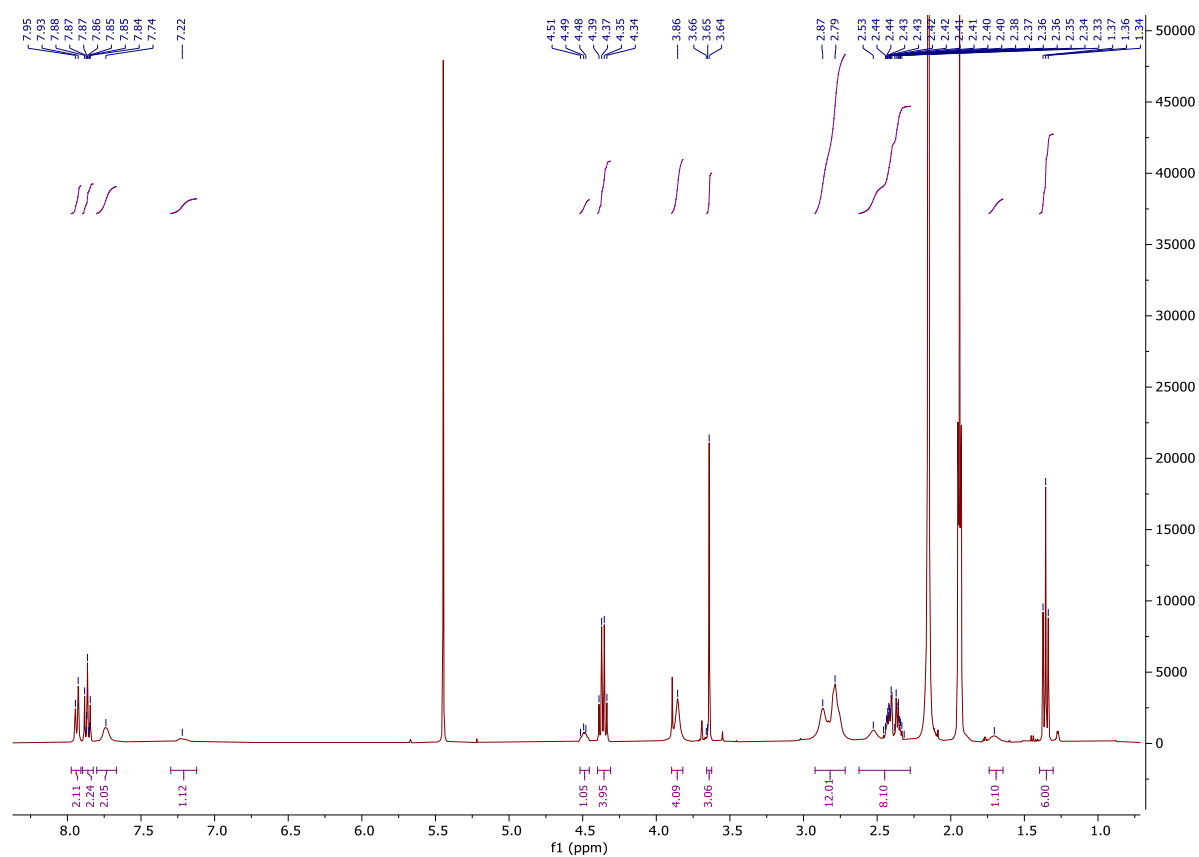
To a solution of diethyl 6,6'-((1,4,7-triazonane-1,4-diyl)bis(methylene))dipicolinate (50 mg, 0.11 mmol, 1.0 eq) in DCE/ACN dry (2:1, 0.6 mL) the L-homoserine derivative (47 mg, 0.22 mmol, 2.0 eq) in DCE/ACN (2:1, 0.6 mL) was added dropwise followed by NaBH<sub>3</sub>CN (35 mg, 0.55 mmol, 5.0 eq) and the mixture was stirred at r.t. for 16 h. The reaction mixture was quenched with a sat. aqueous solution of NaHCO<sub>3</sub> (5 mL) and the aqueous layer was extracted with DCM (8 X 2 mL). The combined organic layers were dried over MgSO<sub>4</sub>, filtered and concentrated under reduced

pressure. The crude was purified by FC (Al<sub>2</sub>O<sub>3</sub> basic III (4.9 % water)) eluting with DCM/MeOH (1:0 then 50:1) to afford the product as a yellow oil (27 mg, 0.05 mmol, 38 %).

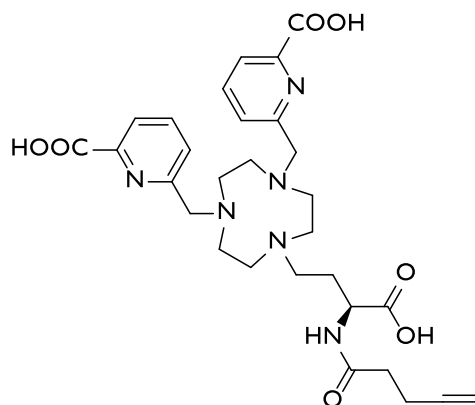
**<sup>1</sup>H NMR** (400 MHz, Acetonitrile-d<sub>3</sub>): δ 7.94 (d, *J* = 7.6 Hz, 2H), 7.86 (t, *J* = 7.7 Hz, 2H), 7.74 (s, 2H), 7.22 (s, 1H), 4.49 (d, *J* = 8.0 Hz, 1H), 4.36 (q, *J* = 7.1 Hz, 4H), 3.86 (s, 4H), 3.64 (s, 3H), 2.93 - 2.71 (m, 12H), 2.62 - 2.31 (m, 8H), 1.70 (s, 1H), 1.36 (t, *J* = 7.1 Hz, 6H).

The analytical data were in accordance with previously reported data.<sup>154</sup>

**<sup>1</sup>H NMR spectrum:**



**(R)-6,6'-((7-(3-carboxy-5-oxonon-8-yn-1-yl)-1,4,7-triazonane-1,4-diyl)bis(methylene))dipicolinic acid: L<sub>A</sub>**



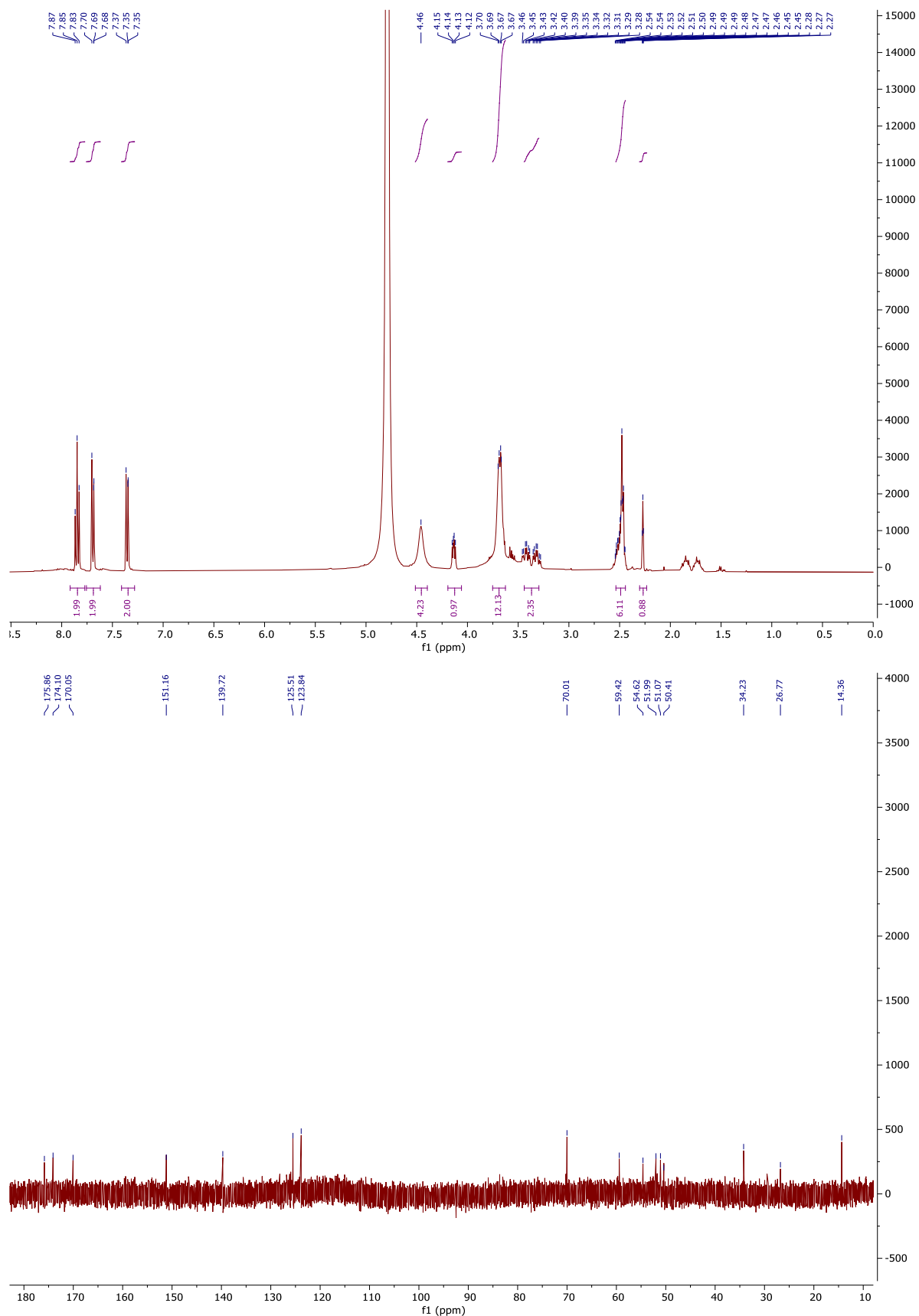
To a solution of the triazacyclononane ester (10 mg, 15  $\mu\text{mol}$ , 1.0 eq) in MeOH/H<sub>2</sub>O (5:1, 1.0 mL), LiOH (1.2 mg, 50  $\mu\text{mol}$ , 3.3 eq) was added and the mixture was stirred at r.t. for 3 h. The crude was diluted with H<sub>2</sub>O (2 mL) and washed with DCM (2 mL). The aqueous phase was then neutralized with aqueous HCl 1M (50  $\mu\text{L}$ ), purified by dialysis in H<sub>2</sub>O and lyophilized to afford the product as a yellow solid (7.5 mg, 12  $\mu\text{mol}$ , 83%).

**HRMS (nanochip-ESI/LTQ-Orbitrap):**  $m/z$  calcd for C<sub>29</sub>H<sub>38</sub>N<sub>6</sub>O<sub>7</sub><sup>+</sup> ([M + H]<sup>+</sup>): 582.2796; Found 582.2791.

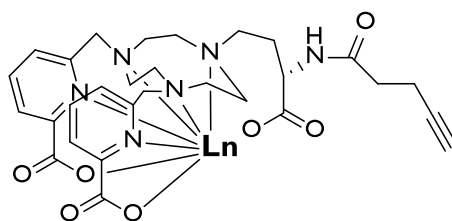
**<sup>1</sup>H NMR** (400 MHz, D<sub>2</sub>O):  $\delta$  7.85 (t,  $J$  = 7.80 Hz, 2H), 7.69 (m, 2H), 7.35 (m, 2H), 4.46 (s, 4H), 4.13 (dd,  $J$  = 7.9, 5.0 Hz, 1H), 3.68 (m, 12H), 3.37 (ddd,  $J$  = 30.4, 12.0, 4.9 Hz, 2H), 2.48 (m, 6H), 2.27 (s, 1H).

**<sup>13</sup>C NMR** (100 MHz, D<sub>2</sub>O):  $\delta$  174.86 (C=O x2), 174.10 (COOH x2), 170.05 (CH<sub>Ar</sub>), 151.16 (CH<sub>Ar</sub>), 139.72 (CH<sub>Ar</sub>), 125.51 (CH<sub>Ar</sub>), 123.84 (CH<sub>Ar</sub>), 70.01 (C<sub>Alkyne</sub>), 59.42 (CH<sub>Alkyne</sub>), 54.62 (CH<sub>2</sub> x2), 50-52 (CH<sub>2</sub> - TACN x6, CH, CH<sub>2</sub>), 34.23 (CH<sub>2</sub>), 26.77 (CH<sub>2</sub>), 14.36 (CH<sub>2</sub>).

$^1\text{H}$  and  $^{13}\text{C}$  NMR spectra:





**Ln(III)-alkyne Complex: [LnL<sub>A</sub>]<sup>168</sup>**

A solution of the ligand (10 mg, 16  $\mu\text{mol}$ , 1.0 eq) in  $\text{H}_2\text{O}$  (500  $\mu\text{L}$ ) was neutralized with HCl 1M, after which  $\text{LnCl}_3$  (20  $\mu\text{mol}$ , 1.2 eq) was added and the mixture was stirred at 37  $^\circ\text{C}$  for 16 h. The pH of the reaction was kept between 5 and 7 until stabilization by addition of  $\text{NH}_4\text{OH}$  0.1M. The crude was purified by dialysis in  $\text{H}_2\text{O}$  and lyophilized to afford the product as a yellow solid (13 mg, 16  $\mu\text{mol}$ , quant.).

**HRMS (ESI/QTOF):**  $m/z$  calcd for  $\text{C}_{29}\text{H}_{34}\text{LaN}_6\text{O}_7^+$  ( $[\text{M} + \text{H}]^+$ ): 718.1625; Found 718.1609.

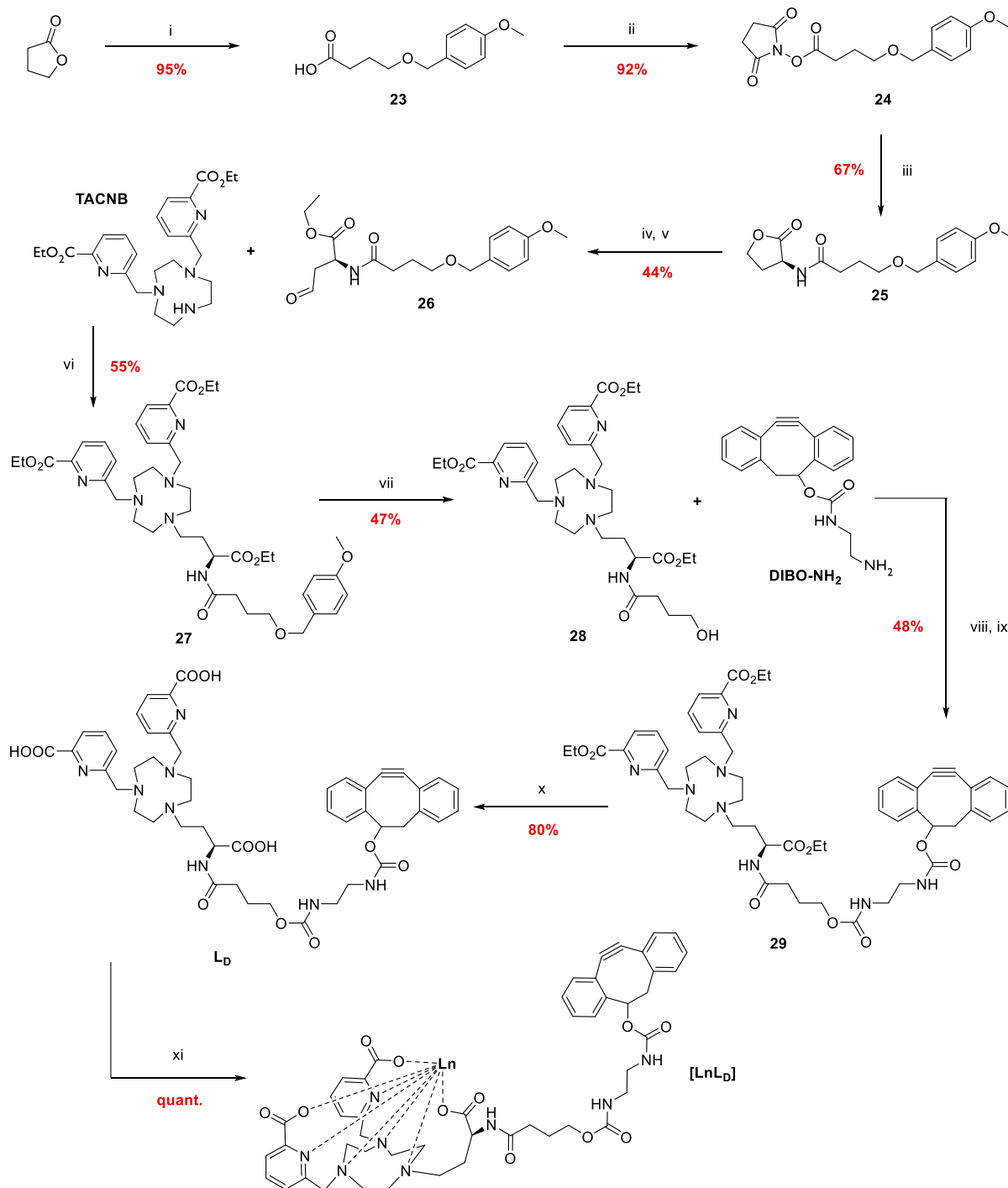
**HRMS (ESI/QTOF):**  $m/z$  calcd for  $\text{C}_{29}\text{H}_{34}\text{EuN}_6\text{O}_7^+$  ( $[\text{M} + \text{H}]^+$ ): 731.1696; Found 731.1691.

**HRMS (ESI/QTOF):**  $m/z$  calcd for  $\text{C}_{29}\text{H}_{34}\text{GdN}_6\text{O}_7^+$  ( $[\text{M} + \text{H}]^+$ ): 736.1652; Found 736.1657.

**HRMS (ESI/QTOF):**  $m/z$  calcd for  $\text{C}_{29}\text{H}_{34}\text{N}_6\text{O}_7\text{Tb}^+$  ( $[\text{M} + \text{H}]^+$ ): 737.1737; Found 737.1745.

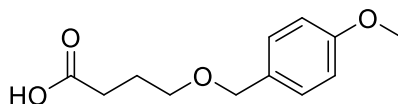
**HRMS (ESI/QTOF):**  $m/z$  calcd for  $\text{C}_{29}\text{H}_{34}\text{N}_6\text{O}_7\text{Yb}^+$  ( $[\text{M} + \text{H}]^+$ ): 752.1872; Found 752.1888.

## 5.9. Synthesis of the cyclooctyne lanthanide (III) ligand and Ln complexes



**Scheme 27: Synthesis of the DIBO-Ln-complexes.** i- PMBBBr, KOH, toluene, reflux, 4 days; ii- NHS, DCC, THF, r.t, 3 h; iii- (S)-(-)- $\alpha$ -amino- $\gamma$ -butyrolactone hydrobromide, Et<sub>3</sub>N, DCM, r.t, 2 h; iv- H<sub>2</sub>SO<sub>4</sub>, EtOH, r.t, 24 h; v- (COCl)<sub>2</sub>, DMSO, Et<sub>3</sub>N, DCM 0 °C, 2 h; vi- AcOH, NaBH(OAc)<sub>3</sub>, DCE, r.t, 16 h; vii- DDQ, DCM/PBS 4:1, r.t, 3 h; viii- 4-nitrophenyl chloroformate, pyridine, DCM, r.t, 16 h; ix- DIPEA, DMF, r.t, 16 h; x- LiOH, EtOH/H<sub>2</sub>O, r.t 4 h; xi- LnCl<sub>3</sub>, H<sub>2</sub>O, 37 °C, 16 h.

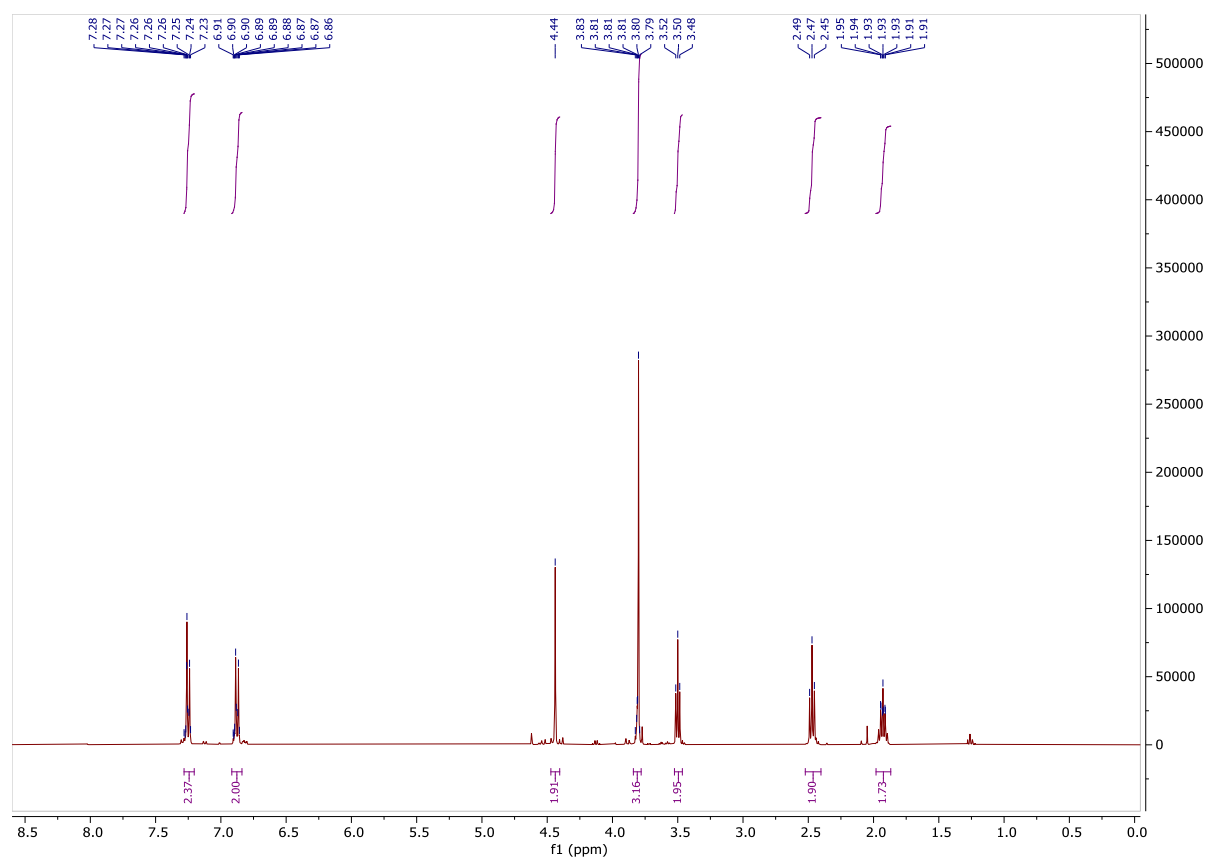
4-((4-methoxybenzyl)oxy)butanoic acid (**23**)<sup>169</sup>



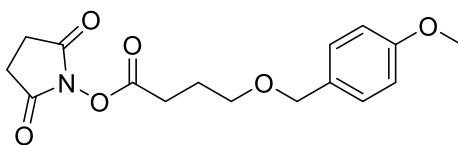
Gamma-butyrolactone (2.02 mL, 26 mmol, 1.0 eq.), PMBBR (9.5 mL, 66 mmol, 2.5 eq.) and KOH (6.8 mg, 106 mmol, 4.0 eq.) were dissolved in dry toluene (100 mL). The mixture was stirred under reflux for 4 days. The mixture was cooled to r.t. and diluted with AcOEt (250 mL) and washed with H<sub>2</sub>O (3x). The combined aqueous phases were acidified with H<sub>2</sub>SO<sub>4</sub> 1M and extracted with DCM (3x). The combined organic phases were dried over MgSO<sub>4</sub>, filtered and concentrated under reduced pressure to afford the product as a yellow oil (5.6 g, 25 mmol, 95%).

**<sup>1</sup>H-NMR** (400 MHz, Chloroform-d):  $\delta$  7.25 (d, 2H), 6.88 (d, 2H), 4.44 (s, 2H), 3.80 (s, 3H), 3.50 (t, J = 6.1 Hz, 2H), 2.47 (t, J = 7.3 Hz, 2H), 1.93 (p, J = 7.4, 6.1, 1.2 Hz, 2H).

<sup>1</sup>H NMR spectrum:



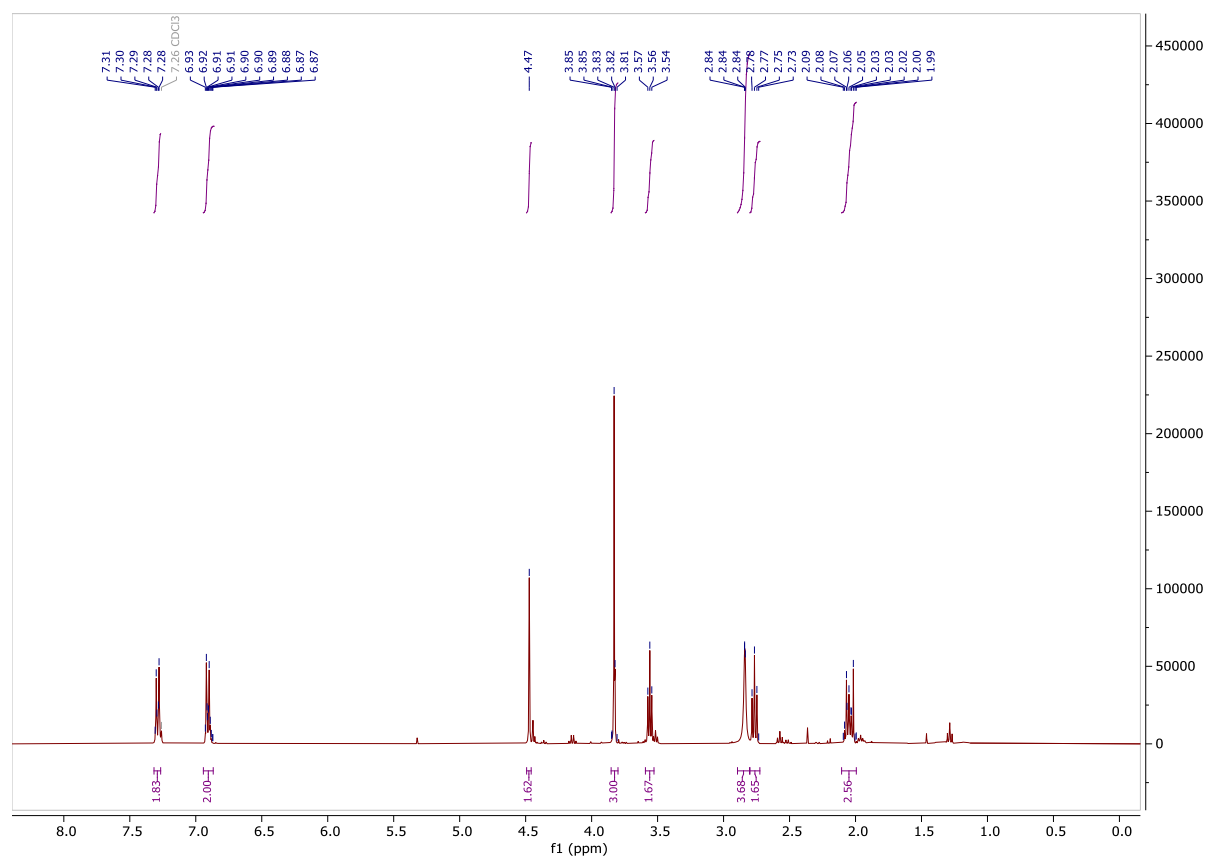
## 2,5-dioxopyrrolidin-1-yl 4-((4-methoxybenzyl)oxy)butanoate (24)

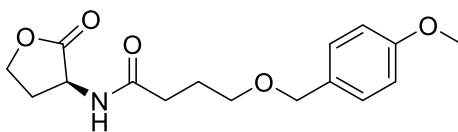


4-((4-methoxybenzyl)oxy)butanoic acid (3.227 g, 14.39 mmol, 1.0 eq.) and *N*-hydroxysuccinimide (NHS) (1.662 g, 14.44 mmol, 1.0 eq.) were dissolved in dry THF (19.2 mL) and cooled to 0 °C. Separately, *N,N'*-Dicyclohexylcarbodiimide (DCC) (2.969 g, 14.39 mmol, 1.0 eq.) was dissolved in dry THF (9.6 mL) and added dropwise to the previous mixture. The reaction was left to stir at 0 °C for 1 h and then at r.t. for 3 h. The mixture was filtered and concentrated under reduced pressure. The residue was redissolved in EtOAc (100 mL) and filtered. The organic layer was washed with sat. aqueous NaHCO<sub>3</sub> (100 mL) and brine (100 mL), then dried over MgSO<sub>4</sub>, filtered and concentrated under reduced pressure. The product was recovered as a yellow oil (4.235 g, 13.18 mmol, 92%).

**<sup>1</sup>H-NMR** (400 MHz, Chloroform-*d*): δ 7.32 – 7.27 (m, 2H), 6.94 – 6.87 (m, 2H), 4.47 (s, 2H), 3.83 (s, 3H), 3.56 (t, *J* = 6.0 Hz, 2H), 2.89 – 2.80 (m, 4H), 2.77 (t, *J* = 7.4 Hz, 2H), 2.11 – 1.99 (m, 3H).

<sup>1</sup>H NMR spectrum:



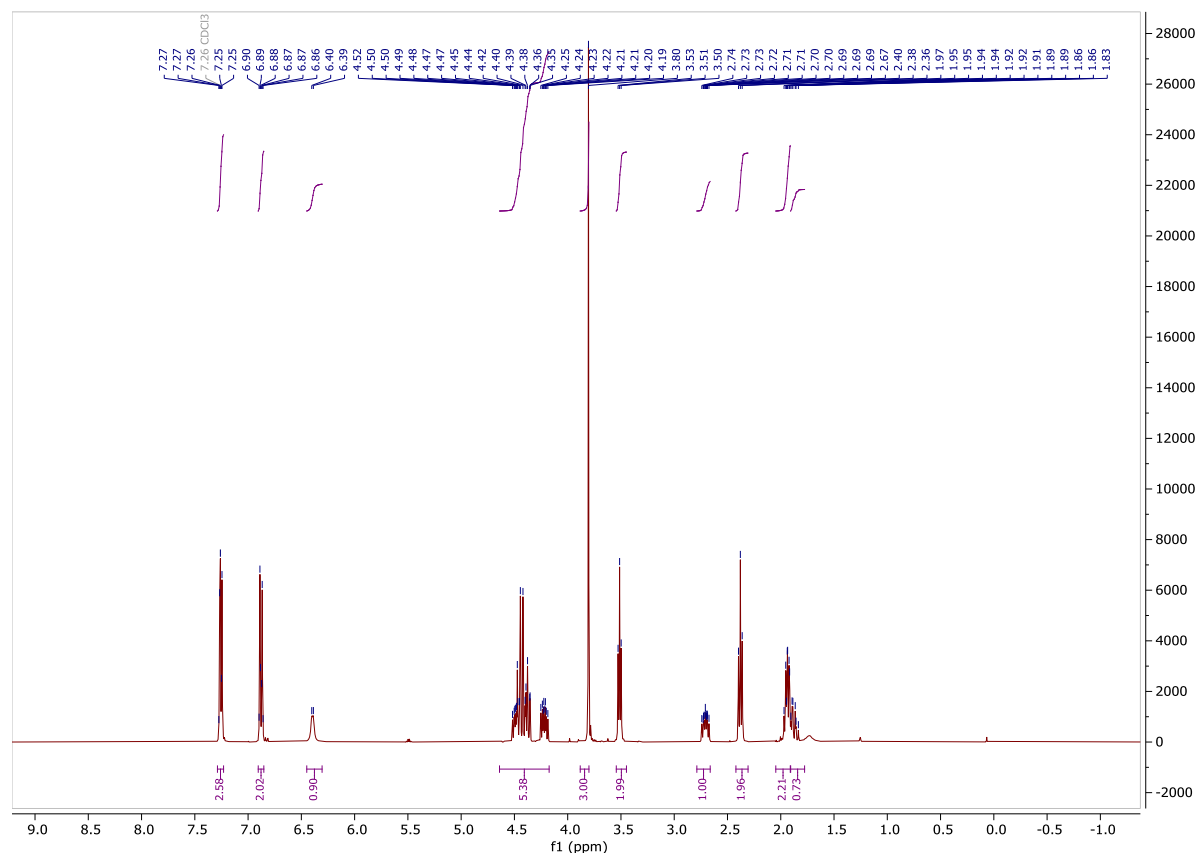
**(S)-4-((4-methoxybenzyl)oxy)-N-(2-oxotetrahydrofuran-3-yl)butanamide (25)**

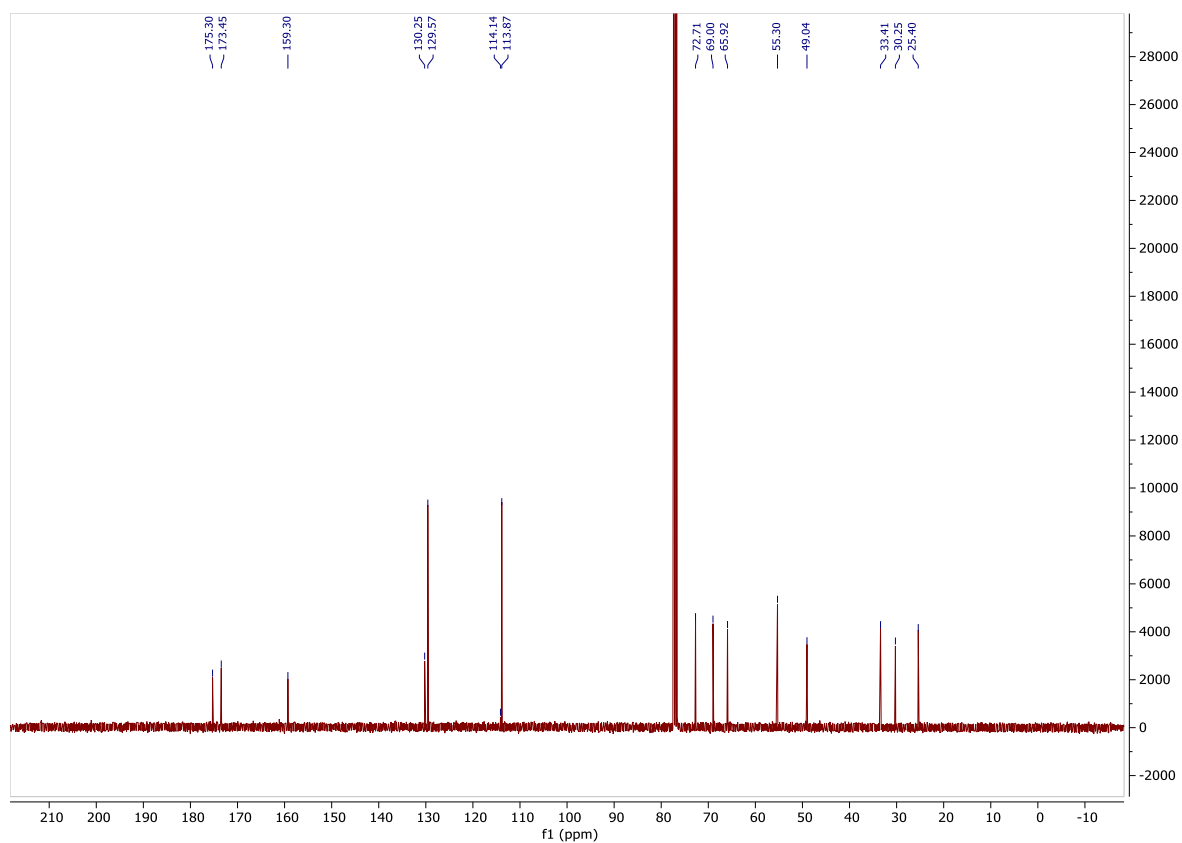
2,5-dioxopyrrolidin-1-yl 4-((4-methoxybenzyl)oxy)butanoate (1.652 g, 5.14 mmol, 1.0 eq.) and (S)-2-amino-4-butyrolactone hydrobromide (1.028 g, 5.65 mmol, 1.1 eq.) were dissolved in dry DCM (50 mL). Et<sub>3</sub>N (2.15 mL, 15.43 mmol, 3.0 eq.) was dissolved in dry DCM (2.6 mL) and the solution was added dropwise to the previous mixture. The reaction was stirred at r.t. for 2 h. The reaction mixture was washed with sat. aqueous NH<sub>4</sub>Cl (50 mL) and extracted with DCM (50 mL). The combined organic layers were dried over MgSO<sub>4</sub>, filtered and concentrated under reduced pressure. The crude was purified by FC eluting with EtOAc/MeOH (1:0 then 25:1) to afford the product as a white powder (1.065 g, 3.46 mmol, 67%).

**<sup>1</sup>H-NMR** (400 MHz, Chloroform-d): δ 7.29 – 7.23 (m, 2H), 6.90 – 6.85 (m, 2H), 6.39 (d, *J* = 6.1 Hz, 1H), 4.64 – 4.17 (m, 5H), 3.80 (s, 3H), 3.51 (t, *J* = 5.8 Hz, 2H), 2.79 – 2.66 (m, 1H), 2.38 (t, *J* = 7.0 Hz, 2H), 2.05 – 1.91 (m, 2H), 1.91 – 1.78 (m, 1H).

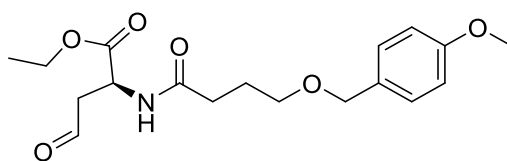
**<sup>13</sup>C-NMR** (101 MHz, Chloroform-d): δ 175.30, 173.45, 159.30, 130.25, 129.57, 114.14, 113.87, 77.34, 77.03, 76.71, 72.71, 69.00, 65.92, 55.30, 49.04, 33.41, 30.25, 25.40.

<sup>1</sup>H and <sup>13</sup>C NMR spectra:





## Ethyl (S)-2-(4-((4-methoxybenzyl)oxy)butanamido)-4-oxobutanoate (26)

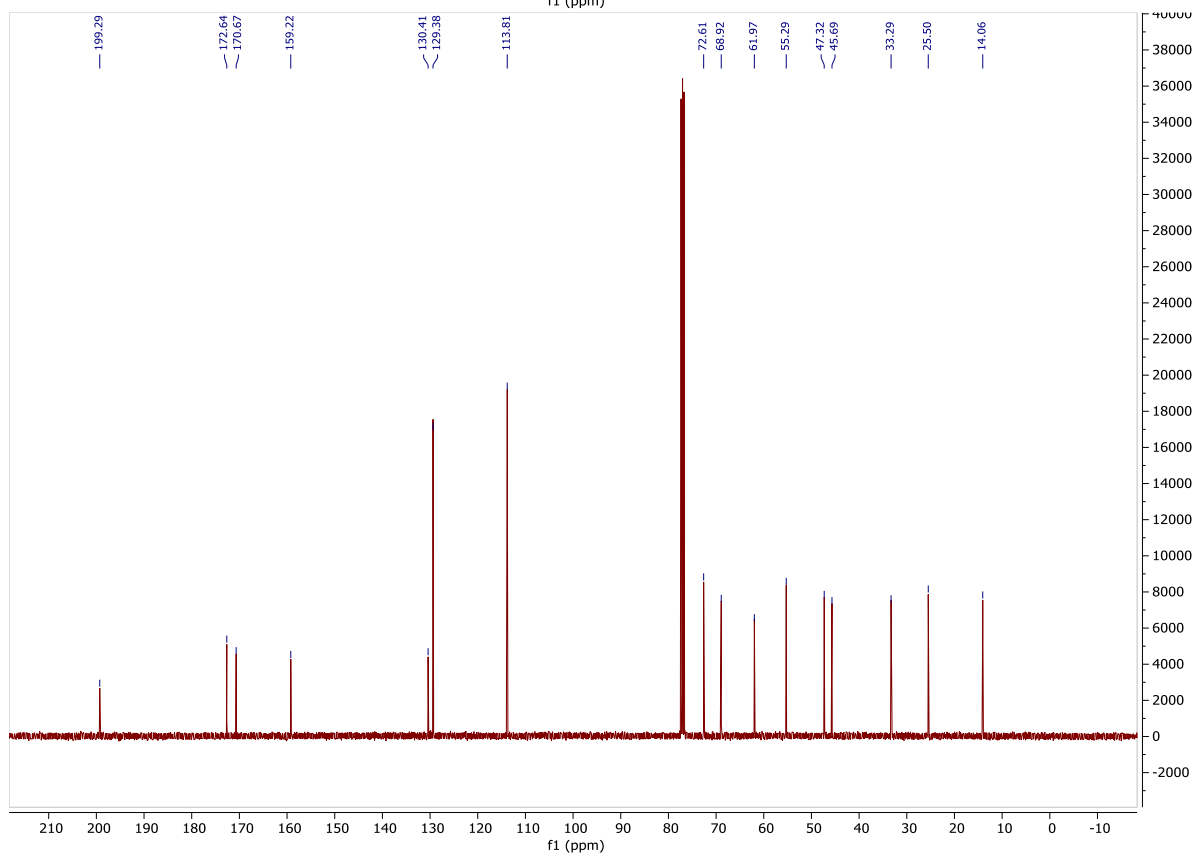
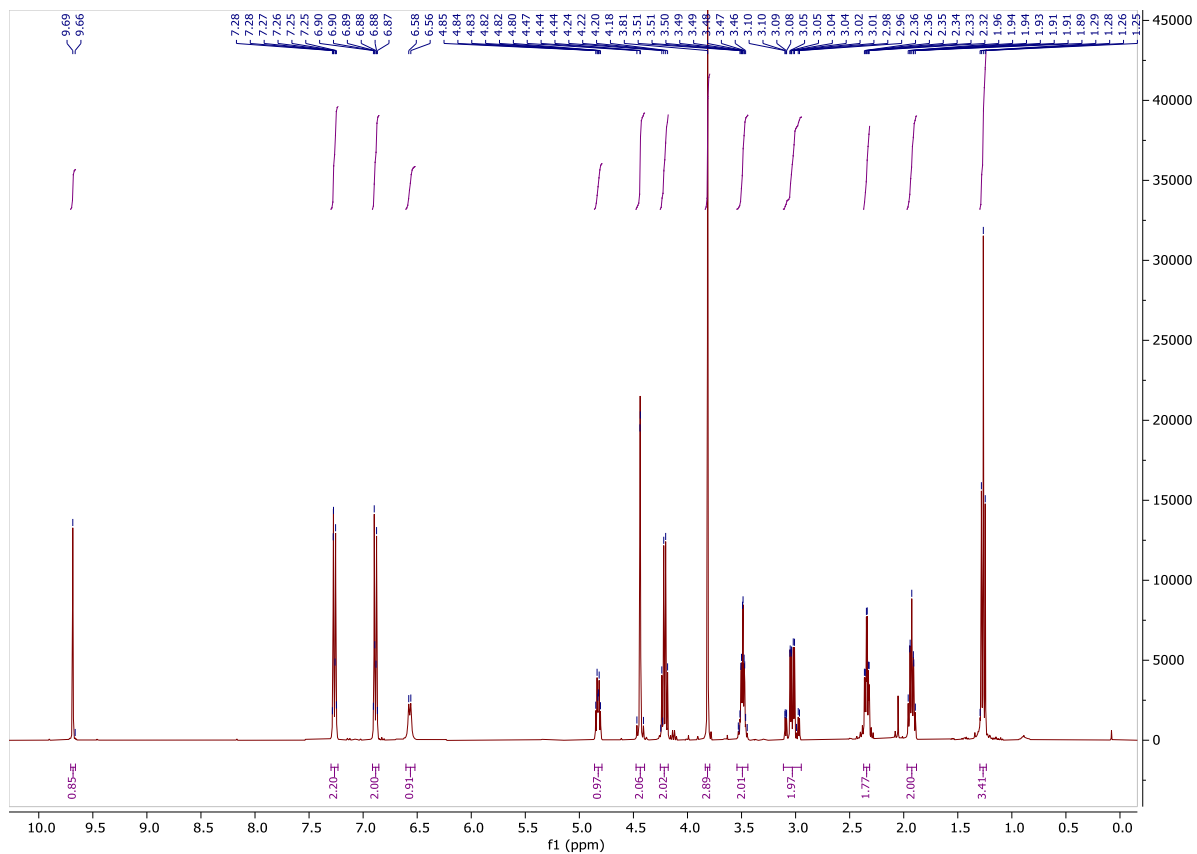


(S)-4-((4-methoxybenzyl)oxy)-N-(2-oxotetrahydrofuran-3-yl)butanamide (503.3 mg, 1.64 mmol, 1.0 eq.) and H<sub>2</sub>SO<sub>4</sub> (100 μL) were dissolved in EtOH (10 mL) and stirred at r.t. for 24 h. The mixture was neutralized with sat. aqueous NaHCO<sub>3</sub> at 0 °C, filtered and concentrated under reduced pressure at 20 °C. The crude was not purified. (COCl)<sub>2</sub> (0.56 mL, 6.55 mmol, 4.0 eq.) was dissolved in dry DCM (10 mL). A solution of DMSO (0.70 mL, 9.82 mmol, 6.0 eq.) in dry DCM was added dropwise and the mixture was stirred at -78 °C for 10 min. A solution of the intermediate in dry DCM (5 mL) was added dropwise and the resulting mixture was stirred at -78 °C for 30 min. Et<sub>3</sub>N (1.83 mL, 13.10 mmol, 8.0 eq.) was added dropwise and the mixture was allowed to warm up to 0 °C and stirred for 2 h. The solution was then allowed to warm up to r.t. for 1 h. The reaction was quenched with H<sub>2</sub>O (10 mL) and extracted with DCM (3x10 mL). The combined organic layers were dried over MgSO<sub>4</sub>, filtered and concentrated under reduced pressure. The crude was purified by FC eluting with PE/EtOAc (1:3) to afford the product as a yellow oil (253.5 mg, 0.72 mmol, 44%).

**<sup>1</sup>H-NMR** (400 MHz, Chloroform-d): δ 9.69 (s, 1H), 7.27 (d, 2H), 6.89 (d, 2H), 6.60 – 6.52 (m, 1H), 4.86 – 4.79 (m, 1H), 4.44 (s, 2H), 4.21 (q, *J* = 7.1 Hz, 2H), 3.81 (s, 3H), 3.49 (td, *J* = 6.1, 2.2 Hz, 2H), 3.11 – 2.95 (m, 2H), 2.34 (td, *J* = 7.2, 3.0 Hz, 2H), 1.97 – 1.88 (m, 2H), 1.26 (t, *J* = 7.1 Hz, 3H).

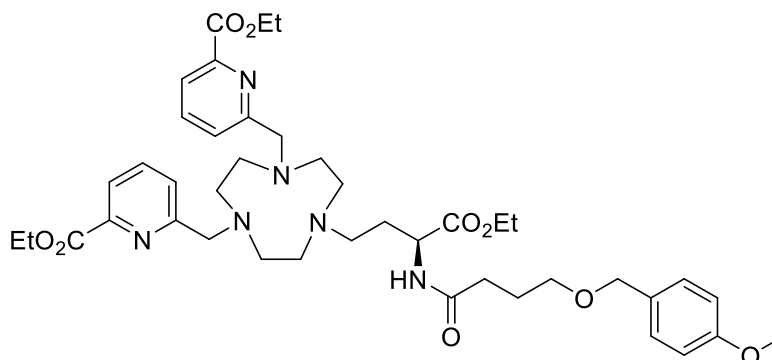
**<sup>13</sup>C-NMR** (101 MHz, Chloroform-d): δ 199.29, 172.64, 170.67, 159.22, 130.41, 129.38, 113.81, 77.36, 77.04, 76.72, 72.61, 68.92, 61.97, 55.29, 47.32, 45.69, 33.29, 25.50, 14.06.

<sup>1</sup>H and <sup>13</sup>C NMR spectra:





## TACNB-OPMB (27)

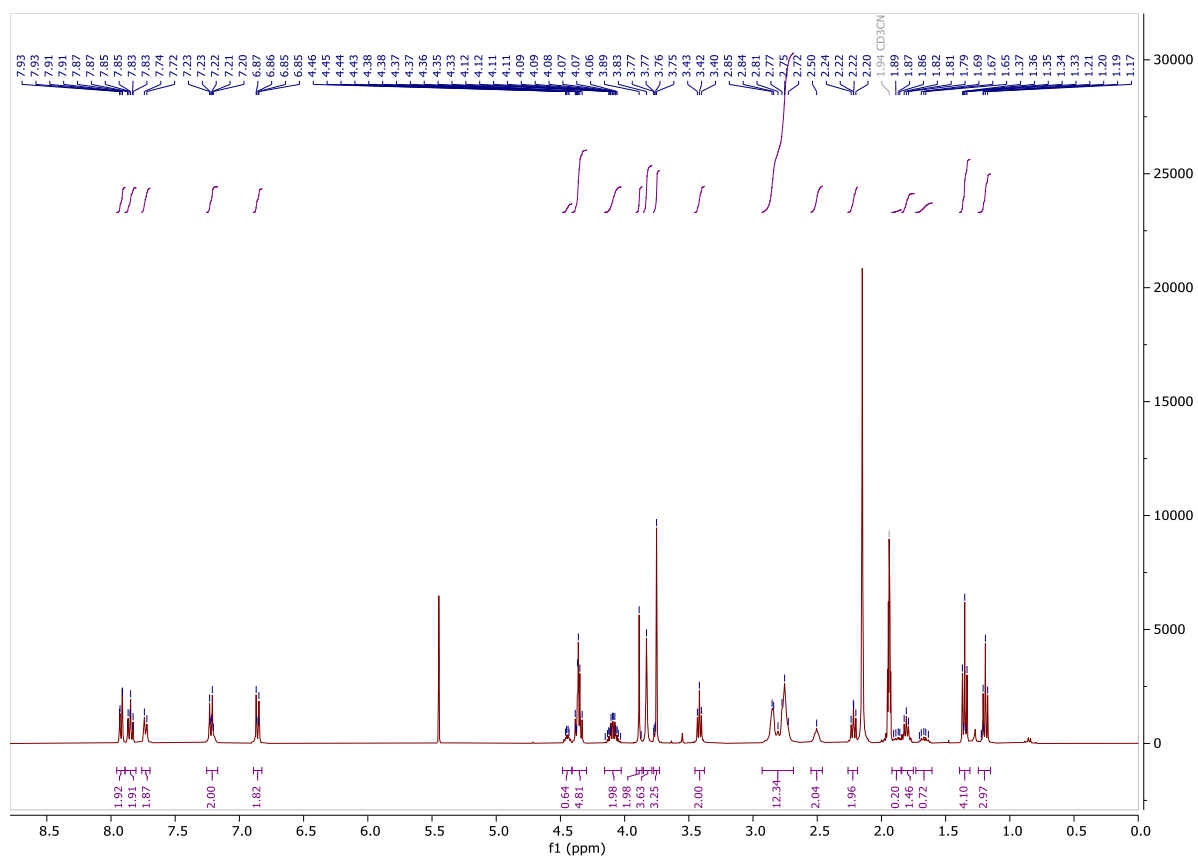


TACNB (153 mg, 0.34 mmol, 1.1 eq.) was dissolved in dry DCE (5 mL). Ethyl (S)-2-(4-((4-methoxybenzyl)oxy)butanamido)-4-oxobutanoate (107.29 mg, 0.31 mmol, 1.0 eq.) and AcOH (17.3  $\mu$ L, 0.30 mmol, 1.0 eq.) were dissolved in dry DCE (2.5 mL) and the mixture was added dropwise to the first solution. The reaction was stirred for 5 h at r.t. under argon.  $\text{NaBH}(\text{OAc})_3$  (320.9 mg, 1.51 mmol, 5.0 eq.) was added and the reaction was stirred for 16 h at r.t. under argon. The mixture was quenched with sat. aqueous  $\text{NaHCO}_3$  (10 mL) and extracted with  $\text{CHCl}_3$  (4x 5 mL). The organic layers were washed with brine (10 mL), dried over  $\text{Na}_2\text{SO}_4$ , filtered and concentrated under reduced pressure. The crude was purified by FC ( $\text{Al}_2\text{O}_3$  basic III (4.9%  $\text{H}_2\text{O}$ )) eluting with DCM/MeOH (1:0 to 30:1) to afford the product as a yellow oil (133.6 mg, 0.17 mmol, 55%).

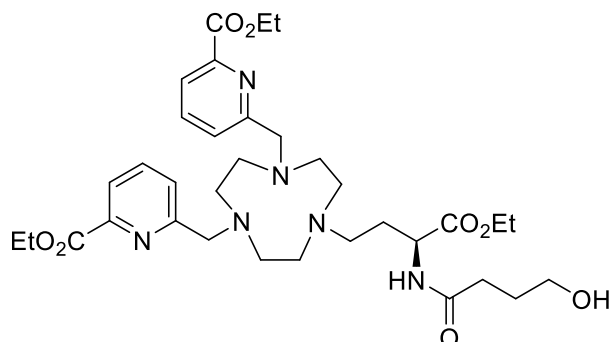
**$^1\text{H-NMR}$**  (400 MHz, Acetonitrile- $d_3$ ):  $\delta$  7.96 – 7.89 (m, 2H), 7.89 – 7.81 (m, 2H), 7.76 – 7.70 (m, 2H), 7.25 – 7.17 (m, 2H), 6.89 – 6.82 (m, 2H), 4.48 – 4.41 (m, 1H), 4.41 – 4.30 (m, 4H), 4.16 – 4.03 (m, 2H), 3.89 (s, 2H), 3.85 – 3.79 (m, 4H), 3.75 (s, 3H), 3.42 (t,  $J = 6.3$  Hz, 2H), 2.93 – 2.69 (m, 12H), 2.55 – 2.46 (m, 2H), 2.22 (t, 2H), 1.92 – 1.85 (m, 1H), 1.81 (t,  $J = 6.8$  Hz, 2H), 1.73 – 1.61 (m, 1H), 1.35 (t,  $J = 7.1$  Hz, 6H), 1.19 (t,  $J = 7.1$  Hz, 3H).

**HRMS** (ESI/QTOF)  $m/z$ :  $[\text{M} + \text{H}]^+$  Calcd for  $\text{C}_{42}\text{H}_{59}\text{N}_6\text{O}_9$  791.4338; Found 791.4356.

$^1\text{H}$  NMR spectrum:



## TACNB-OH (28)

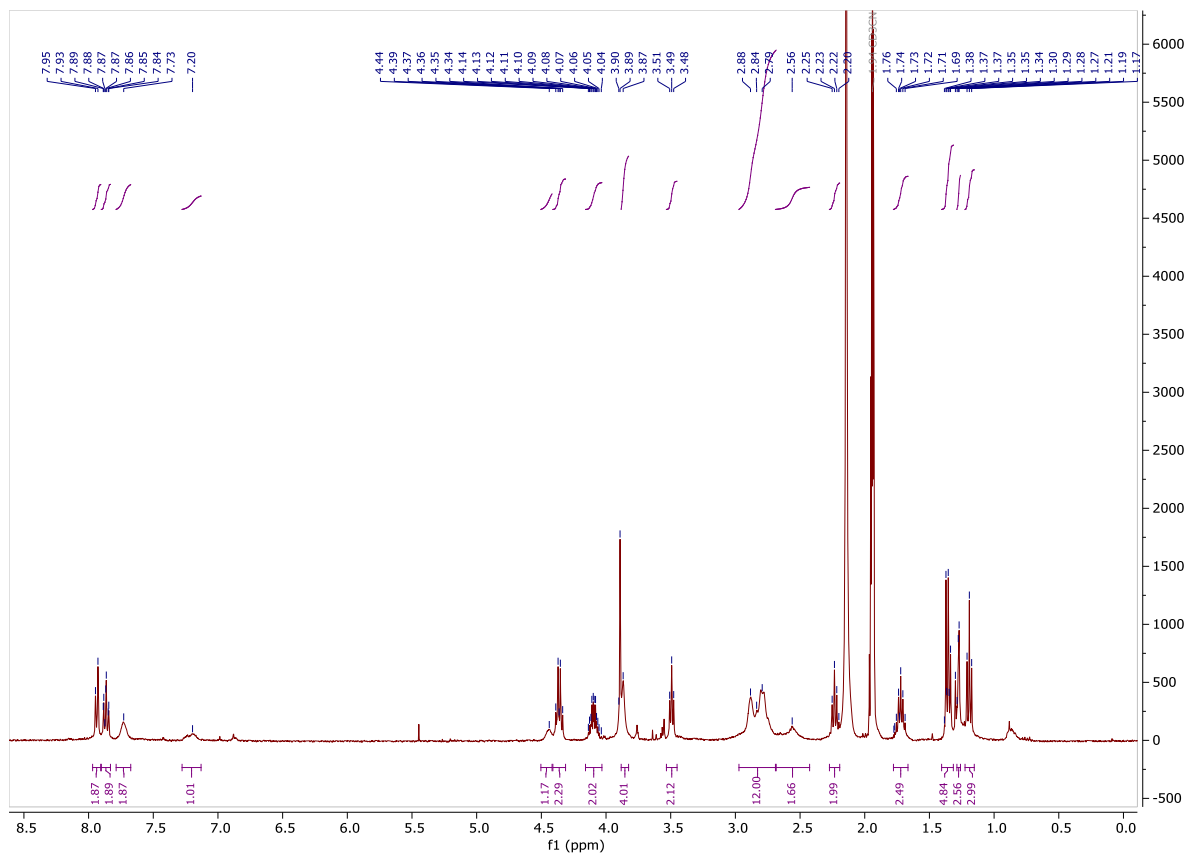


TACN-OPMB (127 mg, 0.16 mmol, 1.0 eq.) was dissolved in DCM (4 mL). PBS (1 mL) was added and the mixture was cooled to 0 °C. DDQ (109.3 mg, 0.48 mmol, 3.0 eq.) was added and the reaction mixture was stirred at 0 °C for 1 h. The reaction was then allowed to warm up to r.t. and stirred for 3 h. A second portion of DDQ (19.1 mg, 0.08 mmol, 0.5 eq.) was added if completion was not reached and the reaction was stirred at r.t. for an additional 30 min. The reaction mixture was ultrasonicated briefly every 60 min. The reaction was quenched directly in the reaction flask with sat aqueous  $\text{Na}_2\text{S}_2\text{O}_3$  (15 mL) and sat. aqueous  $\text{NaHCO}_3$  (15 mL) and then extracted with DCM (3 X 15 mL). The mixture was ultrasonicated for 2 min. after every addition and then transferred to separatory funnel using Pasteur pipette. The organic layers were washed with sat. aqueous  $\text{NaHCO}_3$  (xx mL) and brine (xx mL), dried over  $\text{Na}_2\text{SO}_4$ , filtered and concentrated under reduced pressure. The crude was purified by FC ( $\text{Al}_2\text{O}_3$  basic III (4.9%  $\text{H}_2\text{O}$ )) eluting with DCM/MeOH (1:0 to 20:1) to afford the product as a brown oil (50.7 mg, 0.08 mmol, 47%).

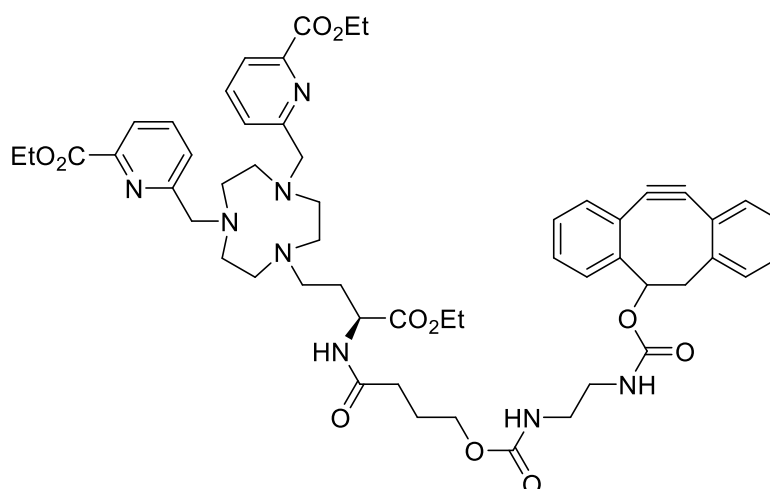
**$^1\text{H-NMR}$**  (400 MHz, Acetonitrile- $d_3$ ):  $\delta$  7.97 – 7.91 (m, 2H), 7.90 – 7.83 (m, 2H), 7.79 – 7.67 (m, 2H), 7.20 (s, 1H), 4.50 – 4.42 (m, 1H), 4.36 (q,  $J = 7.1$  Hz, 4H), 4.16 – 4.03 (m, 2H), 3.88 – 3.83 (m, 4H), 3.49 (t,  $J = 6.2$  Hz, 2H), 2.97 – 2.68 (m, 12H), 2.69 – 2.43 (m, 2H), 2.23 (t,  $J = 6.8$  Hz, 2H), 1.72 (p,  $J = 6.8$  Hz, 2H), 1.41 – 1.31 (m, 6H), 1.29 – 1.26 (m, 2H), 1.19 (t,  $J = 7.1$  Hz, 3H).

**HRMS** (nanochip-ESI/LTQ-Orbitrap)  $m/z$ :  $[\text{M} + \text{H}]^+$  Calcd for  $\text{C}_{34}\text{H}_{51}\text{N}_6\text{O}_8^+$  671.3763; Found 671.3746.

$^1\text{H}$  NMR spectrum:



## DIBO-TACNB-ester (29)

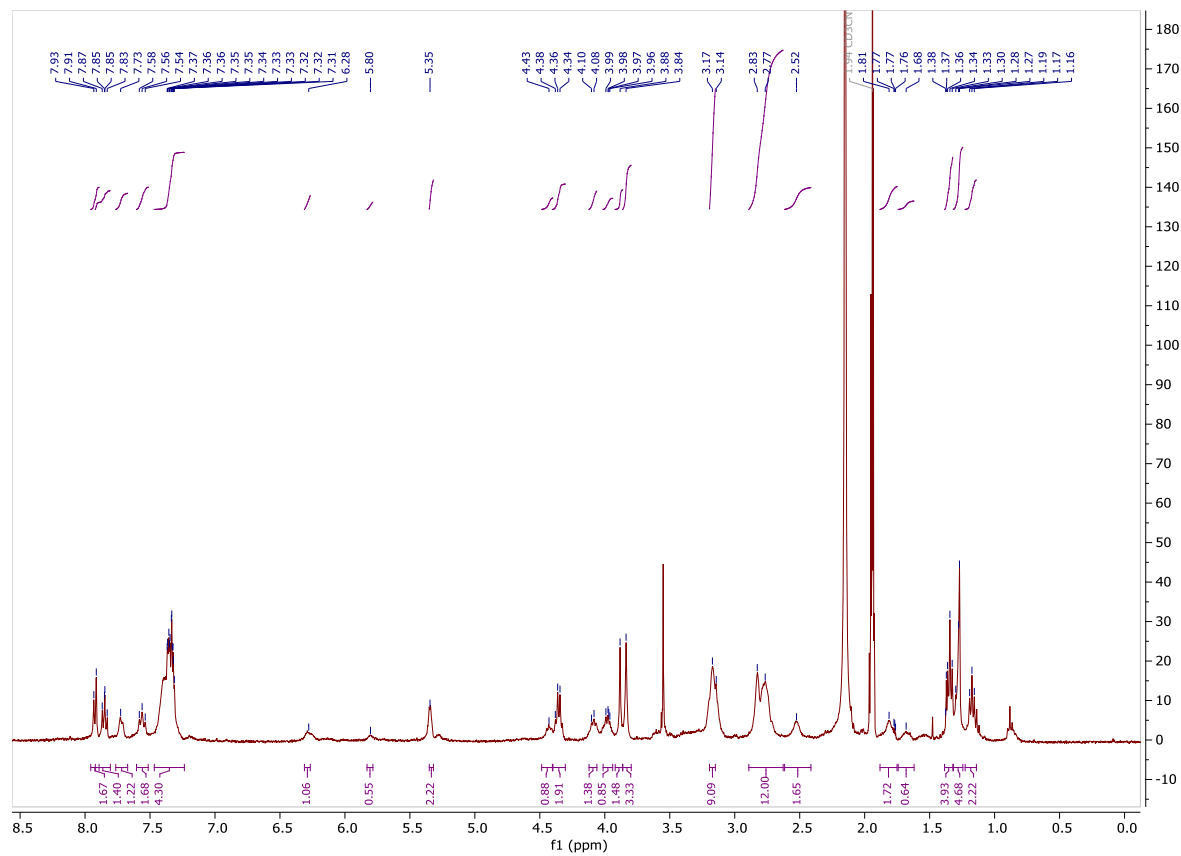


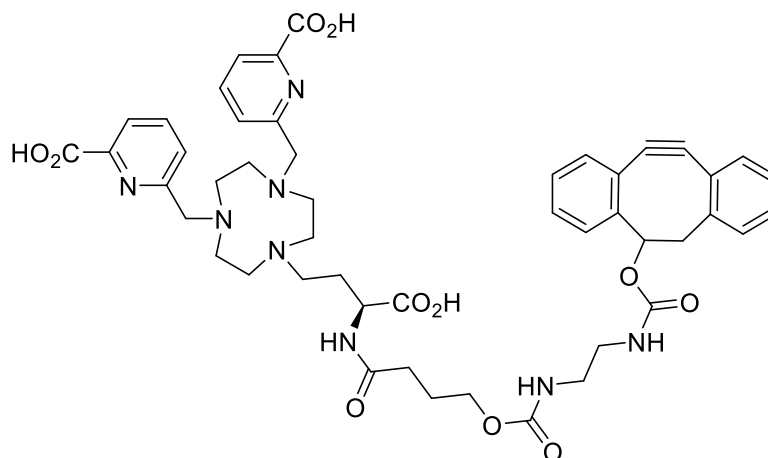
TACN-OH (86.5 mg, 0.13 mmol, 1.0 eq.) was dissolved in dry DCM (4 mL). Separately, 4-nitrophenyl chloroformate (51.98 mg, 0.26 mmol, 2.0 eq.) was dissolved in dry DCM (2 mL) and added to TACN-OH solution. Pyridine (52  $\mu$ L, 0.64 mmol, 5.0 eq.) was then added and the reaction mixture was stirred at r.t. for 16 h under argon. The solution was concentrated under reduced pressure and the residue was dissolved in dry DMF (4 mL). DIBO-NH<sub>2</sub> (79.01 mg, 0.26 mmol, 2.0 eq.) was dissolved in dry DMF (2 mL) and added to the previous mixture. DIPEA (112  $\mu$ L, 0.64 mmol, 5.0 eq.) was then added and the reaction mixture stirred at r.t. for 16 h under argon. The crude was concentrated under reduced pressure and purified by FC (Al<sub>2</sub>O<sub>3</sub> basic III (4.9% H<sub>2</sub>O)) eluting with Hexane/[DCM/MeOH (20:1)] (1:1 then 1:4) to afford the product as a light orange powder (62.7 mg, 0.06 mmol, 48%).

**<sup>1</sup>H-NMR** (400 MHz, Acetonitrile-d<sub>3</sub>):  $\delta$  7.96 – 7.89 (m, 2H, 5,5'-H), 7.92 – 7.81 (m, 2H, 6,6'-H), 7.76 – 7.67 (m, 2H, 7,7'-H), 7.60 – 7.51 (m, 1H, Ar-H), 7.47 – 7.24 (m, 7H, Ar-H), 6.28 (s, 1H, N-H), 5.80 (s, 1H, N-H), 5.35 (s, 2H, 31-H), 4.49 – 4.40 (m, 1H, 18-H), 4.35 (q, J = 7.1 Hz, 4H, 2,2'-H), 4.12 – 4.06 (m, 2H, 20-H), 4.01 – 3.94 (m, 2H, 25-H), 3.92 – 3.86 (m, 1H, 30-H), 3.86 – 3.80 (m, 4H, 9,9'-H), 3.19 – 3.15 (m, 4H, HN-CH<sub>2</sub>-CH<sub>2</sub>-NH), 2.89 – 2.63 (m, 12H, 10-H, 11-H, 12-H, 13-H, 14-H, 15-H), 2.62 – 2.41 (m, 2H, 16-H), 1.88 – 1.75 (m, 2H, 17-H), 1.74 – 1.62 (m, 2H, 24H), 1.35 (t, 6H, 1,1'-H), 1.32 – 1.24 (m, 2H, 24-H), 1.17 (t, J = 7.2 Hz, 3H, 21-H).

**HRMS** (ESI/QTOF) m/z: [M + H]<sup>+</sup> Calcd for C<sub>54</sub>H<sub>67</sub>N<sub>8</sub>O<sub>11</sub><sup>+</sup> 1003.4924; Found 1003.4896.

<sup>1</sup>H NMR spectrum:



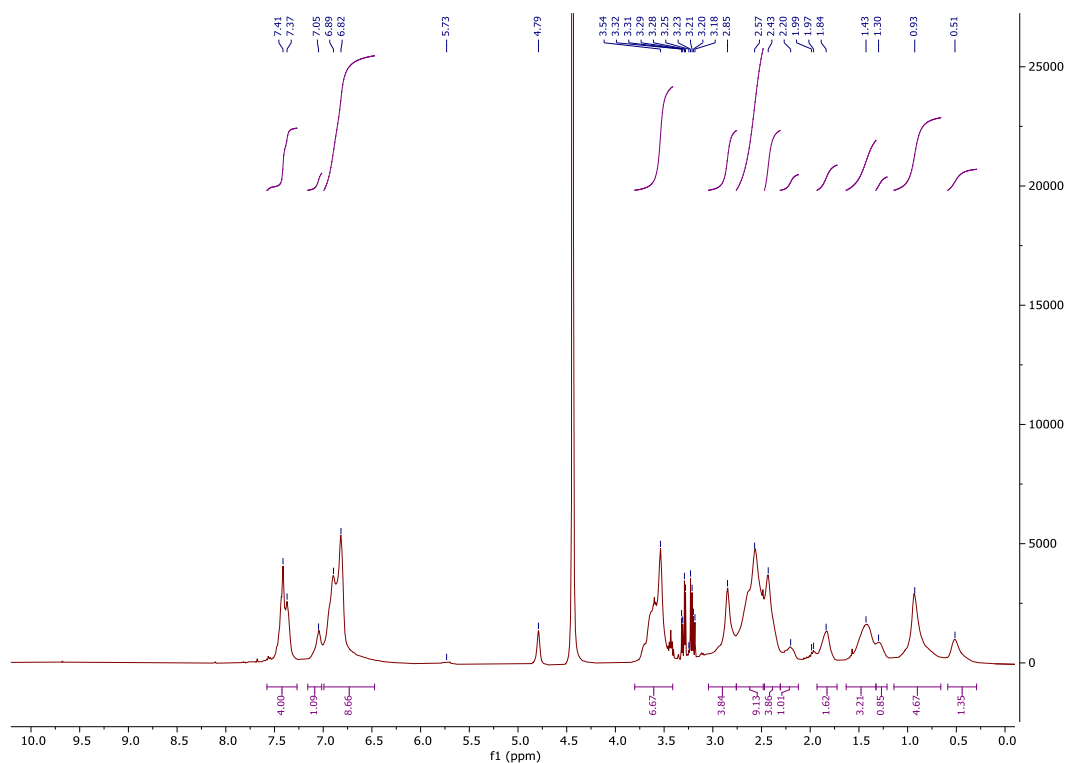
DIBO-TACNB ligand: **L<sub>D</sub>**

TACN-DIBO-ester (30 mg, 0.030 mmol, 1.0 eq.) was dissolved in EtOH (4 mL) and H<sub>2</sub>O (0.5 mL). Separately, LiOH (0.236 mg, 0.10 mmol, 3.3 eq.) was dissolved in H<sub>2</sub>O (0.5 mL) and added dropwise to the previous solution. The mixture was stirred at r.t. for 4 h. EtOH was evaporated under reduced pressure and the aqueous layer was diluted with 10% (v/v) EtOH. The solution was purified by dialysis against H<sub>2</sub>O/EtOH 9:1 for 1 day and then H<sub>2</sub>O for 1 day (MW cut-off 100-500 Da) and freeze dried. The product was recovered as a light brown solid (22.0 mg, 0.02 mmol, 80%).

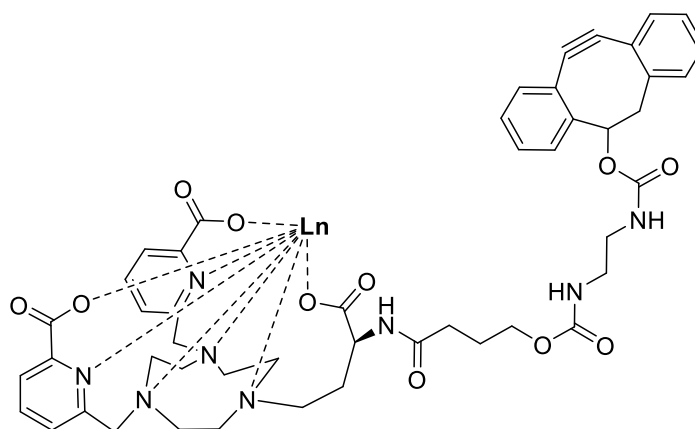
**<sup>1</sup>H NMR (400 MHz, D<sub>2</sub>O):** δ 7.39 (d, 4H), 7.05 (s, 1H), 6.86 (d, 9H), 3.54 (s, 7H), 2.85 (s, 4H), 2.57 (s, 9H), 2.43 (s, 4H), 2.20 (s, 1H), 1.84 (s, 2H), 1.43 (s, 3H), 1.30 (s, 1H), 0.93 (s, 5H), 0.51 (s, 1H).

**HRMS (ESI/QTOF) m/z:** [M + H]<sup>+</sup> Calcd for C<sub>48</sub>H<sub>55</sub>N<sub>8</sub>O<sub>11</sub><sup>+</sup> 919.3985; Found 919.3992.

<sup>1</sup>H NMR spectrum:



### Ln(III)-DIBO Complexes: [LnL<sub>D</sub>] 168



A solution of TACN-DIBO (5 mg, 5.44  $\mu\text{mol}$ , 1.0 eq.) in  $\text{H}_2\text{O}$  (500  $\mu\text{L}$ ) was acidified with  $\text{HCl}$  1M (3x10  $\mu\text{L}$ ). A solution of  $\text{LnCl}_3$  (6.54  $\mu\text{mol}$ , 1.2 eq.) in  $\text{H}_2\text{O}$  (100  $\mu\text{L}$ ) was added and the mixture was stirred at 37  $^\circ\text{C}$  for 16h. The pH of the reaction was kept between 5 and 7 until stabilization by addition of  $\text{NH}_4\text{OH}$  0.1M. The crude was purified by dialysis against  $\text{H}_2\text{O}/\text{EtOH}$  9:1 for 1 day and  $\text{H}_2\text{O}$  for 1 day (MW cut-off 100-500 Da). The product was recovered as an off-white powder in quantitative yield.

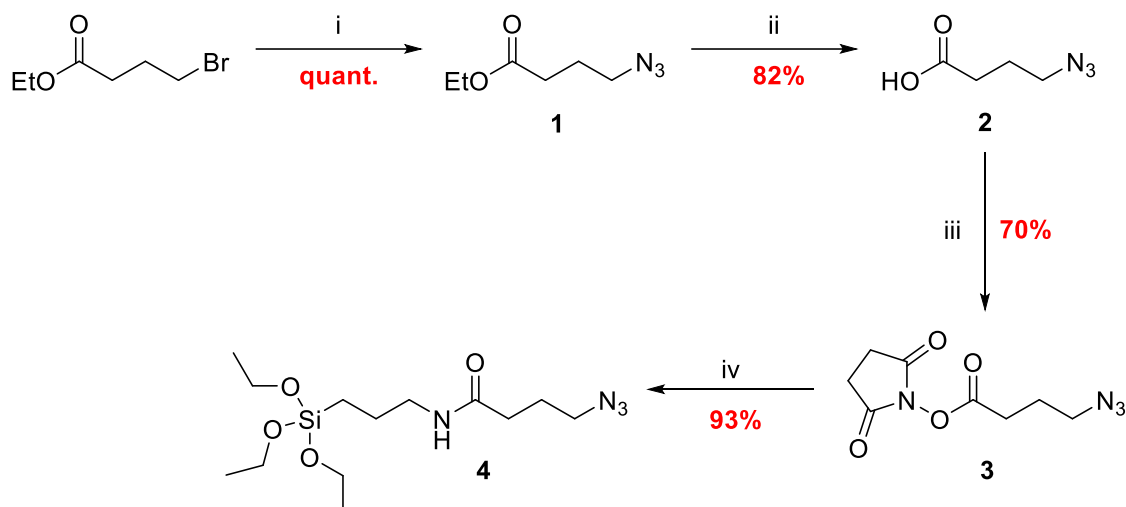
**HRMS** (ESI/QTOF)  $m/z$ :  $[\text{M} + \text{H}]^+$  Calcd for  $\text{C}_{48}\text{H}_{52}\text{EuN}_8\text{O}_{11}^+$  1069.2962; Found 1069.2986

**HRMS** (ESI/QTOF)  $m/z$ :  $[\text{M} + \text{Na}]^+$  Calcd for  $\text{C}_{48}\text{H}_{51}\text{GdN}_8\text{NaO}_{11}^+$  1096.2811; Found 1096.2863

**HRMS** (ESI/QTOF)  $m/z$ :  $[\text{M} + \text{H}]^+$  Calcd for  $\text{C}_{48}\text{H}_{52}\text{N}_8\text{O}_{11}\text{Yb}^+$  1090.3139; Found 1090.3117

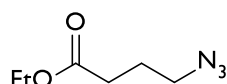


### 5.10. Synthesis of azide modified APTES



**Scheme 28: Synthesis of APTES-N<sub>3</sub>.** i- NaN<sub>3</sub>, MeOH / H<sub>2</sub>O, reflux, 7 h; ii- KOH, MeOH / H<sub>2</sub>O, 0°C to r.t, 6 h; iii- DCC, NHS, DCM, r.t, 4 h; iv- APTES, Et<sub>3</sub>N, DCM, r.t, 5 h.

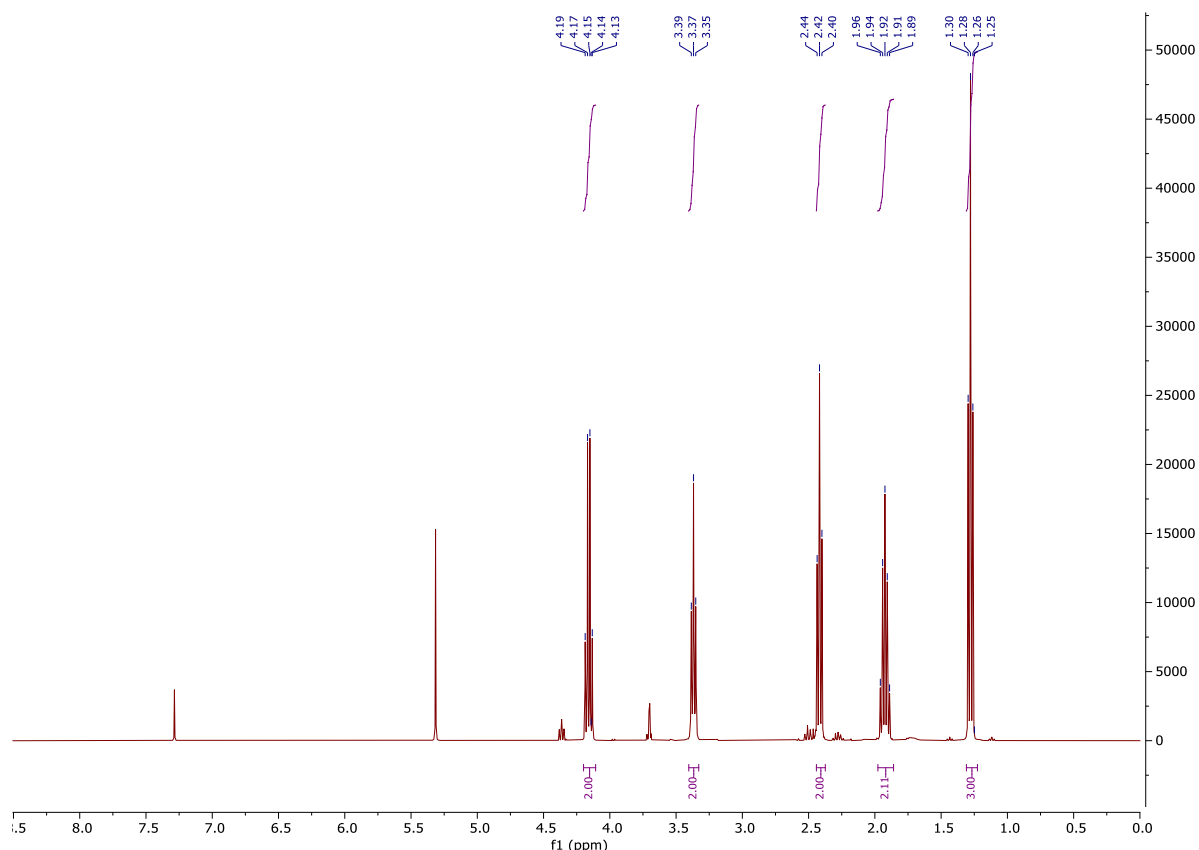
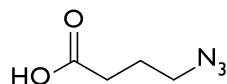
#### Ethyl 4-azidobutanoate (1)



Ethyl 4-bromobutanoate (2.2 mL, 15.4 mmol, 1.0 eq) and NaN<sub>3</sub> (2.0 g, 30.8 mmol, 2.0 eq) were dissolved in a mixture of MeOH / H<sub>2</sub>O (4:1, 30 mL) and the reaction mixture was refluxed for 7 h. MeOH was removed under reduced pressure and the residue was diluted with H<sub>2</sub>O (100 mL). The aqueous layer was extracted with DCM (3 X 100 mL). The combined organic layers were dried over MgSO<sub>4</sub>, filtered and concentrated under reduced pressure. The product (2.55 g, 15.4 mmol, quant.) was obtained as a colorless oil.

**<sup>1</sup>H NMR** (400 MHz, Chloroform-*d*): δ 4.16 (q, *J* = 7.1 Hz, 2H, CH<sub>2</sub> ester), 3.37 (t, *J* = 6.7 Hz, 2H, EtCO<sub>2</sub>-CH<sub>2</sub>-R), 2.42 (t, *J* = 7.2 Hz, 2H, R-CH<sub>2</sub>-N<sub>3</sub>), 1.92 (p, *J* = 7.0 Hz, 2H, R-CH<sub>2</sub>-CH<sub>2</sub>-N<sub>3</sub>), 1.28 (t, *J* = 7.1 Hz, 3H, CH<sub>3</sub> ester).

The analytical data were in accordance with previously reported data.<sup>154,155</sup>

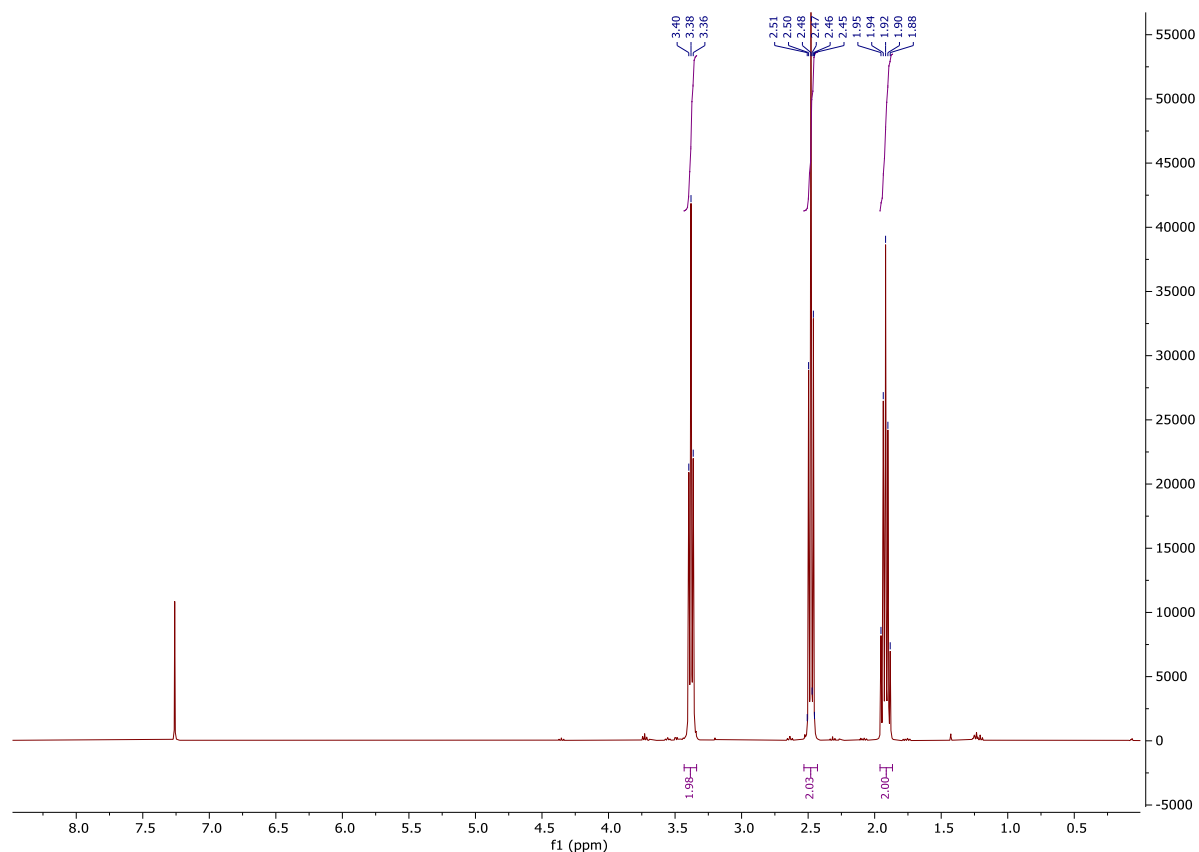
<sup>1</sup>H NMR spectrum:**4-Azidobutanoic acid (2)**

KOH (4.32 g, 77.0 mmol, 5.0 eq) was added to a solution of ethyl 4-azidobutanoate (2.55 g, 15.4 mmol, 1.0 eq) in a mixture of MeOH / H<sub>2</sub>O (55:45, 60 mL) at 0°C. The reaction mixture was allowed to warm up to r.t. and was stirred for 6 h. MeOH was removed under reduced pressure and the residue was diluted with H<sub>2</sub>O (50 mL). The aqueous layer was extracted with DCM (2 X 100 mL), then acidified to pH=1 with aqueous 1M HCl and extracted with Et<sub>2</sub>O (5 X 100 mL). The combined organic layers were dried over MgSO<sub>4</sub>, filtered and concentrated under reduced pressure. The product (1.71 g, 13.3 mmol, 82% yield) was obtained as a colorless oil.

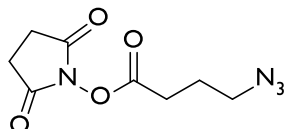
**<sup>1</sup>H NMR** (400 MHz, Chloroform-*d*): δ 3.38 (t, *J* = 6.7 Hz, 2H, HCO<sub>2</sub>-CH<sub>2</sub>-R), 2.48 (t, *J* = 7.2 Hz, 2H, R-CH<sub>2</sub>-N<sub>3</sub>), 1.92 (p, *J* = 7.0 Hz, 2H, R-CH<sub>2</sub>-CH<sub>2</sub>-N<sub>3</sub>).

The analytical data were in accordance with previously reported data.<sup>154,155</sup>

$^1\text{H}$  NMR spectrum:



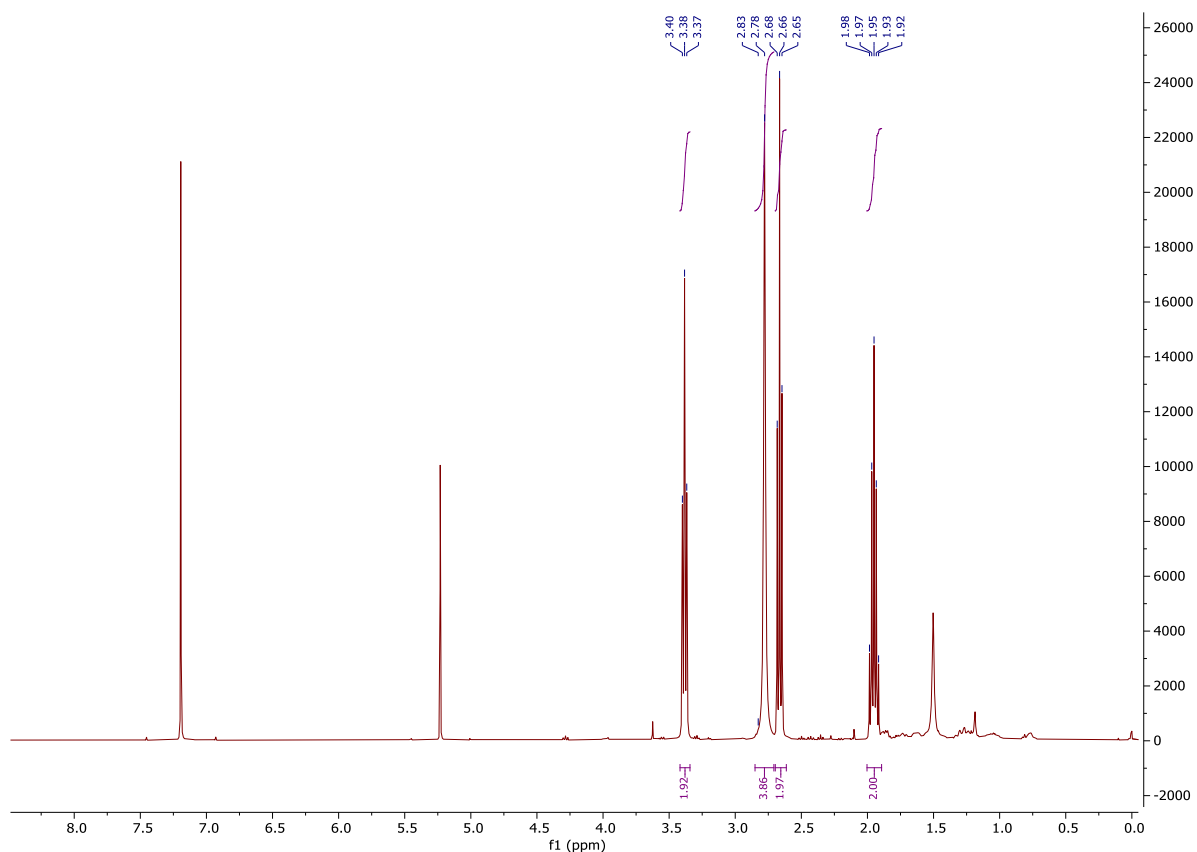
### 2,5-Dioxopyrrolidin-1-yl 4-azidobutanoate (3)



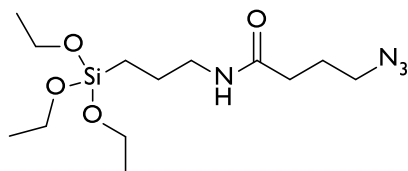
DCC (3.27 g, 15.8 mmol, 1.2 eq) was added to a solution of 4-azidobutanoic acid (1.7 g, 13.2 mmol, 1.0 eq) and NHS (1.83 g, 15.8 mmol, 1.2 eq) in dry DCM (70 mL). The reaction mixture was stirred at r.t for 4 h. Sat. aqueous KCl (70 mL) was added and the organic layer was separated, then washed with  $\text{H}_2\text{O}$  (70 mL), dried over  $\text{MgSO}_4$ , filtered and concentrated under reduced pressure. The crude product was purified by FC eluting with DCM / MeOH (99:1). The product (2.1 g, 9.2 mmol, 70% yield) was obtained as a white solid.

$^1\text{H}$  NMR (400 MHz, Chloroform-*d*):  $\delta$  3.38 (t,  $J = 6.6$  Hz, 2H, Suc-CO<sub>2</sub>-CH<sub>2</sub>-R), 2.78 (s, 4H, 2 X CH<sub>2</sub><sub>suc</sub>), 2.66 (t,  $J = 7.2$  Hz, 2H, R-CH<sub>2</sub>-N<sub>3</sub>), 1.95 (p,  $J = 6.9$  Hz, 2H, R-CH<sub>2</sub>-CH<sub>2</sub>-N<sub>3</sub>).

The analytical data were in accordance with previously reported data. <sup>154,155</sup>

<sup>1</sup>H NMR spectrum:

#### 4-Azido-*N*-(3-(triethoxysilyl)propyl)butanamide: APTES- $N_3$ (4)

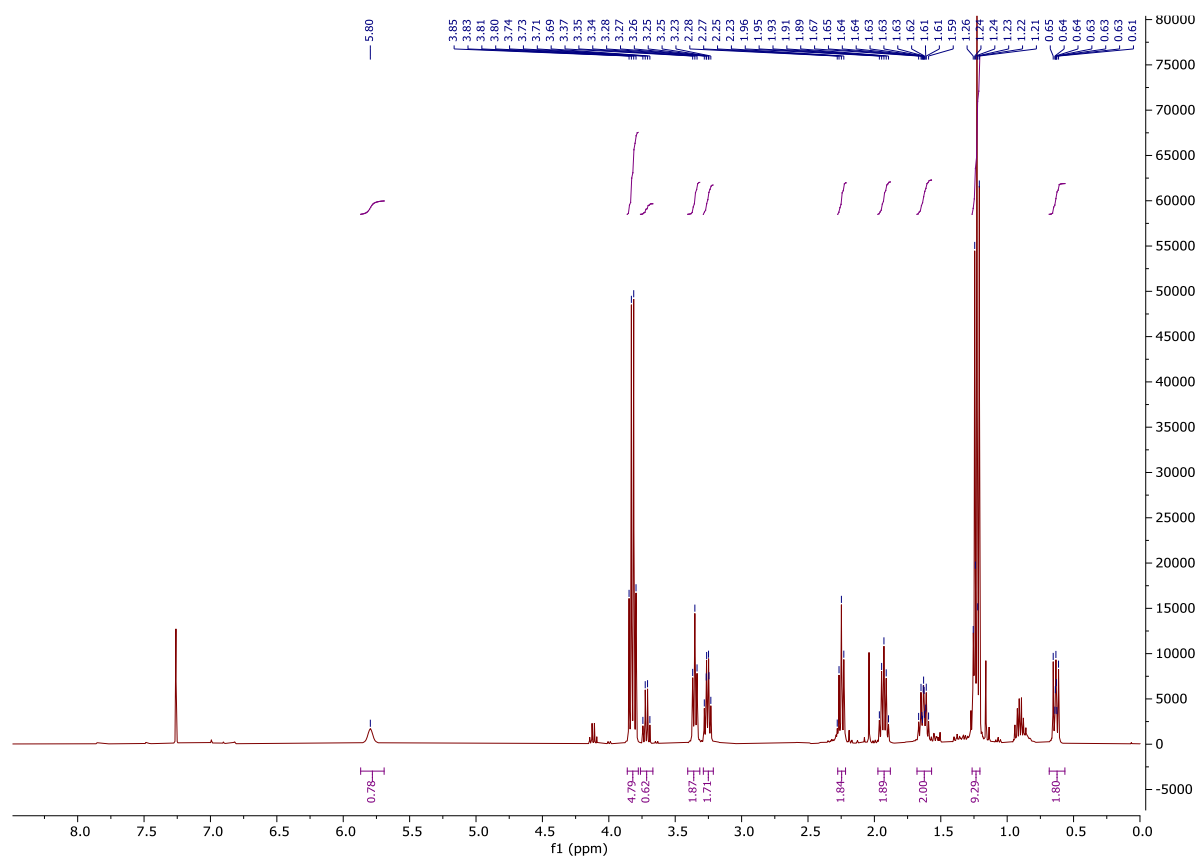


2,5-Dioxopyrrolidin-1-yl 4-azidobutanoate (0.20 g, 0.88 mmol, 1.0 eq) was dissolved in dry DCM (10 mL) under argon atmosphere. APTES (0.20 mL, 0.88 mmol, 1.0 eq) and Et<sub>3</sub>N (0.24 mL, 1.76 mmol, 2.0 eq) were added and the reaction mixture was stirred at r.t for 5 h. The solvent was removed under reduced pressure and the crude product was purified by FC eluting with (6:4 to 4:6). The product (270 mg, 0.82 mmol, 93% yield) was obtained as a colourless oil.

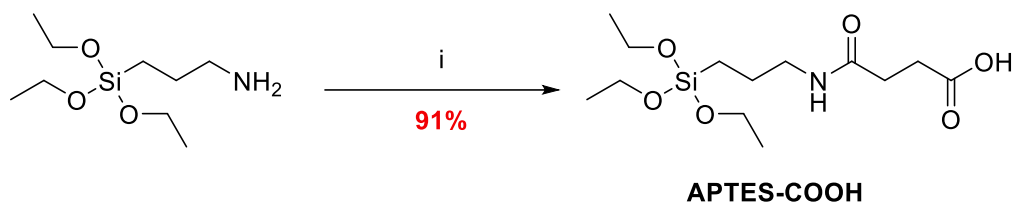
**<sup>1</sup>H NMR** (400 MHz, Chloroform-*d*):  $\delta$  5.80 (s, 1H, *NH*<sub>amide</sub>), 3.82 (q,  $J = 7.0$  Hz, 4H, 2 X *CH*<sub>2</sub>-OSi), 3.72 (q,  $J = 7.0$  Hz, 2H, *CH*<sub>2</sub>-OSi), 3.35 (t,  $J = 6.6$  Hz, 2H, *CH*<sub>2</sub>-CONHR), 3.26 (td,  $J = 6.9, 5.8$  Hz, 2H, *CH*<sub>2</sub>-NHCOR), 2.25 (t,  $J = 7.2$  Hz, 2H, *CH*<sub>2</sub>-N<sub>3</sub>), 1.93 (p,  $J = 6.9$  Hz, 2H, *CH*<sub>2</sub>-*CH*<sub>2</sub>-N<sub>3</sub>), 1.63 (m, 2H, *CH*<sub>2</sub>-*CH*<sub>2</sub>-Si), 1.23 (t,  $J = 7.0$ , 9H, 3 X *CH*<sub>3</sub>-*CH*<sub>2</sub>-OSi), 0.63 (m, 2H, *CH*<sub>2</sub>-Si).

The analytical data were in accordance with previously reported data.<sup>154,155</sup>

<sup>1</sup>H NMR spectrum:



### 5.11. Synthesis of carboxyl modified APTES: APTES-COOH



**Scheme 29: Synthesis of APTES-COOH.** i- succinic anhydride, dioxane, r.t, 1 h.

Succinic anhydride (0.58 g, 5.89 mmol, 1.25 eq) was dissolved in dioxane (5 mL) under stirring at 60°C. The solution was cooled to r.t. and APTES (1.1 mL, 4.7 mmol, 1.0 eq) was added dropwise. The reaction mixture was stirred at r.t. for 1 h. The solution was filtered and the solvent was removed under reduced pressure, to afford **APTES-COOH** (0.99 g, 3.1 mmol, 68% yield) as a yellow oil.

The analytical data were in accordance with previously reported data.<sup>155</sup>

**<sup>1</sup>H NMR** (400 MHz, Chloroform-*d*): δ 6.24 (s, 1H), 3.87 – 3.73 (m, 6H), 3.21 (dq, *J* = 11.9, 6.5 Hz, 2H), 2.64 (ddd, *J* = 7.5, 5.7, 4.2 Hz, 2H), 2.47 (ddd, *J* = 8.4, 5.7, 2.4 Hz, 2H), 1.60 (ddt, *J* = 13.8, 11.6, 4.7 Hz, 2H), 1.31 – 1.07 (m, 9H), 0.65 – 0.54 (m, 2H).

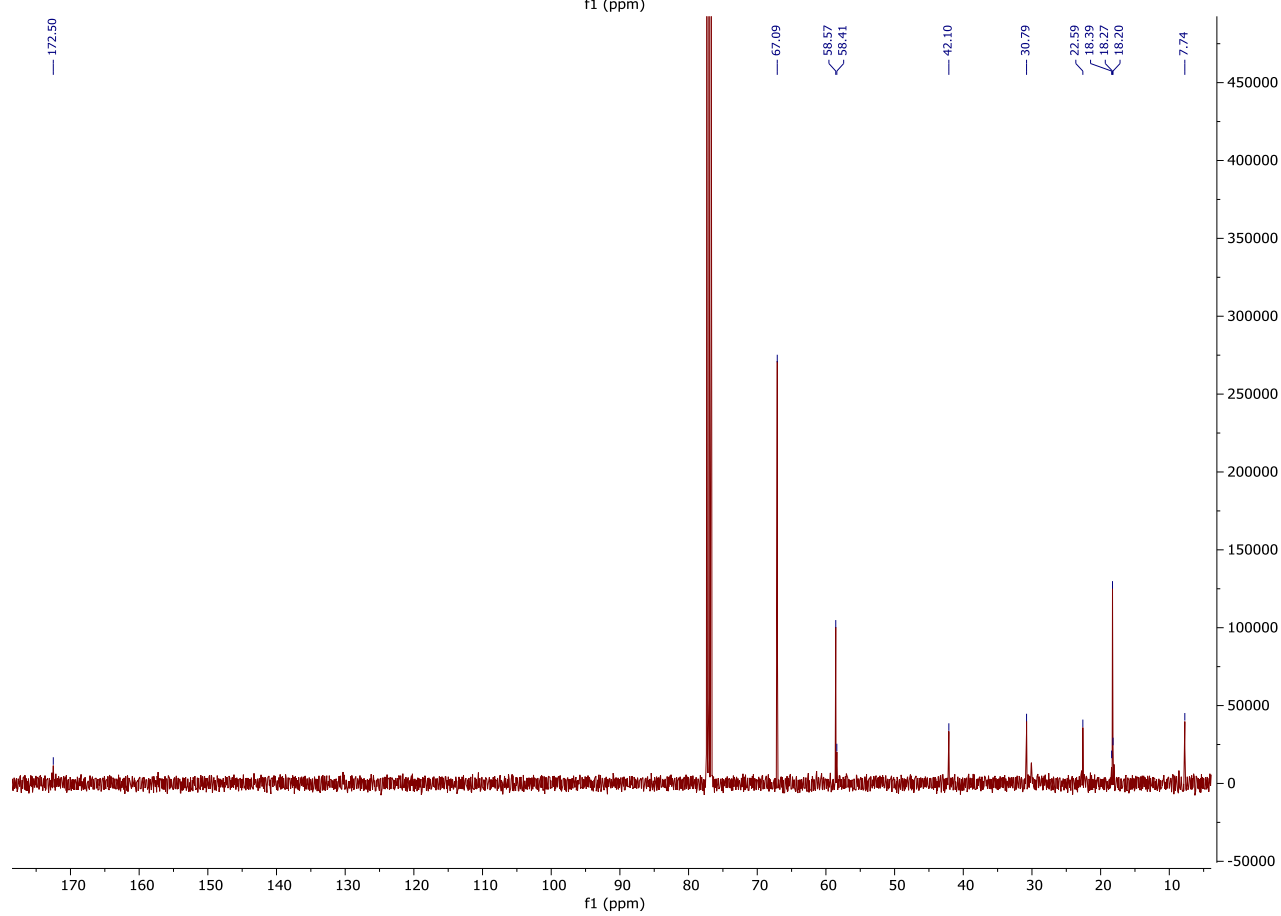
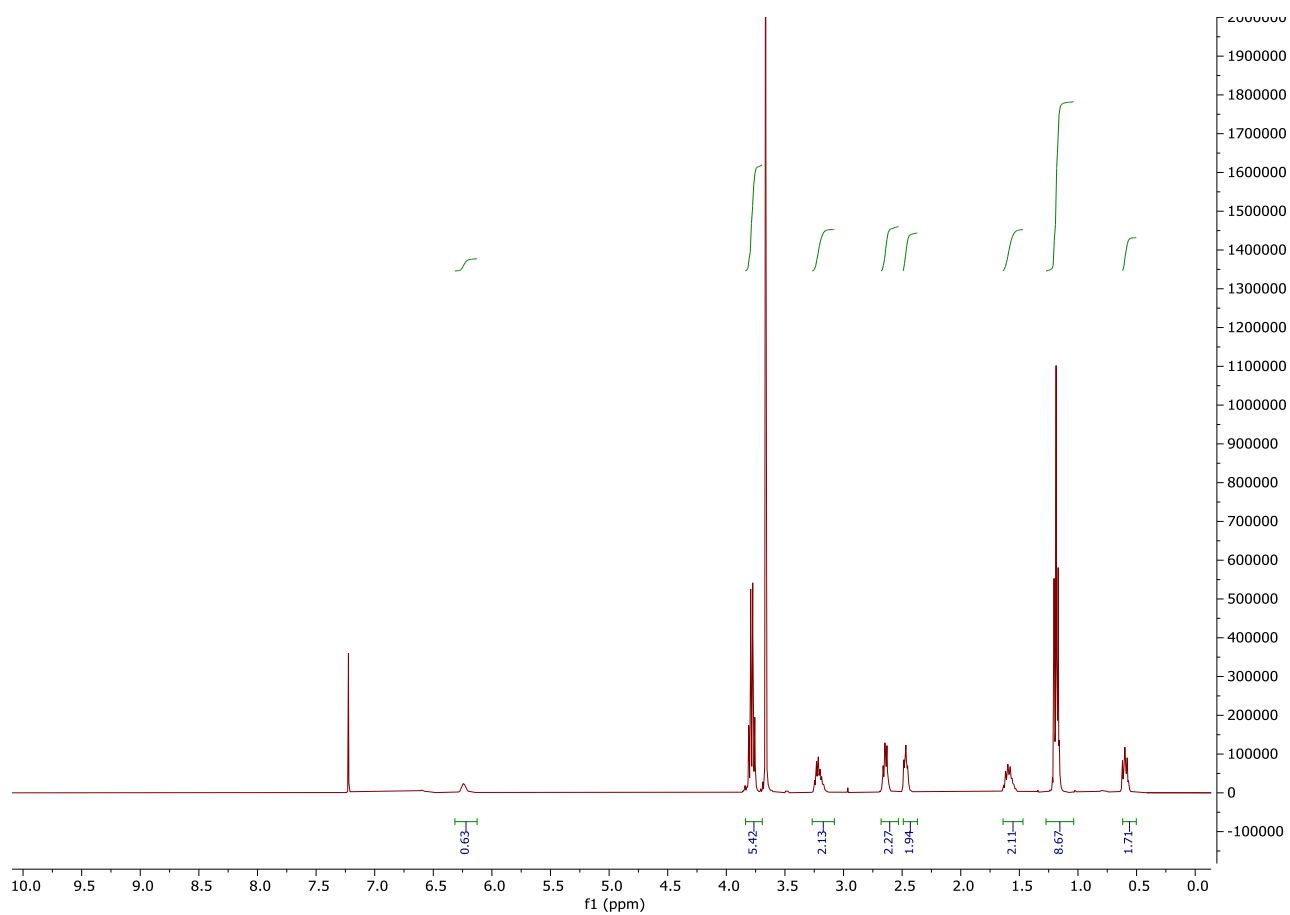
**<sup>13</sup>C NMR** (100 MHz, Chloroform-*d*): δ 172.5, 67.0, 58.6, 58.4, 42.1, 30.8, 22.6, 18.4, 18.3, 18.2, 7.7.

**HRMS** (ESI/QTOF) *m/z*: [M – H]<sup>-</sup> Calcd for C<sub>13</sub>H<sub>26</sub>NO<sub>6</sub>Si<sup>-</sup> 320.1535; Found 320.1540.

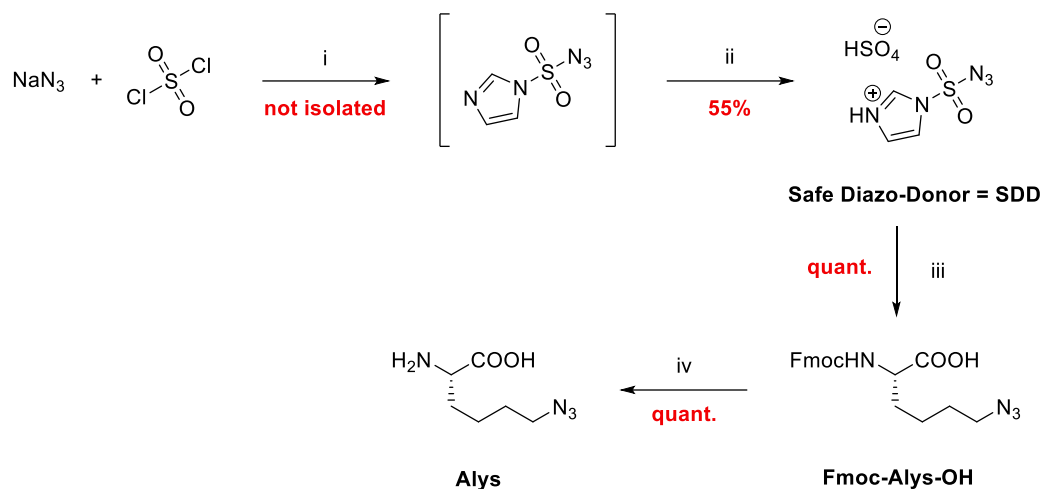
**FTIR** (neat, cm<sup>-1</sup>): 3263, 3091, 2973, 2928, 2884, 1784, 1726, 1669, 1645, 1564, 1433, 1394, 1364, 1346, 1297, 1255, 1225, 1190, 1167, 1101, 1076, 1005, 952, 848, 775, 679.

<sup>1</sup>H and <sup>13</sup>C NMR spectra:

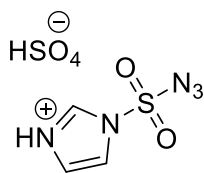
# Experimental



## 5.12. Synthesis of azidolysine (Alys) amino acid



**Scheme 30: Synthesis of Fmoc-Alys-OH.** i- imidazole, dry EtOAc, 0 °C, 20 h; ii- H<sub>2</sub>SO<sub>4</sub>, dry EtOAc, 0 °C, 1 h; iii- Fmoc-Lys-OH, CuSO<sub>4</sub>, NaHCO<sub>3</sub>, MeOH / H<sub>2</sub>O 4:1, r.t, 5 h; iv- piperidine 20% in DMF, r.t, 1 h.

Imidazole-1-sulfonyl azide, hydrogen sulfate salt: SDD <sup>170</sup>

NaN<sub>3</sub> (5.0 g, 77 mmol, 1.0 eq) was suspended in dry EtOAc (80 mL) and cooled to 0 °C under argon. Sulfuryl chloride (6.2 mL, 77 mmol, 1.0 eq) was added dropwise and the reaction mixture was allowed to warm to r.t and stirred for 18 h. The mixture was cooled to 0 °C and imidazole (10.0 g, 146 mmol, 1.9 eq) was slowly added while maintaining an inert atmosphere. The reaction mixture was stirred at 0 °C for 3 h, and then basified by very slow addition of sat. aqueous NaHCO<sub>3</sub> (100 mL). The aqueous layer was discarded and the organic layer was washed with H<sub>2</sub>O (80 mL). After separation, the organic layer was dried over MgSO<sub>4</sub> and filtered. The filtrate was cooled to 0 °C, under argon. Concentrated H<sub>2</sub>SO<sub>4</sub> (4.1 mL, 77 mmol, 1.0 eq) was added dropwise, and the mixture was stirred for 1 h at 0 °C. The reaction was left to slowly warm to r.t. The solution was filtered and the solid was washed with cooled EtOAc. After drying under high vacuum for 24 h, the product was afforded as a white solid (11.5 g, 42 mmol, 55%), and was stored under argon at -20 °C.

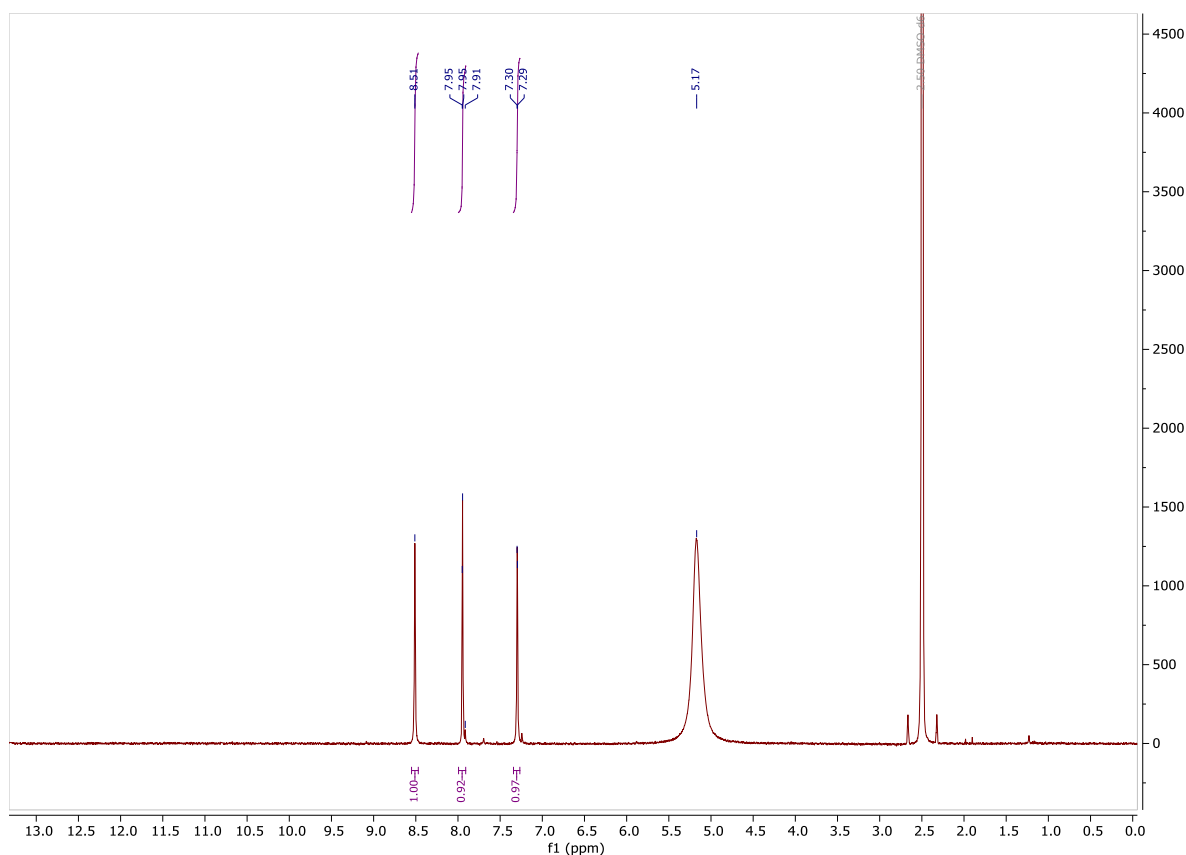
The analytical data were in accordance with previously reported data. <sup>170</sup>

**<sup>1</sup>H-NMR (400 MHz, DMSO-d<sub>6</sub>):** δ 8.51 (s, 1H), 7.95 (d, J = 1.5 Hz, 1H), 7.34 – 7.27 (m, 1H).

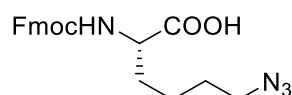
**HRMS (nanochip-ESI/LTQ-Orbitrap) m/z:** [M + Na]<sup>+</sup> Calcd for C<sub>3</sub>H<sub>4</sub>N<sub>5</sub>O<sub>2</sub>SNa<sup>+</sup> 174.0079; Found 174.0080.

<sup>1</sup>H NMR spectrum:





### Fmoc-Alys-OH <sup>171</sup>

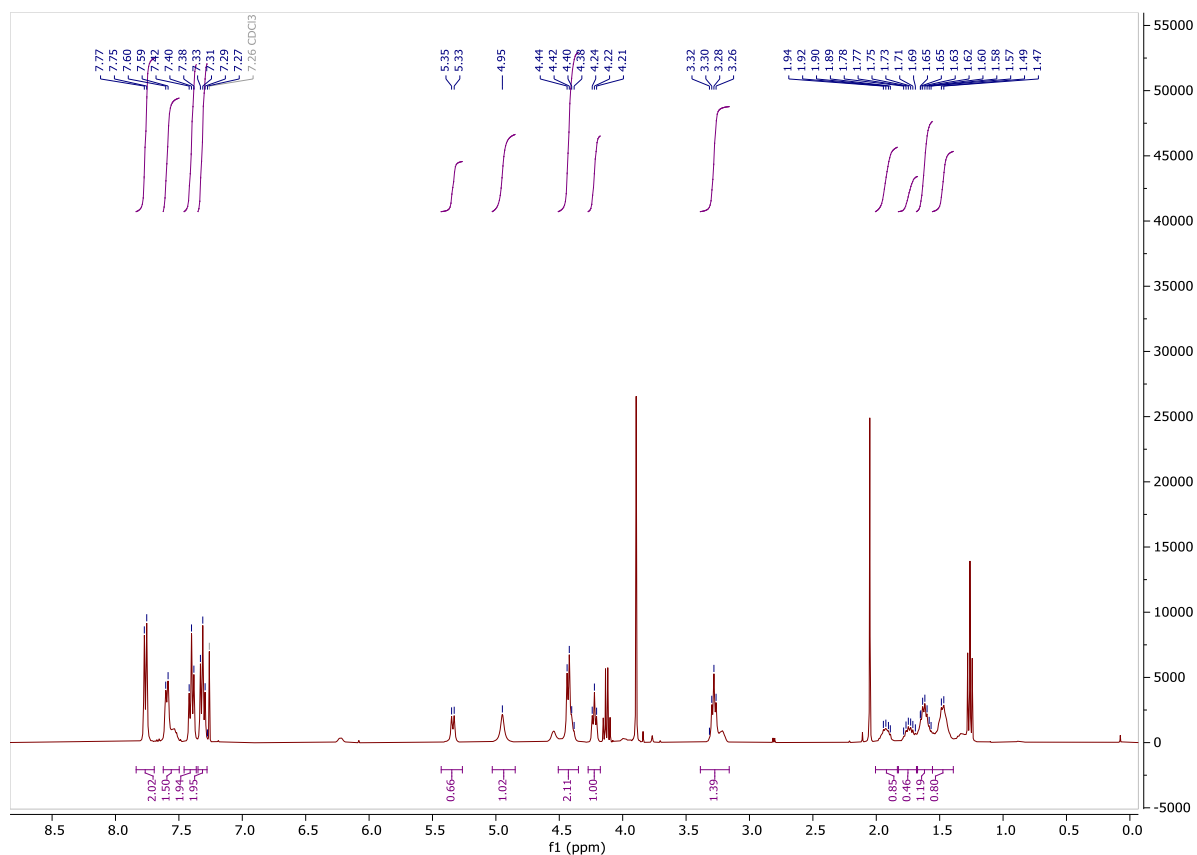
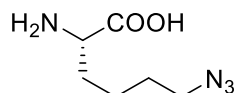


Fmoc-Lys-OH.HCl (1.0 g, 2.7 mmol, 1.0 eq), CuSO<sub>4</sub> (70 mg, 0.41 mmol, 0.15 eq) and NaHCO<sub>3</sub> (0.8 g, 9.5 mmol, 3.5 eq) were suspended in MeOH / H<sub>2</sub>O 4:1 (10 mL). The SDD (0.9 g, 3.3 mmol, 1.2 eq) was added and the pH was maintained to 8-9 by addition of aqueous 1M NaOH (continuous monitoring with pH meter). The reaction mixture was stirred for 5 h at r.t. MeOH was removed under reduced pressure and the residual solution was diluted with sulfate buffer pH 2 (50 mL) and extracted with EtOAc (50 mL, 3 times). The combined organic layers were washed with brine (2 X 50 mL), dried over MgSO<sub>4</sub>, filtered and concentrated under reduced pressure to afford the product as a yellow oil (1.1 g, 2.7 mmol, quant).

The analytical data were in accordance with previously reported data. <sup>171</sup>

**<sup>1</sup>H-NMR** (400 MHz, Chloroform-d): δ 7.76 (d, J = 7.5 Hz, 2H), 7.59 (d, J = 7.5 Hz, 2H), 7.40 (t, J = 7.5 Hz, 2H), 7.31 (t, J = 7.4 Hz, 2H), 5.34 (d, J = 8.2 Hz, 1H), 4.95 (s, 1H), 4.51 – 4.35 (m, 2H), 4.22 (t, J = 6.9 Hz, 1H), 3.28 (t, J = 6.8 Hz, 2H), 2.01 – 1.83 (m, 1H), 1.83 – 1.67 (m, 1H), 1.68 – 1.56 (m, 2H), 1.56 – 1.39 (m, 2H).

**HRMS** (nanochip-ESI/LTQ-Orbitrap) m/z: [M + Na]<sup>+</sup> Calcd for C<sub>21</sub>H<sub>22</sub>N<sub>4</sub>O<sub>4</sub>Na<sup>+</sup> 417.1554; Found 417.1533.

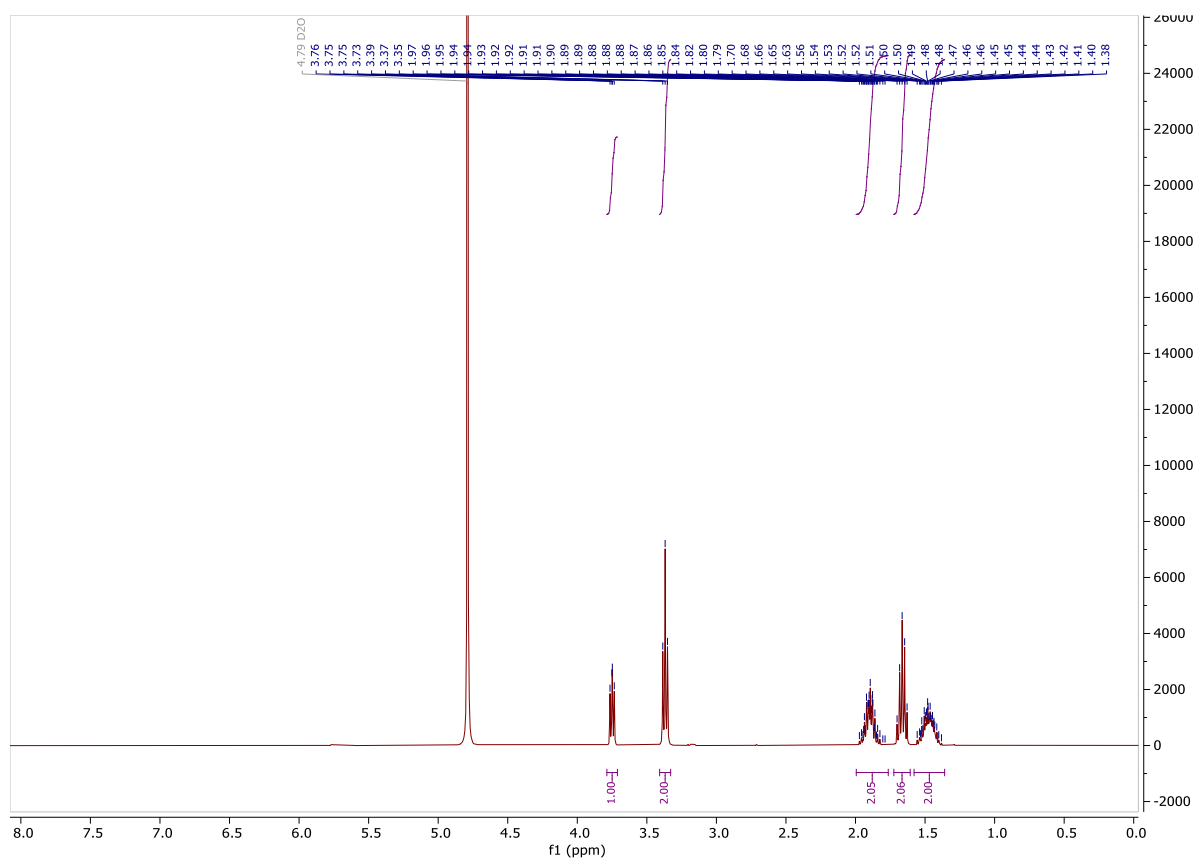
<sup>1</sup>H NMR spectrum:**H-Alys-OH** <sup>171</sup>

Fmoc-Lys(N<sub>3</sub>)-OH (4.6 g, 12 mmol) was dissolved in a piperidine solution (20%) in DMF (100 mL). The mixture was stirred at r.t. for 1h. The solvent was removed under reduced pressure and the residue was dissolved in H<sub>2</sub>O (300 mL). The aqueous layer was washed with CHCl<sub>3</sub> (4 X 300 mL) and lyophilized to afford the crude product as a white solid (3 g, quant.). The crude product was purified by FC (RP-C18) eluting with H<sub>2</sub>O to afford the product as white solid.

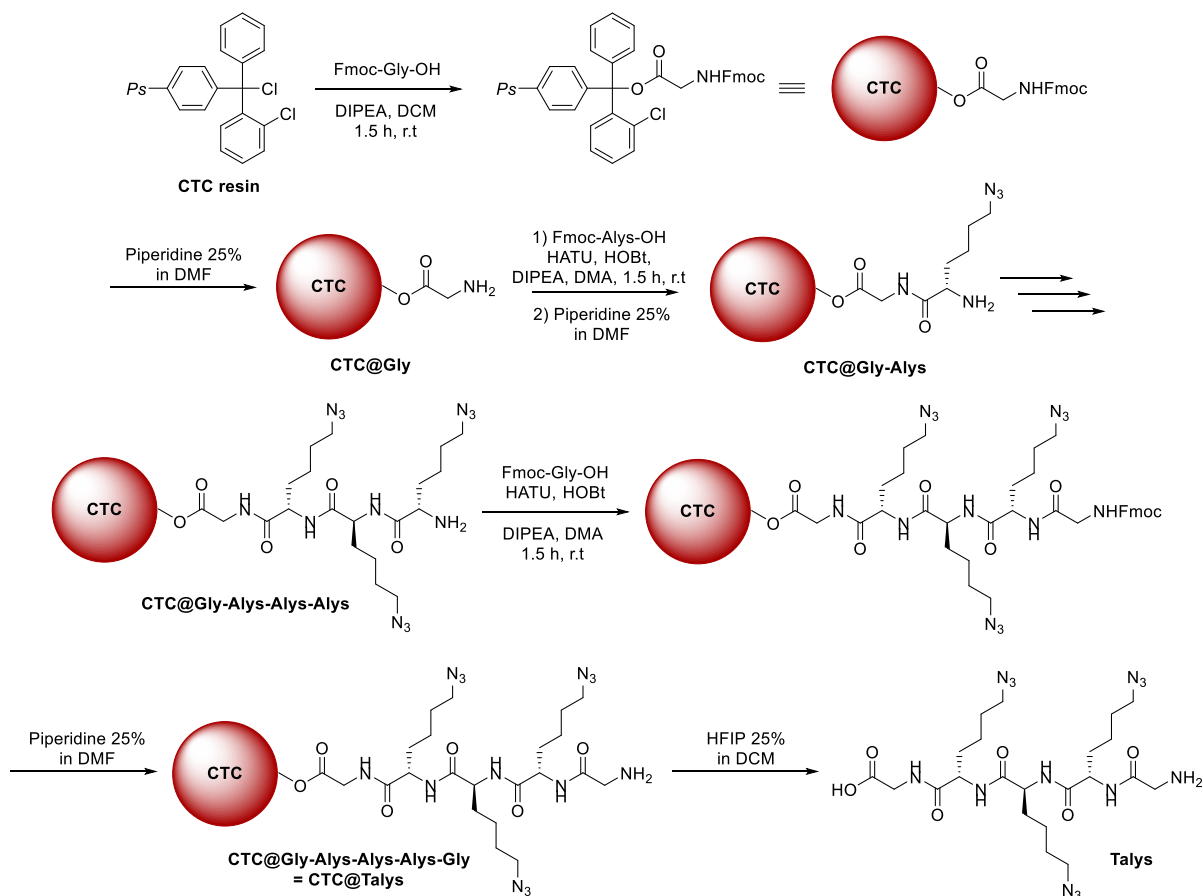
The analytical data were in accordance with previously reported data. <sup>171</sup>

**<sup>1</sup>H-NMR** (400 MHz, D<sub>2</sub>O): δ 3.75 (dd, J = 6.7, 5.6 Hz, 1H, 2-H), 3.37 (t, J = 6.8 Hz, 2H, 6-H), 1.99 – 1.76 (m, 2H, 3-H), 1.67 (p, J = 7.2 Hz, 2H, 5-H), 1.58 – 1.36 (m, 2H, 4-H).

<sup>1</sup>H NMR spectrum:



### 5.13. Synthesis of triazidoalysine (Talys) peptide



Scheme 31: Synthesis of Talys by SPPS.

#### Glycine loading on 2-chlorotrityl chloride resin

The 2-chlorotrityl chloride (CTC) resin (0.5 g, 0.8 mmol, 1.0 eq) was loaded in a solid phase extraction (SPE) tube, swollen for 30 min at r.t. in dry DCM (10 mL), and then washed with dry DCM (3 X 5 mL). Fmoc-Gly-OH (0.5 g, 1.6 mmol, 2.0 eq) was added to the tube, which was degassed by alternating argon / vacuum cycles (3 times). DIPEA (0.55 mL, 3.2 mmol, 4.0 eq) diluted in dry DCM (5 mL) was added and the tube was shaken under argon for 1.5 h at r.t. The resin suspension was filtered and washed with DMA (6 X 5 mL). A mixture of DCM / MeOH / DIPEA (80/15/5, 15 mL) was added. The tube was shaken for 10 min at r.t. and the suspension was filtered; this process was repeated twice. The resin was then washed with DMA (6 X 5 mL).

Cleavage of the Fmoc group was performed by addition of piperidine 25% in DMF (10 mL) and the tube was shaken for 5 min at r.t.. The suspension was filtered and washed with DMA (2 X 5 mL) and DCM (2 X 5 mL). Piperidine 25% (10 mL) was added again and the tube was shaken for 15 min at r.t.. The suspension was filtered. This step was repeated twice. The resin was washed with DMA (5 mL, 6 times), DCM (5 mL, 3 times), MeOH (5 mL, 3 times) and finally DCM again (5 mL, 6 times). The resin was dried under vacuum overnight.

#### Alys successive coupling

The CTC@Gly resin was swollen for 30 min at r.t in DCM (10 mL), then filtered and washed with DCM (5 mL) and DMA (5 mL). A solution of Fmoc-Alys-OH (synthesis described in section 5.12; 0.47 g, 1.2 mmol, 1.5 eq), HATU (0.37 g, 0.96 mmol, 1.2 eq), and HOBt (0.13 g, 0.96 mmol, 1.2 eq) was prepared in DMA (5 mL). DIPEA (0.42 mL, 2.4 mmol, 3.0 eq) was added and the resulting solution was added to the resin. The tube was shaken for 1.5 h at r.t.. The suspension was filtered and washed with DMA (6 X 5 mL) and DCM (6 X 5 mL). The progress of the coupling reaction was monitored by a Kaiser test.

Cleavage of the Fmoc- group was performed as above described.

This protocol was repeated two more times to afford CTC@Gly-Alys-Alys-Alys.

### Final glycine coupling

The CTC@Gly-Alys-Alys-Alys resin was swollen for 30 min at r.t. in DCM (10 mL), then filtered and washed with DCM (5 mL) and DMA (5 mL). A solution of Fmoc-Gly-OH (0.36 g, 1.2 mmol, 1.5 eq), HATU (0.37 g, 0.96 mmol, 1.2 eq), and HOBt (0.13 g, 0.96 mmol, 1.2 eq) was prepared in DMA (5 mL). DIPEA (0.42 mL, 2.4 mmol, 3.0 eq) was added and the resulting solution was then added to the resin. The tube was shaken for 1.5 h at r.t.. The suspension was filtered and washed with DMA (6 x 5 mL) and DCM (6 x 5 mL). The progress of the coupling reaction was monitored by a Kaiser test.

Cleavage of the Fmoc- group was performed as above described.

### Peptide cleavage from resin

The CTC@**Talys** resin was transferred to a flask and hexafluoro-2-propanol (HFIP) 25% in DCM (10 mL) was added. The resin was stirred at r.t. for 1 h, then diluted with HFIP (5 mL) and filtered. This step was repeated twice. The combined filtrates were concentrated under reduced pressure. The crude product was purified by preparative HPLC equipped with a C18 RP Waters OBD column. A linear gradient of solvent B (0.1% TFA in MeCN) over solvent A (0.1% TFA in water) rising linearly from 20% to 45% during  $t = 2.00\text{--}32.00$  min was applied at a flow rate of 14.0 mL/min. Pure fractions containing the desired product were unified and lyophilized to afford **Talys** as a colorless fluffy material (0.38 g, 0.64 mmol, 80%).

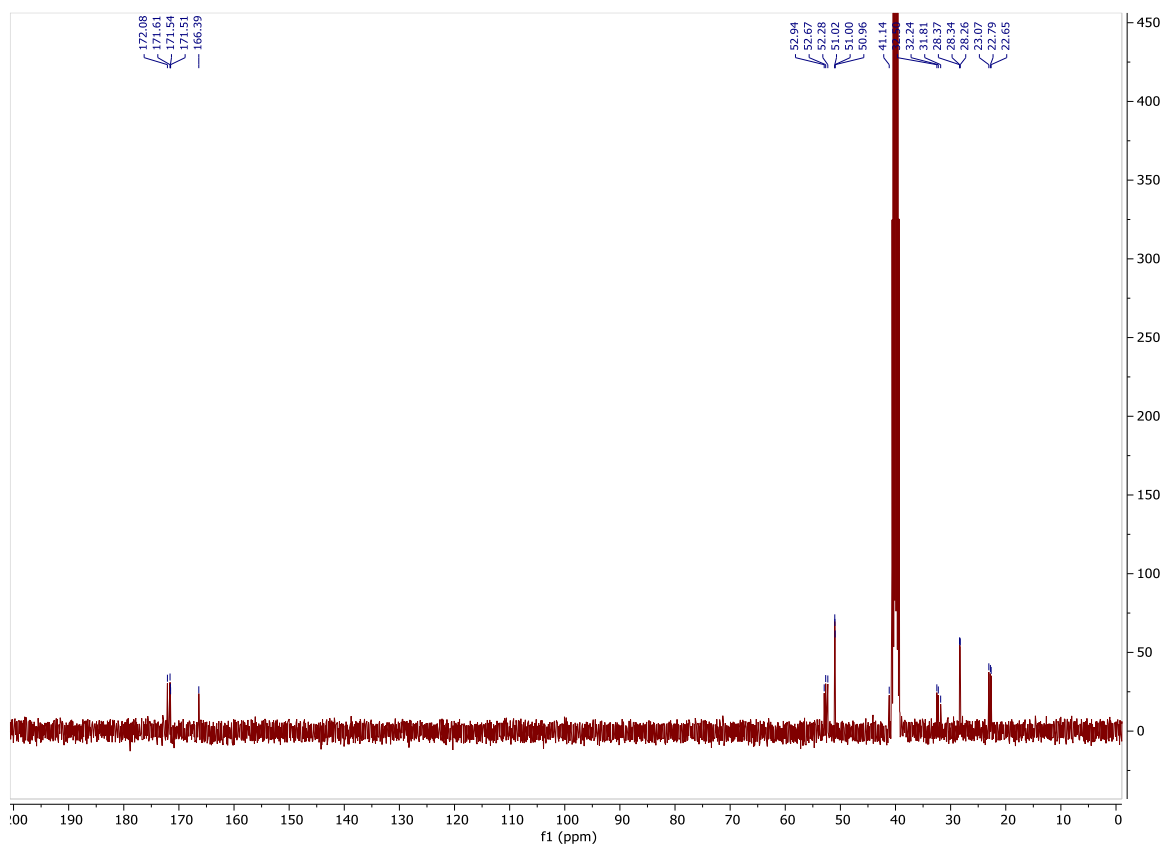
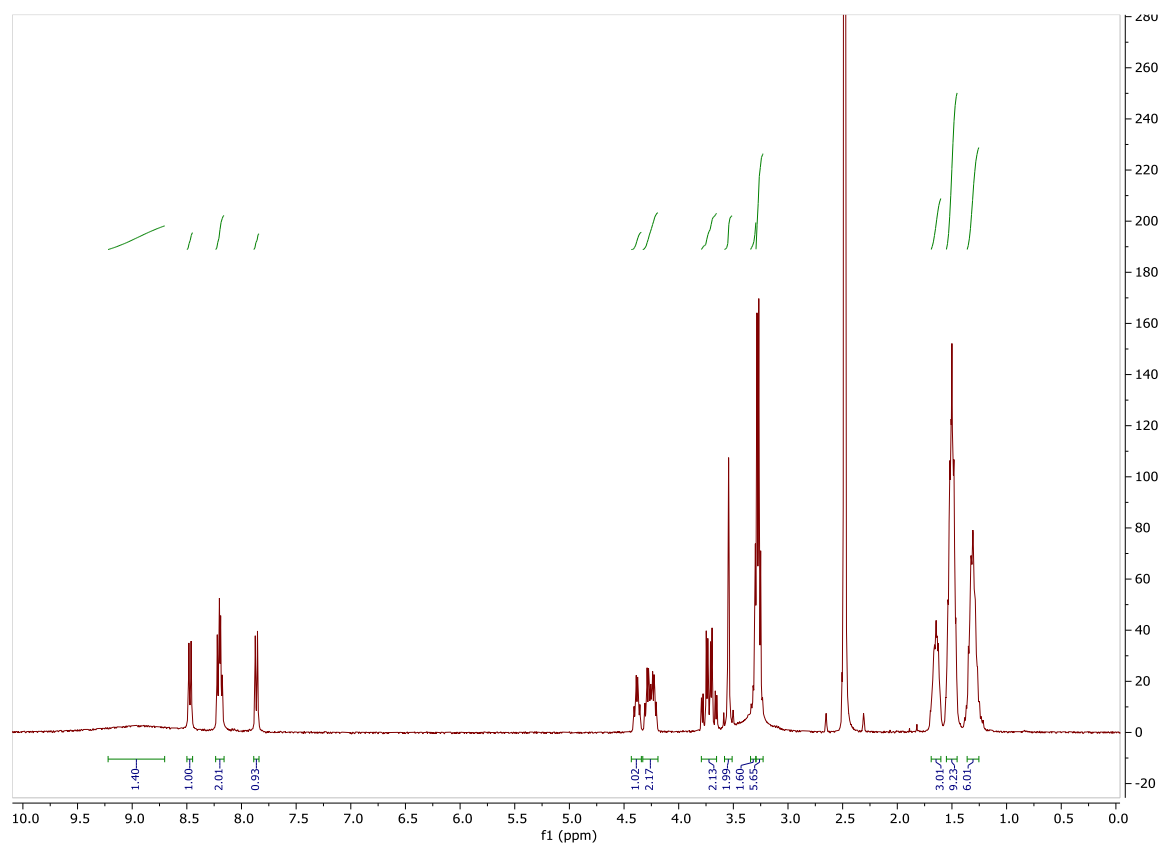
**<sup>1</sup>H NMR** (400 MHz, DMSO-*d*<sub>6</sub>):  $\delta = 8.95$  (s, 1H), 8.49 (d,  $J = 8.1$  Hz, 1H), 8.25 – 8.18 (m, 2H), 7.88 (d,  $J = 8.2$  Hz, 1H), 4.40 (td,  $J = 8.2, 5.1$  Hz, 1H), 4.28 (dtd,  $J = 20.1, 8.3, 5.2$  Hz, 2H), 3.81 – 3.67 (m, 2H), 3.56 (d,  $J = 1.7$  Hz, 2H), 3.36 – 3.31 (m, 2H), 3.31 – 3.25 (m, 6H), 1.71 – 1.62 (m, 3H), 1.52 (dq,  $J = 9.9, 6.7, 6.2$  Hz, 9H), 1.33 (p,  $J = 8.1$  Hz, 6H).

**<sup>13</sup>C NMR** (100 MHz, DMSO-*d*<sub>6</sub>):  $\delta = 172.08, 171.61, 171.54, 171.51, 166.39, 52.94, 52.67, 52.28, 51.02, 51.00, 50.96, 41.14, 32.50, 32.24, 31.81, 28.37, 28.34, 28.26, 23.07, 22.79, 22.65$ .

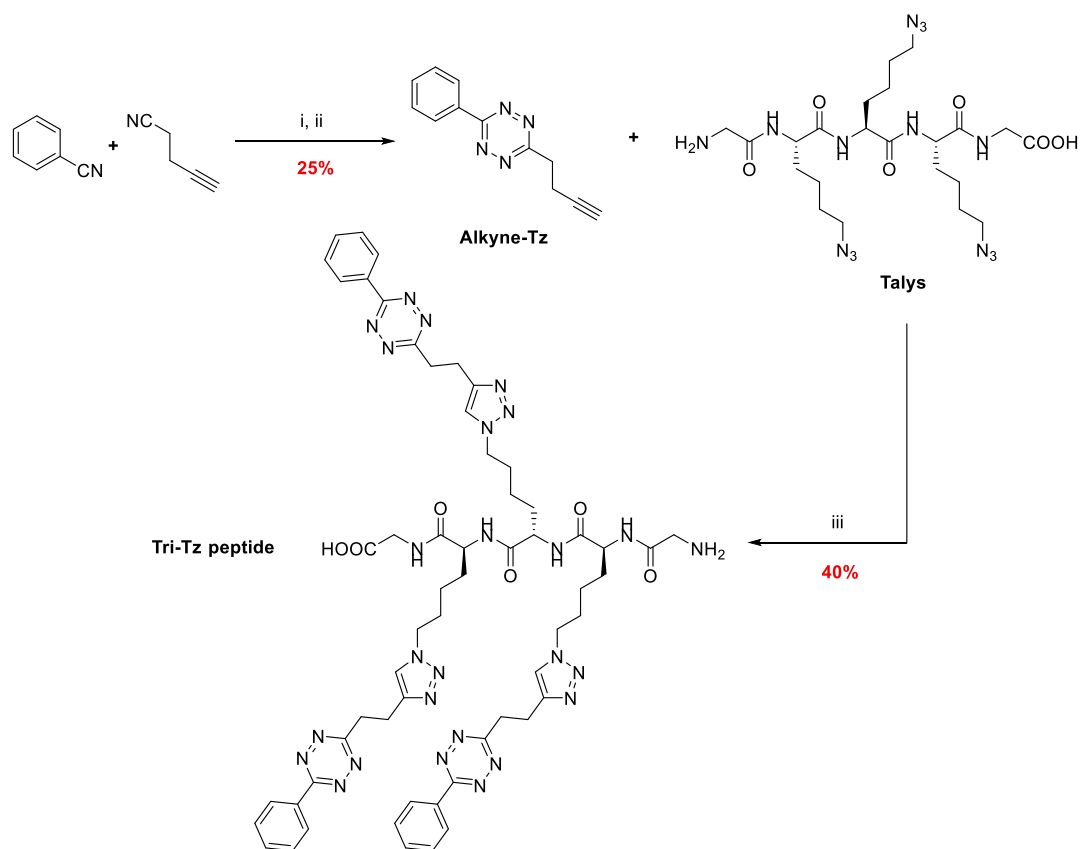
**HRMS** (nanochip-ESI/LTQ-Orbitrap)  $m/z$ :  $[M + H]^+$  Calcd for C<sub>22</sub>H<sub>39</sub>N<sub>14</sub>O<sub>6</sub>N<sup>+</sup> 595.3172; Found 595.3181.

**FTIR** (neat, cm<sup>-1</sup>): 3275, 2942, 2093, 1696, 1662, 1626, 1530, 1429, 1251, 1199, 1182, 1136, 923, 837, 799, 722.

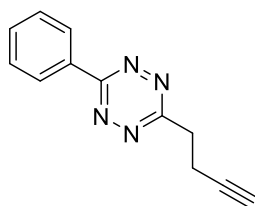
$^1\text{H}$  and  $^{13}\text{C}$  NMR spectra:



## 5.14. Synthesis of tri-tetrazine peptide



**Scheme 32: Talys modification with Tz.** i- mercaptopropionic acid, hydrazine monohydrate, neat, 50 °C, 24 h; ii- NaNO<sub>2</sub>, HCl, H<sub>2</sub>O, r.t, 1 h; iii- CuSO<sub>4</sub>, NaAsc, THTPA, THF/H<sub>2</sub>O 1:1, r.t, 2 h.

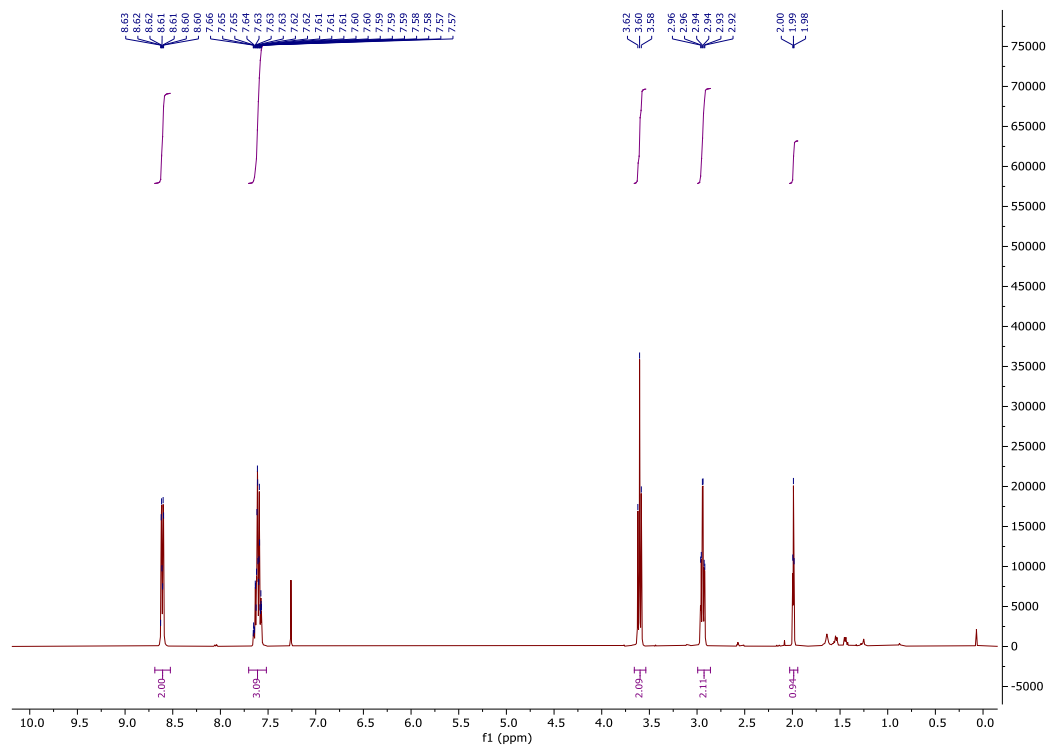
Alkyne-Tz <sup>172</sup>

A mixture of benzonitrile (202  $\mu$ L, 2 mmol, 1.0 eq), 4-pentynenitrile (720  $\mu$ L, 8 mmol, 4.0 eq), and 3- mercaptopropionic acid (88  $\mu$ L, 1 mmol, 0.5 eq) was cooled to 0 °C under argon. Hydrazine monohydrate (1.60 mL, 32 mmol, 16 eq) was added dropwise to the mixture. The reaction mixture was stirred in a sealed vessel, at 50 °C for 24 h. After cooling to r.t, a solution of sodium nitrite (2 g, 30 mmol, 15 eq) in H<sub>2</sub>O (20 mL) was slowly added to the reaction mixture, followed by slow addition of aqueous 1M HCl until gas evolution ceased. The solution was extracted with DCM (3 x 20 mL). The combined extracts were washed with brine (20 mL), dried over Na<sub>2</sub>SO<sub>4</sub> and concentrated under reduced pressure. The crude was purified by FC eluting with a mixture of PE / DCM (3:1 to 1:1). The product was obtained as a pink solid (106 mg, 0.50 mmol, 25%).

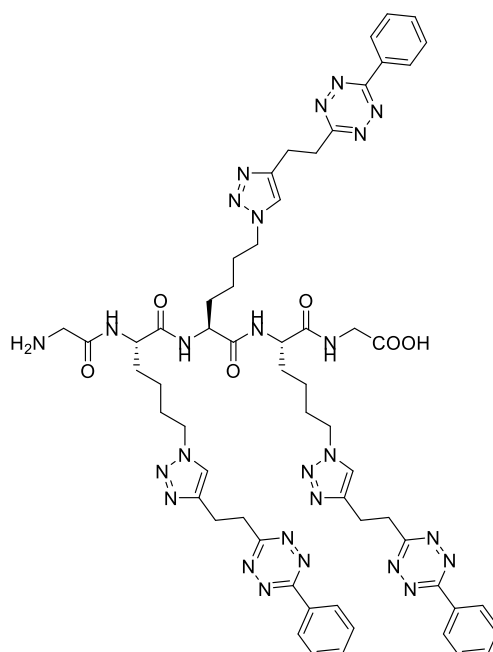
$^1\text{H NMR}$  (400 MHz, Chloroform-*d*):  $\delta$  8.69 – 8.52 (m, 2H), 7.61 (tddd,  $J = 8.8, 6.2, 2.8, 1.6$  Hz, 3H), 3.60 (t,  $J = 7.3$  Hz, 2H), 2.94 (td,  $J = 7.3, 2.6$  Hz, 2H), 1.99 (t,  $J = 2.6$  Hz, 1H).

The analytical data were in accordance with previously reported data. [7]

$^1\text{H NMR}$  spectrum:



### Tri-Tz peptide



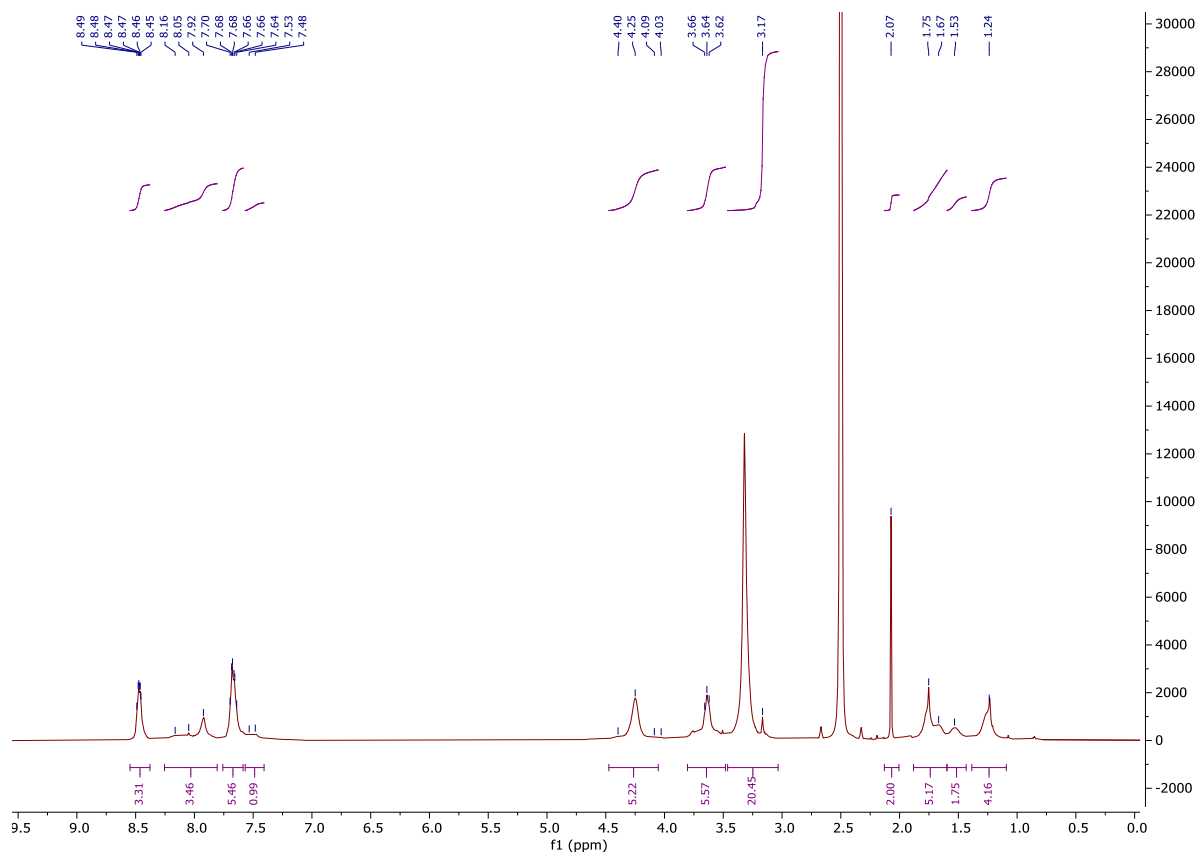


**Talys** (14 mg, 0.020 mmol, 1.0 eq) and **alkyne-Tz** (12.3 mg, 0.066 mmol, 3.3 eq) were dissolved in THF/H<sub>2</sub>O (1:1, 5 mL). CuSO<sub>4</sub>·5H<sub>2</sub>O (4.5 mg, 0.018 mmol, 0.9 eq) and THTPA (7.6 mg, 0.018 mmol, 0.9 eq) were dissolved in H<sub>2</sub>O (0.5 mL). NaAsc (10.4 mg, 0.054 mmol, 2.7 eq) was dissolved in H<sub>2</sub>O (0.5 mL). The three solutions were degassed with argon before mixing. The reaction mixture was stirred for 2 h at r.t. The solvents were evaporated under reduced pressure and the residue was purified by reverse phase column chromatography eluting with H<sub>2</sub>O/ACN (1:0 to 1:1) to afford the product as a pink solid (11.9 mg, 0.010 mmol, 49%).

**<sup>1</sup>H NMR** (400 MHz, DMSO-*d*<sub>6</sub>): δ 8.55 – 8.38 (m, 3H), 8.04 (d, 3H), 7.76 – 7.59 (m, 5H), 7.51 (d, 1H), 4.25 (s, 5H), 3.64 (t, 6H), 3.17 (s, 20H), 2.07 (s, 2H), 1.71 (d, 5H), 1.53 (s, 2H), 1.24 (s, 4H).

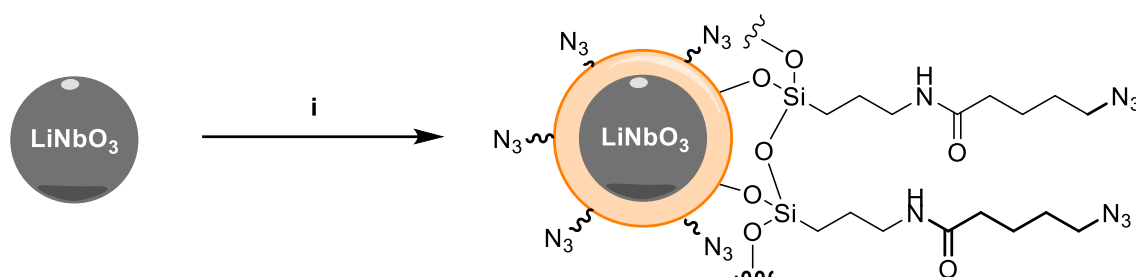
**HRMS** (ESI/QTOF) *m/z*: [M + H]<sup>+</sup> Calcd for C<sub>59</sub>H<sub>68</sub>N<sub>26</sub>O<sub>6</sub><sup>+</sup> 1225.5893; Found 1225.5887.

**<sup>1</sup>H NMR spectrum:**



## 5.15. Nanoparticle silica coating

### Standard Stöber process coating<sup>154,155</sup>



**Scheme 33:** Previously developed LNO silica coating procedure. i- APTES-N<sub>3</sub>, NH<sub>4</sub>OH (25% aq), EtOH/cyclohexane, US, 16 h, 40 °C.

Cyclohexane (1 mL) was added to a suspension of HNPs in EtOH (2 mg, 1 mL) and the suspension was ultra-sonicated for 30 min. A solution of 4-azido-*N*-(3-(triethoxysilyl)propyl)butanamide (10.2 mg, 30 μmol) in EtOH/cyclohexane 1:1 (100 μL) was added the resulting suspension was ultra-sonicated for 30 min. NH<sub>4</sub>OH aq (0.1 mL, 25%) was added and the suspension was ultra-sonicated for 16 h under argon atmosphere (temperature ranging from 40 to 60 °C). The suspension was centrifuged (10 min, 4 700 rpm) and the supernatant was discarded. The residue was washed with EtOH by centrifugation (5 X 1 mL) and the solid residue was suspended in EtOH (1 mL). An aliquot of the LNO@APTES-N<sub>3</sub> HNPs suspension (20 μL) was diluted with PBS 0.1x (1 mL) and ultra-sonicated for 30 min. The diluted aliquot was analysed with a Malvern NanoZ.

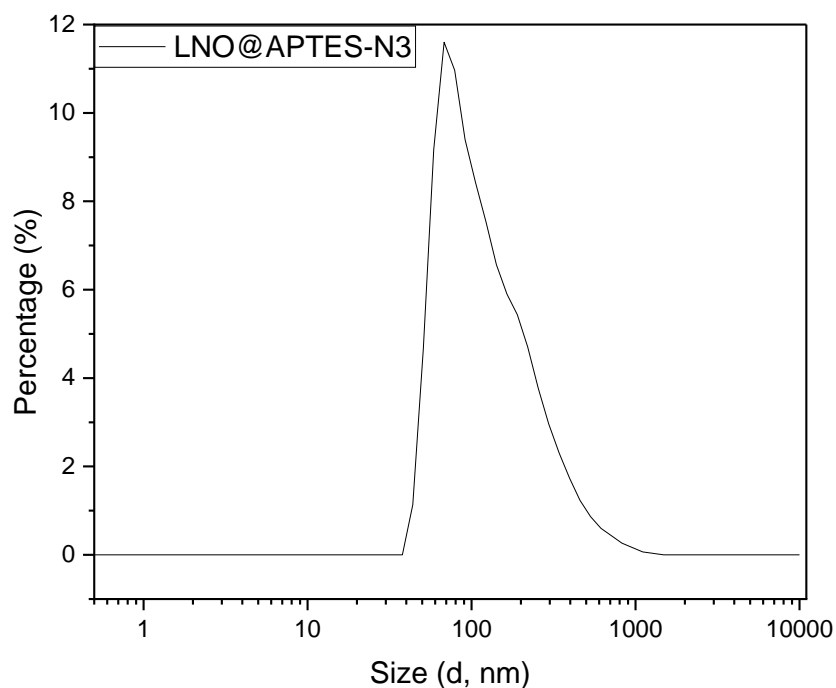
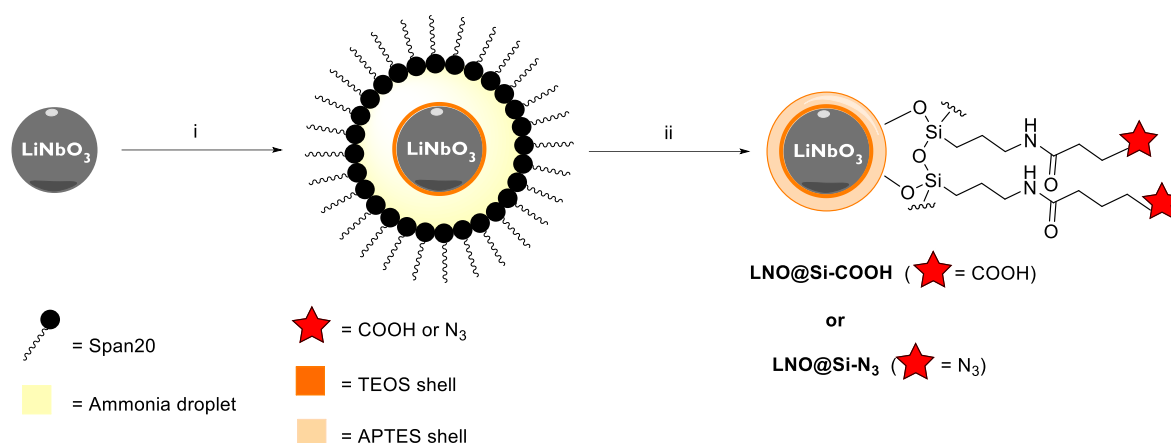


**Figure 39:** DLS Size distribution by number of LNO@APTES-N<sub>3</sub> in PBS 0.1x.

## Microemulsion coating



**Scheme 34: Silanization of LNO NPs using reverse W/O microemulsion method.** i- Span20, NH<sub>4</sub>OH (28% aq), TEOS, heptane, 24 h, r.t. ii- APTES derivative, heptane, 24 h, r.t.

Span-20 (1.0 g) was dissolved in heptane (13 mL) and the solution was stirred at r.t. for 30 min. Aqueous NH<sub>4</sub>OH (28%, 50  $\mu$ L) was added and the solution was stirred at r.t. for 3 h. The size of the resulting micelles was measured by dynamic light scattering (DLS). A suspension of LNO NPs in heptane (10 mg, 1 mL) was added and the mixture was stirred for 1 h. Tetraethyl orthosilicate (TEOS) (60  $\mu$ L, 0.27 mmol) was added and the reaction mixture was stirred for 24 h at r.t. A solution of APTES derivative (APTES-COOH or APTES-N<sub>3</sub>, 0.03 mmol, 1.0 eq) in EtOH was added and the reaction mixture was stirred for 24 h at r.t. The microemulsion was broken by the addition of MeOH (15 mL). The suspension was centrifuged (5 min, 4700 rpm) and the supernatant was discarded. The resulting NPs were washed with EtOH (1 mL, 5 times), centrifuged, and the resulting LNO@COOH NPs or LNO@N<sub>3</sub> NPs were resuspended in EtOH (2 mL).

In the case of LNO@Si-N<sub>3</sub>, a solution of APTES-N<sub>3</sub> in EtOH (300 mg/mL, 30  $\mu$ L, 0.03 mmol, 1.0 eq) was added after 24 h of reaction with TEOS and the mixture was stirred for 24 h at r.t.

In the case of LNO@Si-COOH, a solution of freshly prepared APTES-COOH in EtOH (300 mg/mL, 30  $\mu$ L, 0.03 mmol, 1.0 eq) was added after 24 h of reaction with TEOS and the reaction mixture was stirred for 24 h at r.t.

For DLS measurements, two aliquots of the LNO@Si-COOH NPs or LNO@Si-N<sub>3</sub> NPs suspension (5  $\mu$ L each) were diluted with phosphate-buffered saline (PBS) 0.1x (1 mL, pH 7.4 and pH 3.0), and ultra-sonicated for 20 min. The diluted aliquots were analyzed with a Malvern NanoZ.

For FTIR characterization, an aliquot of the LNO@COOH NPs or LNO@N<sub>3</sub> NPs suspension in EtOH (0.4 mL, 1 mg/mL) was added on top of KBr (200 mg), and dried at 80°C for 12 h before compression (2 min, 10 bars) to form a pellet.

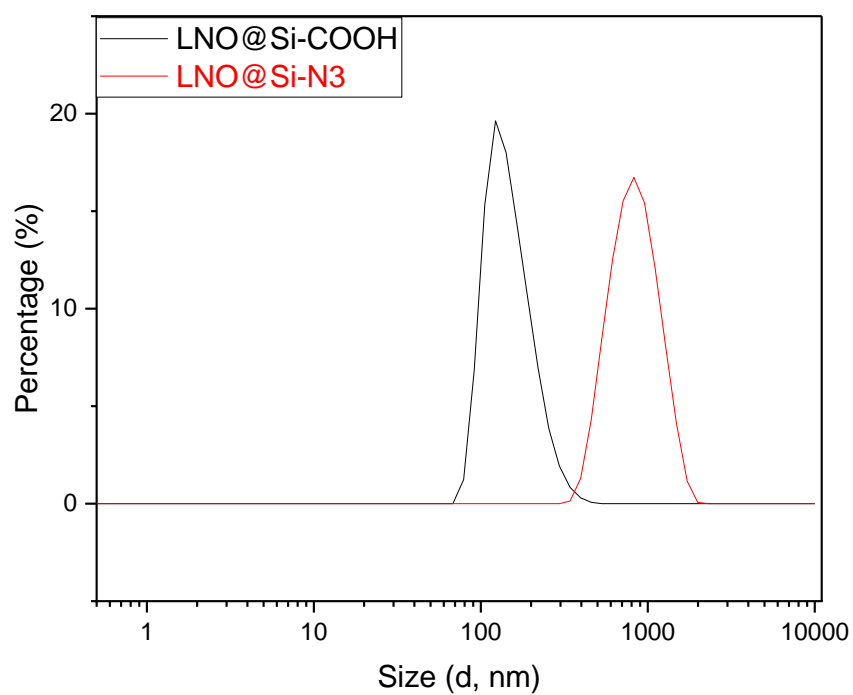
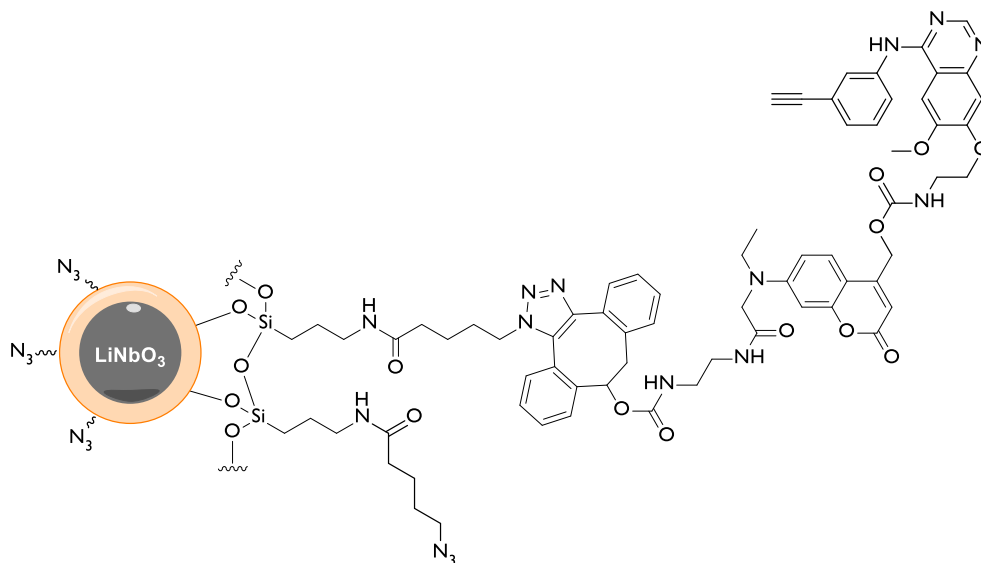


**Figure 40:** DLS Size distributions by number of LNO@Si-COOH (black) and LNO@Si-N<sub>3</sub> (red) in PBS 0.1x.

## 5.16. Nanoparticle functionalization

### LNO@CM-ELA



To a suspension of LNO@APTES- $N_3$  (2 mg) in EtOH (1 mL), were added DMF (1 mL) and a 10 mM solution of DIBO-CM-ELA (50  $\mu$ L, 312.4  $\mu$ g, 0.4  $\mu$ mol) in DMSO. The suspension was ultra-sonicated for 16 h under argon and dark conditions (temperature ranging from 40 to 60  $^{\circ}$ C). The suspension was centrifuged (10 min, 4 700 rpm) and the supernatant kept in a separate flask. The solid residue was sequentially washed and centrifuged with DMF (1 X 1 mL) and EtOH (3 X 1 mL). The combined supernatants were concentrated under reduced pressure, dissolved in DMSO (50  $\mu$ L) and diluted with EtOH (1 mL). The resulting LNO@APTES-CM-ELA HNPs were suspended in EtOH (1 mL).

For DLS measurements and UV-vis absorption analysis, an aliquot of the suspension (20  $\mu$ L) was diluted in PBS 0.1x (1 mL) and ultra-sonicated for 15 min. The aliquot was analysed with a Malvern NanoZ.

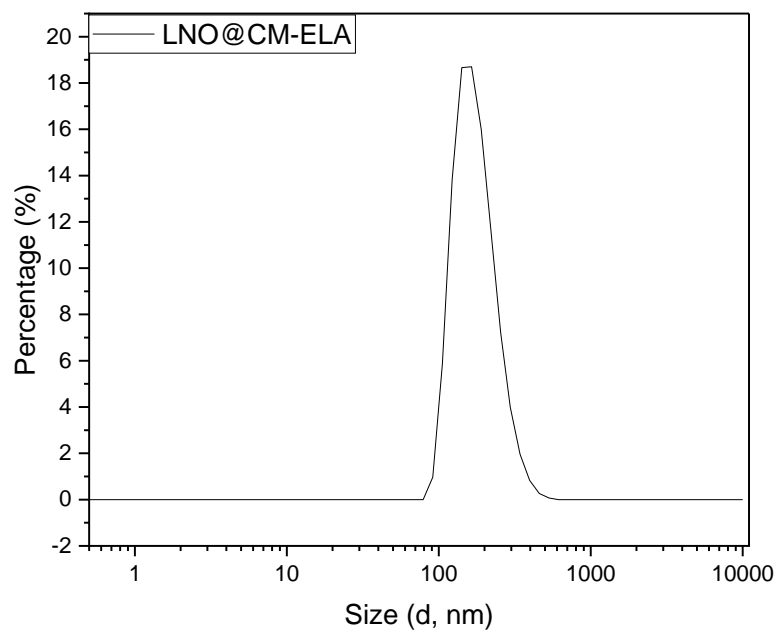
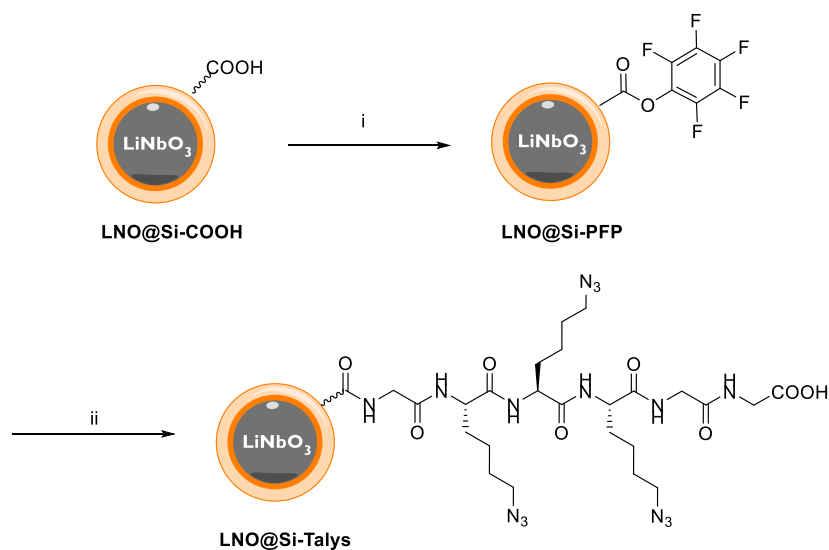


**Figure 41:** DLS Size distribution by number of LNO@CM-ELA in PBS 0.1x.

## LNO@Si-Talys



**Scheme 35: Conjugation of Talys to LNO@COOH.** i- pentafluorophenol, DMAP, EDC dry DMA, 3 h, r.t. ii- Talys, DIPEA, DMA, 3 h, r.t.

A suspension of LNO@Si-COOH NPs in EtOH (1 mL, 1 mg/mL) was centrifuged (5 min, 4700 rpm). The supernatant was discarded and the NPs were suspended in DMA (1 mL). A solution of pentafluorophenol (PFP-OH) (3.4 mg, 18  $\mu$ mol, 6.0 eq) and DMAP (0.074 mg, 0.6  $\mu$ mol, 0.2 eq) in DMA (0.5 mL) was added and the suspension was stirred for 5 min at 0°C. A solution of 1-ethyl-3-(3-dimethylaminopropyl)carbodiimide (EDC) (1.26 mg, 6.6  $\mu$ mol, 2.2 eq) in DMA was added and the suspension was stirred for 5 min at 0°C. The suspension was warmed to r.t and stirred for 3 h. The suspension was centrifuged (5 min, 4700 rpm) and the supernatant discarded. The solid residue was washed with DCM (3 x 1 mL), centrifuged and suspended in DMA (1 mL). A solution of Talys (6.6  $\mu$ mol, 2.2 eq) and DIPEA (50  $\mu$ L, 287  $\mu$ mol, 100 eq) in DMA (1 mL) was added and the suspension was stirred at 37°C (reaction time dependent on derivative) for 3 h. The suspension was centrifuged (5 min, 4700 rpm) and the supernatant discarded. The solid residue was washed with a mixture of DCM:DMA (1:1, 2 x 1 mL) and EtOH (2 x 1 mL), centrifuged and re-suspended in EtOH (1 mL) to afford LNO@Si-Talys NPs.

For DLS measurements, two aliquots of the NP suspension (10  $\mu$ L each) were diluted with PBS 0.1x (1 mL, pH 7.4 and pH 3.0), and ultra-sonicated for 15 min. The diluted aliquots were analysed with a Malvern NanoZ.

For FTIR characterization, an aliquot of the NP suspension in EtOH (0.4 mL, 1 mg/mL) was added to KBr (200 mg), and dried in the oven overnight at 100°C before compression (2 min, 10 bars) to form a KBr pellet.

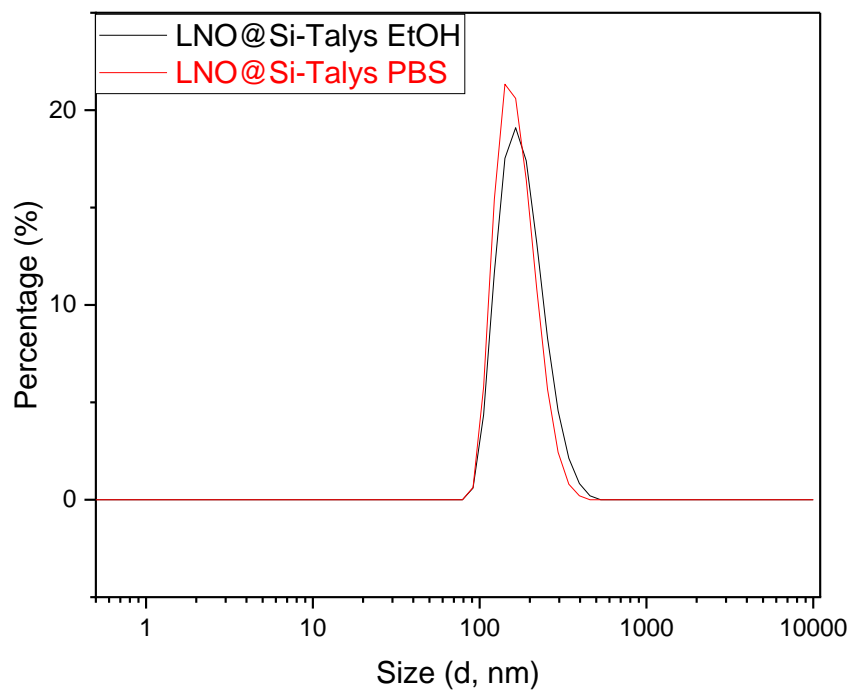
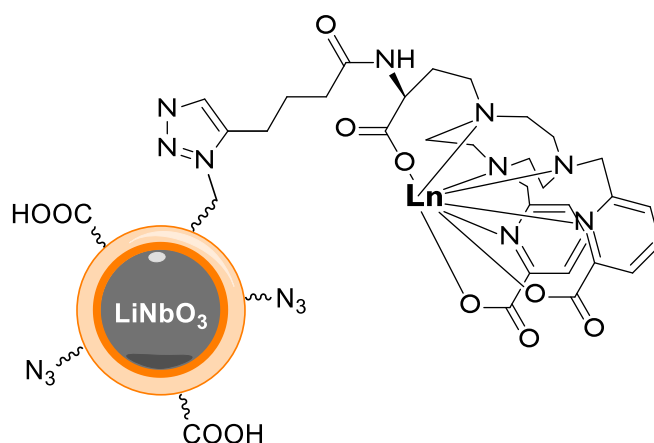


**Figure 42:** DLS Size distributions by number of LNO@Si-Talys in EtOH (black) and PBS 0.1x (red).



## LNO@Si-Talys@[LnLA]



H<sub>2</sub>O (1 mL) was added to a suspension of LNO@Si-Talys NPs (2 mg) in EtOH (1 mL) and the mixture was ultra-sonicated for 5 min. A solution of Ln-alkyne-complex (1 equiv, 4 μmol) in DMSO (100 μL) and a mixture of CuSO<sub>4</sub>·5H<sub>2</sub>O (1 equiv, 4 μmol, 1 mg), NaAsc (1.5 equiv, 6 μmol, 3.6 mg), and THPTA (1 eq, 4 μmol, 1.7 mg) in water (0.5 mL) were added and the suspension was stirred at 37 °C for 1.5 h under argon. The mixture was centrifuged (10 min, 4 700 rpm) and the supernatant discarded. The residue was washed with H<sub>2</sub>O (2 x 1 mL) and DMSO (2 x 1 mL) by centrifugation and the solid residue was suspended in DMSO (1 mL).

For DLS measurements, two aliquots of the NP suspension (10 μL each) were diluted with PBS 0.1x (1 mL, pH 7.4 and pH 3.0), and ultra-sonicated for 15 min. The diluted aliquots were analysed with a Malvern NanoZ.

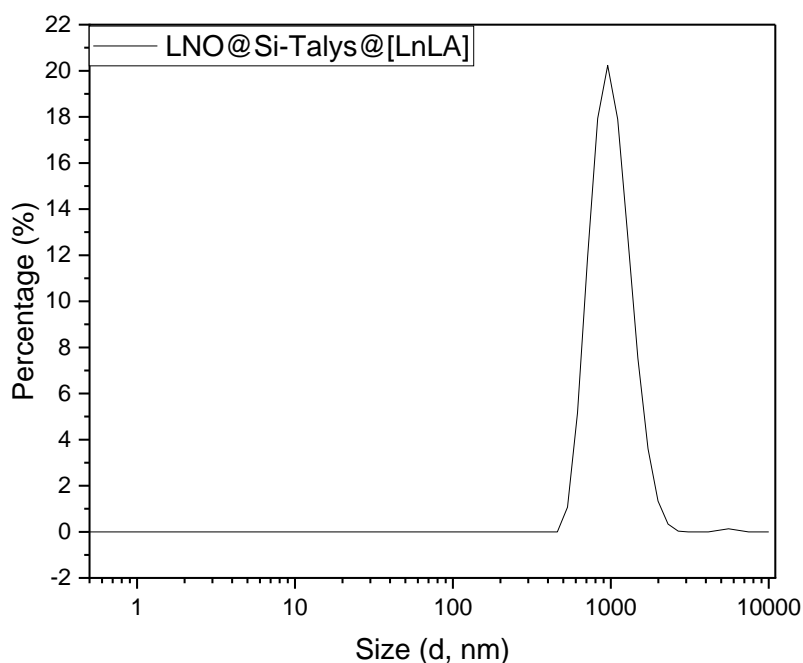
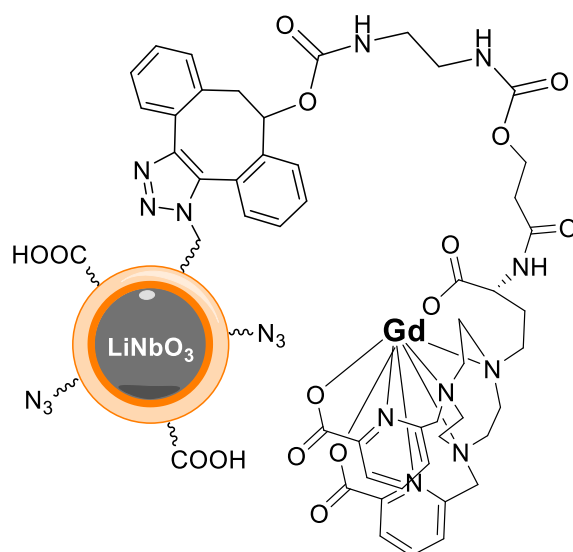


**Figure 43:** DLS Size distribution by number of LNO@Si-Talys@[LnLA] in PBS 0.1x.

## LNO@Si-Alys@[GdLD]



DMF (2.6 mL) was added to a suspension of LNO@Si-Alys (4 mg) in EtOH (2 mL). A solution of [GdLD] (10 mM) in DMF (0.4 mL) was added and the mixture was reacted at 50 °C for 24h. The mixture was centrifuged and the supernatant discarded. The residue was washed with DMF (2 x 2 mL) and EtOH (2 x 2 mL), dried in an oven (100 °C) and the residue was resuspended in EtOH (2 mL, 2 mg/mL) for storage (r.t.).

For DLS measurements, two aliquots (20  $\mu$ L, 0.04 mg) were diluted with PBS buffer 0.1x at pH 7.4 (1 mL) and pH 3.0 (1 mL) and ultra-sonicated for 15 min. The diluted aliquots were analysed by DLS on a Malvern NanoZ.

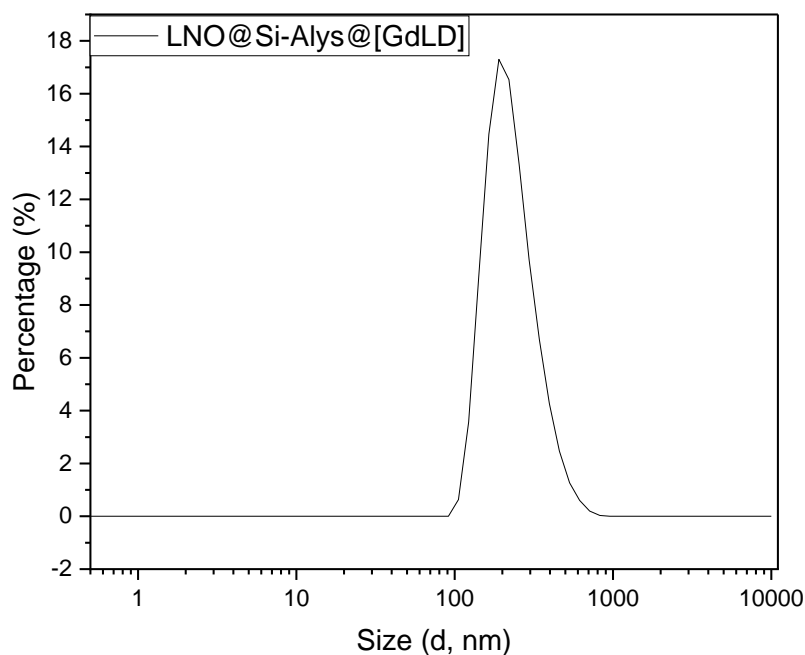


**Figure 44:** DLS Size distribution by number of LNO@Si-Alys@[LnLD] in PBS 0.1x.

### 5.17. Photorelease assays

#### Calibration curves for quantification of erlotinib on LNO@CM-ELA HNPs

The grafting of ELA on LNO@APTES-N<sub>3</sub> NPs was estimated indirectly by measuring the amount of unreacted DIBO-CM-ELA in the supernatant after the functionalization procedure. The recovered supernatant was evaporated *in vacuo*, dissolved in EtOH (1mL) and diluted 10 times in EtOH. The UV-Visible absorption of the supernatant was then measured using a BioTek® Synergy 2 multi-mode reader between 250 and 450 nm with a 1 nm increment in a 96-well plate (Corning® UV-Transparent microplate) and compared to a set of DIBO-CM-ELA standards in EtOH at concentrations ranging from 1 to 250 μM (volume of 150 μL per well). The concentration of ELA was linked to the integral of the absorbance spectrum between 250 and 450 nm. The total amount of ELA grafted was estimated to 27 nmol/mg of LNO NPs.

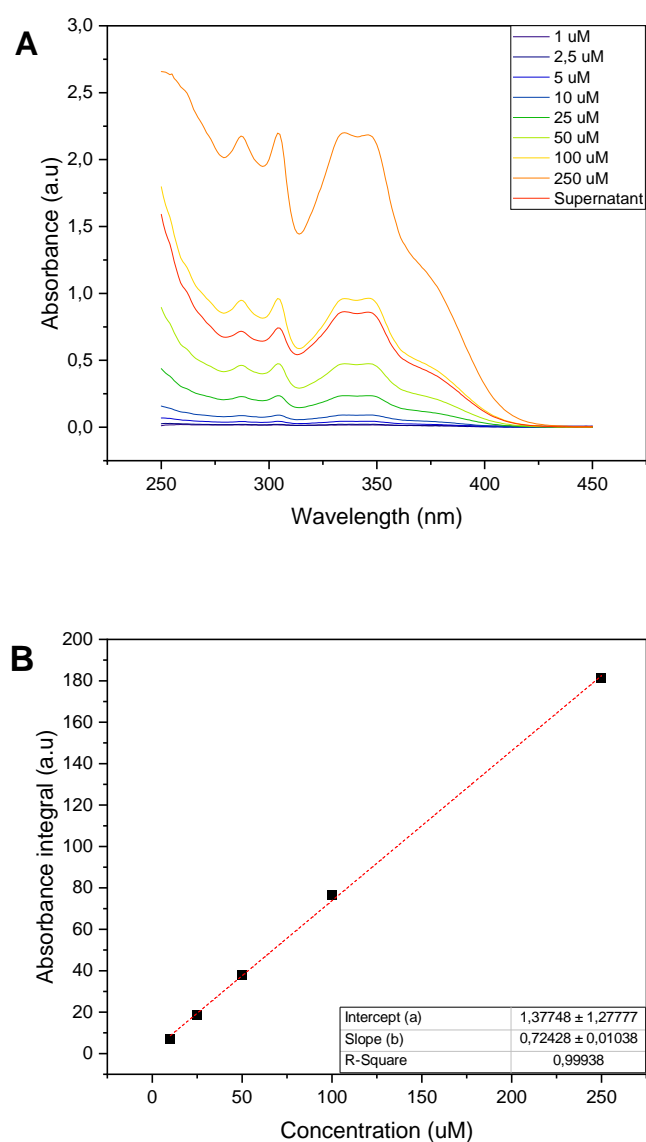


**Figure 45:** Quantification of unreacted CM-ELA in the supernatant from the conjugation reaction of CM-ELA to LNO@APTES-N<sub>3</sub> NPs. **A:** UV-vis absorbance spectra between 250 and 450 nm at different CM-ELA concentrations; **B:** Calibration curve for the indirect determination of conjugated CM-ELA.

### One-photon release of erlotinib from LNO@ CM-ELA HNPs

UV-induced photolysis experiments were performed with a Sylvania UV-light tube (366 nm, 8W). LNO-CM-ELA NPs (150 µg) were suspended in PBS (1 mL; pH = 7.4, 144 mg/L KH<sub>2</sub>PO<sub>4</sub>, 9000 mg/L NaCl, 795 mg/L Na<sub>2</sub>HPO<sub>4</sub>·7H<sub>2</sub>O) and placed in 8 wells borosilicate coverglass polystyrene chambers (Nunc® Lab-Tek® II, Merck) for irradiation at 366 nm. Aliquots (40 µL) of the suspension were withdrawn at the indicated time points, diluted with PBS to 200 µL to achieve a 1:5 dilution ratio and centrifuged (10 min, 13'000 rpm). Quantification of ELA in the supernatant (triplicates) was performed by UHPLC-MS.

### Erlotinib quantification by UHPLC-MS

MS spectra were acquired using the 6530 Accurate Mass Q-TOF LCMS mass spectrometer coupled to the 1290 Infinity UHPLC system (Agilent Technologies, USA). Analysis was performed on an ACQUITY UPLC® BEH C18 1.7µm column, 2.1 mm x 50 mm (Waters) heated at 30°C. The mobile phase was maintained at a flow rate of 0.4 mL/min and contained 0.1% (v/v) formic acid water solution (A), and 0.1% (v/v) formic acid acetonitrile solution (B). Over a 4 min total run, the gradient was: 0-0.5 min, 1-5% B; 0.5-2 min, 5-95% B; 2-2.1 min, 95-1% B; 2.1-4 min, 1% B to re-equilibrate the system in initial conditions. The sample manager system temperature was fixed at 15°C and the injection volume was 5 µL. The ESI source was set in positive ionization mode using the Dual AJS Jet stream ESI Assembly. The QTOF instrument was operated in the 4 GHz High Resolution mode in profile mode. The instrument was calibrated in positive full scan mode using ESI-L+ solution (Agilent Technologies, USA). The TOF mass spectra were acquired over the range of  $m/z$  100-600 at an acquisition rate of 3 spectra/s. ESI AJS settings were as follows: RF drying gas flow, 8 L/min; drying gas temperature, 300 °C; nebulizer pressure, 35 psi; capillary voltage, 3500 V; nozzle voltage, 1000 V; fragmentor voltage, 175 V; skimmer voltage, 65 V; octopole 1 RF voltage, 750 V; Sheath gas temperature, 350 °C; Sheath gas low; 11 L/min. Data were processed using the MassHunter Workstation (Agilent Technologies, USA). Extracted ions chromatograms (XIC) were calculated with a window of ±0.5 min using a mass-extraction-window (MEW) of ±50 ppm. The average peak area of three replicate injections at each concentration was used for each data point.

A stock solution of ELA was prepared at 1 mM in DMSO. Working standards were prepared in PBS 1x at concentrations of 2500 nM, 1000 nM, 500 nM, 250 nM, 100 nM, 50 nM, 25 nM and 10 nM by using serial dilutions of the stock solution. Extracted ions chromatograms (XIC) were based on a retention time (RT) of 2.01 min with a window of ±0.5 min using a mass-extraction-window (MEW) of ± 50 ppm centered on the  $m/z_{\text{theor}}$  335.1502. The average peak area of three replicate injections at each concentration was used for each data point. Calibration curve were fitted with a polynomial order 2 equation, with  $R^2 > 0.99$ .

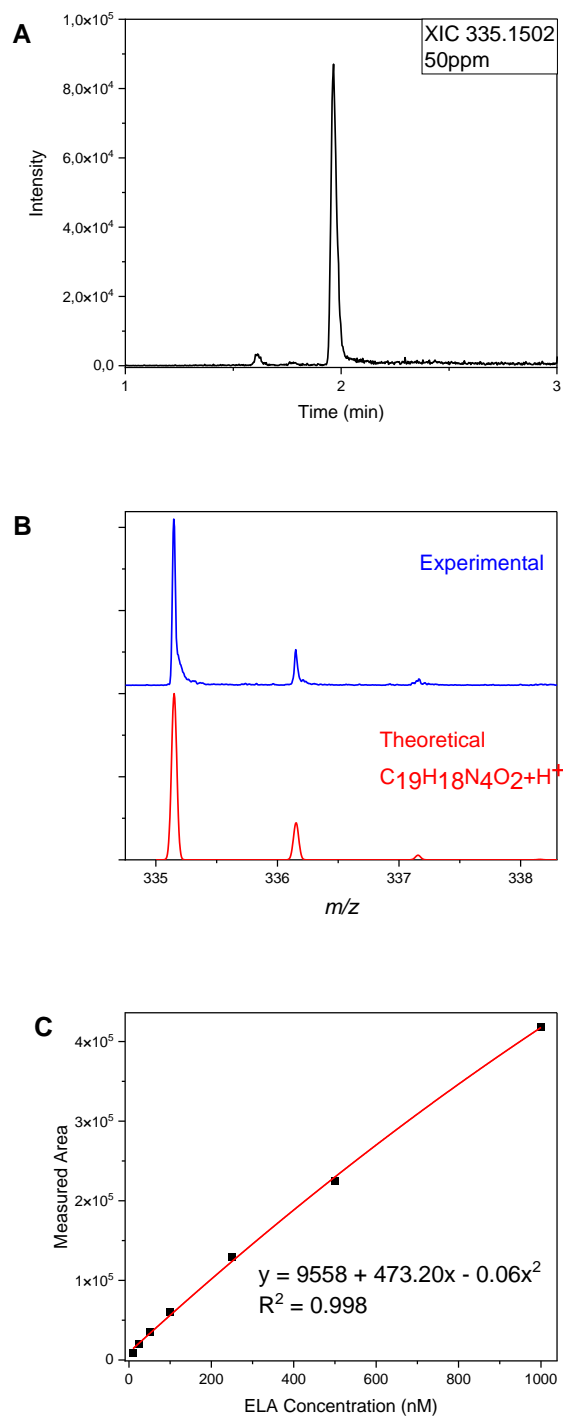


**Figure 46.** **A:** Typical XIC (335.1502 MEW  $\pm$  50 ppm) of an ELA standard at 250 nM eluted after 2.01 min. **B:** Typical MS of ELA standard. **C:** Typical calibration curve for ELA.

### General procedure for two-photons release assay

**Irradiation Setup 1.** In this case, the irradiation source was an amplified Ti:Sapphire laser system (Astrella, Coherent) with 4.9 W average output at 1 KHz repetition rate. The system delivered pulses centered at 790 nm with 35 nm bandwidth corresponding to 27 fs transform limited duration. The actual pulse duration measured by a commercial Second Harmonic Generation Frequency Resolved Optical Gating (SHG-FROG) device (PulseCheck, APE Berlin) yielded

approximately 60 fs. The beam diameter, determined by a beam profiler (Newport) set at the amplifier output, corresponded to approximately 11 mm at  $1/e^2$ . The beam was directed onto the bottom surface of the multi-wells plate by a 45-degree dielectric mirror, without focusing. The peak intensity at the sample corresponded to 87 GW/cm<sup>2</sup> at  $1/e^2$ . LNO@CM-ELA NPs (150 µg) were suspended in PBS (1 mL; pH = 7.4, 144 mg/L KH<sub>2</sub>PO<sub>4</sub>, 9000 mg/L NaCl, 795 mg/L Na<sub>2</sub>HPO<sub>4</sub>·7H<sub>2</sub>O) and placed in 8 wells borosilicate coverglass polystyrene chambers (Nunc® Lab-Tek® II, Merck). The samples were irradiated at 790 nm.

**Irradiation Setup 2.** The setup for comparing the release of ELA at different wavelengths was based on a 680-1300 nm tunable ultrafast system (Insight x3, Spectra-Physics) with 1.4 W average output power at 80 MHz repetition rate. The nominal pulse duration was approximately 120 fs. The experiment was performed at 800, 1000, and 1100 nm. The pulse temporal compression was carefully adjusted to obtain Fourier-limited duration for each condition. The beam diameter, determined by a beam profiler (Newport) set at the laser output, corresponded to approximately 1.36 mm at  $1/e^2$ . The beam was directed onto the bottom surface of the multi-wells plate by a 45 degree dielectric mirror, without focusing. The peak intensity at the sample corresponded to 10 MW/cm<sup>2</sup> at  $1/e^2$ . To account for the smaller beam size compared to the size of the well (12 mm), we used a rotational motor (PRM1-Z8 – Thorlabs) to move continuously the sample with respect to the beam position in a circular pattern ( $2\pi/10$  min). To partially compensate for the lower peak intensity with respect to Setup 1, we applied the irradiation for a longer time span (1 h instead of 15 min).

Aliquots (40 µL) of the suspension were withdrawn at the indicated time points, diluted with PBS to 200 µL to achieve a 1:5 dilution ratio and centrifuged (10 min, 13'000 rpm). Quantification of ELA in the supernatant (triplicates) was performed by UHPLC-MS.

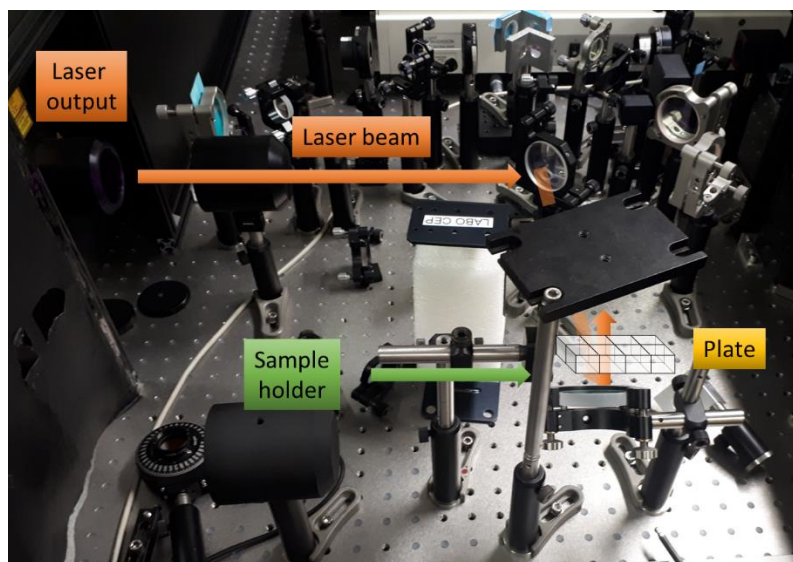


**Figure 47:** Laser experimental setup 1 for HNP irradiation with NIR.

### Detection of ELA release upon irradiation on a tunable MHz laser (setup 2)

Suspension of LNO@CM-ELA NPs (150 µg) in PBS (1 mL; pH = 7.4, 144 mg/L KH<sub>2</sub>PO<sub>4</sub>, 9000 mg/L NaCl, 795 mg/L Na<sub>2</sub>HPO<sub>4</sub>·7H<sub>2</sub>O) were irradiated for 1 h at 800, 1000 and 1100 nm using the irradiation setup 2. Analysis of the supernatants collected from the three different irradiation

conditions was performed by UHPLC-MS. ELA was only detected in the sample which underwent irradiation at 800 nm.

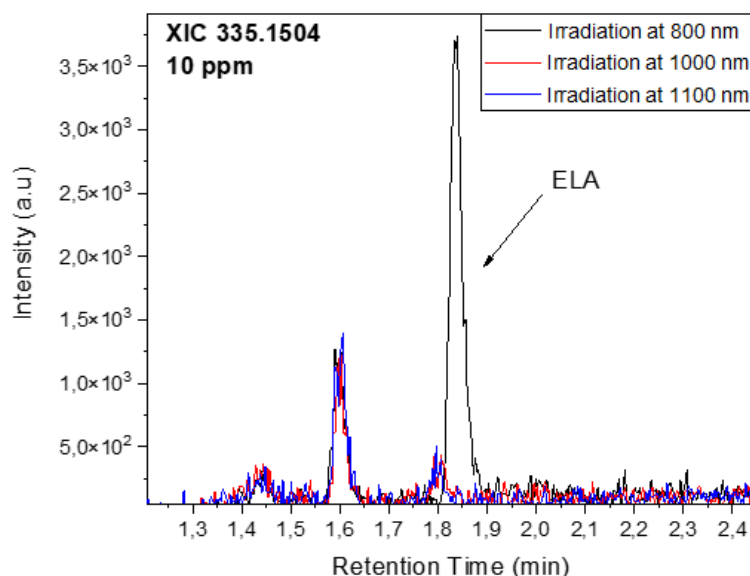


**Figure 48:** XIC (335.1504 MEW  $\pm$  50 ppm) of the samples irradiated at 800 nm (black curve), 1000 nm (red curve) and 1100 nm (blue curve).

### Characterization of UV light- and NIR excitation-triggered release of ELA from LNO@CM-ELA NPs

The amount of ELA released upon UV-A irradiation or NIR excitation was plotted as a function of irradiation time and fitted with a mono-exponential function according to equation (1). Equation (1) was differentiated with respect of time (t) to get the initial release rate constant at a given time point (equation (2)).

$$[ELA] = A(1 - \exp(-k * t)) \quad (1)$$

$$\frac{d}{dt}[ELA]_t = A * k(\exp(-k * t)) \quad (2)$$

A: pre-exponential factor

k: rate constant

t: time

### Release of ELA as a result of UV-A irradiation

UV-induced photolysis experiments were performed with a Sylvania UV-light tube (366 nm, 8W), and ELA release was evaluated by UHPLC-ESI-HRMS.

The UV flux was measured using a photodiode power-meter (S120C – Thorlabs). When set under the UV lamp at the sample position, the measured value was 281.7  $\mu$ W, which corresponds to an intensity of 0.38 mW/cm<sup>2</sup> by taking into account the dimensions of the active sensor surface (0.73

cm<sup>2</sup>). Considering that the dimensions of each square multi-well compartment used for the irradiation is (12 mm)<sup>2</sup>, the corresponding flux per well can be estimated to 265  $\mu$ W.

The ELA concentration values reported are measured in aliquots taken and diluted to a 1:5 ratio in PBS. A time-dependent increase of released ELA was measured upon irradiation of LNO@CM-ELA NPs (0.15 mg/mL in PBS). The initial release rate ( $k_0$ ), calculated at 5 min and normalized from fitted parameters, was estimated at 381 nM·min<sup>-1</sup>.

**Table 9:** Ratio and percentage of ELA released upon irradiation of LNO@CM-ELA NPs (loading 0.15 mg/mL) at 366 nm (UV lamp) in PBS 1x. Aliquots of the suspension were withdrawn at the indicated time points, diluted 1:5 in PBS and centrifuged (10 min, 13'000 rpm). Quantification of ELA in the supernatant was performed by UHPLC-MS on triplicates.

Irradiation time (min)	ELA concentration (nM)	ELA Release (%)
0	30.8 ± 5.7	3.8 ± 0.7
1	167.5 ± 19.0	20.7 ± 2.3
2	241.3 ± 8.9	29.8 ± 1.1
5	341.1 ± 27.7	42.1 ± 3.4
10	454.1 ± 13.4	56.1 ± 1.7
15	453.3 ± 4.9	56.0 ± 0.6
20	532.8 ± 13.0	65.8 ± 1.6

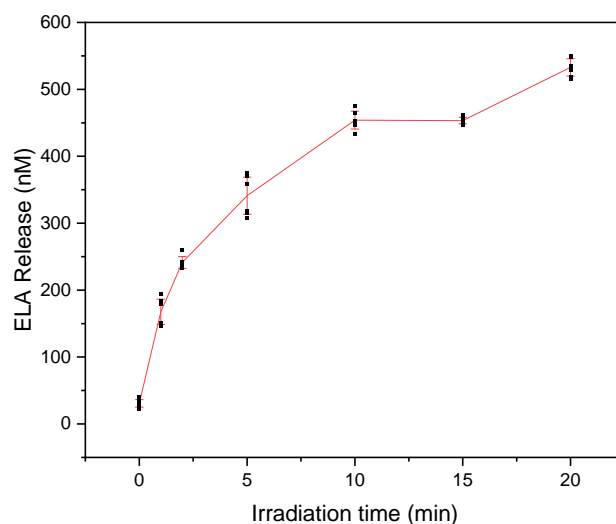


**Figure 49:** Progress of the release of the caged ELA upon irradiation at 366 nm / 8W.

### Release of ELA as a result of NIR excitation



NIR-induced photolysis experiments were performed upon irradiation by the amplified Ti:Sapphire laser system (Astrella, Coherent) at 790 nm, and ELA release was evaluated by UHPLC-ESI-HRMS. The ELA concentration values reported are measured in aliquots taken and diluted to a 1:5 ratio in PBS. A time-dependent increase of released ELA was measured upon irradiation of LNO@CM-ELA NPs (0.15 mg/mL in PBS). The initial release rate ( $k_0$ ), calculated at 5 min and normalized from fitted parameters, was estimated at  $271 \text{ nM} \cdot \text{min}^{-1}$ .

**Table 10:** Ratio and percentage of ELA released upon irradiation of LNO@CM-ELA (loading 0.15 mg/mL) at 790 nm (Ti:sapphire pulsed laser) in PBS 1x. Aliquots of the suspension were withdrawn at the indicated time points, diluted 1:5 in PBS and centrifuged (10 min, 13'000 rpm). Quantification of ELA in the supernatant was performed by UHPLC-MS on triplicates.

Irradiation time (min)	ELA concentration (nM)	ELA Release (%)
0	$14.0 \pm 1.4$	$1.7 \pm 0.2$
1	$88.4 \pm 7.5$	$10.9 \pm 0.9$
2	$162.3 \pm 9.7$	$20.0 \pm 1.2$
5	$272.9 \pm 26.4$	$33.7 \pm 3.3$
10	$318.1 \pm 6.3$	$39.3 \pm 0.8$
15	$333.9 \pm 15.4$	$41.2 \pm 1.9$
20	$389.1 \pm 30.6$	$48.0 \pm 3.8$

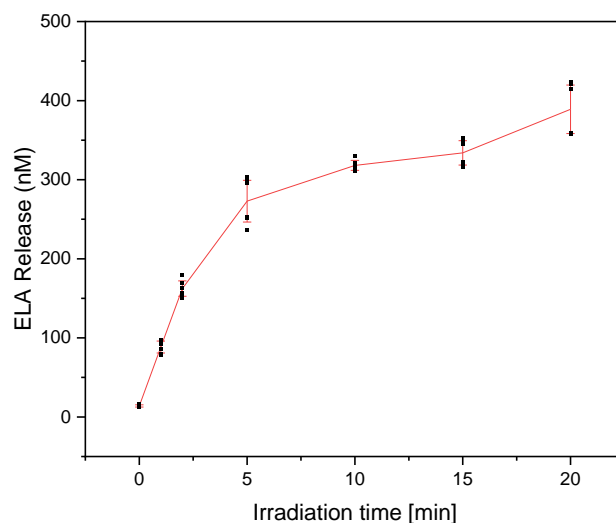


**Figure 50:** Progress of the release of caged ELA upon irradiation with Ti:sapphire pulsed laser system at 790 nm.

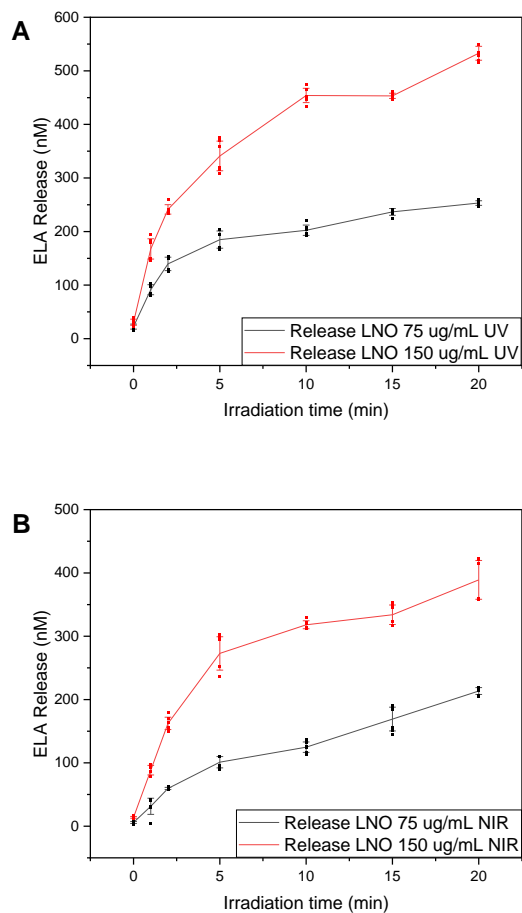


**Figure 51:** Comparison of the release profiles upon irradiation of LNO@CM-ELA at concentrations of 0.075 and 0.15 mg/mL in PBS 1x. **A:** Release upon irradiation at 366 nm. **B:** Release upon irradiation at 790 nm.

## 5.18. *In vitro* experiments

### Cytotoxic effect of erlotinib and ELA

DU145 cells cultured in DMEM containing 10% of FCS were exposed to increasing concentration of either ELA or commercial erlotinib for 72 h at 37°C. Cells were washed two times with PBS and incubated for 2 h with a solution of 3-(4,5-dimethyl-2-thiazoyl)-2,5-diphenyltetrazolium bromide (MTT) in DMEM containing 10% FCS without phenol red. Cells were then lysed by incubation for 15 min with isopropanol/HCl 0.04M. After homogenization, absorbance was measured at 540nm using an Epoch2 Microplate Spectrophotometer (BioTek). Experiments were conducted in triplicates and repeated two times. Means  $\pm$  SD were calculated.

### Cytotoxic effect of the NIR triggered release of ELA

LNO@APTES-CM-ELA NPs or LNO@APTES-N<sub>3</sub> NPs (10 mg/mL in EtOH) were diluted to 0 - 200  $\mu$ g/mL with DMEM containing 10% of FCS and added to 8 wells borosilicate coverglass polystyrene chambers (Nunc® Lab-Tek® II, Merck) containing DU145 cells in DMEM (400  $\mu$ L). Cells were incubated with LNO@APTES-N<sub>3</sub> NPs (150  $\mu$ g/mL), LNO@CM-ELA NPs (150  $\mu$ g/mL), ELA (0.98  $\mu$ M) or DMEM containing 1.5% EtOH as control. After 24 h incubation at 37 °C, the samples were irradiated at 790 nm for 15 min using the setup described above. The samples were incubated at 37 °C for 72 h. Cells were washed with PBS and incubated with a solution of 3-(4,5-dimethyl-2-thiazoyl)-2,5-diphenyltetrazolium bromide (MTT) in DMEM containing 10% FCS without phenol red (1 mM), for 2h. The supernatant was discarded and cells were lysed with isopropanol / HCl 40 mM. Absorbance at 540 nm was measured using a Epoch2 Microplate Spectrophotometer (BioTek) and compared to the values of control cells only incubated in DMEM containing 1.5% EtOH. Experiments were conducted in triplicate wells and repeated three times. Means  $\pm$  SD were calculated.

### Cell imaging

DU145 human prostate cancer cells were grown in DMEM medium supplemented with GlutaMAX™ (GIBCO N ° 61870036), non-essential amino acids (GIBCO N ° 1140035), 10% heat-inactivated fetal bovine serum (FBS) (GIBCO N ° 10270106), and gentamycin (100  $\mu$ g/mL) (GIBCO N ° 15750045). Cells were plated in 35mm Petri dishes with a glass bottom (Mattek, P35G-0.170-14-C) for 24 h, then cell layers were washed once with PBS and LNO NPs (50  $\mu$ g/mL) in DMEM medium without FCS were added for 24 h. After 48 h of incubation, the cell layers were washed twice with PBS, fixed for 20 min using 4% paraformaldehyde (PFA), and finally stained with DAPI (Roth, 6335.1) (1:5000) for 30 min and kept at 4°C until the imaging session.

Cell images were acquired on a Leica SP8 Dive Falcon upright multiphoton microscope coupled pumped by tunable femtosecond laser (Insight X3, Newport Spectra- Physics) using a NA 0.95 water-immersion objective (Leica HC FLUOTAR L 25 $\times$ ). The acquisition spectral range for each channel was selected by the Leica 4Tune system. Images at each excitation wavelength (SHG and DAPI fluorescence at 800 nm, SHG and THG at 1250 nm) were acquired simultaneously. The gains of the detectors were adjusted for each signal.

## 5.19. Lanthanide nanoparticles imaging

### Luminescence experiments

The emission and excitation spectra were recorded at room temperature on a Horiba-Jobin Yvon Fluorolog FL-3-22 fluorimeter equipped with CW 450W Xenon source for fluorescence mode. Data were collected by using a thermoelectrically cooled R2658P PMT (Hamamatsu, range 220-1010 nm) or a NIR PMT (950-1700 nm, thermoelectrically cooled H10330-75 NIR-PMT; Hamamatsu). The spectra were corrected by the instrumental correction function. Data processing was performed with the program Origin 8®.

Life time decays were recorded by using TCSPC Delta time unit, using a Xenon flash tube source. The data were analyzed by using DAS software, by using a mono, bi- or tri-exponential function, and the best fits were kept. They are the averages of at least three independent measurements.

Quantum yield measurements were performed using a G8 GMP integrating sphere [ $\Phi = (E_c - E_a)/(L_a - L_c)$ , where  $E_c$  is the integrated emission spectrum of the sample,  $E_a$  is the integrated "blank" emission spectrum,  $L_a$  is the "blank" absorption, and  $L_c$  is the sample absorption at the excitation wavelength).

Aerated solutions of the samples in DMSO were analysed in a quartz capillary. The concentration was 4 mM for ligand and complexes, and 2mg/mL for all nanoparticles.

### Relaxation measurements

The analyses were performed on permanent magnets (Bruker Minispec spectrometers) with the proton frequencies at 30 MHz (0.7 T) and 60 MHz (1.4 T). LNO@Si-Alys@[GdL<sub>D</sub>] were suspended in H<sub>2</sub>O (600 µL, 2 mg/mL) in 5 mm NMR tubes and ultrasonicated for 30 min. The samples were loaded in the spectrometer, and the temperature was stabilized at 37 °C for 15 min. The longitudinal relaxation time (T<sub>1</sub>) was measured with the inversion recovery method, and the transverse relaxation time (T<sub>2</sub>) was measured with the Carr-Purcell-Meiboom-Gill (CPMG) spin echo sequence. All measurements correspond to an average over 4 scans. The acquisition parameters were adapted from De Matos et al.<sup>167</sup>

The relaxation rate  $R_i$  [s<sup>-1</sup>] was calculated using the equation:

$$R_i = 1/T_i$$

where  $i = 1$  is the longitudinal relaxation and  $i = 2$  is the transversal relaxation of water in the presence of the paramagnetic relaxing agent.

### Agarose phantom relaxation measurements and MRI

LNO@Si-Alys@[GdL<sub>D</sub>] (suspended in water, 4 mg/mL) were mixed with a transparent solution of agarose (1.5%) in PBS (pH = 7.4, 144 mg/L KH<sub>2</sub>PO<sub>4</sub>, 9000 mg/L NaCl, 795 mg/L Na<sub>2</sub>HPO<sub>4</sub>·7H<sub>2</sub>O) at 11 different concentrations: 1.00, 0.75, 0.50, 0.25, 0.20, 0.15, 0.10, 0.05, 0.01, 0.005 and 0.00 mg/mL. The agarose gels were transferred into 5 mm NMR tubes. The T<sub>1</sub> and T<sub>2</sub> relaxation constants were measured at 37 °C and 9.4 T (400 MHz for <sup>1</sup>H) on a Bruker spectrometer equipped with a AVNeo console and 5 mm BBI probe using saturation recovery and CPMG sequences. To avoid relaxation damping during saturation due to high <sup>1</sup>H concentration, the probe was slightly

detuned. The variable T1 relaxation delays were set to 0.001, 0.010, 0.050, 0.075, 0.100, 0.250, 0.500, 0.750, 2.5, 5, 10, and 25 s. The relaxation times T1 were extracted, fitting the data with a monoexponential build-up. The T2 echo delay was set to 2 ms, and the variable CPMG loop counters were set to 2, 4, 6, 8, 10, 12, 16, 24, 32, 48, 64, and 128. The relaxation times T2 were extracted, fitting the data with a monoexponential decay.

For MRI, the NMR tubes were then inserted into a homemade Teflon NMR tube holder phantom. The MRI experiments were performed on a 14.1 T Bruker AVANCE Neo system using ParaVision 360 software (Bruker BioSpin, D). A RAPID Biomedical GmbH volume coil was used for transmission and reception. 2D T1- and T2-weighted contrast images were collected using a gradient-echo sequence/fast low-angle shot (FLASH) with the following parameters: T1-TE/TR = 2.75/500 ms, flip angle = 45°, T2-TE/TR = 12/5000 ms, flip angle = 136.42°, matrix size = 186 × 186, FOV = 27.9 × 27.9 mm<sup>2</sup>, 9 axial 1 mm slices, 1 average. The repetition time (TR) was chosen to yield good contrast between the different samples at 14.1 T based on the T1 and T2 relaxation time range measured at 9.4 T.



## 6. References

---

- (1) Bray, F.; Laversanne, M.; Weiderpass, E.; Soerjomataram, I. The Ever-Increasing Importance of Cancer as a Leading Cause of Premature Death Worldwide. *Cancer* **2021**, *127* (16), 3029–3030. <https://doi.org/10.1002/cncr.33587>.
- (2) Martel, C. de; Georges, D.; Bray, F.; Ferlay, J.; Clifford, G. M. Global Burden of Cancer Attributable to Infections in 2018: A Worldwide Incidence Analysis. *The Lancet Global Health* **2020**, *8* (2), e180–e190. [https://doi.org/10.1016/S2214-109X\(19\)30488-7](https://doi.org/10.1016/S2214-109X(19)30488-7).
- (3) Miller, K. D.; Nogueira, L.; Mariotto, A. B.; Rowland, J. H.; Yabroff, K. R.; Alfano, C. M.; Jemal, A.; Kramer, J. L.; Siegel, R. L. Cancer Treatment and Survivorship Statistics, 2019. *CA: A Cancer Journal for Clinicians* **2019**, *69* (5), 363–385. <https://doi.org/10.3322/caac.21565>.
- (4) Chen, H.; Zhang, W.; Zhu, G.; Xie, J.; Chen, X. Rethinking Cancer Nanotheranostics. *Nat Rev Mater* **2017**, *2* (7), 1–18. <https://doi.org/10.1038/natrevmats.2017.24>.
- (5) Negm, R. S.; Verma, M.; Srivastava, S. The Promise of Biomarkers in Cancer Screening and Detection. *Trends in Molecular Medicine* **2002**, *8* (6), 288–293. [https://doi.org/10.1016/S1471-4914\(02\)02353-5](https://doi.org/10.1016/S1471-4914(02)02353-5).
- (6) Kumar, R.; Srivastava, R.; Srivastava, S. Detection and Classification of Cancer from Microscopic Biopsy Images Using Clinically Significant and Biologically Interpretable Features. *Journal of Medical Engineering* **2015**, *2015*, 1–14. <https://doi.org/10.1155/2015/457906>.
- (7) Kasban, H.; El-Bendary, M. A. M.; Salama, D. H. A Comparative Study of Medical Imaging Techniques. **2015**.
- (8) Bellin, M.-F. MR Contrast Agents, the Old and the New. *European Journal of Radiology* **2006**, *60* (3), 314–323. <https://doi.org/10.1016/j.ejrad.2006.06.021>.
- (9) Chaudhry, A.; Gul, M.; Chaudhry, A. Utility of Computed Tomography Lung Cancer Screening and the Management of Computed Tomography Screen-Detected Findings. *J Thorac Dis* **2018**, *10* (3), 1352–1355. <https://doi.org/10.21037/jtd.2018.03.68>.
- (10) Geisel, J.; Raghu, M.; Hooley, R. The Role of Ultrasound in Breast Cancer Screening: The Case for and Against Ultrasound. *Seminars in Ultrasound, CT and MRI* **2018**, *39* (1), 25–34. <https://doi.org/10.1053/j.sult.2017.09.006>.
- (11) Gambhir, S. S. Molecular Imaging of Cancer with Positron Emission Tomography. *Nat Rev Cancer* **2002**, *2* (9), 683–693. <https://doi.org/10.1038/nrc882>.
- (12) Sajadi, M. M.; Chen, W.; Dilsizian, V. Targeted Bacteria-Specific 18F-Fluoro-Maltohexaose But Not FDG PET Distinguishes Infection From Inflammation\*. *JACC: Cardiovascular Imaging* **2019**, *12* (5), 887–889. <https://doi.org/10.1016/j.jcmg.2018.03.008>.
- (13) Caravan, P. Strategies for Increasing the Sensitivity of Gadolinium Based MRI Contrast Agents. *Chemical Society Reviews* **2006**, *35* (6), 512–523. <https://doi.org/10.1039/B510982P>.

- (14) Brenner, D. J.; Hall, E. J. Computed Tomography — An Increasing Source of Radiation Exposure. *New England Journal of Medicine* **2007**, *357* (22), 2277–2284. <https://doi.org/10.1056/NEJMra072149>.
- (15) Brix, G.; Nekolla, E. A.; Borowski, M.; Noßke, D. Radiation Risk and Protection of Patients in Clinical SPECT/CT. *Eur J Nucl Med Mol Imaging* **2014**, *41* (1), 125–136. <https://doi.org/10.1007/s00259-013-2543-3>.
- (16) Wallis, C. J. D.; Saskin, R.; Choo, R.; Herschorn, S.; Kodama, R. T.; Satkunasivam, R.; Shah, P. S.; Danjoux, C.; Nam, R. K. Surgery Versus Radiotherapy for Clinically-Localized Prostate Cancer: A Systematic Review and Meta-Analysis. *European Urology* **2016**, *70* (1), 21–30. <https://doi.org/10.1016/j.eururo.2015.11.010>.
- (17) Espinosa, E.; Zamora, P.; Feliu, J.; González Barón, M. Classification of Anticancer Drugs—a New System Based on Therapeutic Targets. *Cancer Treatment Reviews* **2003**, *29* (6), 515–523. [https://doi.org/10.1016/S0305-7372\(03\)00116-6](https://doi.org/10.1016/S0305-7372(03)00116-6).
- (18) Shoshan, M. C.; Linder, S. Target Specificity and Off-Target Effects as Determinants of Cancer Drug Efficacy. *Expert Opinion on Drug Metabolism & Toxicology* **2008**, *4* (3), 273–280. <https://doi.org/10.1517/17425255.4.3.273>.
- (19) Jin, S.; Sun, Y.; Liang, X.; Gu, X.; Ning, J.; Xu, Y.; Chen, S.; Pan, L. Emerging New Therapeutic Antibody Derivatives for Cancer Treatment. *Sig Transduct Target Ther* **2022**, *7* (1), 1–28. <https://doi.org/10.1038/s41392-021-00868-x>.
- (20) Tan, S.; Li, D.; Zhu, X. Cancer Immunotherapy: Pros, Cons and Beyond. *Biomed Pharmacother* **2020**, *124*, 109821. <https://doi.org/10.1016/j.biopha.2020.109821>.
- (21) Huang, H.; Lovell, J. F. Advanced Functional Nanomaterials for Theranostics. *Advanced Functional Materials* **2017**, *27* (2), 1603524. <https://doi.org/10.1002/adfm.201603524>.
- (22) De Jong, W. H.; Borm, P. J. Drug Delivery and Nanoparticles: Applications and Hazards. *International Journal of Nanomedicine* **2008**, *3* (2), 133–149. <https://doi.org/10.2147/ijn.s596>.
- (23) Guardia, P.; Labarta, A.; Batlle, X. Tuning the Size, the Shape, and the Magnetic Properties of Iron Oxide Nanoparticles. *J. Phys. Chem. C* **2011**, *115* (2), 390–396. <https://doi.org/10.1021/jp1084982>.
- (24) Nie, S. Understanding and Overcoming Major Barriers in Cancer Nanomedicine. *Nanomedicine (Lond)* **2010**, *5* (4), 523–528. <https://doi.org/10.2217/nnm.10.23>.
- (25) Karaman, D. S.; Desai, D.; Senthilkumar, R.; Johansson, E. M.; Råtts, N.; Odén, M.; Eriksson, J. E.; Sahlgren, C.; Toivola, D. M.; Rosenholm, J. M. Shape Engineering vs Organic Modification of Inorganic Nanoparticles as a Tool for Enhancing Cellular Internalization. *Nanoscale Res Lett* **2012**, *7* (1), 358. <https://doi.org/10.1186/1556-276X-7-358>.
- (26) Schleich, N.; Po, C.; Jacobs, D.; Ucakar, B.; Gallez, B.; Danhier, F.; Pr eat, V. Comparison of Active, Passive and Magnetic Targeting to Tumors of Multifunctional Paclitaxel/SPIO-Loaded Nanoparticles for Tumor Imaging and Therapy. *Journal of Controlled Release* **2014**, *194*, 82–91. <https://doi.org/10.1016/j.jconrel.2014.07.059>.
- (27) Kobayashi, H.; Watanabe, R.; Choyke, P. L. Improving Conventional Enhanced Permeability and Retention (EPR) Effects; What Is the Appropriate Target? *Theranostics* **2013**, *4* (1), 81–89. <https://doi.org/10.7150/thno.7193>.



- (28) Lee, Y.; Thompson, D. h. Stimuli-Responsive Liposomes for Drug Delivery. *WIREs Nanomedicine and Nanobiotechnology* **2017**, *9* (5), e1450. <https://doi.org/10.1002/wnan.1450>.
- (29) Wilhelm, S.; Tavares, A. J.; Dai, Q.; Ohta, S.; Audet, J.; Dvorak, H. F.; Chan, W. C. W. Analysis of Nanoparticle Delivery to Tumours. *Nat Rev Mater* **2016**, *1* (5), 1–12. <https://doi.org/10.1038/natrevmats.2016.14>.
- (30) Byrne, J. D.; Betancourt, T.; Brannon-Peppas, L. Active Targeting Schemes for Nanoparticle Systems in Cancer Therapeutics. *Advanced Drug Delivery Reviews* **2008**, *60* (15), 1615–1626. <https://doi.org/10.1016/j.addr.2008.08.005>.
- (31) Conde, J.; de la Fuente, J.; Baptista, P. Nanomaterials for Reversion of Multidrug Resistance in Cancer: A New Hope for an Old Idea? *Frontiers in Pharmacology* **2013**, *4*.
- (32) Kievit, F. M.; Wang, F. Y.; Fang, C.; Mok, H.; Wang, K.; Silber, J. R.; Ellenbogen, R. G.; Zhang, M. Doxorubicin Loaded Iron Oxide Nanoparticles Overcome Multidrug Resistance in Cancer in Vitro. *Journal of Controlled Release* **2011**, *152* (1), 76–83. <https://doi.org/10.1016/j.jconrel.2011.01.024>.
- (33) Ghorbani, M.; Mahmoodzadeh, F.; Jannat, B.; Maroufi, N. F.; Hashemi, B.; Roshangar, L. Glutathione and pH-Responsive Fluorescent Nanogels for Cell Imaging and Targeted Methotrexate Delivery. *Polymers for Advanced Technologies* **2019**, *30* (7), 1847–1855. <https://doi.org/10.1002/pat.4617>.
- (34) Jędrzak, A.; Grześkowiak, B. F.; Coy, E.; Wojnarowicz, J.; Szutkowski, K.; Jurga, S.; Jesionowski, T.; Mrówczyński, R. Dendrimer Based Theranostic Nanostructures for Combined Chemo- and Photothermal Therapy of Liver Cancer Cells in Vitro. *Colloids and Surfaces B: Biointerfaces* **2019**, *173*, 698–708. <https://doi.org/10.1016/j.colsurfb.2018.10.045>.
- (35) Guo, X.; Zhao, Z.; Chen, D.; Qiao, M.; Wan, F.; Cun, D.; Sun, Y.; Yang, M. Co-Delivery of Resveratrol and Docetaxel via Polymeric Micelles to Improve the Treatment of Drug-Resistant Tumors. *Asian Journal of Pharmaceutical Sciences* **2019**, *14* (1), 78–85. <https://doi.org/10.1016/j.ajps.2018.03.002>.
- (36) Le, N. T. T.; Nguyen Thi, Y. N.; Pham Thi, B. L.; Hoang, N. L.; Nguyen, C. K.; Nguyen, D. H. Nanoliposomes as an Efficient Drug Carrier System for Paclitaxel Delivery. In *7th International Conference on the Development of Biomedical Engineering in Vietnam (BME7)*; Van Toi, V., Le, T. Q., Ngo, H. T., Nguyen, T.-H., Eds.; IFMBE Proceedings; Springer: Singapore, 2020; pp 193–196. [https://doi.org/10.1007/978-981-13-5859-3\\_33](https://doi.org/10.1007/978-981-13-5859-3_33).
- (37) Na, H. B.; Song, I. C.; Hyeon, T. Inorganic Nanoparticles for MRI Contrast Agents. *Advanced Materials* **2009**, *21* (21), 2133–2148. <https://doi.org/10.1002/adma.200802366>.
- (38) Liong, M.; Lu, J.; Kovichich, M.; Xia, T.; Ruehm, S. G.; Nel, A. E.; Tamanoi, F.; Zink, J. I. Multifunctional Inorganic Nanoparticles for Imaging, Targeting, and Drug Delivery. *ACS Nano* **2008**, *2* (5), 889–896. <https://doi.org/10.1021/nn800072t>.
- (39) Kango, S.; Kalia, S.; Celli, A.; Njuguna, J.; Habibi, Y.; Kumar, R. Surface Modification of Inorganic Nanoparticles for Development of Organic-Inorganic Nanocomposites—A Review. *Progress in Polymer Science* **2013**, *38* (8), 1232–1261. <https://doi.org/10.1016/j.progpolymsci.2013.02.003>.

- (40) Cryer, A. M.; Thorley, A. J. Nanotechnology in the Diagnosis and Treatment of Lung Cancer. *Pharmacology & Therapeutics* **2019**, *198*, 189–205. <https://doi.org/10.1016/j.pharmthera.2019.02.010>.
- (41) Saman, N.; Othman, N. S.; Chew, L.-Y.; Mohd Setapar, S. H.; Mat, H. Cetyltrimethylammonium Bromide Functionalized Silica Nanoparticles (MSN) Synthesis Using a Combined Sol-Gel and Adsorption Steps with Enhanced Adsorption Performance of Oxytetracycline in Aqueous Solution. *Journal of the Taiwan Institute of Chemical Engineers* **2020**, *112*, 67–77. <https://doi.org/10.1016/j.jtice.2020.07.008>.
- (42) Kamarudin, N. H.; Abdul Jalil, A.; Triwahyono, S.; Timmiati, S. Microwave-Assisted Synthesis of Mesoporous Silica Nanoparticles as a Drug Delivery Vehicle. *Malaysian Journal of Analytical Science* **2016**, *20*, 1382–1389. <https://doi.org/10.17576/mjas-2016-2006-17>.
- (43) Watermann, A.; Brieger, J. Mesoporous Silica Nanoparticles as Drug Delivery Vehicles in Cancer. *Nanomaterials* **2017**, *7* (7), 189. <https://doi.org/10.3390/nano7070189>.
- (44) Dong, J.-H.; Ma, Y.; Li, R.; Zhang, W.-T.; Zhang, M.-Q.; Meng, F.-N.; Ding, K.; Jiang, H.-T.; Gong, Y.-K. Smart MSN-Drug-Delivery System for Tumor Cell Targeting and Tumor Microenvironment Release. *ACS Appl. Mater. Interfaces* **2021**, *13* (36), 42522–42532. <https://doi.org/10.1021/acsami.1c14189>.
- (45) Nouredine, A.; Maestas-Olguin, A.; Tang, L.; Corman-Hijar, J. I.; Olewine, M.; Krawchuck, J. A.; Tsala Ebode, J.; Edeh, C.; Dang, C.; Negrete, O. A.; Watt, J.; Howard, T.; Coker, E. N.; Guo, J.; Brinker, C. J. Future of Mesoporous Silica Nanoparticles in Nanomedicine: Protocol for Reproducible Synthesis, Characterization, Lipid Coating, and Loading of Therapeutics (Chemotherapeutic, Proteins, siRNA and mRNA). *ACS Nano* **2023**, *17* (17), 16308–16325. <https://doi.org/10.1021/acsnano.3c07621>.
- (46) Yildirim, A.; Ozgur, E.; Bayindir, M. Impact of Mesoporous Silica Nanoparticle Surface Functionality on Hemolytic Activity, Thrombogenicity and Non-Specific Protein Adsorption. *J. Mater. Chem. B* **2013**, *1* (14), 1909. <https://doi.org/10.1039/c3tb20139b>.
- (47) Estevão, B. M.; Miletto, I.; Hioka, N.; Marchese, L.; Gianotti, E. Mesoporous Silica Nanoparticles Functionalized with Amino Groups for Biomedical Applications. *ChemistryOpen* **2021**, *10* (12), 1251–1259. <https://doi.org/10.1002/open.202100227>.
- (48) Carniato, F.; Tei, L.; Botta, M. Gd-Based Mesoporous Silica Nanoparticles as MRI Probes. *European Journal of Inorganic Chemistry* **2018**, *2018* (46), 4936–4954. <https://doi.org/10.1002/ejic.201801039>.
- (49) Luo, X.; Liu, P.; Truong, N. T. N.; Farva, U.; Park, C. Photoluminescence Blue-Shift of CdSe Nanoparticles Caused by Exchange of Surface Capping Layer. *J. Phys. Chem. C* **2011**, *115* (43), 20817–20823. <https://doi.org/10.1021/jp200701x>.
- (50) David Wegner, K.; Hildebrandt, N. Quantum Dots: Bright and Versatile in Vitro and in Vivo Fluorescence Imaging Biosensors. *Chemical Society Reviews* **2015**, *44* (14), 4792–4834. <https://doi.org/10.1039/C4CS00532E>.
- (51) Pandey, S.; Bodas, D. High-Quality Quantum Dots for Multiplexed Bioimaging: A Critical Review. *Advances in Colloid and Interface Science* **2020**, *278*, 102137. <https://doi.org/10.1016/j.cis.2020.102137>.

- (52) Tsoi, K. M.; Dai, Q.; Alman, B. A.; Chan, W. C. W. Are Quantum Dots Toxic? Exploring the Discrepancy Between Cell Culture and Animal Studies. *Acc. Chem. Res.* **2013**, *46* (3), 662–671. <https://doi.org/10.1021/ar300040z>.
- (53) Abdelhamid, H. N.; El-Bery, H. M.; Metwally, A. A.; Elshazly, M.; Hathout, R. M. Synthesis of CdS-Modified Chitosan Quantum Dots for the Drug Delivery of Sesamol. *Carbohydrate Polymers* **2019**, *214*, 90–99. <https://doi.org/10.1016/j.carbpol.2019.03.024>.
- (54) Hornos Carneiro, M. F.; Barbosa, F. Gold Nanoparticles: A Critical Review of Therapeutic Applications and Toxicological Aspects. *Journal of Toxicology and Environmental Health, Part B* **2016**, *19* (3–4), 129–148. <https://doi.org/10.1080/10937404.2016.1168762>.
- (55) Špringer, T.; Homola, J. Biofunctionalized Gold Nanoparticles for SPR-Biosensor-Based Detection of CEA in Blood Plasma. *Anal Bioanal Chem* **2012**, *404* (10), 2869–2875. <https://doi.org/10.1007/s00216-012-6308-9>.
- (56) Alle, M.; Sharma, G.; Lee, S.-H.; Kim, J.-C. Next-Generation Engineered Nanogold for Multimodal Cancer Therapy and Imaging: A Clinical Perspectives. *Journal of Nanobiotechnology* **2022**, *20* (1), 222. <https://doi.org/10.1186/s12951-022-01402-z>.
- (57) Yang, L.; Tseng, Y.-T.; Suo, G.; Chen, L.; Yu, J.; Chiu, W.-J.; Huang, C.-C.; Lin, C.-H. Photothermal Therapeutic Response of Cancer Cells to Aptamer–Gold Nanoparticle-Hybridized Graphene Oxide under NIR Illumination. *ACS Appl. Mater. Interfaces* **2015**, *7* (9), 5097–5106. <https://doi.org/10.1021/am508117e>.
- (58) Chen, J.; Ma, Y.; Du, W.; Dai, T.; Wang, Y.; Jiang, W.; Wan, Y.; Wang, Y.; Liang, G.; Wang, G. Furin-Instructed Intracellular Gold Nanoparticle Aggregation for Tumor Photothermal Therapy. *Advanced Functional Materials* **2020**, *30* (50), 2001566. <https://doi.org/10.1002/adfm.202001566>.
- (59) Alp, E.; Aydogan, N. A Comparative Study: Synthesis of Superparamagnetic Iron Oxide Nanoparticles in Air and N<sub>2</sub> Atmosphere. *Colloids and Surfaces A: Physicochemical and Engineering Aspects* **2016**, *510*, 205–212. <https://doi.org/10.1016/j.colsurfa.2016.06.033>.
- (60) Khalkhali, M.; Rostamizadeh, K.; Sadighian, S.; Khoeini, F.; Naghibi, M.; Hamidi, M. The Impact of Polymer Coatings on Magnetite Nanoparticles Performance as MRI Contrast Agents: A Comparative Study. *DARU J Pharm Sci* **2015**, *23* (1), 45. <https://doi.org/10.1186/s40199-015-0124-7>.
- (61) Sodipo, B. K.; Aziz, A. A. Recent Advances in Synthesis and Surface Modification of Superparamagnetic Iron Oxide Nanoparticles with Silica. *Journal of Magnetism and Magnetic Materials* **2016**, *416*, 275–291. <https://doi.org/10.1016/j.jmmm.2016.05.019>.
- (62) Thakor, A. S.; Jokerst, J. V.; Ghanouni, P.; Campbell, J. L.; Mitra, E.; Gambhir, S. S. Clinically Approved Nanoparticle Imaging Agents. *Journal of Nuclear Medicine* **2016**, *57* (12), 1833–1837. <https://doi.org/10.2967/jnumed.116.181362>.
- (63) Nieciecka, D.; Celej, J.; Żuk, M.; Majkowska-Pilip, A.; Żelechowska-Matysiak, K.; Lis, A.; Osial, M. Hybrid System for Local Drug Delivery and Magnetic Hyperthermia Based on SPIONs Loaded with Doxorubicin and Epirubicin. *Pharmaceutics* **2021**, *13* (4), 480. <https://doi.org/10.3390/pharmaceutics13040480>.
- (64) Mandl, G. A.; Cooper, D. R.; Hirsch, T.; Seuntjens, J.; Capobianco, J. A. Perspective: Lanthanide-Doped Upconverting Nanoparticles. *Methods Appl. Fluoresc.* **2019**, *7* (1), 012004. <https://doi.org/10.1088/2050-6120/aafa3d>.

- (65) Chang, H.; Xie, J.; Zhao, B.; Liu, B.; Xu, S.; Ren, N.; Xie, X.; Huang, L.; Huang, W. Rare Earth Ion-Doped Upconversion Nanocrystals: Synthesis and Surface Modification. *Nanomaterials* **2015**, *5* (1), 1–25. <https://doi.org/10.3390/nano5010001>.
- (66) Li, H.; Liu, X.; Li, X. Solvothermal Synthesis and Modification of NaYF<sub>4</sub>:Yb/Er@NaLuF<sub>4</sub>:Yb for Enhanced up-Conversion Luminescence for Bioimaging. *RSC Advances* **2019**, *9* (72), 42163–42171. <https://doi.org/10.1039/C9RA08921G>.
- (67) Zheng, W.; Huang, P.; Tu, D.; Ma, E.; Zhu, H.; Chen, X. Lanthanide-Doped Upconversion Nano-Bioprobes: Electronic Structures, Optical Properties, and Biodetection. *Chemical Society Reviews* **2015**, *44* (6), 1379–1415. <https://doi.org/10.1039/C4CS00178H>.
- (68) Fan, Y.; Liu, L.; Zhang, F. Exploiting Lanthanide-Doped Upconversion Nanoparticles with Core/Shell Structures. *Nano Today* **2019**, *25*, 68–84. <https://doi.org/10.1016/j.nantod.2019.02.009>.
- (69) Yi, Z.; Li, X.; Xue, Z.; Liang, X.; Lu, W.; Peng, H.; Liu, H.; Zeng, S.; Hao, J. Remarkable NIR Enhancement of Multifunctional Nanoprobes for In Vivo Trimodal Bioimaging and Upconversion Optical/T<sub>2</sub>-Weighted MRI-Guided Small Tumor Diagnosis. *Advanced Functional Materials* **2015**, *25* (46), 7119–7129. <https://doi.org/10.1002/adfm.201503672>.
- (70) Ge, X.; Dong, L.; Sun, L.; Song, Z.; Wei, R.; Shi, L.; Chen, H. New Nanoplatforms Based on UCNPs Linking with Polyhedral Oligomeric Silsesquioxane (POSS) for Multimodal Bioimaging. *Nanoscale* **2015**, *7* (16), 7206–7215. <https://doi.org/10.1039/C5NR00950B>.
- (71) Zeng, S.; Tsang, M.-K.; Chan, C.-F.; Wong, K.-L.; Hao, J. PEG Modified BaGdF<sub>5</sub>:Yb/Er Nanoprobes for Multi-Modal Upconversion Fluorescent, in Vivo X-Ray Computed Tomography and Biomagnetic Imaging. *Biomaterials* **2012**, *33* (36), 9232–9238. <https://doi.org/10.1016/j.biomaterials.2012.09.019>.
- (72) Feng, L.; He, F.; Dai, Y.; Gai, S.; Zhong, C.; Li, C.; Yang, P. Multifunctional UCNPs@MnSiO<sub>3</sub>@g-C<sub>3</sub>N<sub>4</sub> Nanoplatform: Improved ROS Generation and Reduced Glutathione Levels for Highly Efficient Photodynamic Therapy. *Biomaterials Science* **2017**, *5* (12), 2456–2467. <https://doi.org/10.1039/C7BM00798A>.
- (73) Bonacina, L. Nonlinear Nanomedicine: Harmonic Nanoparticles toward Targeted Diagnosis and Therapy. *Mol. Pharmaceutics* **2013**, *10* (3), 783–792. <https://doi.org/10.1021/mp300523e>.
- (74) Yu, J.; Liu, X. Hydrothermal Synthesis and Characterization of LiNbO<sub>3</sub> Crystal. *Materials Letters* **2007**, *61* (2), 355–358. <https://doi.org/10.1016/j.matlet.2006.04.087>.
- (75) Urbain, M.; Riporto, F.; Beauquis, S.; Monnier, V.; Marty, J.-C.; Galez, C.; Durand, C.; Chevolut, Y.; Dantec, R. L.; Mugnier, Y. On the Reaction Pathways and Growth Mechanisms of LiNbO<sub>3</sub> Nanocrystals from the Non-Aqueous Solvothermal Alkoxide Route. *Nanomaterials* **2021**, *11* (1), 154. <https://doi.org/10.3390/nano11010154>.
- (76) Riporto, J.; Urbain, M.; Mugnier, Y.; Multian, V.; Riporto, F.; Bredillet, K.; Beauquis, S.; Galez, C.; Monnier, V.; Chevolut, Y.; Gayvoronsky, V.; Bonacina, L.; Dantec, R. L. Second Harmonic Spectroscopy of ZnO, BiFeO<sub>3</sub> and LiNbO<sub>3</sub> Nanocrystals. *Opt. Mater. Express, OME* **2019**, *9* (4), 1955–1966. <https://doi.org/10.1364/OME.9.001955>.
- (77) Dubreil, L.; Leroux, I.; Ledevin, M.; Schleder, C.; Lagalice, L.; Lovo, C.; Fleurisson, R.; Passemand, S.; Kilin, V.; Gerber-Lemaire, S.; Colle, M.-A.; Bonacina, L.; Rouger, K. Multi-

- Harmonic Imaging in the Second Near-Infrared Window of Nanoparticle-Labeled Stem Cells as a Monitoring Tool in Tissue Depth. *ACS Nano* **2017**, *11* (7), 6672–6681. <https://doi.org/10.1021/acsnano.7b00773>.
- (78) Dempsey, W. P.; Fraser, S. E.; Pantazis, P. SHG Nanoprobes: Advancing Harmonic Imaging in Biology. *BioEssays* **2012**, *34* (5), 351–360. <https://doi.org/10.1002/bies.201100106>.
- (79) Grange, R.; Lanvin, T.; Hsieh, C.-L.; Pu, Y.; Psaltis, D. Imaging with Second-Harmonic Radiation Probes in Living Tissue. *Biomed. Opt. Express*, *BOE* **2011**, *2* (9), 2532–2539. <https://doi.org/10.1364/BOE.2.002532>.
- (80) Le Xuan, L.; Zhou, C.; Slablab, A.; Chauvat, D.; Tard, C.; Perruchas, S.; Gacoin, T.; Villeval, P.; Roch, J.-F. Photostable Second-Harmonic Generation from a Single KTiOPO<sub>4</sub> Nanocrystal for Nonlinear Microscopy. *Small* **2008**, *4* (9), 1332–1336. <https://doi.org/10.1002/sml.200701093>.
- (81) Staedler, D.; Passemard, S.; Magouroux, T.; Rogov, A.; Maguire, C. M.; Mohamed, B. M.; Schwung, S.; Rytz, D.; Jüstel, T.; Hwu, S.; Mugnier, Y.; Le Dantec, R.; Volkov, Y.; Gerber-Lemaire, S.; Prina-Mello, A.; Bonacina, L.; Wolf, J.-P. Cellular Uptake and Biocompatibility of Bismuth Ferrite Harmonic Advanced Nanoparticles. *Nanomedicine: Nanotechnology, Biology and Medicine* **2015**, *11* (4), 815–824. <https://doi.org/10.1016/j.nano.2014.12.018>.
- (82) Sanità, G.; Carrese, B.; Lamberti, A. Nanoparticle Surface Functionalization: How to Improve Biocompatibility and Cellular Internalization. *Frontiers in Molecular Biosciences* **2020**, *7*.
- (83) Nobs, L.; Buchegger, F.; Gurny, R.; Allémann, E. Current Methods for Attaching Targeting Ligands to Liposomes and Nanoparticles. *Journal of Pharmaceutical Sciences* **2004**, *93* (8), 1980–1992. <https://doi.org/10.1002/jps.20098>.
- (84) Bolaños, K.; Kogan, M. J.; Araya, E. Capping Gold Nanoparticles with Albumin to Improve Their Biomedical Properties. *International Journal of Nanomedicine* **2019**, *14*, 6387–6406. <https://doi.org/10.2147/IJN.S210992>.
- (85) Yang, Z.; Xie, Z.; Liu, H.; Yan, F.; Ju, H. Streptavidin-Functionalized Three-Dimensional Ordered Nanoporous Silica Film for Highly Efficient Chemiluminescent Immunosensing. *Advanced Functional Materials* **2008**, *18* (24), 3991–3998. <https://doi.org/10.1002/adfm.200801022>.
- (86) Gamucci, O.; Bertero, A.; Gagliardi, M.; Bardi, G. Biomedical Nanoparticles: Overview of Their Surface Immune-Compatibility. *Coatings* **2014**, *4* (1), 139–159. <https://doi.org/10.3390/coatings4010139>.
- (87) Suk, J. S.; Xu, Q.; Kim, N.; Hanes, J.; Ensign, L. M. PEGylation as a Strategy for Improving Nanoparticle-Based Drug and Gene Delivery. *Advanced Drug Delivery Reviews* **2016**, *99*, 28–51. <https://doi.org/10.1016/j.addr.2015.09.012>.
- (88) Gao, H.; Liu, J.; Yang, C.; Cheng, T.; Chu, L.; Xu, H.; Meng, A.; Fan, S.; Shi, L.; Liu, J. The Impact of PEGylation Patterns on the in Vivo Biodistribution of Mixed Shell Micelles. *International Journal of Nanomedicine* **2013**, *8*, 4229–4246. <https://doi.org/10.2147/IJN.S51566>.
- (89) Guerrero-Martínez, A.; Pérez-Juste, J.; Liz-Marzán, L. M. Recent Progress on Silica Coating of Nanoparticles and Related Nanomaterials. *Advanced Materials* **2010**, *22* (11), 1182–1195. <https://doi.org/10.1002/adma.200901263>.

- (90) Ghimire, P. P.; Jaroniec, M. Renaissance of Stöber Method for Synthesis of Colloidal Particles: New Developments and Opportunities. *Journal of Colloid and Interface Science* **2021**, *584*, 838–865. <https://doi.org/10.1016/j.jcis.2020.10.014>.
- (91) Hardikar, V. V.; Matijević, E. Coating of Nanosize Silver Particles with Silica. *Journal of Colloid and Interface Science* **2000**, *221* (1), 133–136. <https://doi.org/10.1006/jcis.1999.6579>.
- (92) McClements, D. J.; Dickinson, E.; Dungan, S. R.; Kinsella, J. E.; Ma, J. G.; Povey, M. J. W. Effect of Emulsifier Type on the Crystallization Kinetics of Oil-in-Water Emulsions Containing a Mixture of Solid and Liquid Droplets. *Journal of Colloid and Interface Science* **1993**, *160* (2), 293–297. <https://doi.org/10.1006/jcis.1993.1399>.
- (93) Huang, Y.-F.; Wang, Y.-F.; Yan, X.-P. Amine-Functionalized Magnetic Nanoparticles for Rapid Capture and Removal of Bacterial Pathogens. *Environ. Sci. Technol.* **2010**, *44* (20), 7908–7913. <https://doi.org/10.1021/es102285n>.
- (94) Ma, M.; Zhang, Y.; Yu, W.; Shen, H.; Zhang, H.; Gu, N. Preparation and Characterization of Magnetite Nanoparticles Coated by Amino Silane. *Colloids and Surfaces A: Physicochemical and Engineering Aspects* **2003**, *212* (2), 219–226. [https://doi.org/10.1016/S0927-7757\(02\)00305-9](https://doi.org/10.1016/S0927-7757(02)00305-9).
- (95) Yamaura, M.; Camilo, R. L.; Sampaio, L. C.; Macêdo, M. A.; Nakamura, M.; Toma, H. E. Preparation and Characterization of (3-Aminopropyl)Triethoxysilane-Coated Magnetite Nanoparticles. *Journal of Magnetism and Magnetic Materials* **2004**, *279* (2), 210–217. <https://doi.org/10.1016/j.jmmm.2004.01.094>.
- (96) Fu, X.; Qutubuddin, S. Synthesis of Titania-Coated Silica Nanoparticles Using a Nonionic Water-in-Oil Microemulsion. *Colloids and Surfaces A: Physicochemical and Engineering Aspects* **2001**, *179* (1), 65–70. [https://doi.org/10.1016/S0927-7757\(00\)00723-8](https://doi.org/10.1016/S0927-7757(00)00723-8).
- (97) Abraham, L.; Thomas, T.; Pichumani, M. Do Depletant Stabilized Water-in-Oil Microemulsions Have Implications for Nanoencapsulation? *Colloids and Surfaces A: Physicochemical and Engineering Aspects* **2019**, *577*, 440–448. <https://doi.org/10.1016/j.colsurfa.2019.06.006>.
- (98) Ding, H. L.; Zhang, Y. X.; Wang, S.; Xu, J. M.; Xu, S. C.; Li, G. H. Fe<sub>3</sub>O<sub>4</sub>@SiO<sub>2</sub> Core/Shell Nanoparticles: The Silica Coating Regulations with a Single Core for Different Core Sizes and Shell Thicknesses. *Chem. Mater.* **2012**, *24* (23), 4572–4580. <https://doi.org/10.1021/cm302828d>.
- (99) Yi, D. K.; Selvan, S. T.; Lee, S. S.; Papaefthymiou, G. C.; Kundaliya, D.; Ying, J. Y. Silica-Coated Nanocomposites of Magnetic Nanoparticles and Quantum Dots. *J. Am. Chem. Soc.* **2005**, *127* (14), 4990–4991. <https://doi.org/10.1021/ja0428863>.
- (100) Santra, S.; Tapeç, R.; Theodoropoulou, N.; Dobson, J.; Hebard, A.; Tan, W. Synthesis and Characterization of Silica-Coated Iron Oxide Nanoparticles in Microemulsion: The Effect of Nonionic Surfactants. *Langmuir* **2001**, *17* (10), 2900–2906. <https://doi.org/10.1021/la0008636>.
- (101) Aubert, T.; Grasset, F.; Mornet, S.; Duguet, E.; Cador, O.; Cordier, S.; Molard, Y.; Demange, V.; Mortier, M.; Haneda, H. Functional Silica Nanoparticles Synthesized by Water-in-Oil Microemulsion Processes. *Journal of Colloid and Interface Science* **2010**, *341* (2), 201–208. <https://doi.org/10.1016/j.jcis.2009.09.064>.

- (102) Han, Y.; Jiang, J.; Lee, S. S.; Ying, J. Y. Reverse Microemulsion-Mediated Synthesis of Silica-Coated Gold and Silver Nanoparticles. *Langmuir* **2008**, *24* (11), 5842–5848. <https://doi.org/10.1021/la703440p>.
- (103) Bolley, J.; Guenin, E.; Lievre, N.; Lecouvey, M.; Soussan, M.; Lalatonne, Y.; Motte, L. Carbodiimide versus Click Chemistry for Nanoparticle Surface Functionalization: A Comparative Study for the Elaboration of Multimodal Superparamagnetic Nanoparticles Targeting  $\text{Av}\beta 3$  Integrins. *Langmuir* **2013**, *29* (47), 14639–14647. <https://doi.org/10.1021/la403245h>.
- (104) Oh, E.; Susumu, K.; Blanco-Canosa, J. B.; Medintz, I. L.; Dawson, P. E.; Mattoussi, H. Preparation of Stable Maleimide-Functionalized Au Nanoparticles and Their Use in Counting Surface Ligands. *Small* **2010**, *6* (12), 1273–1278. <https://doi.org/10.1002/sml.201000279>.
- (105) Bednarek, C.; Wehl, I.; Jung, N.; Schepers, U.; Bräse, S. The Staudinger Ligation. *Chem. Rev.* **2020**, *120* (10), 4301–4354. <https://doi.org/10.1021/acs.chemrev.9b00665>.
- (106) Johann, K.; Svatunek, D.; Seidl, C.; Rizzelli, S.; A. Bauer, T.; Braun, L.; Koynov, K.; Mikula, H.; Barz, M. Tetrazine- and Trans -Cyclooctene-Functionalised Polypept(o)ides for Fast Bioorthogonal Tetrazine Ligation. *Polymer Chemistry* **2020**, *11* (27), 4396–4407. <https://doi.org/10.1039/D0PY00375A>.
- (107) M. Fratila, R.; Navascuez, M.; Idiago-López, J.; Eceiza, M.; I. Miranda, J.; M. Aizpurua, J.; Fuente, J. M. de la. Covalent Immobilisation of Magnetic Nanoparticles on Surfaces via Strain-Promoted Azide-Alkyne Click Chemistry. *New Journal of Chemistry* **2017**, *41* (19), 10835–10840. <https://doi.org/10.1039/C7NJ01822C>.
- (108) Yoon, H. Y.; Lee, D.; Lim, D.-K.; Koo, H.; Kim, K. Copper-Free Click Chemistry: Applications in Drug Delivery, Cell Tracking, and Tissue Engineering. *Advanced Materials* **2022**, *34* (10), 2107192. <https://doi.org/10.1002/adma.202107192>.
- (109) Gulfam, M.; Sahle, F. F.; Lowe, T. L. Design Strategies for Chemical-Stimuli-Responsive Programmable Nanotherapeutics. *Drug Discovery Today* **2019**, *24* (1), 129–147. <https://doi.org/10.1016/j.drudis.2018.09.019>.
- (110) Bibi, S.; Lattmann, E.; Mohammed, A. R.; Perrie, Y. Trigger Release Liposome Systems: Local and Remote Controlled Delivery? *Journal of Microencapsulation* **2012**, *29* (3), 262–276. <https://doi.org/10.3109/02652048.2011.646330>.
- (111) Liu, D.; Yang, F.; Xiong, F.; Gu, N. The Smart Drug Delivery System and Its Clinical Potential. *Theranostics* **2016**, *6* (9), 1306–1323. <https://doi.org/10.7150/thno.14858>.
- (112) Karimi, M.; Ghasemi, A.; Zangabad, P. S.; Rahighi, R.; Basri, S. M. M.; Mirshekari, H.; Amiri, M.; Pishabad, Z. S.; Aslani, A.; Bozorgomid, M.; Ghosh, D.; Beyzavi, A.; Vaseghi, A.; R. Aref, A.; Haghani, L.; Bahrami, S.; R. Hamblin, M. Smart Micro/Nanoparticles in Stimulus-Responsive Drug/Gene Delivery Systems. *Chemical Society Reviews* **2016**, *45* (5), 1457–1501. <https://doi.org/10.1039/C5CS00798D>.
- (113) Ellis-Davies, G. C. R. Caged Compounds: Photorelease Technology for Control of Cellular Chemistry and Physiology. *Nat Methods* **2007**, *4* (8), 619–628. <https://doi.org/10.1038/nmeth1072>.

- (114) Liu, Q.; Zhan, C.; Kohane, D. S. Phototriggered Drug Delivery Using Inorganic Nanomaterials. *Bioconjugate Chem.* **2017**, *28* (1), 98–104. <https://doi.org/10.1021/acs.bioconjchem.6b00448>.
- (115) Sahu, A.; Kim, M.; Ryu, J.; Son, J.-G.; Lee, E.; Noh, D. Y.; Tae, G. Nanographene Oxide as a Switch for CW/Pulsed NIR Laser Triggered Drug Release from Liposomes. *Materials Science and Engineering: C* **2018**, *82*, 19–24. <https://doi.org/10.1016/j.msec.2017.08.057>.
- (116) Bao, C.; Zhu, L.; Lin, Q.; Tian, H. Building Biomedical Materials Using Photochemical Bond Cleavage. *Advanced Materials* **2015**, *27* (10), 1647–1662. <https://doi.org/10.1002/adma.201403783>.
- (117) Singh, A. K.; Khade, P. K. 7-Methoxy-3-Nitro-2-Naphthalenemethanol—a New Phototrigger for Caging Applications. *Tetrahedron Letters* **2011**, *52* (38), 4899–4902. <https://doi.org/10.1016/j.tetlet.2011.07.043>.
- (118) Thomas III, S. W. New Applications of Photolabile Nitrobenzyl Groups in Polymers. *Macromolecular Chemistry and Physics* **2012**, *213* (23), 2443–2449. <https://doi.org/10.1002/macp.201200486>.
- (119) Givens, R. S.; Lee, J.-I. The P-Hydroxyphenacyl Photoremovable Protecting Group. *ChemInform* **2004**, *35* (23). <https://doi.org/10.1002/chin.200423262>.
- (120) Furuta, T.; Wang, S. S.-H.; Dantzker, J. L.; Dore, T. M.; Bybee, W. J.; Callaway, E. M.; Denk, W.; Tsien, R. Y. Brominated 7-Hydroxycoumarin-4-Ylmethyls: Photolabile Protecting Groups with Biologically Useful Cross-Sections for Two Photon Photolysis. *Proceedings of the National Academy of Sciences* **1999**, *96* (4), 1193–1200. <https://doi.org/10.1073/pnas.96.4.1193>.
- (121) Aujard, I.; Benbrahim, C.; Gouget, M.; Ruel, O.; Baudin, J.-B.; Neveu, P.; Jullien, L. O-Nitrobenzyl Photolabile Protecting Groups with Red-Shifted Absorption: Syntheses and Uncaging Cross-Sections for One- and Two-Photon Excitation. *Chemistry – A European Journal* **2006**, *12* (26), 6865–6879. <https://doi.org/10.1002/chem.200501393>.
- (122) Yu, H.; Li, J.; Wu, D.; Qiu, Z.; Zhang, Y. Chemistry and Biological Applications of Photo-Labile Organic Molecules. *Chemical Society Reviews* **2010**, *39* (2), 464–473. <https://doi.org/10.1039/B901255A>.
- (123) Klán, P.; Šolomek, T.; Bochet, C. G.; Blanc, A.; Givens, R.; Rubina, M.; Popik, V.; Kostikov, A.; Wirz, J. Photoremovable Protecting Groups in Chemistry and Biology: Reaction Mechanisms and Efficacy. *Chem. Rev.* **2013**, *113* (1), 119–191. <https://doi.org/10.1021/cr300177k>.
- (124) Paola Pelliccioli, A.; Wirz, J. Photoremovable Protecting Groups: Reaction Mechanisms and Applications. *Photochemical & Photobiological Sciences* **2002**, *1* (7), 441–458. <https://doi.org/10.1039/B200777K>.
- (125) Falvey, D. E.; Sundararajan, C. Photoremovable Protecting Groups Based on Electron Transfer Chemistry. *Photochem Photobiol Sci* **2004**, *3* (9), 831–838. <https://doi.org/10.1039/b406866a>.
- (126) Horbert, R.; Pinchuk, B.; Davies, P.; Alessi, D.; Peifer, C. Photoactivatable Prodrugs of Antimelanoma Agent Vemurafenib. *ACS Chem. Biol.* **2015**, *10* (9), 2099–2107. <https://doi.org/10.1021/acscchembio.5b00174>.



- (127) Marriott, G. Caged Protein Conjugates and Light-Directed Generation of Protein Activity: Preparation, Photoactivation, and Spectroscopic Characterization of Caged G-Actin Conjugates. *Biochemistry* **1994**, *33* (31), 9092–9097. <https://doi.org/10.1021/bi00197a010>.
- (128) Ah Kim, Y.; Carter Ramirez, D. M.; J. Costain, W.; J. Johnston, L.; Bittman, R. A New Tool to Assess Ceramide Bioactivity: 6-Bromo-7-Hydroxycoumarinyl-Caged Ceramide. *Chemical Communications* **2011**, *47* (32), 9236–9238. <https://doi.org/10.1039/C1CC12345A>.
- (129) Zhang, D.; Zhou, C. Y.; Busby, K. N.; Alexander, S. C.; Devaraj, N. K. Light-Activated Control of Translation by Enzymatic Covalent mRNA Labeling. *Angewandte Chemie International Edition* **2018**, *57* (11), 2822–2826. <https://doi.org/10.1002/anie.201710917>.
- (130) Yang, G.; Liu, J.; Wu, Y.; Feng, L.; Liu, Z. Near-Infrared-Light Responsive Nanoscale Drug Delivery Systems for Cancer Treatment. *Coordination Chemistry Reviews* **2016**, *320–321*, 100–117. <https://doi.org/10.1016/j.ccr.2016.04.004>.
- (131) Shim, G.; Ko, S.; Kim, D.; Le, Q.-V.; Park, G. T.; Lee, J.; Kwon, T.; Choi, H.-G.; Kim, Y. B.; Oh, Y.-K. Light-Switchable Systems for Remotely Controlled Drug Delivery. *Journal of Controlled Release* **2017**, *267*, 67–79. <https://doi.org/10.1016/j.jconrel.2017.09.009>.
- (132) Raza, A.; Hayat, U.; Rasheed, T.; Bilal, M.; Iqbal, H. M. N. “Smart” Materials-Based near-Infrared Light-Responsive Drug Delivery Systems for Cancer Treatment: A Review. *Journal of Materials Research and Technology* **2019**, *8* (1), 1497–1509. <https://doi.org/10.1016/j.jmrt.2018.03.007>.
- (133) Villalba-Rodriguez, A. M.; Parra-Saldivar, R.; Ahmed, I.; Karthik, K.; Malik, Y. S.; Dhama, K.; Iqbal, H. M. N. Bio-Inspired Biomaterials and Their Drug Delivery Perspectives - A Review. *Current Drug Metabolism* **2017**, *18* (10), 893–904. <https://doi.org/10.2174/1389200218666170925113132>.
- (134) Yang, Y.; Lin, Y.; Di, D.; Zhang, X.; Wang, D.; Zhao, Q.; Wang, S. Gold Nanoparticle-Gated Mesoporous Silica as Redox-Triggered Drug Delivery for Chemo-Photothermal Synergistic Therapy. *Journal of Colloid and Interface Science* **2017**, *508*, 323–331. <https://doi.org/10.1016/j.jcis.2017.08.050>.
- (135) Croissant, J. G.; Zink, J. I.; Raehm, L.; Durand, J.-O. Two-Photon-Excited Silica and Organosilica Nanoparticles for Spatiotemporal Cancer Treatment. *Advanced Healthcare Materials* **2018**, *7* (7), 1701248. <https://doi.org/10.1002/adhm.201701248>.
- (136) Lin, Q.; Huang, Q.; Li, C.; Bao, C.; Liu, Z.; Li, F.; Zhu, L. Anticancer Drug Release from a Mesoporous Silica Based Nanophotocage Regulated by Either a One- or Two-Photon Process. *J. Am. Chem. Soc.* **2010**, *132* (31), 10645–10647. <https://doi.org/10.1021/ja103415t>.
- (137) Liu, S.; Li, W.; Gai, S.; Yang, G.; Zhong, C.; Dai, Y.; He, F.; Yang, P.; Doug Suh, Y. A Smart Tumor Microenvironment Responsive Nanoplatform Based on Upconversion Nanoparticles for Efficient Multimodal Imaging Guided Therapy. *Biomaterials Science* **2019**, *7* (3), 951–962. <https://doi.org/10.1039/C8BM01243A>.
- (138) Wong, P. T.; Chen, D.; Tang, S.; Yanik, S.; Payne, M.; Mukherjee, J.; Coulter, A.; Tang, K.; Tao, K.; Sun, K.; Baker Jr., J. R.; Choi, S. K. Modular Integration of Upconverting Nanocrystal-Dendrimer Composites for Folate Receptor-Specific NIR Imaging and Light-Triggered Drug Release. *Small* **2015**, *11* (45), 6078–6090. <https://doi.org/10.1002/smll.201501575>.

- (139) Vuilleumier, J.; Gaulier, G.; De Matos, R.; Ortiz, D.; Menin, L.; Campargue, G.; Mas, C.; Constant, S.; Le Dantec, R.; Mugnier, Y.; Bonacina, L.; Gerber-Lemaire, S. Two-Photon-Triggered Photorelease of Caged Compounds from Multifunctional Harmonic Nanoparticles. *ACS Appl. Mater. Interfaces* **2019**, *11* (30), 27443–27452. <https://doi.org/10.1021/acsami.9b07954>.
- (140) Kircher, M. F.; Willmann, J. K. Molecular Body Imaging: MR Imaging, CT, and US. Part I. Principles. *Radiology* **2012**, *263* (3), 633–643. <https://doi.org/10.1148/radiol.12102394>.
- (141) Bar-Shalom, R.; Valdivia, A. Y.; Blaufox, M. D. PET Imaging in Oncology. *Seminars in Nuclear Medicine* **2000**, *30* (3), 150–185. <https://doi.org/10.1053/snuc.2000.7439>.
- (142) Weissleder, R.; Pittet, M. J. Imaging in the Era of Molecular Oncology. *Nature* **2008**, *452* (7187), 580–589. <https://doi.org/10.1038/nature06917>.
- (143) Tichauer, K. M.; Wang, Y.; Pogue, B. W.; Liu, J. T. C. Quantitative in Vivo Cell-Surface Receptor Imaging in Oncology: Kinetic Modeling and Paired-Agent Principles from Nuclear Medicine and Optical Imaging. *Phys. Med. Biol.* **2015**, *60* (14), R239. <https://doi.org/10.1088/0031-9155/60/14/R239>.
- (144) Martí-Bonmatí, L.; Sopena, R.; Bartumeus, P.; Sopena, P. Multimodality Imaging Techniques. *Contrast Media & Molecular Imaging* **2010**, *5* (4), 180–189. <https://doi.org/10.1002/cmmi.393>.
- (145) Townsend, D. W.; Beyer, T.; Blodgett, T. M. PET/CT Scanners: A Hardware Approach to Image Fusion. *Seminars in Nuclear Medicine* **2003**, *33* (3), 193–204. <https://doi.org/10.1053/snuc.2003.127314>.
- (146) Loeffelbein, D. J.; Souvatzoglou, M.; Wankerl, V.; Martinez-Möller, A.; Dinges, J.; Schwaiger, M.; Beer, A. J. PET-MRI Fusion in Head-and-Neck Oncology: Current Status and Implications for Hybrid PET/MRI. *Journal of Oral and Maxillofacial Surgery* **2012**, *70* (2), 473–483. <https://doi.org/10.1016/j.joms.2011.02.120>.
- (147) Key, J.; Leary, J. F. Nanoparticles for Multimodal in Vivo Imaging in Nanomedicine. *International Journal of Nanomedicine* **2014**, *9*, 711–726. <https://doi.org/10.2147/IJN.S53717>.
- (148) Hong, H.; Wang, F.; Zhang, Y.; Graves, S. A.; Eddine, S. B. Z.; Yang, Y.; Theuer, C. P.; Nickles, R. J.; Wang, X.; Cai, W. Red Fluorescent Zinc Oxide Nanoparticle: A Novel Platform for Cancer Targeting. *ACS Appl. Mater. Interfaces* **2015**, *7* (5), 3373–3381. <https://doi.org/10.1021/am508440j>.
- (149) Kircher, M. F.; Mahmood, U.; King, R. S.; Weissleder, R.; Josephson, L. A Multimodal Nanoparticle for Preoperative Magnetic Resonance Imaging and Intraoperative Optical Brain Tumor Delineation. *Cancer Research* **2003**, *63* (23), 8122–8125.
- (150) Hwang, D. W.; Ko, H. Y.; Lee, J. H.; Kang, H.; Ryu, S. H.; Song, I. C.; Lee, D. S.; Kim, S. A Nucleolin-Targeted Multimodal Nanoparticle Imaging Probe for Tracking Cancer Cells Using an Aptamer. *Journal of Nuclear Medicine* **2010**, *51* (1), 98–105. <https://doi.org/10.2967/jnumed.109.069880>.
- (151) Du, K.; Lei, P.; Dong, L.; Zhang, M.; Gao, X.; Yao, S.; Feng, J.; Zhang, H. In Situ Decorating of Ultrasmall Ag<sub>2</sub>Se on Upconversion Nanoparticles as Novel Nanotheranostic Agent for Multimodal Imaging-Guided Cancer Photothermal Therapy. *Applied Materials Today* **2020**, *18*, 100497. <https://doi.org/10.1016/j.apmt.2019.100497>.

- (152) Rogov, A.; Irondelle, M.; Ramos Gomes, F.; Bode, J.; Staedler, D.; Passemard, S.; Courvoisier, S.; Yamamoto, Y.; Waharte, F.; Ciepielewski, D.; Rideau, P.; Gerber-Lemaire, S.; Alves, F.; Salamero, J.; Bonacina, L.; Wolf, J.-P. Simultaneous Multiharmonic Imaging of Nanoparticles in Tissues for Increased Selectivity. *ACS Photonics* **2015**, *2* (10), 1416–1422. <https://doi.org/10.1021/acsp Photonics.5b00289>.
- (153) Staedler, D.; Magouroux, T.; Hadji, R.; Joulaud, C.; Extermann, J.; Schwung, S.; Passemard, S.; Kasparian, C.; Clarke, G.; Gerrmann, M.; Le Dantec, R.; Mugnier, Y.; Rytz, D.; Ciepielewski, D.; Galez, C.; Gerber-Lemaire, S.; Juillerat-Jeanneret, L.; Bonacina, L.; Wolf, J.-P. Harmonic Nanocrystals for Biolabeling: A Survey of Optical Properties and Biocompatibility. *ACS Nano* **2012**, *6* (3), 2542–2549. <https://doi.org/10.1021/nn204990n>.
- (154) De Matos, R. J. Surface Functionalization of Metal Oxide Harmonic Nanoparticles for Targeted Cancer Imaging, EPFL, Lausanne, 2020. <https://doi.org/10.5075/epfl-thesis-7650>.
- (155) Vuilleumier, J. Functionalization of Second Harmonic Generation Nanoparticles for Theranostic Applications, EPFL, Lausanne, 2019. <https://doi.org/10.5075/epfl-thesis-7330>.
- (156) Clarke, G.; Rogov, A.; McCarthy, S.; Bonacina, L.; Gun'ko, Y.; Galez, C.; Le Dantec, R.; Volkov, Y.; Mugnier, Y.; Prina-Mello, A. Preparation from a Revisited Wet Chemical Route of Phase-Pure, Monocrystalline and SHG-Efficient BiFeO<sub>3</sub> Nanoparticles for Harmonic Bio-Imaging. *Sci Rep* **2018**, *8* (1), 10473. <https://doi.org/10.1038/s41598-018-28557-w>.
- (157) Dantelle, G.; Beauquis, S.; Le Dantec, R.; Monnier, V.; Galez, C.; Mugnier, Y. Solution-Based Synthesis Routes for the Preparation of Noncentrosymmetric 0-D Oxide Nanocrystals with Perovskite and Nonperovskite Structures. *Small* **2022**, *18* (30), 2200992. <https://doi.org/10.1002/sml.202200992>.
- (158) Fröhlich, E. The Role of Surface Charge in Cellular Uptake and Cytotoxicity of Medical Nanoparticles. *International Journal of Nanomedicine* **2012**, *7*, 5577–5591. <https://doi.org/10.2147/IJN.S36111>.
- (159) Stéen, E. J. L.; Jørgensen, J. T.; Johann, K.; Nørregaard, K.; Sohr, B.; Svatunek, D.; Birke, A.; Shalgunov, V.; Edem, P. E.; Rossin, R.; Seidl, C.; Schmid, F.; Robillard, M. S.; Kristensen, J. L.; Mikula, H.; Barz, M.; Kjær, A.; Herth, M. M. Trans-Cyclooctene-Functionalized PeptoBrushes with Improved Reaction Kinetics of the Tetrazine Ligation for Pretargeted Nuclear Imaging. *ACS Nano* **2020**, *14* (1), 568–584. <https://doi.org/10.1021/acsnano.9b06905>.
- (160) Jiang, T.; Laughlin, S. T. Chapter One - Enzyme- or Light-Triggered Cyclopropenes for Bioorthogonal Ligation. In *Methods in Enzymology*; Chenoweth, D. M., Ed.; Chemical Tools for Imaging, Manipulating, and Tracking Biological Systems: Diverse Chemical, Optical and Bioorthogonal Methods; Academic Press, 2020; Vol. 641, pp 1–34. <https://doi.org/10.1016/bs.mie.2020.04.034>.
- (161) Gerber, D. E. EGFR Inhibition in the Treatment of Non-Small Cell Lung Cancer. *Drug Development Research* **2008**, *69* (6), 359–372. <https://doi.org/10.1002/ddr.20268>.
- (162) Russo, A.; Franchina, T.; Rita Ricciardi, G. R.; Picone, A.; Ferraro, G.; Zanghi, M.; Toscano, G.; Giordano, A.; Adamo, V. A Decade of EGFR Inhibition in EGFR-Mutated Non Small Cell Lung Cancer (NSCLC): Old Successes and Future Perspectives. *Oncotarget* **2015**, *6* (29), 26814–26825.

- (163) Engelman, J. A.; Settleman, J. Acquired Resistance to Tyrosine Kinase Inhibitors during Cancer Therapy. *Current Opinion in Genetics & Development* **2008**, *18* (1), 73–79. <https://doi.org/10.1016/j.gde.2008.01.004>.
- (164) Macias-Romero, C.; Zubkovs, V.; Wang, S.; Roke, S. Wide-Field Medium-Repetition-Rate Multiphoton Microscopy Reduces Photodamage of Living Cells. *Biomed. Opt. Express* **2016**, *7* (4), 1458. <https://doi.org/10.1364/BOE.7.001458>.
- (165) Donovalová, J.; Cigáň, M.; Stankovičová, H.; Gašpar, J.; Danko, M.; Gáplovský, A.; Hrdlovič, P. Spectral Properties of Substituted Coumarins in Solution and Polymer Matrices. *Molecules* **2012**, *17* (3), 3259–3276. <https://doi.org/10.3390/molecules17033259>.
- (166) Hong, V.; Presolski, S. I.; Ma, C.; Finn, M. G. Analysis and Optimization of Copper-Catalyzed Azide–Alkyne Cycloaddition for Bioconjugation. *Angewandte Chemie* **2009**, *121* (52), 10063–10067. <https://doi.org/10.1002/ange.200905087>.
- (167) De Matos, R.; Gheata, A.; Campargue, G.; Vuilleumier, J.; Nicolle, L.; Pierzchala, K.; Jelescu, I.; Lucarini, F.; Gautschi, I.; Riporto, F.; Le Dantec, R.; Mugnier, Y.; Chauvin, A.-S.; Mazzanti, M.; Staedler, D.; Diviani, D.; Bonacina, L.; Gerber-Lemaire, S. Gd<sup>3+</sup>-Functionalized Lithium Niobate Nanoparticles for Dual Multiphoton and Magnetic Resonance Bioimaging. *ACS Appl. Nano Mater.* **2022**, *5* (2), 2912–2922. <https://doi.org/10.1021/acsnm.2c00127>.
- (168) *Preparation, Purification, and Characterization of Lanthanide Complexes for Use as Contrast Agents for Magnetic Resonance Imaging.* <https://app.jove.com/t/2844/preparation-purification-characterization-lanthanide-complexes-for> (accessed 2023-11-11).
- (169) Li, Y.; Liu, X. Tunable Acid-Sensitive Ester Protecting Groups in Oligosaccharide Synthesis. *Chemical Communications* **2014**, *50* (24), 3155–3158. <https://doi.org/10.1039/C3CC49205B>.
- (170) Potter, G. T.; Jayson, G. C.; Miller, G. J.; Gardiner, J. M. An Updated Synthesis of the Diazo-Transfer Reagent Imidazole-1-Sulfonyl Azide Hydrogen Sulfate. *J. Org. Chem.* **2016**, *81* (8), 3443–3446. <https://doi.org/10.1021/acs.joc.6b00177>.
- (171) Sminia, T. J.; Pedersen, D. S. Azide- and Alkyne-Functionalised  $\alpha$ - and  $\beta$ -Amino Acids. *Synlett* **2012**, *23* (18), 2643–2646. <https://doi.org/10.1055/s-0032-1317445>.
- (172) Liu, L.; Zhang, D.; Johnson, M.; Devaraj, N. K. Light-Activated Tetrazines Enable Live-Cell Spatiotemporal Control of Bioorthogonal Reactions. *bioRxiv* December 2, 2020, p 2020.12.01.405423. <https://doi.org/10.1101/2020.12.01.405423>.



## 7. Curriculum vitae

---

### Adrian S. Gheata

18.09.1997

Route de Crochy, 14  
1024 Ecublens, Switzerland

Telephone: +41 76 424 75 98

E-mail: [adrian.gheata@epfl.ch](mailto:adrian.gheata@epfl.ch)

### Professional experience

---

#### **Researcher in the development of functionalized biomaterials, Doctoral Thesis | 2020 - 2023**

Pr. GERBER, GBF LABORATORY | EPFL, Switzerland

Development of methods for surface modification of inorganic nanoparticles by coating with silica and functionalization with short peptides. Synthesis of photo-triggered drug delivery systems, grafting on nanoparticles and cellular tests. Synthesis of lanthanide complexes for imaging applications. Collaboration with groups from the Centre Hospitalier Universitaire de Lausanne (CHUV) and the University of Geneva (UNIGE) for cellular testing and imaging. Supervision of master projects and practical laboratory assistants (*Winner of the award for best teaching assistant in 2021*).

#### **Master Thesis | 2019**

Pr. GERBER, GBF LABORATORY | EPFL, Switzerland

Synthetic modification of chitosan-based polymers for gene vector development.

#### **Internship at Xsensio™ | 2018 - 2019**

INNOVATION PARK | EPFL, Switzerland

Investigation of new strategies for the electrochemical detection of lactate, as a biomarker in sweat.

#### **Semester Project in a Laboratory | 2018**

Pr. DYSON, LCOM LABORATORY | EPFL, Switzerland

Valorization of lignin by hydrogenation using a bimetallic catalyst for conversion into commercially interesting molecules.

#### **End of Bachelor Project (ERASMUS exchange) | 2017**

SPIVEY GROUP | Imperial College, London

Enantioselective desymmetrization of a pharmaceutical compound exhibiting a meso-diol group.

#### **Summer Internship at CERN | 2016**

SMB-SE-DOP DEPARTMENT | Geneva, Switzerland

Internship in geomatics as a surveyor.

## Education

---

### **PhD in Organic Chemistry and Nanoparticle Functionalization | 2023**

*EPFL*, Lausanne – Switzerland

### **Project management certificate PRINCE2® Foundation | 2022**

*Axelos Global Best Practice*

### **Master's in Molecular and Biological Chemistry | 2019**

*EPFL*, Lausanne – Switzerland, level 5.31 / 6

### **Bachelor's in Chemistry and Chemical Engineering | 2017**

*EPFL*, Lausanne – Switzerland, level 5.02 / 6

### **Certificate of Advanced English (CAE) | 2014**

*Cambridge*

### **Baccalaureat in Natural Sciences | 2014**

*Lycée International de Ferney Voltaire*, France, level « Very good » with congratulations of the jury

## Skills and Languages

---

**Synthesis:** laboratory techniques, development of synthetic pathway, nanoparticle functionalization, solid phase peptide synthesis, polymer functionalization

**Analytical:** NMR, MS, HPLC, DLS, FTIR, TEM

**Software:** Chemdraw, MestreNova, Topspin, Origin, Microsoft Office

**Romanian:** Mother tongue

**French:** Bilingual (C2)

**English:** Fluent (C1)

**Italian:** Basic (B1)

## Conferences

---

### **SNC (Swiss Nano Convention), Neuchatel | 2023**

*Poster presentation* - Multifunctional coating of lithium niobate nanoparticles for theranostic applications.

### **EuChemS Chemistry Congress, Lisbon | 2022**

*Poster presentation* - Functionalization of harmonic nanoparticles with lanthanide chelates for multimodal imaging applications.

### **SCS (Swiss Chemical Society) Fall Meeting, Zurich | 2022**

*Poster presentation* - Lanthanide-Functionalized Lithium Niobate Nanoparticles for Multimodal Imaging.

### **Galenus NanoGVA Symposium, Geneva | 2021**

*Oral communication* - Photoresponsive Nanocarriers based on Harmonic Nanoparticles for Cancer Theranostics.

**Nanomedicine International Conference, Milan | 2021**

*Poster presentation* - Functionalization of harmonic nanoparticles for multimodal imaging and theranostic applications.

**SCS (Swiss Chemical Society) Fall Meeting, Online | 2021**

*Virtual Poster* - Functionalized harmonic nanoparticles for cancer theranostics and multimodal imaging.

**SCS (Swiss Chemical Society) Fall Meeting, Online | 2020**

*Virtual Poster* - Functionalization of harmonic nanoparticles for ultra sensitive imaging and theranostic applications.

## Publications

---

Nonclassical Nucleation and Crystallization of LiNbO<sub>3</sub> Nanoparticles from the Aqueous Solvothermal Alkoxide Route.

Riporto, F., Dhouib, A., **Gheata, A.**, Beaucquis, S., Molina, E., Guené-Girard, S., Galez, C., Bornet, A., Gautier-Luneau, I., Gerber-Lemaire, S., Monnier, V., Le Dantec, R. and Mugnier, Y., **2023**. *Small*, in press.

Modulating the Surface Properties of Lithium Niobate Nanoparticles by Multifunctional Coatings Using Water-in-Oil Microemulsions.

**Gheata, A.**, Spada, A., Wittwer, M., Dhouib, A., Molina, E., Mugnier, Y. and Gerber-Lemaire, S., **2023**. *Nanomaterials*, 13(3), p.522.

Photoresponsive Nanocarriers Based on Lithium Niobate Nanoparticles for Harmonic Imaging and On-Demand Release of Anticancer Chemotherapeutics.

**Gheata, A.**, Gaulier, G., Campargue, G., Vuilleumier, J., Kaiser, S., Gautschi, I., Riporto, F., Beauquis, S., Staedler, D., Diviani, D. and Bonacina, L., **2022**. *ACS Nanoscience Au*, 2(4), pp.355-366.

Gd<sup>3+</sup>-Functionalized Lithium Niobate Nanoparticles for Dual Multiphoton and Magnetic Resonance Bioimaging.

De Matos, R., **Gheata, A.**, Campargue, G., Vuilleumier, J., Nicolle, L., Pierzchala, K., Jelescu, I., Lucarini, F., Gautschi, I., Riporto, F. and Le Dantec, R., **2022**. *ACS Applied Nano Materials*, 5(2), pp.2912-2922.